Université de Lille

Sciences et Technologies

THÉSE

Présentée pour l'obtention du grade de:

Docteur de l'Université de Lille 1

Spécialité:

Sciences de la Matière, du Rayonnement et de l'Environnement

Soutenue le 31 janvier, 2018 par

Lei Li

Monitoring of aerosol chemical composition by remote sensing: Verification of the concept and methodology development

Jury composé de:

Lorraine A. REMER	Professor, U. of Maryland, Baltimore	Rapporteuse
Mian CHIN	Senior Scientist, NASA Goddard Space Flight Center	Rapporteuse
Gregory L. SCHUSTER	Senior Scientist, NASA Langley Research Center	Examinateur
Daven K. HENZE	Associate Professor, U. of Colorado, Boulder	Examinateur
Philippe GOLOUB	Professor, U. of Lille 1	Examinateur
Yevgeny DERIMIAN	Chargé de recherche, CNRS/U. of Lille 1	Co-encadrant
Oleg DUBOVIK	Directeur de recherche, CNRS/U. of Lille 1	Directeur de Thèse

Laboratoire d'Optique Atmosphérique
U.F.R de Physique Fondamentale
Université Lille 1- Sciences et Technologies
59655-Villeneuve d'Ascq, France

Résumé

La détermination de la composition chimique des aérosols atmosphériques est essentielle pour le climat terrestre et l'environnement. Néanmoins, les mesures in situ qui permettent d'accéder à cette composition sont limitées et les modèles de chimie-transport peuvent ne pas représenter bien la réalité. Notre travail de thèse a consisté à développer une nouvelle approche afin de remonter à la composition des aérosols à grande échelle par télédétection. Les modèles de mélange des composants des aérosols, soit par proportion en volume soit par l'approximation de Maxwell Garnett qui relient les propriétés optiques à la composition, ont été incorporés dans l'algorithme de restitution des propriétés atmosphériques (GRASP). La nouveauté du concept réside dans la restitution directe des composants chimiques de l'aérosol plutôt que dans une estimation indirecte à partir des propriétés optiques retrouvées. Les tests synthétiques ont montré une sensibilité des observations de satellite POLDER/PARASOL à la présence d'éléments chimiques clés des aérosols. La méthodologie a ensuite été appliquée aux mesures réelles. Les caractéristiques optiques dérivées de PARASOL en utilisant le module de composition chimique ont montré un bon accord (R de ~ 0,9 pour l'épaisseur optique) avec nos mesures de la référence — le réseau AERONET. La méthodologie a aussi été appliquée aux mesures de AERONET. Les variabilités spatiale et temporelle de la composition de l'aérosol ainsi retrouvée correspondent bien à nos attentes. La composition obtenue a également été validée à l'aide de données de campagne du terrain et a pu être comparée avec les simulations réalisées avec le modèle chimie-transport GOCART.

Mots-clés: aérosol atmosphérique, composition chimique des aérosols, télédétection, observations par satellite, observations photométriques

Abstract

Determination of atmospheric aerosol chemical composition has a great importance for Earth's climate and environment. However, in situ measurements that enable determination of aerosol composition are limited in time and space, while simulations by chemical transport models may not accurately describe the reality. The current thesis presents a novel methodology for monitoring of aerosol composition by remote sensing on large spatial and temporal scale. Namely, the volume-weighted and Maxwell-Garnett models, which link the aerosol optical properties and aerosol composition, were incorporated into the first versatile algorithm (GRASP) that derives the atmospheric properties from remote sensing. The concept proposes the direct retrieval of fractions of aerosol compositions instead of post-processing estimate of the aerosol composition from the retrieved optical properties (refractive index, aerosol sizes). The tests showed sufficient sensitivity of the POLDER/PARASOL satellite observations to presence of key aerosol compositions. Then, the methodology was applied for the real PARASOL measurements. The aerosol optical characteristics derived from PARASOL using the aerosol composition module demonstrated a good agreement with our reference measurements – AERONET ground-based network (e.g., R of ~ 0.9 for AOT). The methodology was then applied to the AERONET measurements as well. The obtained spatial and temporal patterns of aerosol composition agree well with known physical expectations. The retrieved aerosol composition was inter-compared with available field campaign data and with GEOS-5/GOCART chemical transport model simulations.

Keywords: atmospheric aerosol, aerosol composition, remote sensing, satellite observation, photometric observation

Acknowledgements

First of all, I would like to express my sincere gratitude to my mentors, Oleg Dubovik and Yevgeny Derimian, for their wise guidance and continuous support. Their patience and illuminating instruction made it possible for me to reach this stage of my research. Thanks to Yevgeny Derimian for his hearty participation and assistance in my first steps in France. I'm grateful to Zhengqiang Li from Institute of Remote Sensing and Digital Earth, CAS. Thanks for his supporting and encouraging me to make the PhD thesis in LOA.

Thanks to the CaPPA project (Chemical and Physical Properties of the Atmosphere) that is funded by the French National Research Agency (ANR) through the PIA (Programme d'Investissement d'Avenir) under contract "ANR-11-LABX-0005-01" and thanks to the former director of CaPPA Labex project, Didier Tanré.

I am deeply indebted to the members of the jury, Philippe Goloub, Gregory L. Schuster, Lorraine A. Remer, Mian Chin, and Daven K. Henze for their well-focused questions and for the discussions that is helpful to shape and polish my thesis manuscript. I'm grateful to Gregory L. Schuster from NASA for his instructive advice and useful suggestions on implementing the optimum configuration of aerosol composition conversion model in the algorithm.

Special thanks to Tatyana Lapionak, Fabrice Ducos, David Fuertes, Pavel Litvinov, Anton Lopatin, Xin Huang, Benjamin Torres and all of the GRASP team for their continued technical support of the scientific codes used in this thesis.

I sincerely appreciate to Anne Priem, Marie-Lyse Liévin, Romain De Filippi, François Thieuleux and all the members of LOA for their support and hospitality in the laboratory life.

Thanks to my friends and fellow students Cheng Chen, Qiaoyun Hu, Luica Deaconu, Laura Rivellini, Florin Unga, Ioana Popovici for the Laser Game and all the fun.

Finally, my thanks would go to my beloved family for their loving considerations and great confidence in me all through these years and thank you for being there all the time.

Contents

List of Figures

List of Tables

Chapter 1

Introduction

"Reading is to the mind what exercise is to the body."

------ Joseph Addison

1.1 General context

Aerosol is generally defined as a suspension of solid particles or liquid droplets in a gas, with diameters in the range of 10^{-9} – 10^{-4} m (Seinfeld et al., 1998; Bernstein et al., 2004; Finlayson-Pitts, et al., 1997; Hinds, 1999). Such particles suspended in the atmosphere originate from a wide variety of natural and anthropogenic sources. Primary particles are directly emitted from sources such as biomass burning, incomplete combustion of fossil fuels, volcanic eruptions, and wind-driven or traffic-related suspension of road, soil, and dust, sea salt, and biological materials. Secondary particles are defined as the particles formed by gas-to-particle conversion (nucleation and condensation) in the atmosphere. Figure 1.1 shows the main sources and sinks of atmospheric aerosol. There are two main sinks of aerosol: dry deposition and wet deposition. Depending on aerosol properties and meteorological conditions, the lifetime of aerosol in the atmosphere ranges from hours to weeks (Raes et al., 2000; Williams et al., 2002).

Aerosols (sometimes referred to particulate matter or "PM", especially in air quality applications) exert a variety of impacts on the environment. Exposure to PM is the fourth largest overall health risk factor globally and the largest environmental risk factor leading to more than 6 million deaths annually (~ 12% of total deaths) (Ault and Axson, 2017). Aerosols concentrated near the surface are correlated with severe health effects including enhanced mortality, cardiovascular, lung cancer, respiratory, and allergic diseases (Dockery et al., 1989; Pope et al., 1991, 2002, 2004, 2009; Pope and Dockery, 1992; Brook et al., 2010; Wellenius

et al., 2012; Bernstein et al., 2004; Gauderman et al., 2004; Katsouyanni et al., 2001; Samet et al., 2005; Dockery et al., 1993; Schwartz et al., 1996), as well as with new associations still being identified, such as those with Parkinson's and Alzheimer's diseases (Ritz et al., 2016; Jung et al., 2015). Comprehensive investigations, understanding, and controlling of aerosol health effects need to consider not only the particulate and components of aerosols, but also their chemical reactivity and aging (Pöschl, 2002).

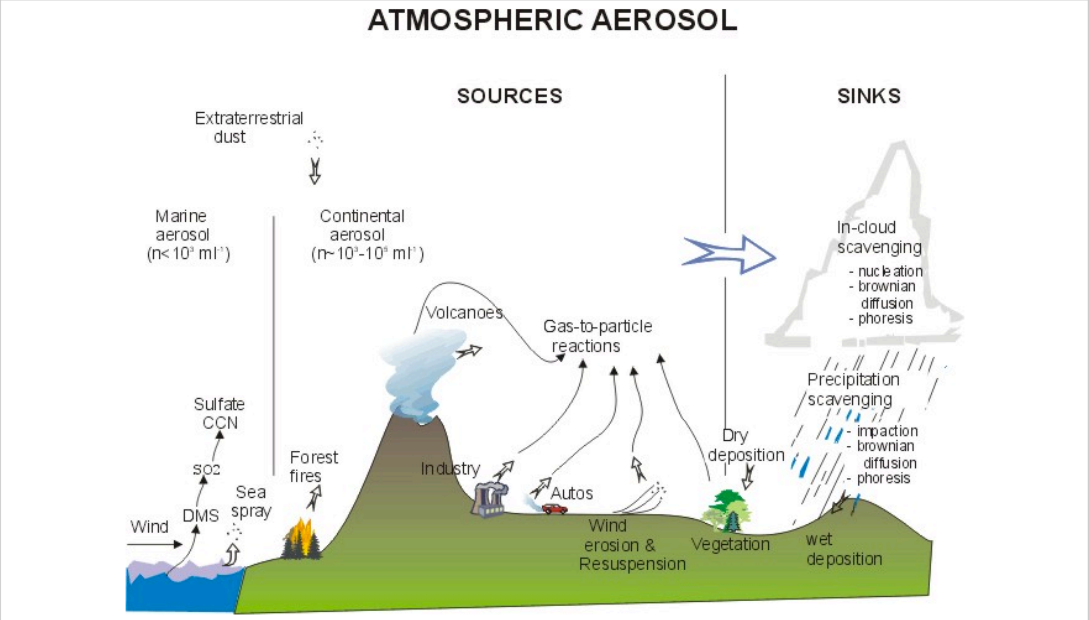

Figure 1.1: The main sources and sinks of atmospheric aerosol, taken from https://www.e-education.psu.edu/meteo300/node/671.

Atmospheric aerosols play an important role in the complex physico-chemical processes that impact Earth's climate. Aerosols influence the climate directly and indirectly (see Figure 1.2). Aerosol direct effect is associated with scattering and absorption of radiation that influences the radiative balance of the Earth-atmosphere system. The sign of the radiative forcing can be positive or negative depending on aerosol properties (chemical compositions, single scattering albedo) and surface albedo (Haywood and Shine, 1995; Haywood and Boucher, 2000). The indirect effect refers to aerosol influence on radiative properties, amount and lifetime of clouds (Ramanathan et al., 2001). Aerosol indirect effects could be subdivided into three different parts: Twomey (Twomey, 1974, 1977), Albrecht (Albrecht, 1989) and semi-direct effects, as illustrated in Figure 1.2. In Twomey effect, aerosol affects cloud formation by providing additional nuclei for droplet or ice crystals growth, referring to the enhanced reflection of solar radiation due to the more but smaller cloud droplets (Boucher, 1999; Lohmann et al., 2003; Lohmann and Feichter, 2005; Lohmann and Hoose, 2009). In Albrecht effect, aerosol changes clouds lifetime (Albrecht, 1989) and other cloud properties

like liquid water content and cloud top height (Pincus and Baker, 1994). The evaporation of cloud droplets within the clouds is increased as the absorption of solar radiation in clouds, which may affect the presence of clouds. Such effect is called the semi-direct effect. All indirect effects are highly dependent upon aerosol quantity, altitude (Koch and Del Genio, 2010), cloud type (Feingold et al., 2003) and the local meteorological conditions. Aerosol chemical composition affects their ability to act as cloud condensation nuclei (CCN) and rain development in a number of ways. For example, soluble particles mostly composed of sulfates or nitrates are effective CCN because they rapidly reach their critical size under relatively low supersaturation (Radke, 1983; Leaitch et al., 1982). The presence of soluble species (e.g., sulfate) converts mineral dust particles into effective giant CCN (Levin et al., 1996; Levi and Rosenfeld, 1996).

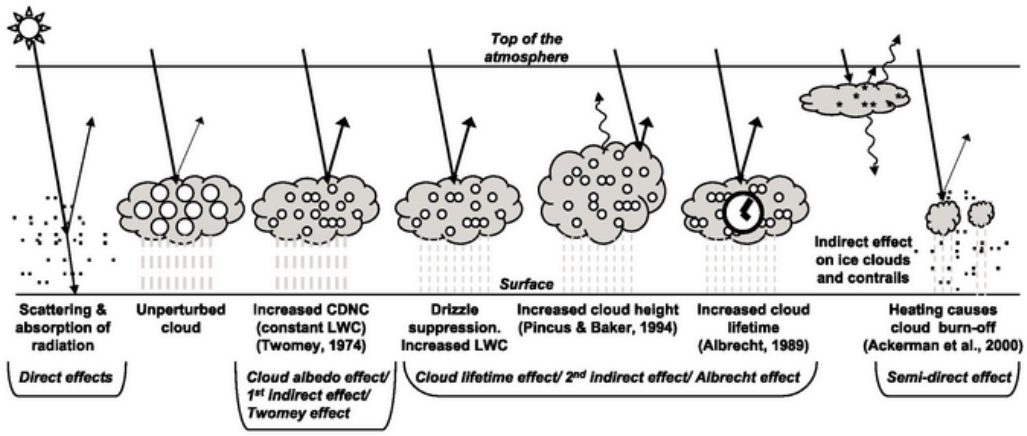

Figure 1.2: Schematic diagram showing the various radiative mechanisms associated with cloud effects that have been identified as significant in relation to aerosols (courtesy of Haywood and Boucher, 2000). The small black dots represent aerosol particles and the larger open circles represent cloud droplets. Straight lines symbolize the incident and reflected solar radiation, and wavy lines symbolize terrestrial radiation. The filled white circles indicate cloud droplet number concentration (CDNC). The unperturbed cloud contains larger cloud drops as only natural aerosols are available as cloud condensation nuclei, whereas the perturbed cloud contains numerous smaller cloud drops as both natural and anthropogenic aerosols are available as cloud condensation nuclei (CCN). The vertical grey dashes symbolize rainfall, and LWC refers to the liquid water content.

Radiative forcings change the energy fluxes of solar radiation and terrestrial radiation; it can be associated with anthropogenic or natural changes in atmospheric compositions, Earth surface properties, or solar activity. Negative forcing indicates cooling of the Earth's surface-atmosphere system, whereas positive forcing indicates the warming. The current aerosol radiative forcing relative to that in pre-industrial times is estimated to be around -1 to -2 W/m^2, as opposed to a greenhouse gas forcing of about +2.4 W/m^2 (Houghton et al., 2001; Lohmann and Feichter, 2005; Andreae et al., 2005). Figure 1.3 illustrates the sign and

intensity of radiative forcings of the main constituents in the atmosphere. The radiative forcings of greenhouse gases are estimated with a very high level of scientific understanding. However, radiative forcings of aerosols have large uncertainty and the level of scientific understanding of indirect aerosol effect on climate is low (Myhre et al., 2013). One of the greatest challenges in estimating the aerosol impacts on climate is the immense diversity, not only in particle size, composition and origin, but also in their spatial and temporal distribution (Chin et al., 2009b). Because of the limited accuracy in the knowledge of aerosol sources, compositions and properties, the actual effects of aerosols on climate and health are still far from being well understood and quantified. Specifically, the aerosol columnar properties and compositions together with wide spatial and extensive temporal coverage are important for aerosol forcing estimations and climatic studies both on global and regional scale (Pilinis et al., 1995; Costa et al., 2004).

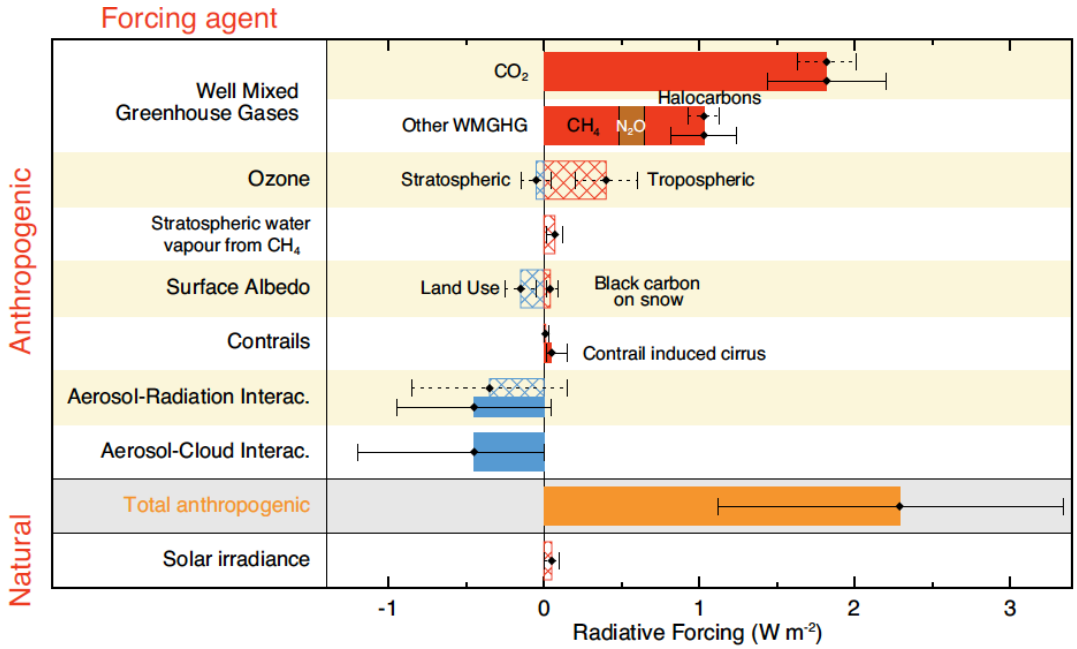

Figure 1.3: Radiative forcing of climate between 1750 and 2011, according to IPCC 2013 (Myhre et al., 2013).

Atmospheric aerosol can also have an effect on the environment via biogeochemical cycles. For example, mineral dust and iron oxide contained in minerals have an effect on marine productivity through deposition and brining the nutrients to phytoplankton and ocean life (Zhu et al., 1993). The iron oxide imposes effects on the rate of nitrogen fixation by microorganisms to influence the global carbon cycle (Sarthou et al., 2003; Mills et al., 2004; Moore et al., 2002).

1.2 Motivation

Information about atmospheric aerosol chemical composition has a great importance for monitoring and understanding of various aspects of climate and environment. This information can be obtained by laboratory analysis of sampled aerosol. However, the in-situ measurements require considerable effort and represent only small areas without providing results on wide spatial and temporal scale. It is known that chemical transport models are able to represent chemical component concentrations with wide spatial and temporal coverage. The capability of aerosol model simulation has developed rapidly in the past decade. There were only a few global models that could evaluate one or two aerosol components in the late 1990s, but now a few dozen global models can simulate a comprehensive suite of aerosols in the atmosphere. However, the models have uncertainties because they are initialized by gridded emission inventories that are highly uncertain in the present day. For example, the carbon emissions inventories can be uncertain with a factor of two and this uncertainty is carried forward to the model output (Bond et al., 1998; Cooke et al., 1999; Streets et al., 2001). In addition, prediction of the natural components, such as dust or iron concentrations, depends on wind speeds and local mineralogy, and thus can be even more uncertain (Kaufman et al., 2005a).

Currently, global observations of aerosols from satellites (mainly aerosol optical thickness) have well-defined accuracies, which can provide an opportunity to validate model simulations at large spatial and temporal scales. Using data integration or objective analysis, the information on aerosols obtained from satellite measurements can be applied to constrain aerosol model simulations and the assessment of aerosol direct radiance forcing (e.g., Collins et al., 2001; Yu et al., 2003, 2004, 2006; Liu et al., 2005; Zhang et al., 2008a). The aim of data assimilation is to minimalize the discrepancies between the models and observations, and to form an optimal estimation of aerosol distributions. The integration can fill gaps in satellite retrievals and make global distributions of aerosol have good agreement with ground-based measurements (Yu et al., 2003, 2006; Liu et al., 2005). In order to reduce large aerosol simulation uncertainties, the inverse modeling can be used. For instance, Dubovik et al. (2007) showed the ability to retrieve global aerosol sources by inverse modeling relying on satellite observations. Therefore, the integration of models with satellite retrievals practice provides a possibility of improving aerosol simulations of the pre- and post-satellite eras. However, besides the aerosol emission sources, an accurate modeling of atmospheric aerosols and their effects also requires information about particles composition and complex atmospheric processes. In order to evaluate the aerosol mass concentrations, models should include not

only the aerosol and precursor emissions, but also the chemical transformation, transport, and removal processes. The lack of comprehensive dataset providing multiple constraints for the key parameters simulated in the model has hindered the improvement of model simulation. Specifically, improving the capability of aerosol composition estimation will require improved remote sensing and in situ observations to discriminate among aerosol components. The constraints of large model diversities in aerosol composition, size, vertical distribution and mixing state should be based on reliable measurements with adequate spatial and temporal coverage. For a realistic and meaningful assessment of the aerosol chemical compositions, it is crucial to constrain the model results globally by comparing them with global coverage observations. The retrieved aerosol compositions from satellite observations can therefore improve the accuracy and capability of model simulation of aerosols (including components and atmospheric processes) and aerosol direct radiative forcing. The accuracy and specification of the aerosol composition as retrieved from satellite observations should also approach the requirements of the chemical transport models. At the same time, the challenge is to formulate the aerosol composition parameters that can be successfully retrieved by remote sensing measurements given their sensitivity to the aerosol optical properties and complex refractive index in particular.

An example of satellite observations that provide global coverage is POLDER/PARASOL (Deschamps et al., 1994; Tanré et al., 2011) space instruments. The implementation of multi-wavelength, multi-angle and polarization measuring capabilities has made it possible to derive the particle properties (size, shape and absorption) (Dubovik et al., 2011; Waquet et al., 2013) that are essential for characterizing and estimating aerosol compositions from satellite observations. So far, the aerosol compositions with global or large coverage cannot be retrieved from satellite measurements. However, following the idea of Schuster et al. (2005, 2009, 2016) and applications for ground-based network of Sun/sky photometers AERONET, a method of retrieving the aerosol composition from remote sensing observations can be incorporated into the satellite retrievals as well. The current PhD work presents an effort on methodology development of aerosol composition retrieval from satellite remote sensing and incorporation of aerosol composition retrieval into the GRASP (Generalized Retrieval of Aerosol and Surface Properties) algorithm (Dubovik et al., 2011, 2014), which is designed to retrieve an extended set of atmospheric parameters from remote sensing data including satellite observations with wide spatial and extensive temporal coverage.

1.3 Objectives

The main objective of this PhD work is to offer an approach that monitors the aerosol compositions from space-borne remote sensing observations, which can provide observationally-based results with wide spatial and extensive temporal coverage. Such objective is expected to both reduce the influence of aerosol modeling uncertainties on the retrieval results, and to provide additional constraints in situations where remote sensing observations do not have enough sensitivity to refractive index variability throughout the measured spectral range. That is, the variability of complex refractive index is constrained in the retrieval by the assumed aerosol composition conversion model. At present, the most advanced methods that involve retrieval of aerosol compositions from remote sensing measurements fit the intermediate retrieval of the refractive index (Schuster et al., 2005, 2009, 2016; Arola et al., 2011; Wang et al., 2013; Li et al., 2013, 2015). In the approach suggested in this thesis work, the algorithm should retrieve aerosol compositions directly from remote sensing measurements, without intermediate retrieval of the complex refractive index. The developments are also dedicated to satellite observations in order to provide wide spatial and extensive temporal coverage. The developed algorithm should then be applicable for ground-based Sun/sky photometric measurements because this type of measurements usually presents a higher sensitivity to aerosol absorption than the satellite remote sensing.

One of the principal difficulties is the identification of an adequate model for linking refractive index to aerosol compositions. Indeed, on the one hand, the conversion model should cover entire range of aerosol complex refractive index and, on the other hand, it should provide unique correspondence between each spectral realization of refractive index and aerosol compositions. Therefore, the primary objective is focusing on identification of an optimal “physico-chemistry to refractive index” conversion model. Firstly, using a simplified volume-weighted conversion model to test the retrieval approach and minimize the uncertainties of retrievals. Secondly, the volume-weighted conversion model is updated with the Maxwell-Garnett conversion model when the optimum configuration is found. In addition, a series of sensitivity tests using synthetic data were conducted. Such approach distinguishes amongst the assumed aerosol compositions and provides more accurate information about both vertical and columnar properties of aerosols.

The last but not least objective of this work is to apply the realization of the proposed algorithm in a variety of realistic application scenarios, including both satellite observations and ground-based remote sensing measurements.

The technique involves finding the best combination of aerosol composition fraction by fitting the complete set of PARASOL observations in all spectral channels and including both measurements of total radiances and linear polarization. The aim is also that the product will become a useful data for the modelers to evaluate their model results, within the uncertainties of our retrieval, over regions where otherwise no data on aerosol composition is available.

1.4 Thesis layout

This PhD thesis consists of seven following chapters.

First chapter provides a general context, motivation and objectives of thesis.

Second chapter is a summary of aerosol properties, as well as the remote sensing techniques both ground-based and space-borne satellite measurements.

Third chapter is dedicated to a detailed summary of the GRASP algorithm and provides description of the developed in this thesis work aerosol composition to optics conversion. The chapter also deals with the sensitivity tests of the approach to illustrate both the possibilities and limitations of the aerosol composition retrievals.

Fourth chapter contains detailed illustrations and discussions of the algorithm performance derived from real POLDER/PARASOL satellite observations over Africa. In this chapter, the spatial and temporal properties of aerosol composition retrieved by two different aerosol composition conversions are discussed in detail. This chapter also uses the ground-based AERONET measurements to validate the retrievals of aerosol optical properties obtained from the new aerosol composition model approach and compares the composition retrievals with the GEOS-5/GOCART model simulation.

Fifth chapter investigates the distributions of atmospheric aerosol compositions on a global scale.

Sixth chapter shows the application of the aerosol composition approach to ground-based AERONET measurements in a variety of typical aerosol cases.

Seventh chapter contains the conclusions and perspective of the whole work, as well as the limitations of the algorithm.

Chapter 2

Remote sensing of atmospheric aerosols

"All the resources we need are in the mind."

------ Theodore Roosevelt

2.1 Atmospheric aerosol properties

Atmospheric aerosol particles have three principal sets of properties: microphysical, optical and chemical. Microphysical property characterizes the morphology (size and shape) of the particles, optical property characterizes the interactions (scattering and absorption) between aerosol particles and light, and chemical property characterizes the species and fractions of aerosol compositions.

2.1.1 Microphysical properties

Aerosol particles could be characterized by shape and size, which describe their microphysical properties. The shape of aerosol particles is variable and may be irregular, whereas droplet aerosols are mostly spherical. Studies of scanning electron microscopy have shown that solid aerosol particles could have different shapes associated with their compositions and sources (e.g., cubic: salts, lattice: dust, and agglomerates of spheres: soot).

Particle size is one of the key parameters for characterizing the aerosol physical properties. It extends over four orders of magnitude, from a few nanometers to several tens of microns. Because the particles have complex shapes and undergo reactions (nucleation, coagulation and condensation) during the time that they exist in the atmosphere, it is difficult to describe the size of particles. Suitable for the characterization of the size, an aerodynamic diameter is

often used, which is defined as the diameter of a spherical particle with a density of 1 g/cm^3 should be to present the same setting velocity as the particle under review. As shown in Figure 2.1, aerosol particles are classified into separate modes according to their sizes (aerodynamic diameter), formation process and atmospheric age. There are three most commonly observed modes: nucleation (also called "Aitken", A), accumulation (B) and coarse mode (C). Nucleation and accumulation mode particles can be collectively called fine mode.

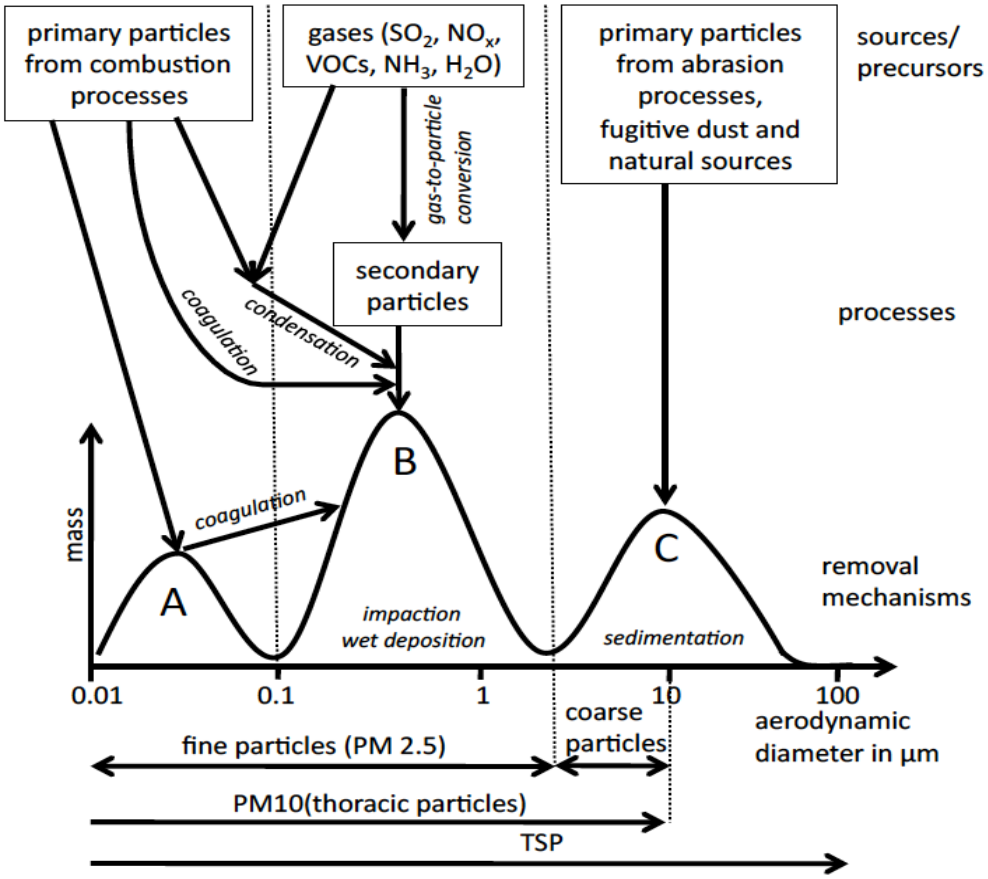

Figure 2.1 Schematic view of the size ranges of atmospheric aerosols in the vicinity of the sources and the principal processes involved (courtesy of Kacenelenbogen, 2008).

The nucleation mode particles with diameter between 0.01 to 0.1 µm are formed from ambient temperature gas-to-particle conversion and condensation of hot vapour during combustion processes. These particles act as nuclei for the condensation of low vapour pressure gaseous species, making them to grow into the larger mode. The particles induced by gas-to-particle conversion processes, with diameter less than 0.01 µm, are known as ultrafine particles. Such smallest particles have been observed in bursts of very large numbers in the presence of either biogenic or anthropogenic emissions under favorable local conditions in many different environments, including forests (Kulmala et al., 2004) and coastal zones (O'Dowd et al., 2002), and have been referred to as the nucleation mode.

The accumulation mode represents a radius between 0.1 to 1.0 μm. The particles in such mode are generated from the aggregation of smaller particles, from the condensation of gases or the re-evaporation of droplets. In addition, the incomplete combustion of fuels (e.g., coal, gasoline) and wood can produce particles in the size of accumulation mode. Such particles are comprised by substantial amounts of organic materials as well as soluble inorganics such as ammonium, nitrate and sulfate.

The coarse mode corresponds to particles with diameter larger than 1 μm. These particles are primarily produced by mechanical processes and introduced directly into the atmosphere from both natural and anthropogenic sources. Dust, soil and biological particles blown into the atmosphere by winds are the significant sources. The bursting of bubbles in the ocean also generates coarse particles. It is noted that anthropogenic coarse particles could be generated in the industrial and agricultural activities.

Mathematically, the lognormal distribution can well describe a population covering a wide range of sizes. Variation in the number of particles n as a function of the natural logarithm of the radius r can be expressed as:

$$n(r) = \frac{dN}{dlnr} = \frac{n_0}{\sigma_0\sqrt{2\pi}} exp[-\frac{(lnr-lnr_0)^2}{2\sigma_0^2}], \quad (2.1)$$

where $n(r)$ represents the number of particles within the natural logarithm of the radius between lnr and $lnr + dlnr$, r_0 represents the modal radius, σ_0 represents the standard deviation of the natural logarithm of the radius and n_0 represents the number of particles in the mode considered.

The distribution of the surface area (S(r)) is more appropriate for characterizing the chemical reactions involved in aerosol particles, but can also be used in remote sensing applications. It can be expressed as:

$$\frac{dS}{dlnr} = \frac{S_0}{\sigma_2\sqrt{2\pi}} exp[-\frac{(lnr-lnr_2)^2}{2\sigma_2^2}], \quad (2.2)$$

where S_0 represents the surface area of particle in the mode considered

The distribution of volume is widely used in remote sensing, but also to evaluate the mass of aerosols and is written as:

$$\frac{dV}{dlnr} = \frac{V_0}{\sigma_3\sqrt{2\pi}} exp[-\frac{(lnr-lnr_3)^2}{2\sigma_3^2}], \quad (2.3)$$

where r_3 and σ_3 represents the modal radius and the standard deviation of the natural logarithm of the radius, respectively. V_0 is the volume concentration of particles. Knowing that the standard deviations remain unchanged ($\sigma_0 = \sigma_2 = \sigma_3$).

The most used is bi-modal lognormal size distribution. A multi-modal distribution can be implemented simply by a sum of lognormal distributions.

2.1.2 Optical characteristics

Aerosol optical depth and extinction coefficient, Ångström Exponent, complex refractive index, single scattering albedo and phase matrix are the key optical parameters that are important for determination of the aerosol radiation effects.

Aerosol optical depth

Aerosol optical depth (also called aerosol optical thickness, AOT) is a measure of the amount of incident light either scattered or absorbed by airborne particles. The aerosol optical depth is a dimensionless quantity, the integral of the product of particle number concentration and particle extinction cross-section along a path length through the atmosphere, usually measured vertically.

From the Bouguer-Lambert-Beer law, the sun irradiance E(λ, z) at wavelength λ at an altitude z above sea level is expressed as (Bohren and Huffman, 1983):

$$E(\lambda, z) = t_g(\lambda, z)E_0(\lambda)e^{-\tau(\lambda,z)m}, \tag{2.4}$$

where $E_0(\lambda)$ characterizes the extraterrestrial sun irradiance, $t_g(\lambda, z)$ characterizes the gaseous transmission, m characterizes an airmass proportional to $1/cos(\theta_s)$ when refraction is neglected, θ_s characterizes a solar zenith angle, $\tau(\lambda, z)$ characterizes the spectral total optical depth of the atmospheric layer from altitude z to the top of the atmosphere and it consists of aerosol extinction and molecular (Rayleigh) scattering optical depths, written as:

$$\tau(\lambda, z) = \tau^a_{ext}(\lambda, z) + \tau^m_{ext}(\lambda, z). \tag{2.5}$$

The thickness of optical absorption and scattering comprise aerosol optical depth τ^a_{ext} representing the extinction of radiation by aerosol layer integrated along the atmospheric column. It is written as:

$$\tau^a_{ext}(\lambda, z) = \int_z^{TOA} \sigma^a_{ext}(\lambda, z')dz'. \tag{2.6}$$

Thus,

$$\sigma^a_{ext} = \frac{d\tau^a_{ext}}{dz}. \tag{2.7}$$

For spherical aerosols, the extinction coefficient $\sigma^a_{ext}(\lambda, z)$ (m^{-1}) is defined as:

$$\sigma_{ext}(\lambda, z) = \int_0^{\infty} \pi r^2 Q_{ext}(m, r, z, \lambda)n(r, z)dr, \tag{2.8}$$

where the extinction efficiency factor Q_{ext} is associated with the complex refractive index m, the particle size r, altitude z and the wavelength λ.

Ångström parameter

Ångström Exponent (Ångström, 1929) α is determined by the spectral dependence of the aerosol optical depth and provides information on the particle size. It is written as:

$$\tau(\lambda) = \tau(\lambda_0)(\frac{\lambda}{\lambda_0})^{-\alpha}. \quad (2.9)$$

The stronger the spectral dependence of the aerosol optical depth, the larger the Ångström coefficient, and the smaller are the particles. If the value of Ångström Exponent is 0, it indicates the very large particles such as desert dust. If the value of Ångström Exponent is about 2, it indicates dominance of very fine particles such as urban pollution aerosol (Eck et al., 1999). It is noted that sometimes Ångström Exponent can have a slightly negative value when a population of large particles distributed on a single mode.

Complex refractive index

The complex refractive index of aerosol is related to particles composition and also affects aerosol optical properties such as the phase matrix and the single scattering albedo. It is expressed as:

$$m = n + ik, \quad (2.10)$$

where n and k represent, respectively, real and imaginary parts of the complex refractive index.

The real part n indicates the speed of propagation in the medium and provides information on the deflection of light by the particle. For atmospheric aerosol it ranges generally from 1.33 (aerosol saturated water) to 1.55 (mineral aerosol), but can reach even higher than 1.95 in the visible range for soot particles (Bond and Bergstrom, 2006). The imaginary part k is associated with the absorption properties of aerosols. It is nearly 0 for purely scattering aerosols (e.g., ammonium nitrite) and 0.79 for the most absorbing aerosols (e.g., soot particles) (Bond and Bergstrom, 2006).

Single-scattering albedo

The single-scattering albedo ω_0 (SSA) is defined as the ratio of the scattering coefficient to the extinction coefficient of an ensemble of particles and is expressed as:

$$\omega_0 = \frac{\sigma_{scat}}{\sigma_{ext}}. \quad (2.11)$$

The absorption properties are directly associated with aerosol chemical compositions, as well as with the refractive indices of the aerosols. More the aerosol particles are absorbing, higher the imaginary part of the refractive index is, and smaller ω_0 is. The absorption of aerosol is mainly determined by the presence of black carbon (BC), e.g., the SSA at 0.55 μm wavelength is equal to 0.15 to 0.30 (Bond and Bergstrom, 2006), whereas for brown carbon (BrC) and absorbing mineral dust (due to iron oxides) the SSA at 0.55 μm is about 0.75 (Tanré et al., 2001; Schnaiter et al., 2005). Whereas for other non-absorbing species such as sulfates, organic carbon (OC), sea salt and non-absorbing dust the SSA at 0.55 μm is 0.98 to 1 (Penner et al., 2001; Cooke et al., 1999; Hess et al., 1998).

Phase function

Phase function describes the angular distribution of light scattering by a particle or an ensemble of particles. It is normalized as:

$$\int_{4\pi} P(\Omega) d\Omega = 4\pi, \tag{2.12}$$

where Ω is the solid angle. The scattering angle Θ is defined as the angle between the incident and scattering directions. If $\mu = \cos(\Theta)$, then

$$\int_{-1}^{1} P(\mu) d\mu = 2, \tag{2.13}$$

when the phase function presents a rotation symmetry in the azimuthal angle, which is the case of spherical particles and non-spherical randomly oriented particles. The phase function of aerosol is highly anisotropic with a very sharp diffraction peak for scattering angles between 0° and 5°.

The asymmetry parameter (g), indicating the moment of first order in the decomposition of the phase function in Legendre moments, is expressed as:

$$g = \frac{1}{2}\int_{-1}^{1} \mu P(\mu) d\mu. \tag{2.14}$$

The parameter g ranges from -1 for entirely back-scattering particles, to 0 for isotropic (uniform) scattering, to +1 for entirely forward-scattering, which provides information on the symmetry forward/back distribution of the particles scattering.

2.1.3 Chemical composition

Information about aerosol chemical composition can be crucial for studying aerosol effects on various atmospheric processes. At the same time, the atmospheric aerosol chemical composition is very complex and variable. Depending on the various sources and transformations undergone in the atmosphere, each particle may have individual composition.

Atmospheric aerosol generally consists of different amounts of crustal elements, carbonaceous compounds (elemental and OC) and other organic materials, sulfate, nitrate, ammonium and sea salt. Fine particles are primarily composed of sulfate, nitrate, ammonium, elemental and OC and certain trace metals (e.g., lead, cadmium, nickel, copper, etc.). The major components of coarse particle fraction are dust, crustal elements, nitrate, sodium, chloride and biogenic organic particles (e.g., pollen, spores, plant fragments, etc.). Crustal materials contained mostly in the coarse particle fraction predominantly originate from windblown mineral dust. The compositions and amounts of crustal materials are quite different as their different local geology and surface conditions at the emission areas.

Carbonaceous materials constitute a large but highly variable fraction of the atmospheric aerosol. The carbonaceous fraction of the aerosol consists of both elemental carbon or BC and OC that are mainly generated from combustion processes. The ratio of elemental to total carbon strongly depends on the sources. The main sources of elemental carbon particles are biomass and fossil fuel burning. OC particles are not only emitted from anthropogenic origin (burning of petroleum, wood, garbage, cooking meat, etc.), they can also be produced by secondary organic aerosol (SOA) formation during the atmospheric oxidation of biogenic or anthropogenic volatile organic compounds (VOC). VOCs come from combustion processes (fossil fuel and biomass) and have little chemical reactivity (Andreae and Crutzen, 1997).

The main precursors of sulfate component in the troposphere are sulfur dioxide (SO_2) emitted from anthropogenic sources and volcanoes, and dimethyl sulfide from biogenic sources, especially from marine planktons. In the stratosphere, sulfate aerosols mostly convert from carbonyl sulfide. According to the availability of gaseous ammonia to neutralize the sulfuric acid formed from SO_2, sulfate in aerosol particles is present as sulfuric acid, ammonium sulfate and intermediate compounds (Adams et al., 1999). Most SO_2 is converted to sulfate either in the gas phase or in cloud droplets that later evaporate (Weber et al., 1999).

Correspondingly, nitrate is formed mainly from the oxidation of atmospheric nitrogen dioxide (NO_2). Ammonium salts are also common compositions of atmospheric aerosols. They are formed during the reactions between ammonia (NH_3) and various acids, like sulfuric (H_2SO_4) and nitric acids (HNO_3). When atmospheric ammonia neutralizes these acids, ammonium sulfate ($(NH_4)_2SO_4$) and ammonium nitrate (NH_4NO_3) particles are formed.

The emission of sea salt is determined by wind on the surface of the ocean. Sea salt is dominant contributor of both light scattering and cloud nuclei. It is noted that the main source of chloride (Cl^-) is sea spray, but ammonium chloride (NH_4Cl) particles are formed during the reaction between ammonia and hydrochloric acid (HCl).

Therefore, in generally, typical chemical compositions of aerosols can vary at different locations, times, weather conditions and particle size fractions. In addition, aerosol chemical compositions can also be categorized by their water solubility. In continental regions, most of smaller particles are water-soluble as well as some types of coarse particles are water soluble, like sea salt particles over oceans. Most water-soluble aerosol compositions are hygroscopic. When aerosol particles contain water-soluble materials, the size of these particles can increase as the hygroscopic growth. Highly soluble particles (e.g., ammonium sulfate, ammonium nitrate and sodium chloride) are efficient cloud condensation nuclei (CCN). However, several particles are poorly soluble or insoluble in water such as particles derived from soil dust or volcanoes (e.g., metal oxides, silicates, clay minerals). At the same time, physico-chemical transformations during atmospheric transport can make hygroscopic even originally insoluble particles (e.g., Usher et al., 2003; Laskin et al., 2005).

2.2 Atmospheric aerosol remote sensing

The methods of aerosol remote sensing are categorized into two different groups: active and passive remote sensing. Both active and passive remote sensing observations can be implemented by the ground-based instruments or space-based sensors. Relying on these two different platforms, there are numerous investigations of atmospheric aerosols in recently years. Ground-based measurements provide good temporal but poor spatial coverage, whereas space-based measurements have the opposite characteristics. In the current work, the developments are primary dedicated to a space-based sensor POLDER. Since the ground-based photometric measurements are expected to have even better sensitivity to aerosol complex refractive index, the algorithm is tested with such type of measurements as well.

2.2.1 Ground-based remote sensing

In this section an overview of ground-based photometric measurements is provided. The specific focus is on observations by AERONET (AErosol RObotic NETwork) because these measurements are further employed in the presented study.

Observations by ground-based instruments generally can provide very detailed and accurate information about aerosol properties (Nakajima et al., 1996; Dubovik and King, 2000). At present, there are numerous global and regional networks consist of passive or/and active ground-based observations. The global AERONET (Holben et al., 1998) and South-Eastern SKYNET (Nakajima et al., 2007) networks of Sun photometers are passive remote sensing observations. The lidar networks including EARLINET (Bösenberg, 2000), ALiNe (Antuña et al., 2006), Cis-Linet (Chaikovsky et al., 2006) and GALION (Bösenberg and Hoff,

2007; Wandinger et al., 2004) are active remote sensing observations. Aerosol data provided by these networks with highly valuable information for investigating aerosol is widely applied to validate satellite observations and constrain aerosol properties in climate simulation efforts (Kinne et al., 2003, 2006; Textor et al., 2006; Koch et al., 2009).

AERONET (Holben et al., 1998) is a federation of regional and national network deployed in the 1990s by collaboration of the NASA (National Aeronautics and Space Administration) with LOA (Laboratoire d'Optique Atmosphérique, University of Lille) in the form of automatic stations for monitoring atmospheric aerosols. The original French component of the network is the AERONET/PHOTONS network (PHOtométrie pour le Traitement Opérationnel de Normalisation Satellitaire). The AERONET project was conducted to facilitate the characterization of the aerosol properties and validation of satellite measurements with reliable monitoring of global aerosol optical and microphysical properties. The global distribution of all available sites of the AERONET is shown in Figure 2.2. AERONET users are allowed to visualize and download data by choosing different periods and locations from the website.

The Sun and sky photometer (Cimel Électronique 318) was chosen as standard instrument for the AERONET. Such instrument covers a spectral range from 0.340 to 1.640 μm by 8 or 9 spectral channels. All instruments provide direct Sun and angular measurements of distribution of sky radiance in almucantar and principal plane configurations at least within the spectral channels of 0.440, 0.670, 0.870 and 1.020 μm. Direct Sun measurements are performed every 15 minutes and sky radiances are acquired every hour both for almucantar and principal plane configurations when the optical airmass is less than 2 to minimize the variations in radiance due to the change in optical airmass (Holben et al., 1998). The instrument is equipped with two robot axes allowing movements in azimuth and zenith plans. As a consequence, it covers any point in the celestial vault with an accuracy of 0.05° and a field of view of 1.2°. There are additional triplet observations of direct Sun measurements in 30 seconds afterwards per each wavelength, which is used for operational cloud screening (Smirnov et al., 2000).

All data collected by the AERONET Sun photometers are processed with the same algorithm (version 2) in the NASA's Goddard Space Flight Center (GSFC). There are several levels of data quality: level 1.0 indicates raw data; level 1.5 contains cloud screened, but final calibration is not applied; level 2.0 with cloud screening and final calibration is available after an operation period (about several months) as the re-calibrated.

Measurements performed within the AERONET could be divided into two groups: direct Sun measurements and sky radiance measurements. The direct Sun measurements allow the

determination of the attenuation of sunlight passing through the atmosphere containing aerosol particles, molecules, and absorbing gases at each spectral channel $I(\lambda)$, which is defined as the total optical depth of the atmosphere (τ). Under cloud-free conditions, the total optical depth (τ) consists of the aerosol scattering and absorption (τ_a), the molecular scattering or Rayleigh scattering (τ_m) and the gaseous absorption (τ_g). Therefore, the aerosol optical thickness (τ_a) can be derived from the total optical depth if the molecular optical thickness (τ_m) and the gaseous absorptions (τ_g) are known. The AOT is retrieved at wavelengths of 0.340, 0.380, 0.440, 0.500, 0.670, 0.870, 1.020 and 1.640 μm because of low or no absorption by atmospheric gases at these channels. The number of wavelength could vary with the different instrument types, but all instruments within the network utilize at least four standard spectral channels: 0.440, 0.670, 0.870 and 1.020 μm.

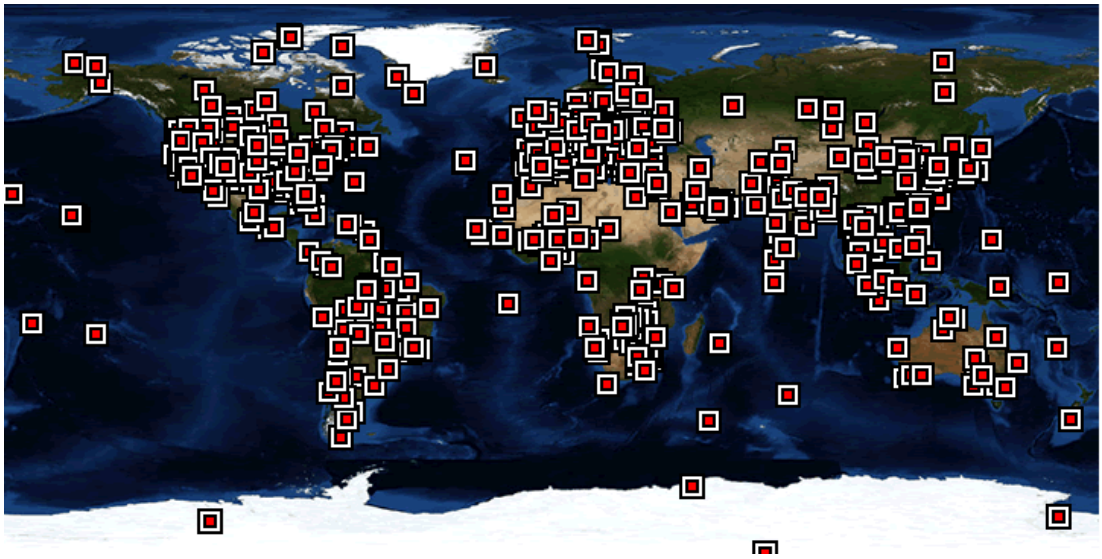

Figure 2.2: The global distribution of all available sites of the AERONET network, taken from https://aeronet.gsfc.nasa.gov/.

There are two geometries followed within AERONET to perform the sky radiance measurements: almucantar and principal plane (illustrated in Figure 2.3). The Sun photometers keep the zenith angle equal to the solar zenith angle θ_s in the almucantar configuration. The measurement sequence contains a direct Sun measurement executed previously to almucantar; afterwards the instrument covers the range from 3° to 180° of azimuth angles in both right and left branches. The observation angles of almucantar are depicted in Table 2.1. The sequence is repeated for each channel and the entire measurement takes about 5 minutes.

The almucantar radiance values are averaged between right and left branches when they are used in the AERONET inversion algorithm. This operation procedure is performed only for almucantar measurements and allows eliminating data contaminated by clouds: the

measurements with differences in radiances more than 20% between right and left branches are disregarded.

The azimuth angle remains equal to the solar azimuth angle in the principal plane geometry and the sky radiance measurements are performed for the different zenith angles (listed in Table 2.1) after a direct Sun measurement.

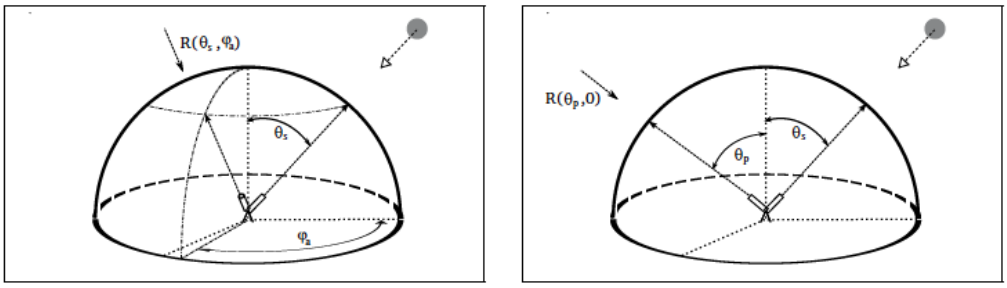

Figure 2.3: Illustrations of the two geometries (left: the almucantar; right: the principal plane) used for the measurements of the sky radiances (Torres, 2012).

The relations between the scattering angles (Θ), the observation angles (θ_v, ϕ_v), and the solar zenith and azimuth angles (θ_s, ϕ_s) are $\cos(\Theta) = cos^2(\theta_s) + sin^2(\theta_s)\cos(\phi_v - \phi_s)$ in the case of almucantar geometry and $\cos(\Theta) = \cos(\theta_v \mp \theta_s)$ for the principal plane geometry (Nakajima et al., 1996), where the sign is minus when $\phi_v - \phi_s = 0^\circ$ and plus for the case of $\phi_v - \phi_s = 180^\circ$. Consequently, the scattering angle observed with the almucantar geometry is limited by $0^\circ \leq \Theta \leq 2\theta_s$ reaching its maximum when $\phi_s = 180^\circ$. The maximum scattering angle in the principal plane measurement is the value of the maximum angle (θ_M) from the set of values of the principal plane (see Table 2.1), which fulfills the condition $\theta_m < 90^\circ - \theta_s$.

Table 2.1: Observation angles for sky radiance measurements in the almucantar and principal plane geometries. In the almucantar, angles are azimuth positions relative to the azimuth solar position (with two branches, right and left from the Sun). In the principal plane, angles are zenith angles relative to the zenith solar position (negative means below the Sun).

Measurement type	Observation angles
Almucantar	0, 2.0, 2.5, 3.0, 3.5, 4.0, 4.5, 5.0, 6.0, 6.0, 8.0, 10.0, 12.0, 14.0, 16.0, 18.0, 20.0, 25.0, 30.0, 35.0, 40.0, 45.0, 50.0, 60.0, 70.0, 80.0, 90.0, 100.0, 110.0, 120.0, 130.0, 140.0, 160.0, 180.0
Principal plane	0, -6.0, -5.0, -4.5, -4.0, -3.5, -2.5, -2.0, 2.0, 2.5, 3.0, 3.5, 4.0, 4.5, 5.0, 6.0, 6.0, 8.0, 10.0, 12.0, 14.0, 16.0, 18.0, 20.0, 25.0, 30.0, 35.0, 40.0, 45.0, 50.0, 60.0, 70.0, 80.0, 90.0, 100.0, 110.0, 120.0, 130.0, 140.0

The multi-wavelength and multi-angle sky radiance measurements provide the bulk of information about aerosol optical properties. The optical and microphysical properties of the aerosol particles (e.g., size distribution, single scattering albedo, refractive index and phase

function) can be retrieved from these measurements by the inversion algorithm (Dubovik and King, 2000).

2.2.2 Satellite remote sensing

Satellite remote sensing is used for characterizing the temporal heterogeneities of aerosol distributions on a global or large spatial scale. The space instruments providing global monitoring of aerosol properties (e.g., King et al., 1999; Kokhanovsky et al., 2007) have been developed and launched (Winker et al., 2007). Monitoring of aerosols from space has been performed for several decades and is planned for the coming decade with enhanced capabilities (King et al., 1999; Mishchenko et al., 2007b). The Advanced Very High Resolution Radiometer (AVHRR) provided radiance observations in the visible and near infrared wavelengths that are sensitive to aerosol properties over the ocean (Husar et al., 1997; Mishchenko et al., 1999). The Total Ozone Mapping Spectrometer (TOMS) was suitable for investigating biomass burning smoke and dust, though with limited sensitivity near the surface (Hsu et al., 1996; Herman et al., 1997). TOMS is also suitable for retrieving aerosol single-scattering albedo from space (Torres et al., 2005), because its ultraviolet (UV) channels are sensitive to aerosol UV absorption with little surface interferences, even over land (Torres et al., 1998). The sensors (TOMS/OMPS and successive Ozone Monitoring Instrument (OMI)) have provided multi-decadal climatology of AOT that is helpful to understand the aerosol distributions and its long-term variability (Torres et al., 2002; Veihelmann et al., 2007; Massie et al., 2004; Mishchenko et al., 2007a; Zhao et al., 2008).

Satellite aerosol retrievals are becoming sophisticated. Now, satellites can provide information about the angular dependence of radiance and polarization at multiple wavelengths from UV through the infrared (IR) with fine spatial resolution. From these observations, retrieved aerosol products include not only optical depth at one wavelength, but also spectral optical depth and some information about particle size over both ocean and land. Here are some examples of such new and enhanced sensors:

1) MODIS: MODerate resolution Imaging Spectroradiometer

MODIS, which was launched aboard NASA's *Terra* and *Aqua* satellites in December 1999 and May 2002, performs near global daily observations of atmospheric aerosols in a wide spectral range (Remer et al., 2005). There are two independent MODIS aerosol algorithms, one for deriving aerosols over land and the second for aerosols over ocean. Over cloud- and surface-screened areas, aerosol properties are retrieved by seven of 36 channels from 0.47 to 2.13 μm (Martins et al., 2002; Li et al., 2004). Over vegetated land, AOT retrieved at three visible channels has a high accuracy of $\pm$ 0.05 $\pm$ 0.2τ (Kaufman et al., 1997; Remer et al.,

2005; Levy et al., 2007). A deep-blue algorithm that can retrieve aerosol over bright deserts on an operational basis has an estimated accuracy of 20 – 30% (Hsu et al., 2004). Over ocean, MODIS has the capability of retrieving AOT with greater accuracy, i.e., ± 0.03 ± 0.05τ (Tanré et al., 1997; Remer et al., 2002, 2005, 2008), as well as quantitative aerosol size parameters (e.g., fine-mode fraction of AOD, which is an important parameter to distinguish anthropogenic aerosols from natural ones and estimate the direct forcings of anthropogenic aerosols) (Kaufman et al., 2002a, 2005a; Remer et al., 2005).

2) MISR: Multi-angle Imaging SpectroRadiometer

MISR was launched into a Sun-synchronous polar orbit, crossing the equator about 10:30 local time, in December 1999, aboard the NASA Earth Observing System's *Terra* satellite. MISR measures upwelling short-wave radiance in four narrow spectral bands centered at 0.446, 0.558, 0.672, and 0.866 μm and at nine distinct zenith angles, ranging from 70° forward to 70° aftward along the spacecraft track (Diner et al., 2002; Martonchik et al., 2004; Kahn et al., 2005). Because of the wide range of along-track view angles, the information of MISR observations can be used to evaluate the surface contribution to the top of atmosphere radiances more accurately and retrieve aerosols over both ocean and land surfaces, including bright desert and sun glint regions (Martonchik et al., 1998, 2004; Kahn et al., 2005). The scattering angle ranging from about 60° to 160° in midlatitude makes MISR multi-angle data feasible to yield information about particle size (Kahn et al., 1998; Chen et al., 2008) and shape (Kalashnikova and Kahn, 2006). AOT retrieved from MISR measurements has an accuracy of 20% or ± 0.05 of coincident AERONET measurements (Kahn et al., 2005; Abdou et al., 2005).

3) POLDER: Polarization and Directionality of the Earth's Reflectance

POLDER is an unique aerosol sensor that consists of wide field-of-view imaging spectro-radiometer, which can measure multi-spectral, multi-directional and polarized radiances (Deuzé et al., 2001). The observed radiances can be exploited to better separate the atmospheric contribution from the surface contribution over both land and ocean. POLDER-1 and -2 flew onboard the ADEOS (Advanced Earth Observing Satellite) from November 1996 to June 1997 and April to October of 2003, respectively. A similar POLDER instrument was carried aboard on the PARASOL satellite launched in December 2004 in order to be part of the A-Train, providing the observations from March 2005 to November 2013. Because of the polarized and directional signatures, POLDER data are better suited to select the aerosol model in the inversion algorithm and to determine the size and shape of particles over the ocean (Tanré et al., 2011). When the scattering angle range is large enough (90° – 160°), PARASOL can discriminate large spherical marine aerosols from non-spherical desert

aerosols, retrieve the effective radius of the accumulation and coarse modes and evaluate the real part of the refractive index. In addition, over highly reflective land surfaces, PARASOL is using the polarized radiance to reduce the surface contribution (Tanré et al., 2011).

Aerosol products retrieved from satellite measurements include not only AOT at single wavelength or multi-wavelength, but also some information about particle size over both ocean and land, as well as more direct measurements of polarization and phase function. The accuracy of AOT retrieved from these sensors is about 0.05 or 20% (Remer et al., 2005; Kahn et al., 2005), but that for aerosol microphysical properties, which is helpful to distinguish aerosol types, is generally low.

Table 2.2 shows a summary of major satellite measurements including passive remote sensing, active remote sensing. In recently years, algorithms are being developed to infer aerosol properties (e.g., absorption, SSA) from satellite observations (Kaufman et al. 2002a; Torres et al., 2005). The retrieved aerosol microphysical properties can help separate anthropogenic aerosols from natural aerosols to estimate the anthropogenic component of aerosol direct radiative forcing (Kaufman et al., 2005a; Bellouin et al. 2008; Yu et al., 2008). However, in order to infer aerosol number concentrations and examine indirect aerosol radiative effects from space, significant efforts are needed to measure aerosol size distribution with much improved accuracy, characterize aerosol type (dust, biomass burning, marine, etc.) (Mishchenko et al., 2007b), account for impacts of water uptake on aerosol optical thickness, and fix the fraction of aerosols that is at the level of the clouds (Kapustin et al., 2006; Rosenfeld, 2006). It is noted that satellite remote sensing is not sensitive to particles with diameter much smaller than 0.1 μm, which mainly serve as cloud condensation nuclei.

In summary, despite the retrieval accuracy from satellites is lower than from ground-based Sun photometers, the remote sensing from space can provide a better coverage and information on spatial distribution of aerosol concentration (aerosol optical thickness) and properties. Indeed, since the satellite retrievals entail additional and major sensitivities to surface scattering properties, it may be not possible that satellite remote sensing of aerosol will exceed the Sun photometer accuracy and information content. Nevertheless, major advances have been made during the past decade in distinguishing aerosol types from space, and the retrievals became useful for evaluating aerosol transport model simulations.

Table 2.2: Summary of major satellite measurements currently available for the tropospheric aerosol characterization and radiative forcing research (Chin et al., 2009b).

Properties	Sensor/ Platform	Parameters	Spatial coverage	Temporal coverage
Loading	AVHRR/NOAA-series	Optical depth	~ daily coverage of global ocean	1981-present
	TOMS/Nimbus, ADEOS1, EP		~ daily coverage of global land and ocean	1979-2001
	POLDER-1, -2, PARASOL			1997-present
	MODIS/Terra, Aqua			2000-present (Terra) 2002-present (Aqua)
	MISR/Terra		coverage of global land and ocean, including bright desert and nadir sun-glint	2000-present
	OMI/Aura		~ daily coverage of global land and ocean	2005-present
Size shape	AVHRR/NOAA-series	Ångström exponent	global ocean	1981-present
	POLDER-1, -2, PARASOL	Fine-mode fraction, Ångström exponent, non-spherical fraction	global land+ocean	1997-present
	MODIS/Terra, Aqua	Fine-mode fraction	global land+ocean (better quality over ocean)	2000-present (Terra) 2002-present (Aqua)
		Ångström exponent		
		effective radius	global ocean	
		Asymmetry factor		
	MISR/Terra	Ångström exponent, small, medium, large fractions, non-spherical fraction	global land+ocean	2000-present
Absorption	TOMS/Nimbus, ADEOSI, EP	Absorbing aerosol index, single-scattering albedo, absorbing optical depth	global land+ocean	1979-2001
	OMI/Aura			2005-present
	MISR/Terra	Single-scattering albedo (2-4bins)		2000-present

2.3 Remote sensing of aerosol composition

According to the aerosol scattering and absorbing properties, the aerosol particles can be divided into two categories: light-absorbing components and pure scattering (nonabsorbing) components. The radiative impacts of aerosols at the top of the atmosphere could change in sign from cooling to warming in regions of highly absorbing aerosols (Chylek and Coakley, 1974; Charlock and Sellers, 1980; Haywood and Shine, 1995). There are two kinds of

absorbing aerosols that are commonly found in the atmosphere: absorbing carbon and mineral dust, especially the mineral dust containing iron oxides (Sokolik and Toon, 1999).

Light-absorbing carbon produced from combustions of organic matter is an important component of atmospheric aerosol. The complex refractive index of light-absorbing carbon in atmospheric aerosols is dependent on the type of the fuel and the conditions of combustion (Bond and Bergstrom, 2006). Based on the origin of the material, combustion conditions, morphological characteristics, chemical composition and optical properties (Andreas and Gelencsér, 2006; Schkolnik et al., 2007), the term black carbon (BC), associated with elemental carbon or soot in the literatures, is used to define the strongly light-absorbing carbon in the atmosphere, which is composed of aggregated graphite spheres (Andreae and Gelencsér, 2006). BC radiative forcing is second after CO_2 radiative forcing as a contributor to global warming (Ramanathan and Carmichael, 2008; Bond et al., 2013). However, the range of uncertainty for BC forcing is much larger than the range of uncertainty for CO_2 forcing. Meanwhile, the term brown carbon (BrC) is used for strongly wavelength-dependent light-absorbing carbon particles whose absorption is greater at near-ultraviolet and blue wavelengths (Jacobson, 1999; Kirchstetter et al., 2004; Kanakidou et al., 2005; Hoffer et al., 2006; Schnaiter et al., 2006; Sun et al., 2007; Dinar et al., 2008; Chen and Bond, 2010), to distinguish these particles from BC.

Mineral dust particles have a strong spectral signature, with the stronger absorption at the UV and blue wavelengths. Iron oxide is an important component that affects the ability of mineral dust aerosol to absorb sunlight at short wavelength. Hematite and goethite are different forms of “free” iron, and they typically appear together as well (Arimoto et al., 2002; Lafon et al., 2006; Shi et al., 2012; Formenti et al., 2014a). The presence of iron in mineral dust particles is also important for its biogeochemical and radiative impacts (Jickells et al., 2005; Mahowald et al., 2005). Variable concentrations of iron oxide influence climate through altering the dust’s radiative properties (Sokolik and Toon, 1999). Although the regional distribution of the iron concentration is important for climate studies, it is difficult to obtain since it requires in-situ aerosol sampling or simulation of complex natural processes. In addition, mineral dust particles can be contaminated by anthropogenic aerosol particles (e.g., carbonaceous aerosols) producing from biomass burning. Separating the absorption associated with light-absorbing carbon from the absorption associated with mineral dust (especially iron oxides) is not trivial (Derimian et al., 2008). Thus, determining the relative proportions of BC, BrC and iron oxide in atmospheric aerosols is a necessary step for retrieving aerosol composition. Several approaches can be used to evaluate iron oxide or light-absorbing carbon concentrations in aerosol particles, e.g., in-situ sampling of

atmospheric aerosol particles with further laboratory analysis and employed chemistry transport model simulations. An additional approach is modeling of aerosol optical properties (Sokolik and Toon, 1999), which can be employed for deriving concentrations of aerosol compositions. Dubovik et al. (2002a) showed that the spectral absorption of light-absorbing aerosols is distinct from that of mineral dust. Schuster et al. (2005) inferred the BC column content and BC specific absorption from AERONET retrievals by assuming that BC is the source of all significant aerosol absorption in the AERONET retrievals. Based on the spectral variability of the imaginary refractive index, Koven and Fung (2006) retrieve hematite concentrations at dust sites, while Arola et al. (2011) retrieve BrC from AERONET retrievals. Wang et al. (2013) add single-scatter albedo as an additional constraint to such refractive index approach (Schuster et al., 2005; Arola et al., 2011) and make it feasible to distinguish BC, BrC and dust simultaneously. Similarly, Li et al. (2013, 2015) investigate the microphysical, optical and chemical properties of atmospheric aerosols by fitting the AERONET complex refractive indices measured at Beijing and Kanpur. Recently, Schuster et al. (2016) using the AERONET size distributions and complex refractive indices to retrieve the relative proportion of carbonaceous aerosols (BC and BrC) and free iron minerals (hematite and goethite) in fine and coarse modes particles.

Currently, the most advanced methods (Schuster et al., 2005, 2009, 2016; Arola et al., 2011; Wang et al., 2013; Li et al., 2013, 2015) that involve retrieval of aerosol composition from remote sensing measurements fit the intermediate retrieval of the refractive index such as measured in AERONET. It is noted that these retrievals of aerosol compositions can be obtained only from ground-based remote sensing measurements, which is possible to be employed in the satellite retrieval algorithm.

Chapter 3

GRASP algorithm description

"For success, attitude is equally as important as ability."

------ Walter Scott

This chapter describes in detail the GRASP algorithm, which is a rigorous, versatile and accessible at https://www.grasp-open.com, as well as the development of a new aerosol composition conversion model designed to retrieve aerosol composition fraction. The aerosol composition conversion approach proposed in this work is integrated in the standard inversion procedure, which general structure is shown in Figure 3.1 (courtesy of Dubovik et al., 2011). The algorithm is divided into several interacting but rather independent modules to enhance its flexibility. The straightforward exchange of limited parameters makes the interactions between the modules minimized. The "Forward Model" and "Numerical Inversion" are the two most complex and elaborated modules in the algorithm. The "Forward Model" is developed in a quite universal way to quantitatively simulate the measured atmospheric radiation emitted by the surface or atmospheric objects with given properties. The "Numerical Inversion" module, which can be used in any other application, even not related to atmospheric remote sensing, includes general mathematical operations not related to the particular physical nature of the inverted observations. Numerical inversion is implemented as a statistically optimized fitting of observations based on the multi-term least squares method (LSM), which combines the advantages of a variety of approaches and provides transparency and flexibility in developing algorithms that invert passive or active observations and derive several groups of unknown parameters (Dubovik et al., 2004). As a consequence of such organization of the algorithm, it can equally be applied (with minimal changes) to invert observations from satellite sensors or from the ground-based remote sensing. The following several sections provide a full description of the "Forward Model" and "Numerical Inversion"

algorithm modules, as well as the new development of aerosol composition conversion part (schematically presented by red dashed frames in Figure 3.1).

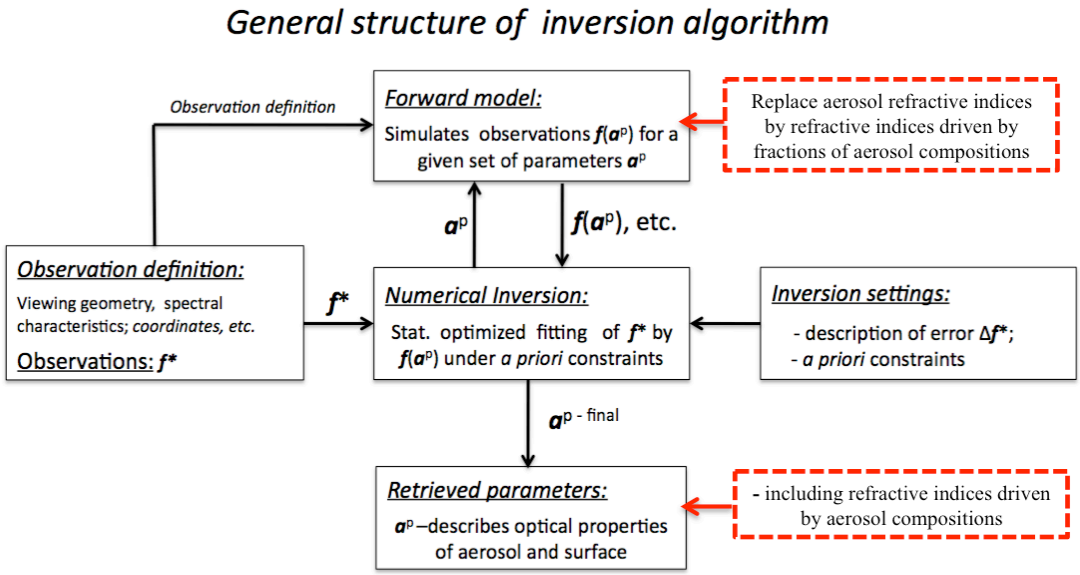

Figure 3.1: The general structure of GRASP algorithm with aerosol composition conversion model, courtesy of Dubovik et al. (2011). The red dashed frames represent modifications for the composition inversion approach.

Depending on the input data, the algorithm is designed to retrieve columnar and vertical aerosol properties and surface reflectance globally. In order to achieve reliable retrieval from PARASOL observations, the algorithm simultaneously derives retrievals from a large group of pixels within one or several images. This multi-pixel retrieval approach takes advantage of known limitations on spatial and temporal variability in both aerosol and surface properties to provide satellite retrievals of higher consistency and smoothness. Because the retrieval over each single pixel can benefit from coincident aerosol information from neighboring pixels, and from the information about surface reflectance obtained in preceding and consequent observations over the same pixel (Dubovik et al., 2011, 2014). Although the algorithm is tuned for inverting PARASOL observations, some aspects of aerosol parameterization and inversion implementation (in particular a priori constraint settings) can be modified and adjusted for optimizing the algorithm performance if it is applied to other remote sensing observations.

3.1 Forward model

This section presents description of the forward model implemented in the GRASP retrieval algorithm. The description largely relies on the algorithm in the study of Dubovik et al. (2011), however, as illustrated in Figure 3.1, the forward model was modified for the retrievals of aerosol composition fractions. Namely, the new parameters, such as fractions of

aerosol composition, are presented. Note that the complex refractive index in this approach is not retrieved, but calculated based on fraction of aerosol composition. Following is the detailed description that accounts for the relevant modifications.

The new composition approach is also proposed to invert the POLDER/PARASOL observations including the total radiance in six window channels (0.440, 0.490, 0.565, 0.670, 0.865 and 1.02 μm) and the linear polarization in three of these channels (0.490, 0.670 and 0.865 μm) in Table 3.1. In the POLDER/PARASOL window channels, the absorption of atmospheric gases can be calculated from the available information of ancillary observations and it has rather minor contributions. The water vapor absorption can be corrected by the procedure of Deuzé et al. (2001) using PARASOL measurements in 0.91 μm spectral band. In addition, the minor absorption of ozone, NO_2 and O_2 can be obtained from the climatology data. Thus, the modeling of aerosol properties (extinction, single scattering albedo and phase matrix) is the most challenging part. These properties depend on particle size, shape and composition of aerosol. All these characteristics are determined by the parameters included in the vector of unknowns and correspondingly they are inferred from the observations.

For the ocean surface, the reflection properties mainly affected by the wind speed at sea level can be retrieved by the same model (Cox and Munk, 1954), which was employed in the operational POLDER algorithm (Deuzé et al., 2001; Herman et al., 2005; Tanré et al., 2011). While the reflection properties of the land surface may vary significantly according to the differences of conditions. There are some alterable subroutines, (e.g., the Ross-Li model (1981), Nadal and Bréon (1999), Rahman et al. (1993) and Maignan et al. (2009)), for the retrievals of land surface reflection.

Therefore, the forward model of reflected radiances measured by POLDER/PARASOL consists of three main sections: aerosol single scattering, surface reflection and solving vector radiative transfer equation. The forward model is designed by means of adapting the atmospheric modeling strategies and computer routines developed within previous POLDER and AERONET activities, as well as some important modifications required for optimizing the forward modeling performance. For example, the models of land surface reflectance have been introduced into the radiative transfer calculations. These modifications allowed the performance of the inversion procedure to achieve the standards required for operational processing (achieving sufficient speed of computations, etc.).

Table 3.1: List of measured and retrieved characteristic considered in POLDER/PARASOL algorithm with aerosol composition conversion model, modified from Dubovik et al. (2011).

POLDER/PARASOL measurements	
Measurements type:	
$I(\mu_0;\mu_1;\varphi_0;\varphi_1;\lambda_i) = I(\Theta_j;\lambda_i)$	– I reflected total radiances
$Q(\mu_0;\mu_1;\varphi_0;\varphi_1;\lambda_i) = Q(\Theta_j;\lambda_i)$	– Q component of the Stokes vector
$U(\mu_0;\mu_1;\varphi_0;\varphi_1;\lambda_i) = U(\Theta_j;\lambda_i)$	– U component of the Stokes vector
Observation specifications:	
Angular:	$I(\Theta_j;\lambda_i)$, $Q(\Theta_j;\lambda_i)$ and $U(\Theta_j;\lambda_i)$ measured in up to 16 viewing directions, that may cover the range of scattering angle Θ from ~ 80° to 180°
Spectral:	$I(\Theta_j;\lambda_i)$ measured in 6 window channels λ_i = 0.440, 0.490, 0.565, 0.670, 0.865 and 1.02 μm $Q(\Theta_j;\lambda_i)$ and $U(\Theta_j;\lambda_i)$ measured in 3 window channels λ_i = 0.490, 0.670, and 0.865 μm
Retrieved characteristic	
Aerosol parameters:	
C_v	– total volume concentration of aerosol ($\mu m^3/\mu m^2$)
$dV(r_i)/dlnr$	– $(i = 1,\dots,N_r)$ values of volume size distribution in N_i size bins r_i normalized by C_v
C_{sph}	– fraction of spherical particles
$Frac(F_i)$	– $(i = 1,\dots,N_f)$ the fraction of composition in fine mode
$Frac(C_i)$	– $(i = 1,\dots,N_c)$ the fraction of composition in coarse mode
h_0	– mean height of aerosol layer
$n(\lambda_i)$	– $(i = 1,\dots,N_\lambda = 6)$ the real part of the refractive index at every λ_i wavelength, calculated by the fraction of composition
$k(\lambda_i)$	– $(i = 1,\dots,N_\lambda = 6)$ the imaginary part of the refractive index at every λ_i wavelength, calculated by the fraction of composition
Surface reflection parameters:	
Rahman et al. (1993) model:	
$\rho_0(\lambda_i)$	– $(i = 1,\dots,N_\lambda = 6)$ first RPV BRDF parameter (characterizes intensity of reflectance)
$\kappa(\lambda_i)$	– $(i = 1,\dots,N_\lambda = 6)$ second RPV BRDF parameter (characterizes anisotropy of reflectance)
$\theta(\lambda_i)$	– $(i = 1,\dots,N_\lambda = 6)$ third RPV BRDF parameter (characterizes forward/backscattering contributions)
$h_0(\lambda_i)$	– $(i = 1,\dots,N_\lambda = 6)$ fourth RPV BRDF parameter (characterizes hot spot effect)
Note: $h_0(\lambda)$ is retrieved only for the observation conditions: $\pm 7.5°$ close to backscattering. In other situations, it is fixed as related to $h_0(\lambda) = \rho_0(\lambda)$	
Maignan et al. (2009) model:	
$B(\lambda_i)$	– $(i = 1,\dots,N_\lambda = 6)$ free parameter
Option: algorithm allows using alternative surface model: Ross-Li model for BRDF and Nadal-Breon model for BPDF	

3.1.1 Aerosol single scattering properties

The modeling of the aerosol scattering matrices has been implemented following the ideas of Dubovik and King (2000) and Dubovik et al. (2002b, 2006).

The atmospheric aerosol is modeled as an ensemble of randomly oriented spheroids to infer aerosol non-sphericity. AERONET operational retrievals (Dubovik et al., 2006) model the particles for each size bin as a mixture of spherical and non-spherical aerosol components. Therefore, aerosol particles of non-spherical component have size-independent distribution of shapes and the modeling of the total aerosol optical thickness τ of non-spherical aerosol can be expressed as:

$$\tau(\lambda) = \int_{r_{min}}^{r_{max}} \int_{\varepsilon_{min}}^{\varepsilon_{max}} c_\tau^\varepsilon(\lambda; k; n; r; \varepsilon) \frac{dN(\varepsilon)}{d\ ln\varepsilon} \frac{dN(r)}{d\ lnr} d\ ln\varepsilon\ d\ lnr, \quad (3.1)$$

where $c_\tau^\varepsilon(\lambda; k; n; r; \varepsilon)$ describes the extinction cross-sections of spherical particle and randomly oriented spheroid, λ is the wavelength, n and k is the real and imaginary part of the refractive index, respectively, ε denotes spheroid axis ratio ($\varepsilon = a/b$, a is the axis of spheroid rotational symmetry, b is the axis perpendicular to the axis of spheroid rotational symmetry), r denotes the radius of volume equivalent sphere. The usage of r and ε is convenient for distinguishing the effect of particle shape and size in analysis of aerosol mixture light scattering (Mishchenko and Travis, 1997). Then the functions $dN(r)/\mathrm{d}lnr$ and $dN(\varepsilon)/\mathrm{d}ln\varepsilon$ describe the number particle size and the number particle shape distribution respectively. In the new composition approach, the real and imaginary part of the refractive index are not retrieved directly from the observations. They are calculated by the retrieved fraction of aerosol composition and the refractive index of each composition assumed in the conversion model.

In addition, because the utilization of both the volume size distribution and logarithm of radius is a convenient way to perform the algorithm. The usage of both the volume of particle (instead of number) and logarithmic scale in binning of the size distribution contributes to optimize the approximation. Therefore, volume size distribution $dV(r)/dlnr$ is often chosen to retrieve aerosol characteristic in the algorithms applied to invert the optical data of high sensitivity to aerosol particle size. For example, a similar size distribution representation was used to retrieve aerosol properties from ground-based sky-radiometers (Nakajima et al., 1983, 1996). Dubovik et al. (2006) found that the accuracy of the calculations remains practically unchanged if the aerosol size bins corresponding to very small and very large particles have been eliminated. The contributions of smaller and larger particles into POLDER/PARASOL observations are negligible. Dubovik et al. (2011) have demonstrated that sufficiently

accurate modeling of POLDER/PARASOL observations can be achieved if the shape of each single bin is optimized, which is also used in the present new composition approach.

3.1.2 Modeling surface reflectance

The algorithm for modeling the reflective properties of ocean surface is similar to the currently operational POLDER algorithm (Deuzé et al., 2001; Herman et al., 2005; Tanré et al., 2011). The Cox and Munk model (Cox and Munk, 1954) is implemented to estimate the Fresnel's reflection on the agitated sea surface. The water leaving radiance is approximately isotropic (Voss et al., 2007) and its polarization is negligible (e.g., Chami et al., 2001; Chowdhary et al., 2006; Ota et al., 2010), which is taken into account by Lambertian unpolarized reflectances. The whitecap reflectance, driven by the wind speed at sea surface (Koepke, 1984), is also taken into account by Lambertian unpolarized reflectances. At short wavelengths, the seawater reflectance depending on the properties of oceanic water cannot be ignored. Therefore, the magnitude of seawater reflectance at short wavelengths and the wind speed are inferred together with aerosol or have a priori information.

The previous aerosol retrieval algorithm (Deuzé et al., 2001) over land does not consider the detailed directional scattering properties of total reflectance by land surface. Therefore, the "Forward model" is improved to account adequately for both total and polarized properties of surface reflectance. The effects of directionality of land surface reflectance are often estimated by semi-empirical models driven by some internal parameters. For example, the Ross-Li model (Ross, 1981; Li and Strahler, 1992; Wanner et al., 1995) is successfully used for the characterization of directional properties of land surface reflectance derived from MODIS observation by Justice et al. (1998). The Rahman-Pinty-Verstraete (RPV) model (Rahman et al., 1993) is applied to analyze the observations of MISR (Martonchik et al., 1998) and SEVIRI (Govaerts et al., 2010; Wagner et al., 2010). The comparisons of Ross-Li model and RPV model demonstrate that these two models can comparably reproduce the multi-angle observations of land surfaces (Maignan et al., 2004, 2009; Litvinov et al., 2010, 2011).

Most theoretical models developed for approximating observed the Bidirectional Polarization Distribution Function (BPDF) are based on the Fresnel equations of light reflection from the surface. For example, Nadal and Bréon (1999) have proposed a two-parameter non-linear function of the Fresnel reflection to characterize the atmospheric aerosol over land surface based on POLDER observations of land surface reflectance. Recently, Maignan et al. (2009) have introduced a new linear BPDF model with one free parameter, which one can fit the POLDER observations analogously to the non-linear model (Nadal and Bréon, 1999).

The Rahman et al. (1993) and Maignan et al. (2009) formulations, chosen as primary models for BRDF and BPDF, have limited accuracy (Litvinov et al., 2010, 2011). There is an alterable subroutine of changing BRDF by the Ross-Li model and BPDF by Nadal and Bréon (1999) formulation.

3.1.3 Forward radiative transfer

The atmospheric multiple scattering effects employed in PARASOL operational retrievals (Deuzé et al., 2001; Herman et al., 2005; Tanré et al., 2011) are estimated by the successive order of scattering radiative transfer algorithm (Lenoble et al., 2007). The radiation properties measured by passive remote sensing show negligible circular polarization of the electromagnetic field (Hansen, 1971). In the present, the successive order of scattering radiative transfer code allows calculations of atmospheric radiances for several aerosol components (N_k). The defined vertical profile of spectral extinction and altitude independent phase matrix and single scattering albedo, which are determined by microphysical model of atmospheric aerosol, are used to describe each aerosol component. For example, the vertically invariant altitude independent phase matrix and single scattering albedo are driven by: the size distribution $dV_k(r_i)/dlnr$ ($\mu m^3/\mu m^2$) giving the aerosol particle volume in the total atmospheric column per unit of surface area; the real $n_k(\lambda)$ and imaginary $k_k(\lambda)$ parts of the complex refractive index related to aerosol composition fraction; and the fraction of the spherical particles $C_{k,sph}$. The spectral dependence of optical thickness $\tau_k(\lambda)/\tau_k(\lambda_i)$ is also vertically invariant and dependent on these parameters, while the absolute value of $\tau_k(\lambda)$ is also determined by the total volume of the aerosol in the atmospheric column: $C_{k,V} = \sum_{i=1,\dots,N_i}(\frac{dV_k(r)_i}{dlnr})$.

The accuracy of radiative transfer calculations is significantly determined by the number of terms *M* used in the expansion of the phase matrix into Legendre polynomials and number of terms *N* used in Gaussian quadrature for zenithal integration. The values required by the inequality $4N - 1 > 2M$ can maintain conservation of energy in the successive order of scattering integration. Although the larger values *M* and *N* may provide more accurate calculation, the longer calculation time is needed. Dubovik and King (2000) demonstrated that the successful retrieval could be inferred using the approximate and quick calculations of the first derivatives to invert the observations of ground-based radiometers. At the same time, the retrieval time can be obviously decreased because the calculation of the first derivatives is the most time consuming component of Newtonian's retrieval algorithms. The study of Dubovik et al. (2011) has shown that it is not sufficient for conducting retrieval from satellite observations using single scattering approximation. However, the Jacobians estimated

numerically as finite differences on basis of the full radiative transfer calculations implemented with significantly reduced values of *M* and *N* provide fast and accurate retrievals (Dubovik et al., 2011).

Rozanov and Lyapustin (2010) discussed the comparisons of different methods implementing the phase matrix truncation in their studies. The use of truncation is optional but recommended in the PARASOL algorithm. The utilization of the phase matrix truncation allows for decreasing the number of terms *M* in the expansion of the truncated phase function and *N* in the Gaussian quadrature for azimuth integration. Dubovik et al. (2011) demonstrated that accurate PARASOL retrievals could be inferred using the suggested values (calculating the fit to PARASOL observations: *M*=21 and *N*=10; calculating Jacobian matrices: *M*=15 and *N*=7).

The successive order of scattering radiative transfer code needs the phase function values at N_{ang} angles corresponding to the points of Gaussian quadrature. Such values can be provided by the software (Dubovik et al., 2006), which can generate aerosol single scattering properties and provide the phase function for the set of fixed scattering angles allowing sufficiently accurate modeling of angular variability of scattering. Additionally, the speed of aerosol single scattering modeling is determined by the number of the scattering angles used. The study of Dubovik et al. (2011) demonstrated that POLDER/PARASOL observations could be adequately modeled with set of $N_{ang} = 35$ selected scattering angles.

3.2 Numerical inversion

This section presents description of numerical inversion employed in the GRASP retrieval algorithm. The description is largely relies on the algorithm in the study of Dubovik et al. (2011) with several modifications for retrieving aerosol composition. Namely, the fractions of aerosol composition are presented instead of the complex refractive index. In the composition approach, the complex refractive index is calculated based on fractions of aerosol composition.

In contrast to the majority of existing satellite retrieval algorithms, this module attempts to develop an aerosol satellite retrieval using statistically optimized multivariable fitting. Such strategy has no dependence on the preassumed classes of potential solutions. Instead the solution is sought in a continuous space of solutions under statistically formulated criteria optimizing the error distribution of the retrieved parameters. The implementation of some components of such a strategy was pursued in the previous developments of retrieval algorithms (Martonchik et al., 1998; Chowdhary et al., 2002, 2005; Waquet et al., 2007, 2009;

Hasekamp and Landgraf, 2005, 2007; Govaerts et al., 2010) for processing satellite observations.

There are many detailed descriptions of inversion methods in earlier studies (Tikhonov and Arsenin, 1977; Twomey, 1977; Tarantola, 1987; Press et al., 1993; Rodgers, 2000; Doicu, 2010). Following the developments of previous studies (Dubovik and King, 2000; Dubovik, 2004; Dubovik et al., 2008), Dubovik et al. (2011) focused on illuminating the relationships among different inversion methods established in atmospheric optics and unifying the key ideas of these methods into a single inversion procedure. In contrast to the standard inverse methods, the methodology has several original features optimized for remote sensing applications. For example, the methodology addresses such important aspects of inversion optimization as accounting for errors in the satellite observations, inversion of multi-source data with different levels of accuracy, accounting for a priori and ancillary information, estimating retrieval errors, clarifying potential of employing different mathematical inverse operations (e.g., comparing iterative versus matrix inversion methods), accelerating iterative convergence (Dubovik, 2004). Dubovik et al. (2011) propose a generally multi-term Least Square type formulation taking complementarily the advantages of a variety of practical inversion approaches (Phillips, 1962; Tikhonov, 1963; Twomey, 1963; Kalman, 1960). Such approach providing significant transparency and flexibility in development of remote sensing algorithm can derive a set of continuous characteristics, such as vertical profiles, size distributions.

Two scenarios can be chosen for inverting satellite observations: single-pixel retrieval and multi-pixel retrieval. The single-pixel retrieval is a conventional approach for inverting satellite observations over each single pixel completely independently. The multiple-pixel retrieval is a newly instrument for inverting observations over a group of pixels simultaneously with extra a priori constraints on the inter-pixel variability of the retrieved parameters. Such constraints are expected to improve the reliability of the retrieval.

3.2.1 Single-pixel observation fitting

The retrieval algorithm consists of a multi-term least squares method (LSM) that implements statistically optimum fitting of several sets of observations with a priori constraints under assumption of normally distributed uncertainties. It solves the system of equations:

$$\begin{cases} \boldsymbol{f}^* = \boldsymbol{f}(\boldsymbol{a}) + \Delta\boldsymbol{f} \\ \boldsymbol{0}^* = (\Delta\boldsymbol{a})^* = \boldsymbol{S}\,\boldsymbol{a} + \Delta(\Delta\boldsymbol{a}). \\ \boldsymbol{a}^* = \boldsymbol{a} + \Delta\boldsymbol{a}^* \end{cases} \tag{3.2}$$

Here, $\boldsymbol{f}^*$ denotes a vector of the PARASOL measurements, $\Delta\boldsymbol{f}$ denotes a vector of measurement uncertainties, $\boldsymbol{a}$ denotes a vector of unknowns. The second equation in Eq. (3.2) characterizes the a priori smoothness assumptions that constrain the variability of size distribution and the spectral dependencies of parameters of surface reflectance model. The matrix $\boldsymbol{S}$ includes the coefficients for calculating m-th differences of $dV(r_j)/dlnr$, $Frac(i)$, $\rho_0(\lambda_j), \kappa(\lambda_j), \theta(\lambda_j)$. It is noted that $n(\lambda_j)$ and $k(\lambda_j)$ are calculated by the fraction ($Frac(i)$) of aerosol composition. $\mathbf{0}^*$ represents vector of zeros and $\Delta(\Delta\boldsymbol{a})$ represents vector of the uncertainties that characterizes the deviations of the differences from the zeros. This equation indicates that all these m-th differences are equal to zeros within the uncertainties $\Delta(\Delta\boldsymbol{a})$. The third equation in Eq. (3.2) includes the vector of a priori estimates $\boldsymbol{a}^*$, as well as the vector of the uncertainties ($\Delta\boldsymbol{a}^*$) in a priori estimates.

The assumption of lognormal error distribution was applied to account for the non-negative character of the observed radiances and retrieved aerosol ($dV(r_j)/dlnr$) and surface reflectance ($\rho_0(\lambda_j)$) parameters. The noise distribution is obviously the most appropriate for the positively defined values. The lognormal noise distribution indicates that the logarithms of the observed positively defined values are normally distributed. Therefore, because of the convenience of formulating the statistically optimized solution of Eq. (3.2), the logarithmic transformation is used for both measured $\boldsymbol{f}_j$ and retrieved $\boldsymbol{a}_i$ parameters. The detailed discussions can be found in the studies of Dubovik and King (2000) and Dubovik (2004). Correspondingly, the errors $\Delta\boldsymbol{f}$, $\Delta(\Delta\boldsymbol{a})$, and $\Delta\boldsymbol{a}^*$ are assumed normally distributed.

The statistically optimized solution of Eq. (3.2) defined on the base of Maximum Likelihood Method corresponds to the minimum of the following quadratic form:

$$\Psi(\boldsymbol{a}^P) = \Psi_f(\boldsymbol{a}^P) + \Psi_\Delta(\boldsymbol{a}^P) + \Psi_a(\boldsymbol{a}^P)$$

$$= \frac{1}{2}((\Delta\boldsymbol{f}^P)^T\,(\boldsymbol{W}_f)^{-1}\,\Delta\boldsymbol{f}^P + \gamma_\Delta(\boldsymbol{a}^P)^T\Omega\boldsymbol{a}^P + \gamma_a(\boldsymbol{a}^P - \boldsymbol{a}^*)^T\boldsymbol{W}_a^{-1}(\boldsymbol{a}^P - \boldsymbol{a}^*)). \quad (3.3)$$

In non-linear case, the minimum can be obtained using the iterative procedure:

$$\boldsymbol{a}^{P+1} = \boldsymbol{a}^P - t_P\Delta\boldsymbol{a}^P, \quad (3.4)$$

where $\Delta\boldsymbol{a}^P$ represents a solution of the p-th so-called, in statistical estimation formalism, Normal System

$$\boldsymbol{A}_P\Delta\boldsymbol{a}^P = \nabla\Psi(\boldsymbol{a}^P). \quad (3.5)$$

The matrix in the left side of Eq. (3.5) is known as Fisher Matrix $\boldsymbol{A}_P$ and the right side of Eq. (3.5) denotes the gradient $\nabla\Psi(\boldsymbol{a}^P)$ of quadratic form $\Psi(\boldsymbol{a}^P)$ in the vicinity of $\boldsymbol{a}^P$:

$$\boldsymbol{A}_P = \boldsymbol{K}_P^T\boldsymbol{W}_f^{-1}\boldsymbol{K}_P + \gamma_\Delta\boldsymbol{\Omega} + \gamma_a\boldsymbol{W}_a^{-1}, \quad (3.6)$$

$$\nabla\Psi(\boldsymbol{a^P}) = \boldsymbol{K_P^T W^{-1}}\Delta\boldsymbol{f}^P + \gamma_\Delta \boldsymbol{\Omega a}^P + \gamma_a \boldsymbol{W_a^{-1}}(\boldsymbol{a}^P - \boldsymbol{a}^*), \quad (3.7)$$

where $\Delta\boldsymbol{f}^P = \boldsymbol{f}(\boldsymbol{a}^P) - \boldsymbol{f}^*$, $\boldsymbol{K}_P$ is Jacobi matrix of the first derivatives $\frac{\partial f_j(a^P)}{\partial a_i}$. Fisher Matrix $\boldsymbol{A}_P$ also can be considered as so-called Hessian matrix of second-order partial derivatives of the quadratic form $\Psi(\boldsymbol{a}^P)$ (Bevington, 1969; Tarantola, 1987). Thus, Eq. (3.5) can be expressed as:

$$(\nabla\nabla\Psi(\boldsymbol{a}^P))\Delta\boldsymbol{a}^P = \nabla(\boldsymbol{a}^P), \quad (3.8)$$

where $\nabla\nabla^T\Psi(\boldsymbol{a}^P)$ is the matrix with the elements $\{\nabla\nabla^T\Psi(\boldsymbol{a}^P)\}_{ji} = \left.\frac{\partial^2\Psi(a)}{\partial a_j \partial a_i}\right|_{\boldsymbol{a}=\boldsymbol{a}^P}$.

In the current inversion strategy, all equations are expressed by means of weighting matrices ($\boldsymbol{W}$), which is defined as $\mathbf{W} = (1/\varepsilon^2)\boldsymbol{C}$ (dividing the corresponding covariance matrix $\boldsymbol{C}$ by its first diagonal element ε^2). This formal transformation of the inversion equations allows rather transparent interpretation of Lagrange multipliers γ determining the contributions of a priori terms into solution (Dubovik and King, 2000, Dubovik et al., 2011). The Lagrange multipliers γ_a and γ_Δ can be written as (Dubovik and King, 2000): $\gamma_\Delta = \varepsilon_f^2/\varepsilon_\Delta^2$ and $\gamma_a = \varepsilon_f^2/\varepsilon_a^2$, where ε_f^2, ε_Δ^2 and ε_a^2 represents the first diagonal elements of corresponding covariance matrices $\boldsymbol{C}_f$, $\boldsymbol{C}_\Delta$ and $\boldsymbol{C}_a$, respectively. It is noted that if one can assume a simplified situation when the POLDER observations $\boldsymbol{f}^*$, a priori estimates of differences $(\Delta\boldsymbol{a})^*$ and a priori estimates of parameters $\boldsymbol{a}^*$ are independent and have the same accuracy, i.e., $\boldsymbol{C}_f = \varepsilon_f^2\boldsymbol{I}_{(N_f\times N_f)}$, $\boldsymbol{C}_\Delta = \varepsilon_\Delta^2\boldsymbol{I}_{(N_\Delta\times N_\Delta)}$ and $\boldsymbol{C}_a = \varepsilon_a^2\boldsymbol{I}_{(N_a\times N_a)}$, then corresponding weighting matrices are simply equal to the unity matrices: $\boldsymbol{W}_f = \boldsymbol{I}_{(N_f\times N_f)}$, $\boldsymbol{W}_\Delta = \boldsymbol{I}_{(\boldsymbol{N_\Delta}\times\boldsymbol{N_\Delta})}$ and $\boldsymbol{W}_a = \boldsymbol{I}_{(N_a\times N_a)}$. It should be noted that straightforward increasing of N_f by adding similar observations is not necessarily beneficial for the retrieval (Dubovik, 2004).

The coefficient $t_P \le 1$ in Eq. (3.4) is adjusted to provide monotonic decrease of $\Psi(\boldsymbol{a}^P)$, i.e.,

$$\Psi(\boldsymbol{a}^{P+1}) < \Psi(\boldsymbol{a}^P). \quad (3.9)$$

The minimum value of the above quadratic form can be theoretically estimated as follows:

$$\Psi(\boldsymbol{a}) \approx (N_f + N_\Delta + N_{a^*} - N_a)\,\varepsilon_f^2. \quad (3.10)$$

Once the value of measurement error (ε_f^2) is known, Eq. (3.10) can be used to verify the consistency of the retrieval.

In addition, the control of "measurement residual" $\Psi_f(\boldsymbol{a}^P)$ is a very useful tool to diagnose the dynamics of the retrieval. In generally, since the weights of a priori terms $\Psi_\Delta(\boldsymbol{a}^P)$ and

$\Psi_a(\boldsymbol{a}^P)$ are minor compared to the weight of the "measurement residual" term $\Psi_f(\boldsymbol{a}^P)$, the contributions of the a priori residual terms in Eq. (3.3) should not be significant. However, when the solution approximation is very far from the solution, $\Psi_f(\boldsymbol{a}^P)$ is dominated by linearization errors and has much higher value than the expected measurement noise. Consequently, the weight of the a priori term should be increased because the accuracy of a priori data is independent of the iteration. Correspondingly, the enhanced impact of a priori data can improve the convergence of non-linear fitting. For example, the strength of a priori constraints is adjusted dynamically as a function of the measurement residual $\Psi_f(\boldsymbol{a})$ in developed POLDER/PARASOL algorithm:

$$\varepsilon_f^2(\boldsymbol{a}^P) \approx \frac{\Psi_f(\boldsymbol{a}^P)}{(N_f - N_a)}, \tag{3.11}$$

where $\Psi_f(\boldsymbol{a}^P)$ is the accuracy of the POLDER observation fit at the p-th iteration and shows the process of how the iterations converge to the solution. In the last iteration, when the solution estimate $\boldsymbol{a}^{Plast}$ is expected to be in a small vicinity of the actual solution, the value of the residual $\Psi_f(\boldsymbol{a})$ of the measurement fit can be estimated as:

$$\Psi_f(\boldsymbol{a}^{Plast}) \approx (N_f - N_a)\varepsilon_f^2. \tag{3.12}$$

Therefore, Eq. (3.11) can adjust the values of the Lagrange multipliers and enhance the contribution of a priori constraints in the previous iterations.

The present inversion procedure is driven by the limited set of the input characteristics including the weighting matrices $\boldsymbol{W}\ldots$ and corresponding variances $\varepsilon\ldots$. The vector of POLDER/PARASOL measurements consists of two components.

$$\boldsymbol{f}^* = \begin{pmatrix} f_I^* \\ f_P^* \end{pmatrix}, \tag{3.13}$$

where subscript "I" and "P" represents the total reflectance observations and the observations of the degree of linear polarization, respectively. Because of the different accuracies of the total radiance and degree of linear polarization, the covariance matrix assumed for logarithms measurements $\boldsymbol{f}^*$ has the array structure:

$$\boldsymbol{C}_f = \begin{pmatrix} \boldsymbol{C}_I & \boldsymbol{0} \\ \boldsymbol{0} & \boldsymbol{C}_P \end{pmatrix} = \begin{pmatrix} \varepsilon_I^2 \boldsymbol{I}_I & \boldsymbol{0} \\ \boldsymbol{0} & \varepsilon_P^2 \boldsymbol{I}_P \end{pmatrix}. \tag{3.14}$$

Accordingly, the weighting matrix $\boldsymbol{W}_f$ is expressed as:

$$\boldsymbol{W}_f = \begin{pmatrix} \boldsymbol{I}_I & \boldsymbol{0} \\ \boldsymbol{0} & \gamma_P \boldsymbol{I}_P \end{pmatrix}, \tag{3.15}$$

where $\boldsymbol{I}$… symbolize the unity matrices of corresponding dimension and γ_P indicates a ratio of the total and polarized reflectance variances, it is defined as:

$$\gamma_P = \varepsilon_P^2/\varepsilon_I^2. \tag{3.16}$$

It is noted that the variance of the errors in measurements of total reflectance is expected at the level of 2% relative to the magnitude of observed radiance $\boldsymbol{I}$. While, the variance of the errors in measurements of the degree of linear polarization is expected at the absolute level of 1%. In Eq. (3.14), it assumes the simplest structure of the covariance matrix when intensity and polarization observations are equally accurate for all spectral channels and angles of observations. If there is more detailed available information about covariance matrix, it can be trivially integrated into Eqs. (3.13) – (3.16).

Comparing to the methodology of Rodgers (2000), the retrieval was constrained here using exclusively the a priori smoothness constraints as discussed in the 3.2.3.

3.2.2 Multiple-pixel observation fitting

The algorithm implements the measurement fitting for a group of pixels and it is constrained by the extra a priori limitations on inter-pixel variability of aerosol and/or surface reflectance properties. Since the information content of the reflected radiation from single pixel is sometimes insufficient for a unique retrieval of all retrieved parameters, such approach can obtain more stable satellite data inversions. If the properties of aerosol and/or surface reflectance are the same for a certain time period or over some area, one can trivially achieve higher redundancy in the retrieval by applying single pixel algorithm to the observations collected from such multiple pixels. In order to make the multi-pixel retrieval more robust and reliable, a priori known statistical limitations serving as an extra constraint is indispensable. With such concept in a frame of statistical estimation formalism, Dubovik et al. (2008) improve the global aerosol inverse modeling retrievals. Quaife and Lewis (2010) employ a similar concept to impose temporal smoothness constraints on the variability of surface reflectance for inverting linear kernel-driven BRDF models from MODIS observations. In addition, application of the multi-pixel approach is only a tool for imposing extra spatial and temporal constraints on the retrieved aerosol and surface parameters. When a group of pixels is inverted together, this approach is also convenient for rigorous accounting for cross-pixel coupling in this forward modeling of reflected radiances. This coupling caused by multiple light scattering effects can introduce some dependence of reflected radiances over observed pixel on the properties of surface and aerosol over neighboring pixels. It is known as adjacency effect in satellite remote sensing and sometimes adds some errors to the aerosol retrieval. Although this effect is significant for high-resolution observations, it is negligible

for satellite images with resolution ~2 km and larger (Tanré et al., 1981; Kaufman, 1982; Lyapustin and Kaufman, 2001). In this algorithm, it does not take into account the adjacency effect because the resolution of POLDER/PARASOL observation is about 5.3 km × 6.2 km.

In order to make the equations more compact, Eq. (3.2) can be expressed as (for *i*-th single pixel):

$$\begin{cases} \boldsymbol{f}_i^* = \boldsymbol{f}_i(\boldsymbol{a}) + \Delta\boldsymbol{f}_i \\ \mathbf{0}_i^* = \boldsymbol{S}_i\boldsymbol{a}_i + \Delta(\Delta\boldsymbol{a}_i) \Rightarrow \boldsymbol{f}_i^* = \boldsymbol{f}_i(\boldsymbol{a}_i) + \Delta\boldsymbol{f}_i. \\ \boldsymbol{a}_i^* = \boldsymbol{a}_i + \Delta\boldsymbol{a}_i^* \end{cases} \tag{3.17}$$

Correspondingly, the inversion of multi-pixel observations is a solution to the following combined system of equations:

$$\begin{cases} \boldsymbol{f}_1^* = \boldsymbol{f}_1(\boldsymbol{a}_1) + \Delta\boldsymbol{f}_1 \\ \boldsymbol{f}_2^* = \boldsymbol{f}_2(\boldsymbol{a}_2) + \Delta\boldsymbol{f}_2 \\ \boldsymbol{f}_3^* = \boldsymbol{f}_3(\boldsymbol{a}_3) + \Delta\boldsymbol{f}_3 \\ \cdots \\ \mathbf{0}_x^* = \boldsymbol{S}_x\boldsymbol{a} + \Delta(\Delta_x\boldsymbol{a}) \\ \mathbf{0}_y^* = \boldsymbol{S}_y\boldsymbol{a} + \Delta(\Delta_y\boldsymbol{a}) \\ \mathbf{0}_t^* = \boldsymbol{S}_t\boldsymbol{a} + \Delta(\Delta_t\boldsymbol{a}) \end{cases}, \tag{3.18}$$

where the subscript "*i*" (*i*=1, 2, 3, …) is the number of each single pixel. The total vector of unknowns $\boldsymbol{a}$ is combined by the vectors of unknowns $\boldsymbol{a}_i$ of each *i*-th pixel:

$$\boldsymbol{a} = \begin{pmatrix} \boldsymbol{a}_1 \\ \boldsymbol{a}_2 \\ \boldsymbol{a}_3 \\ \cdots \end{pmatrix}. \tag{3.19}$$

The matrices $\boldsymbol{S}_x$, $\boldsymbol{S}_y$ and $\boldsymbol{S}_t$ include the coefficients for calculating *m*-th differences (numerical equivalent of *m*-th derivatives) of spatial or temporal inter-pixel variability for each retrieved parameter a_k characterizing $dV(r_j)/dlnr$, $Frac(i)$, $\rho_0(\lambda_j)$, $\kappa(\lambda_j)$, $\theta(\lambda_j)$. It is noted that $n(\lambda_j)$ and $k(\lambda_j)$ are calculated by the fraction ($Frac(i)$) of aerosol composition. $\mathbf{0}_x^*$, $\mathbf{0}_y^*$, $\mathbf{0}_t^*$ denote vectors of zeros and $\Delta(\Delta_x\boldsymbol{a})$, $\Delta(\Delta_y\boldsymbol{a})$ and $\Delta(\Delta_t\boldsymbol{a})$ denote vectors of the uncertainties describing the deviations of the differences from the zeros.

Formally, using the same sequence of the functions as shown in the single pixel case, the solution of the multi-pixel system can be implemented. However, the minimized quadratic form $\Psi(\boldsymbol{a}^P)$, its gradient $\nabla\Psi(\boldsymbol{a}^P)$ and Fisher Matrix $\boldsymbol{A}_P$ formulated for inversion of combined multi-pixel Eq. (3.18) would be expressed by corresponding single-pixel terms:

$$\Psi(\boldsymbol{a}^P) = \left(\sum_{i=1}^{N_{pixels}} \Psi_i(\boldsymbol{a}^P)\right) + \frac{1}{2}(\boldsymbol{a}^P)^T\boldsymbol{\Omega}_{inter}\boldsymbol{a}^P, \tag{3.20}$$

$$\boldsymbol{A}_P = \left[\begin{pmatrix} \boldsymbol{A}_{1,P} & \cdots & \mathbf{0} \\ \vdots & \ddots & \vdots \\ \mathbf{0} & \cdots & \boldsymbol{A}_{N,P} \end{pmatrix} + \boldsymbol{\Omega}_{inter}\right], \tag{3.21}$$

$$\nabla\Psi(\boldsymbol{a}^P) = \begin{bmatrix} \nabla\Psi_1(\boldsymbol{a}_1^P) \\ \nabla\Psi_2(\boldsymbol{a}_2^P) \\ \cdots \\ \nabla\Psi_N(\boldsymbol{a}_N^P) \end{bmatrix} + \boldsymbol{\Omega}_{inter}\boldsymbol{a}^P, \tag{3.22}$$

where $\Psi_i(\boldsymbol{a}^P)$, $\nabla\Psi_i(\boldsymbol{a}^P)$ and $\mathbf{A}_{i,P}$ describe for $\boldsymbol{N}$ single pixels. The smoothing inter-pixel matrix $\boldsymbol{\Omega}_{inter}$ is written as:

$$\boldsymbol{\Omega}_{inter} = \gamma_x \boldsymbol{S}_x^T \boldsymbol{S}_x + \gamma_y \boldsymbol{S}_y^T \boldsymbol{S}_y + \gamma_t \boldsymbol{S}_t^T \boldsymbol{S}_t. \tag{3.23}$$

$\nabla\Psi(\boldsymbol{a}^P)$ is not equal to a simple sum of $\nabla\Psi_i(\boldsymbol{a}_i^P)$ and the inter-pixel matrix $\boldsymbol{\Omega}_{inter}$ has non-zero non-diagonal elements. Hence the solution of the multi-pixel system ($\boldsymbol{N}$ pixels) is not equivalent to the solution of $\boldsymbol{N}$ independent single pixel systems. In addition, since the matrix Ω_{inter} is very sparse and transparent, in contrast to other calculations performed in the inversion, computer time required for definition of these smoothing terms is insignificant. Another difference is that the multi-pixel approach requires solving the N_{pixel} pixels joint Normal System that can have rather high dimension. Meanwhile, the Fisher matrix A_P is also very sparse and a number of numerical tools are available for optimizing the solution of linear system. There are also some differences between single-pixel and multi-pixel approaches about the smoothness constraints on variability of aerosol and surface parameters as discussed in the 3.2.3.

3.2.3 A priori smoothness constraints of fitting

This section presents smoothness constraints of fitting in the GRASP retrieval algorithm. The smoothness constraints are the same as that in the study of Dubovik et al. (2011) except the smoothness constraints of refractive index. Namely, in the composition approach, the smoothness constraints on spectral variability of complex refractive index are determined by the fraction of aerosol composition in the conversion model.

3.2.3.1 A priori smoothness constraints in single-pixel fitting

The vector $\boldsymbol{a}$ consists of several components:

$$\boldsymbol{a} = (\boldsymbol{a}_v\ \boldsymbol{a}_{frac}\ \boldsymbol{a}_{sph}\ \boldsymbol{a}_{Vc}\ \boldsymbol{a}_h\ \boldsymbol{a}_{brdf,1}\ \boldsymbol{a}_{brdf,2}\ \boldsymbol{a}_{brdf,3}\ \boldsymbol{a}_{bpdf})^T, \tag{3.24}$$

where $\boldsymbol{a}_v$, $\boldsymbol{a}_{frac}$, $\boldsymbol{a}_{sph}$ represents the component of the vector $\boldsymbol{a}$ corresponding to the $dV(r_i)/dlnr$, $Frac(i)$ and C_{sph}, respectively, $\boldsymbol{a}_h$ characterizes the logarithm of mean altitude of the aerosol layer h_a. The element $\boldsymbol{a}_{Vc}$ denotes the logarithms of total volume concentration, while $\boldsymbol{a}_v$ includes logarithms of values $dV(r)/dlnr$ normalized by total volume concentration. The three components ($\boldsymbol{a}_{brdf,1}, \boldsymbol{a}_{brdf,2}, \boldsymbol{a}_{brdf,3}$) are related to the logarithms of spectrally dependent parameters ($\rho_o(\lambda)$, $\kappa(\lambda)$ and $\theta(\lambda)$) included in RPV model. The

vector $\boldsymbol{a}_{bpdf}$ includes the logarithms of the spectrally dependent free parameter $B(\lambda)$ employed in Maignan et al. (2009) model.

In the POLDER/PARASOL algorithm, the a priori smoothness constraints are imposed on several different components of the vector $\boldsymbol{a}$. Specifically, the matrix $\boldsymbol{S}$ has the array structure as:

$$\boldsymbol{Sa} = \begin{pmatrix} S_v & \mathbf{0} & \mathbf{0} & \mathbf{0} & \mathbf{0} & \mathbf{0} \\ 0 & 0 & 0 & 0 & 0 & 0 \\ 0 & 0 & 0 & 0 & 0 & 0 \\ 0 & 0 & 0 & 0 & 0 & 0 \\ 0 & 0 & 0 & 0 & 0 & 0 \\ \mathbf{0} & \mathbf{0} & S_{brdf,1} & \mathbf{0} & \mathbf{0} & \mathbf{0} \\ \mathbf{0} & \mathbf{0} & \mathbf{0} & S_{brdf,2} & \mathbf{0} & \mathbf{0} \\ \mathbf{0} & \mathbf{0} & \mathbf{0} & \mathbf{0} & S_{brdf,3} & \mathbf{0} \\ \mathbf{0} & \mathbf{0} & \mathbf{0} & \mathbf{0} & \mathbf{0} & S_{bpdf} \end{pmatrix} \begin{pmatrix} \boldsymbol{a}_v \\ a_{frac} \\ a_{sph} \\ a_{Vc} \\ a_h \\ \boldsymbol{a}_{brdf,1} \\ \boldsymbol{a}_{brdf,2} \\ \boldsymbol{a}_{brdf,3} \\ \boldsymbol{a}_{bpdf} \end{pmatrix}, \quad (3.25)$$

where the corresponding matrices $\boldsymbol{S}_{...}$ have different dimensions and describe differences of different order. The lines in Eq. (3.25) corresponding to $\boldsymbol{a}_h, \boldsymbol{a}_{Vc}, \boldsymbol{a}_{sph}, \boldsymbol{a}_{frac}$ contain only zeros because no smoothness constraint can be applied. The errors Δ ($\Delta\boldsymbol{a}$) are assumed independent for different components of the vector $(\Delta\boldsymbol{a})^*$ and the smoothness matrix in Eqs. (3.3) – (3.8) has the array structure as:

$$\gamma_\Delta\Omega = \begin{pmatrix} \gamma_{\Delta,1}\Omega_1 & \mathbf{0} & \mathbf{0} & \mathbf{0} & \mathbf{0} & \mathbf{0} \\ 0 & 0 & 0 & 0 & 0 & 0 \\ 0 & 0 & 0 & 0 & 0 & 0 \\ 0 & 0 & 0 & 0 & 0 & 0 \\ 0 & 0 & 0 & 0 & 0 & 0 \\ \mathbf{0} & \mathbf{0} & \gamma_{\Delta,2}\Omega_2 & \mathbf{0} & \mathbf{0} & \mathbf{0} \\ \mathbf{0} & \mathbf{0} & \mathbf{0} & \gamma_{\Delta,3}\Omega_3 & \mathbf{0} & \mathbf{0} \\ \mathbf{0} & \mathbf{0} & \mathbf{0} & \mathbf{0} & \gamma_{\Delta,4}\Omega_4 & \mathbf{0} \\ \mathbf{0} & \mathbf{0} & \mathbf{0} & \mathbf{0} & \mathbf{0} & \gamma_{\Delta,5}\Omega_5 \end{pmatrix}, \quad (3.26)$$

where $\boldsymbol{\Omega}_i = \boldsymbol{S}_i^T \boldsymbol{W}_i^{-1} \boldsymbol{S}_i$ uses the derivative matrices $\mathbf{S}_i$ (i=1, …, 5), $\mathbf{S}_v$, $\mathbf{S}_{brdf,1}$, $\mathbf{S}_{brdf,2}$, $\mathbf{S}_{brdf,3}$, S_{bpdf}. If the covariance matrices of errors Δ ($\Delta\boldsymbol{a}$) have the structure $\mathbf{C}_{\Delta,i} = \varepsilon_{\Delta,i}^2 \boldsymbol{I}_{(N_{\Delta,i} \times N_{\Delta,i})}$ for each components of $(\Delta\boldsymbol{a})^*$, the quadratic form $\Psi_\Delta(\boldsymbol{a}^P)$ in Eqs. (3.3) – (3.8) can be expressed as:

$$2\Psi_\Delta(\boldsymbol{a}^P) = \gamma_\Delta\,(\boldsymbol{a}^P)^T \boldsymbol{\Omega}\, \boldsymbol{a}^P = \sum_{i=1,\ldots,5} 2\Psi_{\Delta,i}(\boldsymbol{a}^P) = \sum_{i=1,\ldots,5} \gamma_{\Delta,i} (\boldsymbol{a}_i^P)^T \boldsymbol{\Omega}_i \boldsymbol{a}_i^P, \quad (3.27)$$

where $\gamma_{\Delta,i} = \varepsilon_f^2 / \varepsilon_{\Delta,i}^2$.

The idea of imposing the smoothness constraints on a single retrieved function $y(x_i)$ was proposed by Phillips (1962), Tikhonov (1963) and Twomey (1963). It is usually considered to be an implicit constraint on derivatives in these original papers. Following the ideas of Dubovik and King (2000), Dubovik (2004) and Dubovik et al. (2011), this algorithm

considers smoothness constraints explicitly as a priori estimates of the derivatives of the retrieved characteristic $y(x_i)$. The values of m-th derivatives g_m of the function $y(x)$ characterize the degree of its non-linearity and, therefore, can be used as a measure of $y(x)$ smoothness. These derivatives g_m can be approximated by differences between values of the function $a_i = y(x_i)$ in discrete points x_i.

Dubovik and King (2000) and Dubovik (2004) related the strength of a priori smoothness constraints in a priori known deviations of derivatives from zeros in second line of Eq. (3.2) to the integral norm of the derivatives, which can be defined as:

$$b_i = \int_{x_{min}}^{x_{max}} \left(\frac{d^m y_i(x)}{d^m x}\right)^2 dx, \tag{3.28}$$

where b_i describes the smoothness of the physical continuous function $y_i(x)$. If the values of function $y_i(x)$ are known at N_i discrete points x_i, the norm of the m-th derivatives can be approximated as:

$$b_i = \int_{x_{min}}^{x_{max}} \left(\frac{d^m y_i(x)}{d^m x}\right)^2 dx \approx \sum_{j=m+1}^{N_i} \left(\frac{\Delta^m y_i(x_j)}{\Delta_m(x_j)}\right)^2 \Delta_m(x_j) = (a_i^P)^T \boldsymbol{\Omega}_{g,i} \boldsymbol{a}_i^P, \tag{3.29}$$

where $\boldsymbol{\Omega}_{g,i} = (\boldsymbol{S}_{g,i})^T \boldsymbol{W}_i^{-1} \boldsymbol{S}_{g,i}$, $\mathbf{S}_{g,i}$ characterizes the matrices of the coefficient for estimating derivatives $\mathrm{g}_{m,i}(\mathrm{x}_j)$, $\mathbf{W}_i$ characterizes diagonal weighting matrix with the elements $\{\mathbf{W}_i\}_{jj} = 1/\Delta_{m,i}(x_j)$. Therefore, the relation of the multiplier $\gamma_{\Delta,i} = \varepsilon_f^2 / \varepsilon_{\Delta,i}^2$ in Eq. (3.27) to the known values of b_i can be written as:

$$\gamma_{\Delta,i} = \frac{\varepsilon_f^2}{(b_i^m)^{max}}, \tag{3.30}$$

where

$$(b_i^m)^{max} = \int_{x_{min}}^{x_{max}} \left(\frac{d^m y_i^{ns}(x)}{d^m x}\right)^2 dx. \tag{3.31}$$

Here, $y_i^{ns}(x)$ is the most unsmooth real function $\mathrm{y}_i(x)$. Therefore, the smoothness a priori condition imposed by the second line in Eq. (3.2) allows any function $\mathrm{y}_i(x)$ to be solution that has norm of m-th derivatives b_i^m smaller than $(b_i^m)^{max}$. Such definition means the second component in Eq. (3.2) defining the derivatives equal zeros: $\boldsymbol{g}_i^* = \mathbf{0}_i^* = \mathbf{0} + \Delta_{i,g}$. It is assumed that the errors Δ_g are independent for each i-th (i = 1, 2, …, 5) component of vector $\boldsymbol{a}$. Such errors Δ_g have the diagonal covariance matrix with the elements of the diagonal defined as: $\{\boldsymbol{C}_{g,i}\} = \varepsilon_{g,i}^2(\Delta_{m,i}(x_j))$. The deviation of estimates $g_{m,i}(x_j)$ from zero is assumed to have variance $\varepsilon_{g,i}^2/(\Delta_{m,i}(x_j))$. Therefore, the strength of a priori constraint imposed on each retrieved function ($dV(r)/dlnr$, $\rho_0(\lambda)$, $\kappa(\lambda)$, $\theta(\lambda)$ and $B(\lambda)$) is defined by calculating

values of $(b_i^m)^{max}$ using most unsmooth examples of corresponding physical functions, such as most unsmooth size distributions, spectral dependencies of BRDF parameters.

3.2.3.2 A priori smoothness constraints in multiple pixel fitting

The 3.2.2 section discusses the simultaneous inversion of a group of pixels. The multi-pixel approach employs expected continuity in pixel-to-pixel variability of aerosol and land surface properties as an additional retrieval constraint. In addition, the pixel group ($N_x \times N_y \times N_t$) has limited size. The properties of aerosol and surface observed at the edges of a pixel group and the pixel-neighbors located just outside of the $N_x \times N_y \times N_t$ pixel group may have certain continuities. Such constraints enforcing continuity of retrieved properties during different pixel groups can be rather logically added to the inversion formulations. Adding extra terms in Eqs. (3.20) – (3.23) can implement the additional conditions of continuity of aerosol and surface properties with the values of corresponding parameters in the neighborhood of the inverted pixel group. For example, the minimized quadratic form $\Psi(\boldsymbol{a}^p)$, its gradient $\nabla\Psi(\boldsymbol{a}^p)$ and Fisher Matrix $\boldsymbol{A}_p$ will include the extra-terms $\Psi_{edge}(\boldsymbol{a}^p)$, $\nabla\Psi_{edge}(\boldsymbol{a}^p)$ and $(\boldsymbol{A}_p)_{edge}$ accordingly. Such additional terms are rather transparent and can be computed with very minor effort. Because of the natural limitations of computer resources, the inversion of satellite observations over large geographical areas and extended time periods can be inverted sequentially by small pixel groups of limited $N_x \times N_y \times N_t$ size. Such sequential retrieval is nearly equivalent to simultaneous inversion of all data by adding intergroup constraints. It is noted that the retrieval for each small pixel group would not take advantage of the information contained in the observations over the pixels inverted in subsequent retrieval acts, while the retrieval can fully benefit from all preceding retrievals. Since the spatial and temporal correlations of both aerosol and surface properties have rather limited range, using the inter-parcel continuity constraints sequential pixel parcel-by-parcel retrieval can produce the extended fields of the retrieved parameters. The high consistency of those fields is enforced by unified inter-pixel constraints.

The multi-pixel retrieval approach discussed in the above sections benefits from the limited spatial variability of aerosol or land surface reflectance for different pixels or temporary for the same pixel. However, sometimes it is reasonable to assume that some parameters do not change at all from pixel to pixel. Specifically, most of the aerosol parameters and the land surface reflectance parameters are assumed diurnally constant in the retrieval algorithm developed for geostationary observations (Govaerts et al., 2010). Thus, a possibility of assuming the inter-pixel invariant parameters can be a useful option for constraining the retrieval and verifying the importance of neglected variations.

Inclusion of those assumptions would enforce high correlation between corresponding retrieved parameters and make them practically equal. However, the enforcement of full dependence of the retrieved parameters has deficiencies. For example, the increase of γ_t would produce a strong increase in the smoothness matrices $\boldsymbol{\Omega}_{inter}$ and $\boldsymbol{\Omega}_{edge}$ into the total Fisher matrix in Eqs. (3.20) – (3.23). Correspondingly, the dominant contributions of $\boldsymbol{\Omega}_{inter}$ and $\boldsymbol{\Omega}_{edge}$ would result in degenerated Normal systems. Therefore, if the properties of aerosol or surface in different pixel are same, the retrievals of a single group of those constant parameters for many pixels seem more logical than the retrievals of several groups of parameters (one group per each pixel) forced by the enhanced smoothness constraints to have very close values in different pixels. However, since practical implementation of the algorithm allowing easy increase or decrease in the number of fixed parameters is logistically very challenging, the algorithm based on the straightforward strategy looses flexibility. Thus, the approach that uses the general formulation of the inversion strategy by the inter-pixel smoothness constraints even for some retrieval scenarios when some derived parameters do not change in different observations (for example, some parameters of BRDF are intra-day independent over the same pixel) or one set of observation (for example, some parameters of BRDF are spectrally independent in any single pixel) is recommended.

The approach is the following. First, it is assumed that every single parameter driving the forward model is retrieved. Under such assumption, the Normal system is built. Then, using simple modification of the Normal system without any other changes to fix several parameters equal in the inversion. It is noted that the Fisher matrix $\boldsymbol{A}^{(N)}$ and gradient $\nabla\Psi^{(N)}$ for deriving N parameters a_i are defined. Then if $n+1$ parameters are assumed to equal ($a_i = a_{i_k}$ ($k = 1, \ldots, n+1$)), it is better to decrease number of the retrieved parameters and recalculate Fisher matrix and gradient for new decreased set of the retrieved parameters. Such new Fisher matrix and gradient can be obtained easily from the Fisher matrix and gradient calculated for original set of retrieved parameters. For example, the retrieval can be implemented simply by decreasing the dimensions of the Fisher matrix and gradient by summing up $n+1$ of lines and columns of the equal parameters. Therefore, the solution can be obtained by solving modified Normal system with Fisher matrix $\boldsymbol{A}^{(N-n)}$ and gradient $\nabla\Psi^{(N-n)}$ of smaller dimensions: $(N-n)\times(N-n)$ and $(N-n)$, respectively.

3.3 Physico-chemistry to refractive index conversion model

One of the most challenging aspects of measuring aerosol physicochemical properties is that the impacts of aerosols on climate and health are collectively determined by the properties of the individual particles. Field and laboratory studies demonstrate that aerosols have complex morphologies and phase behavior (You et al., 2012; Virtanen et al., 2010; Buajarern et al., 2007). The complex behavior caused by the phase and internal structure within particles can ultimately impact climate-relevant properties. Since such complex properties show that beyond knowing chemical mixing state, a further level of detail is needed, which is regarded as physicochemical mixing state (an example of the detail possible with physicochemical mixing state shown in Figure 3.2) (Ault and Axson, 2017). Chemical mixing state provides information on primary versus secondary components, but ignores spatial information and other physical properties. Physicochemical mixing state provides chemical detail information as well as the spatial information and/or physical properties such as morphology, internal structure and the spatial distribution of species. The complexity of coupling physical properties and chemical mixing state is a factor contributing to the studies of aerosol in spectroscopic measurements (Ault and Axson, 2017).

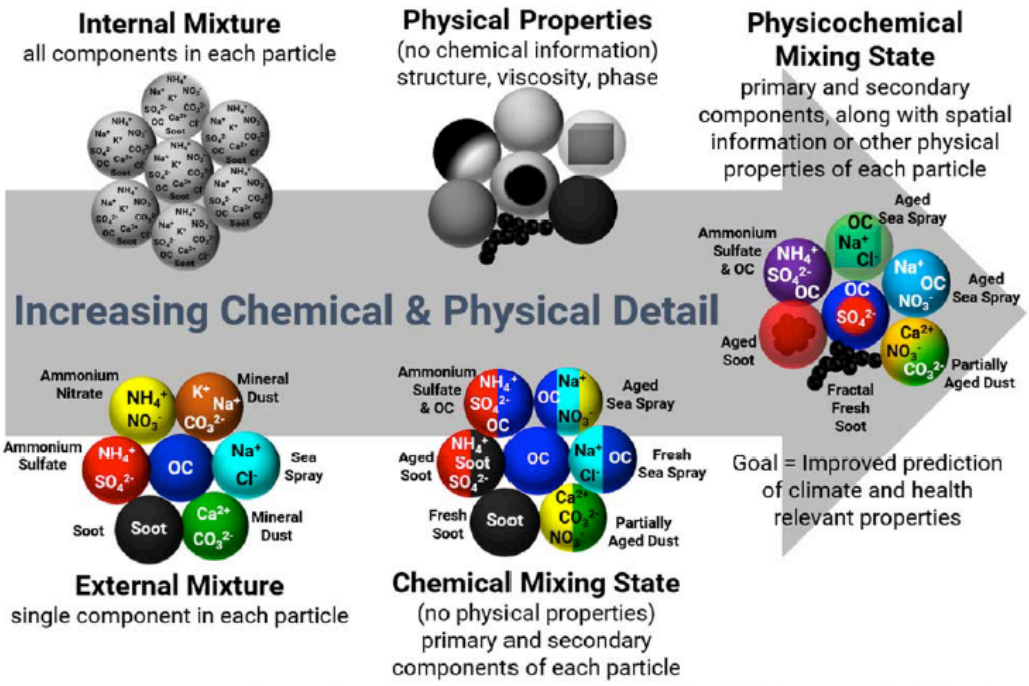

Figure 3.2: Illustrations of particle composition with increasing complexity and detail. The locations of the colors in the chemical mixing state particles are not meant to convey spatial distribution, only the presence of both primary and secondary components (Ault and Axson, 2017).

The previous GRASP algorithm can achieve a robust retrieval of complete aerosol properties including information about aerosol particle sizes, shape, absorption and refractive index, while without aerosol composition information. This thesis work presented an attempt to increase the physical and chemical detail information derived from remote sensing retrievals. The approach consist in modifying the "Forward model" by relating aerosol refractive index with fractions of some main aerosol compositions and direct retrieval of these fractions. In order to implement the idea of retrieving aerosol composition from remote sensing, it is imperative to identify a set aerosol components, combination of which refractive indices covers all possible solutions. At the same time, optical properties of these components should be sufficiently different to be distinguished in the measured signal. The components should also be representative for atmospheric aerosol and be as close as possible to aerosol composition implemented in global transport modeling. Information about relation of composition to aerosol microphysical properties, e.g., size fraction, should also be respected. Therefor the approach is called "physico-chemistry to refractive index" conversion model. The identification and development of the conversion model, as well as a series of sensitivity tests using synthetic data, are presented in the following.

3.3.1 Size-independent volume-weighted conversion model

3.3.1.1 Definition and assumption

The volume-weighted conversion model, which is the simplest conversion model, provides aerosol refractive index using the fraction and refractive index of each composition employed in the conversion model. The volume-weighted conversion model estimates the aerosol refractive index by Eq. (3.32) for particles of all sizes:

$$m(\lambda) = \frac{\sum_{i=1}^{j} Frac_i m_i(\lambda)}{\sum_{i=1}^{j} Frac_i}, \tag{3.32}$$

where $m(\lambda)$ represents the complex refractive index at the wavelength of λ. $Frac_i$ (i = 1, 2, …, j) represents the fraction of each composition and m_i represents the complex refractive index of composition, correspondingly.

Considering the limited information contained in the satellite remote sensing measurements and the optical discriminations among the compositions in the aerosols, it is assumed that aerosols can be composed of carbonaceous particles, mineral dusts, iron oxide and water for all sizes. The complex refractive indices of assumed aerosol compositions employed in such model are shown in Figure 3.3. Note that the refractive indices of all the selected components are different by their absolute values or by their spectral dependence; e.g., at some wavelengths the imaginary part of iron oxide is similar to carbonaceous or dust,

but the entire spectral dependence is very different. Here iron oxide is an important component that affects the ability of mineral dust aerosol to absorb sunlight at short wavelength. Dust is a non-absorbing component, such as quartz. They are the same in the conversion model for size-dependent case.

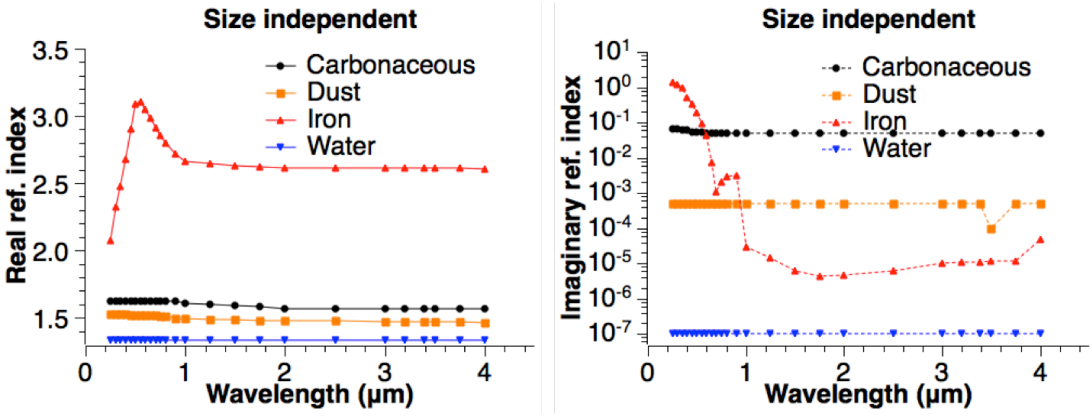

Figure 3.3: The refractive indices of assumed aerosol compositions employed in the size-independent volume-weighted conversion model. The parameters of carbonaceous particles are calculated from Bond and Bergstrom (2006) and Sun et al. (2007). The parameters of dust refer to Ghosh (1999). The parameters of iron oxide refer to Longtin et al. (1988). The parameters of water refer to Lesins et al. (2002).

3.3.1.2 Sensitivity test

With the size-independent volume-weighted conversion model, a series of sensitivity tests are conducted using synthetic data. First, using the assumed fractions of aerosol composition and the associated information (such as viewing geometry, spectral characteristic, coordinates, etc.) the PARASOL/POLDER synthetic measurements of radiances and polarization properties are created by the forward calculations. Then, the synthetic measurements are fitted by the numerical inversion procedure and fractions of the aerosol compositions are retrieved. Abscissa in the first panel of the Figure 3.4 shows the range of the assumed fractions. Figure 3.4 shows very good correlations between the assumed and the retrieved fractions of aerosol composition, as well as between the derived optical parameters (AOD, single-scattering albedo, refractive index). It demonstrates that using the size-independent volume-weighted conversion model, the inversion procedure is able to distinguish amongst the aerosol compositions employed in the model. The retrievals are not sensitive to the initial guess. However, the inconvenience of this model is that the BC and BrC are not distinguished, but grouped into one component (carbonaceous) that characterizes the strongly absorbing aerosols.

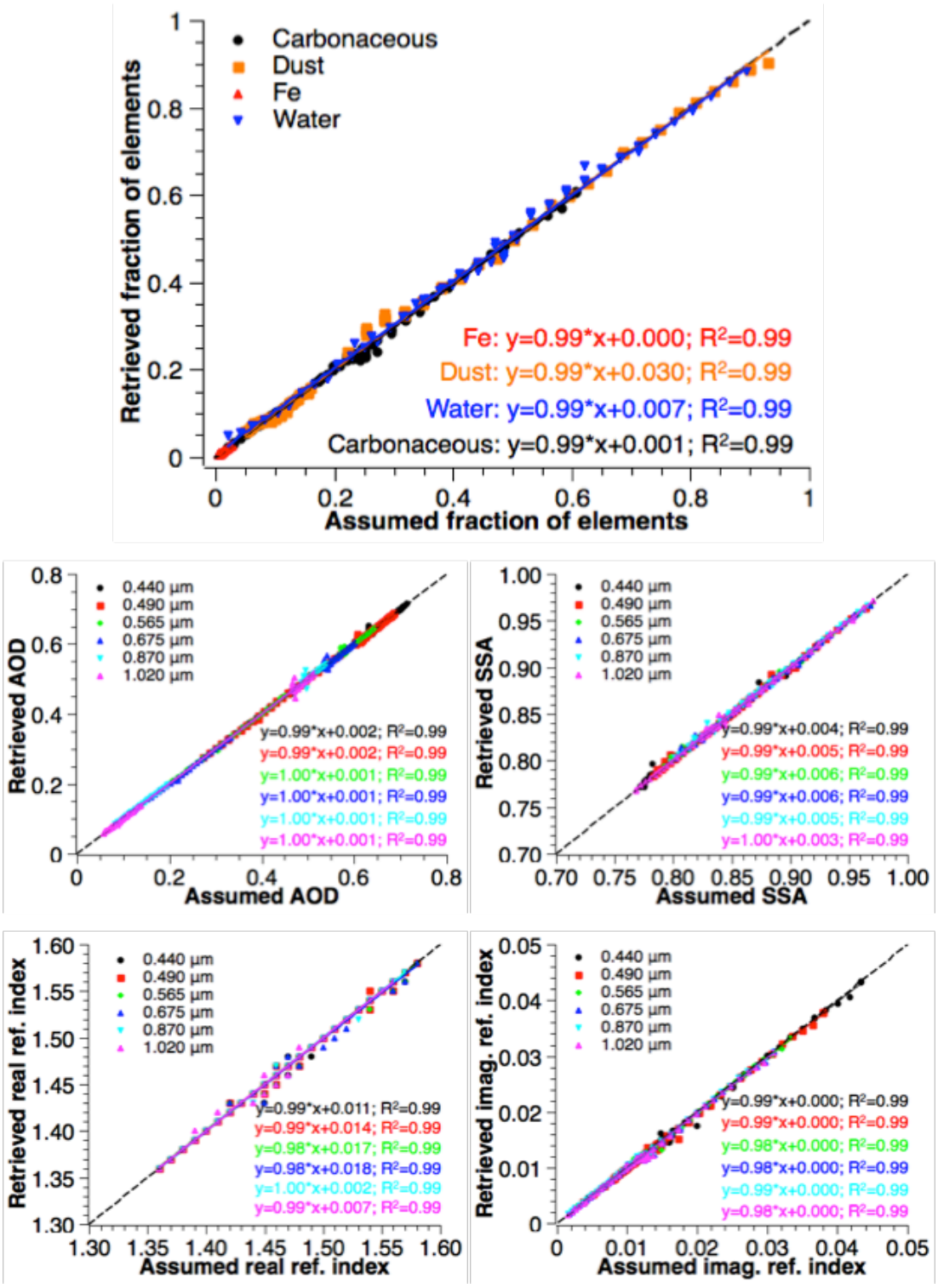

Figure 3.4: The sensitivity tests of size-independent volume-weighted conversion model.

With the size-independent conversion model, the POLDER/PARASOL retrieval is set to retrieve only one aerosol mode. The algorithm derives single values of fractions of aerosol composition and spherical particles for particles of all sizes.

3.3.2 Size-dependent volume-weighted conversion model

3.3.2.1 Definition and assumption

To derive information on BC and BrC separately, a new set of fractions was tested; that is the elements considered are BC, BrC, iron oxide, mineral dust and aerosol water content. However, because BrC and iron oxides (hematite and goethite) have similar strong spectral dependencies for the imaginary index with significant absorption at ultraviolet through mid-visible wavelengths (Kerker et al., 1979; Chen and Cahan, 1981; Derimian et al., 2008; Chen and Bond, 2010), mixtures of BrC and iron oxide cannot be unambiguously partitioned on the basis of the imaginary index alone. In order to retrieve BrC and iron oxide simultaneously, an option solution is separating these two compositions by the particle size. It is known that the fine mode is dominated by carbonaceous absorbing particles and the coarse mode is dominated by mineral dust aerosol, where the iron oxides are commonly present. Therefore, suggested is employment of the size dependent conversion aerosol composition model. It is assumed that the fine mode particles are comprised of BC, BrC, dust and water; the coarse mode particles consist of dust, iron oxide and water. Therefore, in the size-dependent conversion model, the refractive index is presented separately for fine and coarse modes, as follows:

$$m_F(\lambda) = \frac{\sum_{i=1}^{j} Frac(F_i)\, m_{F_i}(\lambda)}{\sum_{i=1}^{j} Frac(F_i)}, \tag{3.33}$$

$$m_C(\lambda) = \frac{\sum_{i=1}^{j} Frac(C_i)\, m_{C_i}(\lambda)}{\sum_{i=1}^{j} Frac(C_i)}, \tag{3.34}$$

where “F” and “C” denotes fine and coarse mode, respectively. The refractive indices of compositions employed in the size-dependent conversion model are shown in Figure 3.5. It is noted, however, that OC (non-absorbing organic carbon) and non-absorbing mineral dust have similar complex refractive index (Koepke et al., 1997; Ghosh et al., 1999), which makes impossible their distinguishing in the fine mode. Therefore, in the presented size-dependent approach, the OC and the fine dust appear as the same element. However, the Ångström Exponent is suggested to be use for attribution of the derived fraction to one of the elements. Separation by the Ångström Exponent is expected to be particularly useful in areas affected by dust or biomass burning only. The assumption may lead to uncertainty in mixed cases.

3.3.2.2 Sensitivity test

In order to investigate the sensitivity of POLDER/PARASOL observations to the parameters retrieved using the size-dependent volume-weighted conversion model, a similar

series of sensitivity tests are conducted using the synthetic data as discussed in 3.3.1.2. The correlations shown in Figure 3.6 indicate that the size-dependent volume-weighted conversion model allows the algorithm to retrieve the fractions of aerosol compositions employed in fine and coarse modes, respectively. Indeed, the number of the retrieved parameters is increased in this case (from four fractions to seven fractions), however, the sufficiency of the information content tests shows that the retrievals are not sensitive to the initial guess.

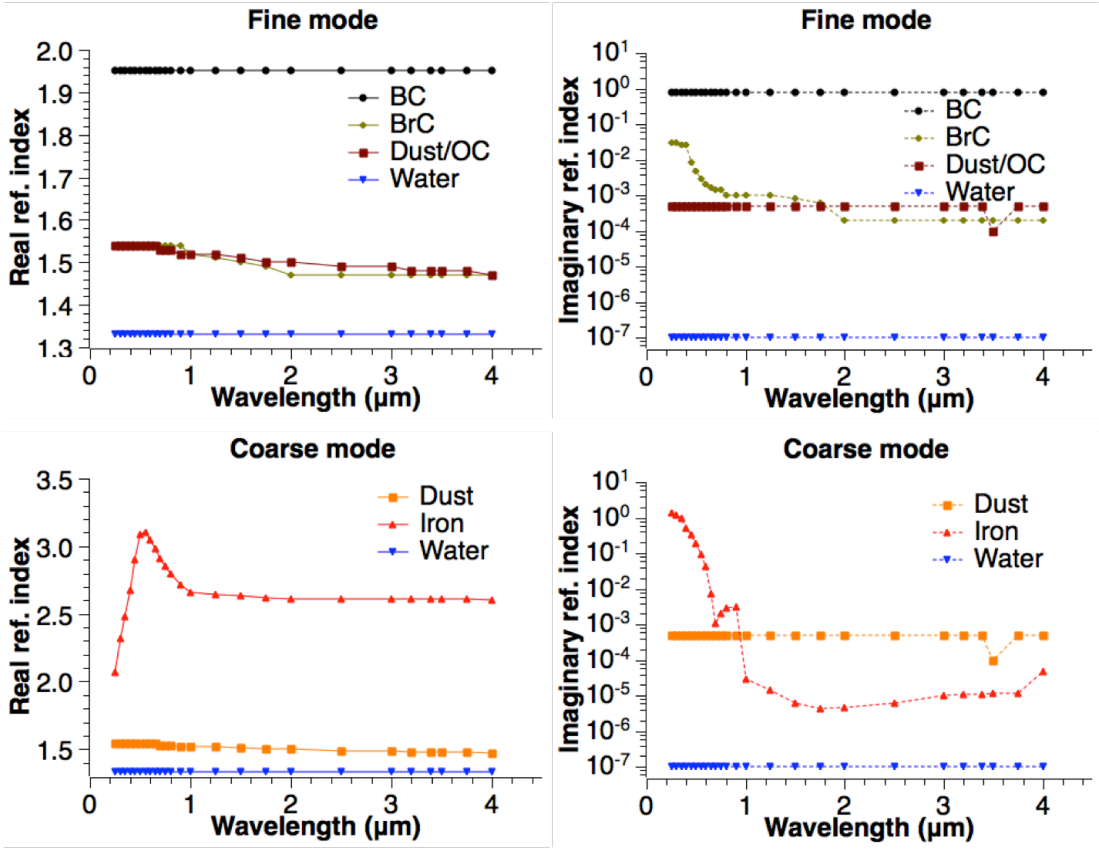

Figure 3.5: The refractive indices of assumed aerosol compositions employed in the size-dependent volume-weighted conversion model. The parameters of BC refer to Bond and Bergstrom (2006). The parameters of BrC refer to Sun et al. (2007). The parameters of dust refer to Ghosh (1999). The parameters of iron oxide refer to Longtin et al. (1988). The parameters of water refer to Lesins et al. (2002).

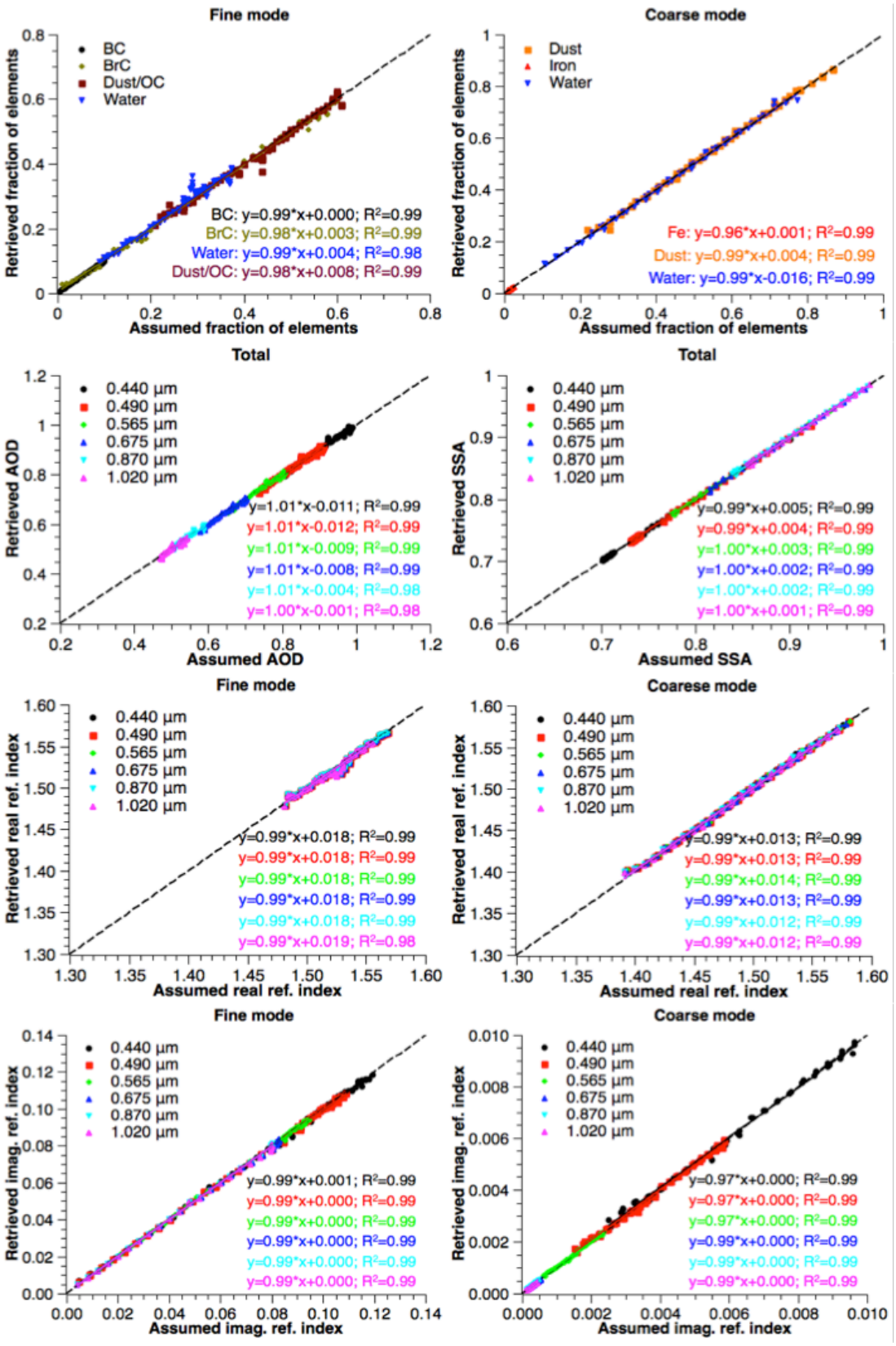

Figure 3.6: The sensitivity tests of size-dependent volume-weighted conversion model.

3.3.2.3 Uncertainty

In the present size-dependent conversion model, OC and fine dust can be retrieved as the same element in the fine mode. Because these two elements have similar complex refractive index (Ghosh, 1999; Koepke et al., 1997; Arola et al., 2011), their distinguishing by the

presented algorithm is impossible. This may lead to an artificial fine dust fraction, especially in regions affected biomass burning. Figure 3.7 shows the uncertainties caused by the assumption of OC and fine dust. First, using the assumed fractions of composition averaged over biomass burning regions and the OC refractive index in fine mode to create the PARASOL/POLDER synthetic measurements of radiances and polarization properties. Then, the synthetic measurements are fitted by the numerical inversion procedure employed the dust refractive index in fine mode and fractions of the aerosol compositions are retrieved, showing the biomass burning cases that can have uncertainties induced by the assumption of OC and fine dust refractive indices. The uncertainties in BC, BrC, iron oxide, water and coarse dust are less than 5%, and the uncertainties in fine dust or OC are around 10%.

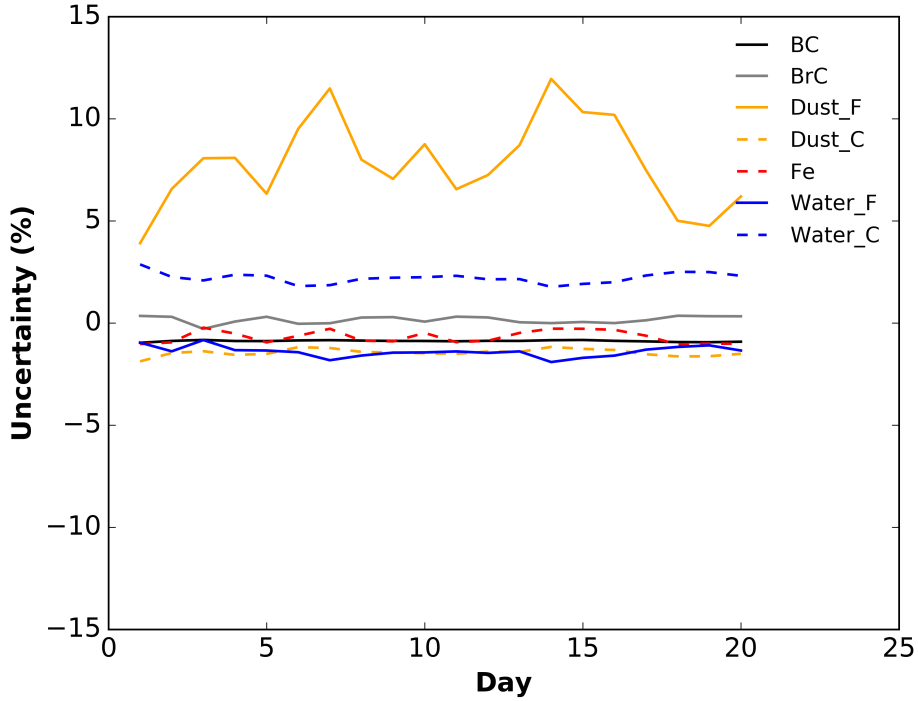

Figure 3.7: The uncertainty of OC and fine dust assumed as same composition in fine mode of size-dependent Maxwell-Garnett conversion model. The solid lines represent the aerosol compositions in fine mode and the dashed lines represent the aerosol compositions in coarse mode. “F” and “C” denotes the fine particles and coarse particles, respectively.

3.3.3 Size-dependent Maxwell-Garnett conversion model

3.3.3.1 Definition and assumption

The volume-weighted conversion model is a straightforward and transparent approach that facilitated understanding of sensitivity limits of POLDER/PARASOL measurements to the aerosol composition and determining an optimum configuration of the algorithm. At the same time, the Maxwell-Garnett mixing rule has been extensively applied in many studies for

retrieval of aerosol composition from ground-based remote sensing measurements (Schuster et al., 2005, 2009, 2016; Li et al., 2013, 2015; Wang et al., 2013). Figure 3.8 illustrates a general logistics of an effective refractive index calculation using a conversion model that is based on Maxwell-Garnett effective medium approximation.

The first step in this approach is creation of a "host" and calculation of refractive index of the host, which can be formed by water and soluble inorganic species (e.g., ammonium nitrite, ammonium sulfate, sea salt).

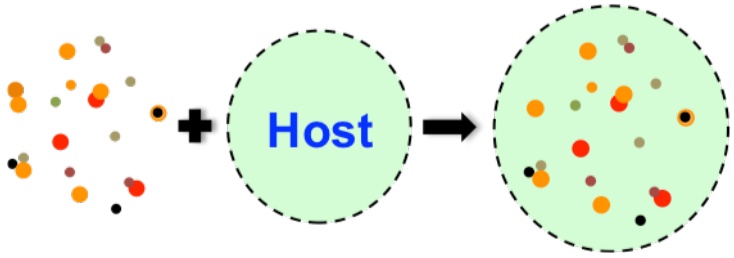

Figure 3.8: Illustration of Maxwell-Garnett conversion model.

It is well know that inorganic salt aerosols are mostly hygroscopic by nature and exhibit the property of deliquescence in humid air (Tang, 1979). The phase transition from a solid particle to a saline droplet (host) usually occurs spontaneously when the relative humidity reaches a specific value, known as the deliquescence point, that is specific to the chemical composition of the aerosol particle (Orr et al., 1958; Tang, 1976; Tang and Munkelwitz, 1993). The refractive indices of hygroscopic aerosols change with the additional amount of water that is absorbed in response to changing relative humidity. These changes in refractive index, including also the changes in specific density, size and mass fraction, have been measured very accurately as functions of relative humidity (Tang and Munkelwitz, 1991, 1994; Tang, 1996). The measurements are made at the HeNe laser wavelength of 0.633 μm, and parametric formulas derived for the changes in real part of the refractive index, specific density, size and water activity as functions of mass fraction.

In present approach, the host is assumed to depend on the properties and the proportions of ammonium nitrate and water because relative humidity of deliquescence of ammonium nitrate is low. The real and imaginary refractive indices of water are smoothly interpolated utilizing measured data (Hale and Querry, 1973; Palmer and Williams, 1974; Downing and Williams, 1975; Tang and Munkelwitz, 1991; Kou et al., 1993). The real refractive index of dry ammonium nitrate is spectrally extrapolated from water refractive index using refractive index proportionality measured by Tang (1996). The imaginary refractive index of dry ammonium nitrate is linearly extrapolated from measurements for a solution of ammonium nitrate with mass fraction of 40% (Gosse et al., 1997) using Tang (1996) proportionality.

Outside of the measurement interval, the imaginary refractive index of ammonium nitrate is assumed to be the same as that for pure water.

For droplets ("host") the equilibrium relative humidity is increased by the Kelvin effect due to the surface tension of the droplet curvature according to Eq. (3.35):

$$\%RH = 100a_w exp(\frac{4\gamma M}{\rho RTD}), \tag{3.35}$$

where a_w and γ are, respectively, the water activity and surface tension of a bulk solution of composition and density ρ. M is the molecular weight of water, R is the gas constant, and T is the absolute temperature. The curvature effect is generally neglected in droplet growth/evaporation computations for aerosol particles in the optical size range. Therefore, $\%RH$ is given by $100a_w$. Newton-Raphson iteration is used to obtain mass fraction X for the specified relative humidity using the water activity (a_w), which is expressed as (Tang, 1996):

$$a_w = 1.0 - 0.365 * X - 0.09155 * X^2 - 0.2826 * X^3. \tag{3.36}$$

Ammonium nitrate solution refractive index for the mass fraction X is used to obtain a refractive index proportionality factor that can linearly interpolate the relative humidity dependence of both real and imaginary refractive index between the dry ammonium nitrate and pure water values, written as Eq. (3.37) (Tang et al., 1981). Kou et al. (1993) suggest that linear interpolation is appropriate for changes in refractive index due to changing mass fraction for ammonium nitrate. Relative humidity is used to compute the refractive index of the host solution $Host_m$, using partial molar theory (Tang and Munkelwitz, 1991, 1994; Tang, 1996).

$$Host_m = \begin{cases} 1.3337 + 0.119X, X \leq 0.205 \\ 1.3285 + 0.145X, X > 0.205 \end{cases}. \tag{3.37}$$

A detailed description and FORTRAN subroutines for calculating of host complex refractive index is accessible at the website of GACP (Global Aerosol Climatology Project, https://gacp.giss.nasa.gov/data_sets/). The second step aims to calculate the refractive index of a mixture composed of inclusions embedded in the host. Therefore, once the refractive index of the host has been computed, the refractive index of the mixture is computed using the Maxwell-Garnett equations. The Maxwell-Garnett effective medium approximation allows the computation of the average dielectric function based upon the average electric fields and polarizations of a host matrix with embedded inclusions, and is the appropriate effective medium approximation for mixtures of insoluble particles suspended in solution (Bohren and Huffman 1983; Lesins et al., 2002).

The dielectric functions of aerosols are not typically tabulated in the literature, so they must be computed from the refractive index. Once the dielectric functions are know for the host and its constituents, the Maxwell-Garnett dielectric function may be calculated for a homogeneous material, which (for example, a 2-component mixture) can be expressed as (Bohren and Huffman, 1983):

$$\varepsilon_{MG} = \varepsilon_m \left[1 + \frac{3(f_1 \frac{\varepsilon_1 - \varepsilon_m}{\varepsilon_1 + 2\varepsilon_m} + f_2 \frac{\varepsilon_2 - \varepsilon_m}{\varepsilon_2 + 2\varepsilon_m})}{1 - f_1 \frac{\varepsilon_1 - \varepsilon_m}{\varepsilon_1 + 2\varepsilon_m} - f_2 \frac{\varepsilon_2 - \varepsilon_m}{\varepsilon_2 + 2\varepsilon_m}} \right], \tag{3.38}$$

where ϵ_m, ϵ_1, and ϵ_2 are the complex dielectric functions of the host matrix and inclusions, and f_1, f_2 are the volume fractions of the inclusions. The corresponding complex refractive index of the mixture can be obtained by Eqs. (3.39) – (3.40):

$$m_r = \sqrt{\frac{\sqrt{\varepsilon_r^2 + \varepsilon_i^2} + \varepsilon_r}{2}}, \tag{3.39}$$

$$m_i = \sqrt{\frac{\sqrt{\varepsilon_r^2 + \varepsilon_i^2} - \varepsilon_r}{2}}, \tag{3.40}$$

where ε_r and ε_i denote the real and imaginary components of the mixture dielectric function, ε_{MG}.

The aerosol refractive index is therefore derived by two described above steps using relative humidity and the fractions of aerosol composition employed in the conversion model. The detailed refractive indices of inclusions embedded in the host of the present aerosol composition conversion model are shown in Figure 3.9. Based on the considerations that the size-dependent aerosol composition model is required for separation between BC, BrC and iron oxides, the same model was also used in the case of Maxwell-Garnett mixing rule.

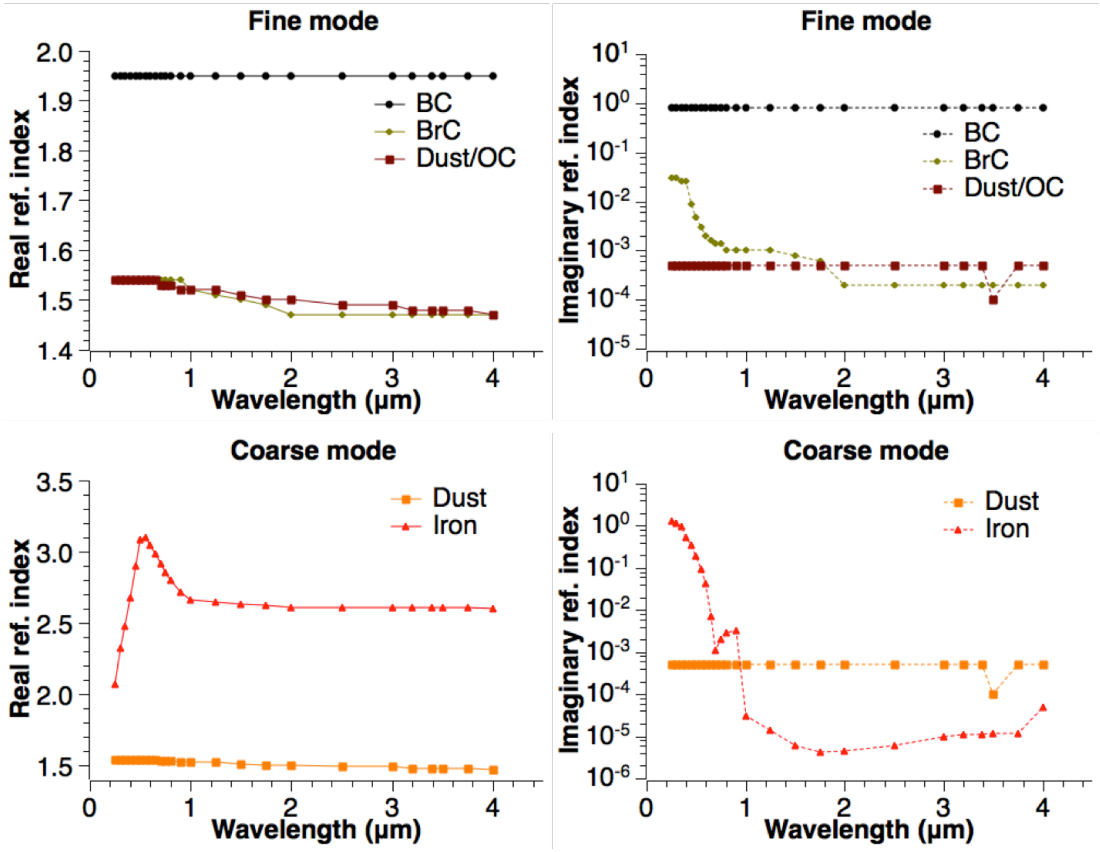

Figure 3.9: The refractive indices of assumed aerosol compositions embedded in the host of the size-dependent Maxwell-Garnett conversion model. The parameters of BC refer to Bond and Bergstrom (2006). The parameters of BrC refer to Sun et al. (2007). The parameters of dust refer to Ghosh (1999). The parameters of iron oxide refer to Longtin et al. (1988).

3.3.3.2 Sensitivity test

Figure 3.10 presents results of tests of POLDER/PARASOL measurements sensitivity to aerosol elements and RH considered in the size-dependent Maxwell-Garnett conversion model. Similarly to the Figures 3.4 and 3.6, abscissas in the first panel of Figure 3.10 present the range of the assumed aerosol composition fractions in fine and coarse modes. Good correlations between the assumed and the retrieved fractions of composition and optical parameters (AOT, single-scattering albedo, refractive index) in Figure 3.10 demonstrate that utilization of the size-dependent Maxwell-Garnett conversion model allows the algorithm to distinguish the assumed aerosol compositions in fine and coarse modes, as well as the ammonium nitrate and water in the host. Despite Maxwell-Garnett conversion model implies more aerosol compositions (soluble species like ammonium nitrate), the tests to sufficiency of informative content still show that stable results are not sensitive to initial guess.

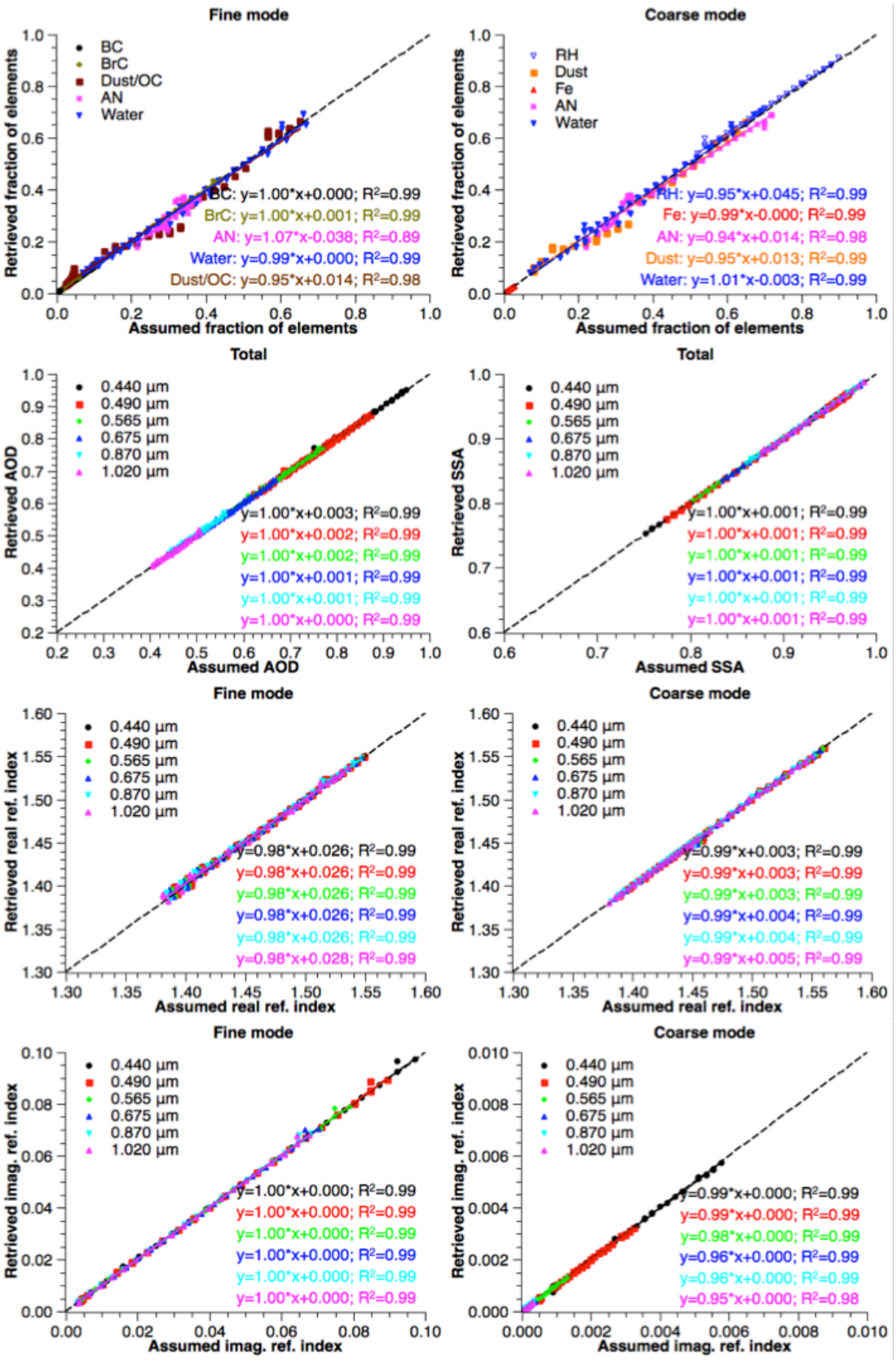

Figure 3.10: The sensitivity tests of size-dependent Maxwell-Garnett conversion model. AN represents ammonium nitrate in the host and RH represents the relative humidity. RH is shown in the panel of coarse mode for a purpose of convenience; note that it is used for host refractive index calculation of fine and coarse particles.

3.3.3.3 Uncertainty

In the present size-dependent Maxwell-Garnett conversion model, the host refractive index is calculated by ammonium nitrate and water, which may lead to some uncertainties of the aerosol compositions in the retrievals. Because in the realistic atmospheric aerosols, there are a variety of soluble inorganic species, such as ammonium nitrate, ammonium sulfate, sea salt. Figure 3.11 shows the uncertainties caused by the assumption of ammonium nitrate and ammonium sulfate. First, using the host of ammonium nitrate and water with the other assumed fractions of aerosol composition to create the PARASOL/POLDER synthetic measurements of radiances and polarization properties. Then, the synthetic measurements are fitted by the numerical inversion procedure employed the host of ammonium sulfate and fractions of the other aerosol compositions are retrieved, showing the uncertainties induced by the assumption of ammonium nitrate. The uncertainties in BC, BrC, iron oxide and dust are less than 0.5%, and the uncertainties in water and inorganic soluble (ammonium nitrate) are around 5%. Such uncertainties of the host are attributed to the differences of hygroscopicity between ammonium nitrate and ammonium sulfate (Tang and Munkelwitz, 1991, 1994; Tang, 1996).

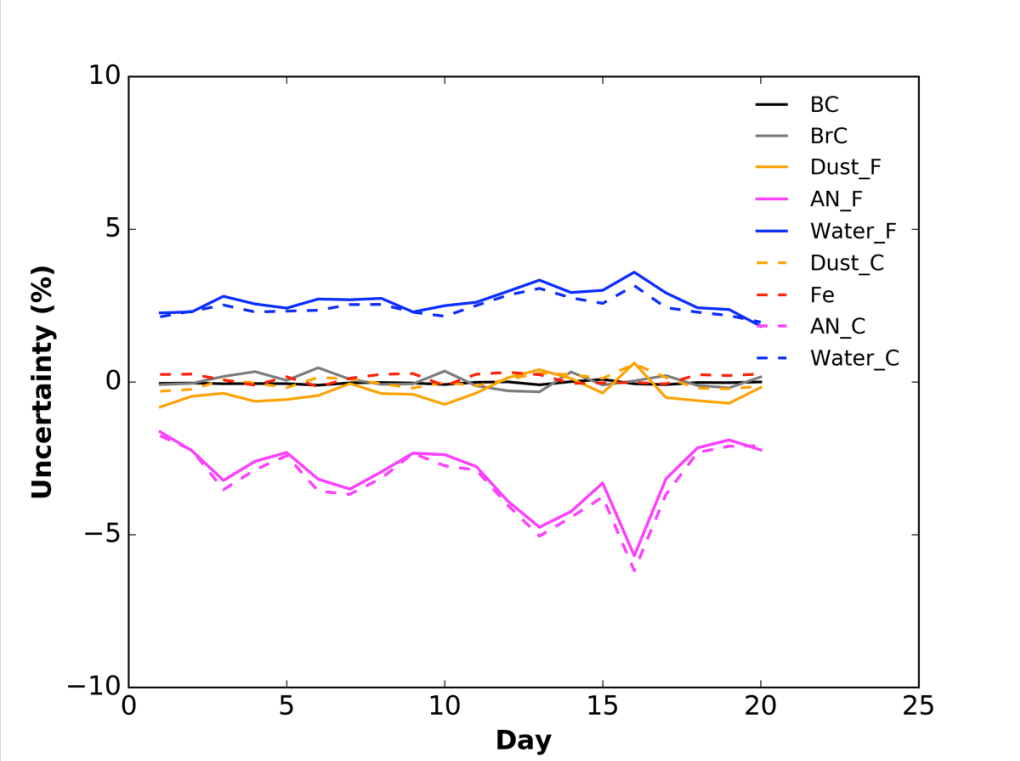

Figure 3.11: The uncertainty of soluble inorganic species assumed in size-dependent Maxwell-Garnett conversion model. The solid lines represent the aerosol compositions in fine mode and the dashed lines represent the aerosol compositions in coarse mode. “F” and “C” denotes the fine particles and coarse particles, respectively.

Chapter 4

Retrieval of aerosol composition from POLDER/PARASOL observations over Africa

"The man who has made up his mind to win will never say 'impossible'."

------Napoleon Bonaparte

Africa is the largest source of mineral dust aerosols over the world (Laurent et al., 2008) as dust emission takes place primarily in a few preferential source regions, mostly located in the world's arid zones, notably the Sahara desert (Herman et al., 1997; Prospero et al., 2002; Torres et al., 2002; Washington et al., 2003; Zhang and Christopher, 2003). Mineral dust originated from Africa is transported mainly towards the Atlantic Ocean and the Mediterranean Sea. The African dust is emitted from numerous sources with varying intensity, seasonality and frequency (Goudie and Middleton, 2001; Prospero et al., 2002; Laurent et al., 2008). For example, the Bodélé depression located northeast of Lake Chad consists of a series of ephemeral lakes that collect erosion from several sources (Mounkaila et al., 2003). It is known as the most vigorous dust source caused by locally strong winds associated with the Bodélé Low-Level Jet (LLJ) (Washington and Todd, 2005; Washington et al., 2006).

Besides dust emission, the African continent is also affected by strong biomass burning events all year round, which is attributed to widespread savannah fires and agricultural fires. Approximately 80% of all global biomass burning takes place in the tropical region (Keil and Haywood, 2003), with about 440 million hectares of land exposed to fire annually (Scholes and Andreae, 2000). An estimated one third of total global pyrogenic emissions are produced

from burning occurring on the African continent (Alleaume et al., 2005). The intensity and variability of biomass burning in Africa follow a well-determined seasonal cycle associated with the seasonal shift in the Inter-Tropical Convergence Zone (ITCZ). The emissions of biomass burning from the south regions of northern Africa reach the peaks during the dry season (Northern Hemisphere winter - DJF), and then more intense emissions occurring in southern Africa during the months of JJA and SON. It is known that biomass burning alters regional aerosol and trace gas composition (Crutzen et al., 1979; Seiler and Crutzen, 1980; Crutzen and Andreae, 1990; Andreae and Merlet, 2001), impacts atmospheric chemistry, radiative balance and biogeochemical cycles (e.g., Liousse et al., 1996; Garstang et al., 1998; Dubovik et al., 2000; Tyson and Gatebe, 2001; Kaufman et al., 2002b; Takemura et al., 2002). Africa is under the influences of biomass burning and dust aerosols with significant seasonal variation.

It should be mentioned here that in addition to African continent, the West Asia is also an important dust source. For instance, previous studies (Prospero et al., 2002; Ginoux et al., 2012; Léon and Legrand, 2003) show that about 65% of the southwest Asian arid terrain is able to be a potential dust source. There are several arid to semi-arid countries with substantial sources of dust, including the Margo Desert to the east of the Sistan Basin, Registan Desert in southern Afghanistan, the large dry lake of Hamoun-e Mashkel in western Pakistan south of the Sistan Basin and the broad plains of the Makran Desert located on the Iran-Pakistan border, along the coastal plain of the Oman Sea, the Karakum Desert along the east coast of the Caspian Sea (Orlovsky et al., 2005) and Qobustan in Azerbaijan on the west side of the Caspian Sea (Ginoux et al., 2012). Most of West Asia is under the influence of mineral dust aerosols originated from these sources of dust.

Therefore, since dust and biomass burning aerosol present significant seasonal and spatial variation, investigating their compositions using satellite observations can enable highly important information, especially because very few ground-based data exists in desert regions, e.g., Sahara Desert. The current chapter presents retrievals and analysis of aerosol composition from POLDER/PARASOL observations over Africa. As it was presented in the previous chapter, there are two different aerosol composition conversion models: volume-weighted model and Maxwell-Garnett model. This chapter presents a detailed discussion of the aerosol composition inferred by the both conversion models, which also account for the size-dependent composition. Then, the ground-based AERONET measurements and field campaign data from literature are applied to validate the results of the retrievals using aerosol composition module. Finally, a comparison of GRASP composition retrievals with GEOS-5/GOCART model simulation is discussed. The retrievals can provide a possibility to

evaluate the chemical transport model simulations with large coverage observations in order to reduce the uncertainties of the simulations.

4.1 Volume-weighted conversion model retrieval

4.1.1 Black carbon

Aerosols from vegetation fires consist predominantly of fine carbonaceous particles in combination with various products, mostly referred as BC (Pósfai et al., 2003). The BC emission depends on vegetation types and fire intensity (Reid and Hobbs, 1998). Figure 4.1 shows the retrieved seasonal and interannual variations of BC columnar volume concentration over Africa and Arabian Peninsula. Note that the years 2006 to 2008 are presented because only this period was processed at the time of the manuscript writing. The results show two seasonal peaks of BC concentration one in the winter season (DJF) over northern Africa and another one during SON mostly over southern Africa. BC concentration during MAM has a lower magnitude and the area of coverage in comparison to other three seasons. The average values and percentages (here the values are calculated over the region as shown in the Figures and all values in Chapter 4 are the same) of BC concentration during MAM are the smallest, up to half, of the values during DJF and SON accordingly (see Table 4.1). Both Figure 4.2 and Table 4.2 indicate that BC concentration in May is the smallest one during all months.

During the Northern Hemisphere winter season (DJF), the agricultural burning is intense across the sub-Sahelian region of Africa. BC generated from such agricultural burning extends for thousands of kilometers from east to west across the continent. As shown in Figure 4.1 and 4.2, BC concentration in northern Africa is more over land near the west coast, especially from Senegal south to Gabon on the equator, and over the Gulf of Guinea. It is because the savanna fires occur in the humid Guinean and southern Sudanese zones where the total biomass loading is high during this period (Delmas et al., 1991; Menaut et al., 1991). It is noted that BC over the ocean is generally transported from biomass burning areas by prevailing trade winds. BC concentration during DJF, especially in January, has the highest average values and the percentages as shown in Table 4.1 and 4.2. It is attributed to the percentage of BC emitted, which is determined by intensity and efficiency of the burning. For example, flaming fires produce a higher percentage of BC than smoldering fires (Kaufman et al., 2002b; Pósfai et al., 2003). Duncan et al. (2003) also obtained stronger TOMS Aerosol Index (AI) signal from biomass burning over such areas. It is noteworthy that mineral dust transported from the Sahara desert and arid parts of the Sahel is also present with high concentration in the same time, which is discussed in 4.1.3 and 4.1.4.

During the months of JJA and SON, BC is mostly concentrated over southern Africa. Overall, the average value and the percentages of BC for entire Africa during SON are larger than those during JJA, which is attributed to the different areas and intensity of the fires during these two seasons. Many field campaigns (e.g., Southern Africa Fire-Atmosphere Research Initiative (SAFARI-92) (Lindesay et al., 1996), the Southern Africa Atmosphere Research Initiative (SA'ARI) (Helas et al., 1995), the Ben MacDhui High-Altitude Trace Gas and Aerosol Transport Experiment (BHATTEX) (Piketh et al., 1999b), Aerosol Recirculation and Rainfall Experiment (ARREX) (Terblanche et al., 2000), and the Southern African Fire Research Initiative (SAFARI-2000) (Swap et al., 2003)) carried out in southern Africa have demonstrated that stable atmospheric conditions predominate over southern Africa during the dry season. The largest source of biomass burning material in southern Africa during JJA and SON is savanna vegetation (Swap et al., 2002, 2003). Biomass burning is also carried out largely as part of regional agricultural practices in southern Africa (Maenhaut et al., 1996; Eck et al., 2003). The presented retrieval results are indeed in line with the previous studies. As illustrated in Figure 4.2 and Table 4.2, in southern Africa, the average value and the percentages of BC begin to increase in June, reach the peaks in August and September, and then decrease in October. The variations of the retrieved BC are consistent with the biomass burning activity progressing from north to south, beginning in June, peaking in July and August and then decreasing in intensity until late October when the dry season comes to an end (Cahoon et al., 1992; Maenhaut et al., 1996; Liousse et al., 1996; Swap et al., 1996). In addition, a small part of BC is observed to leave the continent from the southeastern coast of South Africa, especially near Mozambique (e.g., JJA in 2008 in Figure 4.1), which is associated with the recirculation of aerosols and trace gases occurring in a significant extent, on local, regional and subcontinental scales as the stable layers generated by the anticyclonic nature of atmospheric circulation over the region (Torres et al., 2002).

There are also some interannual variations of BC concentration during the period 2006 – 2008 (Figure 4.1 and Table 4.1), such as BC concentration during DJF in 2007 is higher than those in 2006 and 2008. Interannual variability is likely due to both year-to-year variations in climate and fires intensity. The emissions of biomass burning are variable during different years can be partly attributed to an ENSO-induced drought in Africa that decreases the amount of biomass available for burning (Barbosa et al., 1999). Interannual variability also depends primarily on the amount of rainfall received during the seasons when burning typically occurs, with most burning in the driest years (Gleason et al., 1998). However, since most fires in Africa are in the savannas with relatively low fuel loads compared to forests and

high burn frequency, the interannual variation in fire activity is expected to be less than in other regions, such as south America, (e.g., Delmas et al., 1991; Menaut et al., 1991).

Note that the BC columnar volume concentration (mm^3/m^2), which is directly retrieved by the algorithm, was converted to columnar mass concentration (mg/m^2) using the density value of 1.8 g/cm^3 (Park et al., 2004; Bond and Bergstrom, 2006).

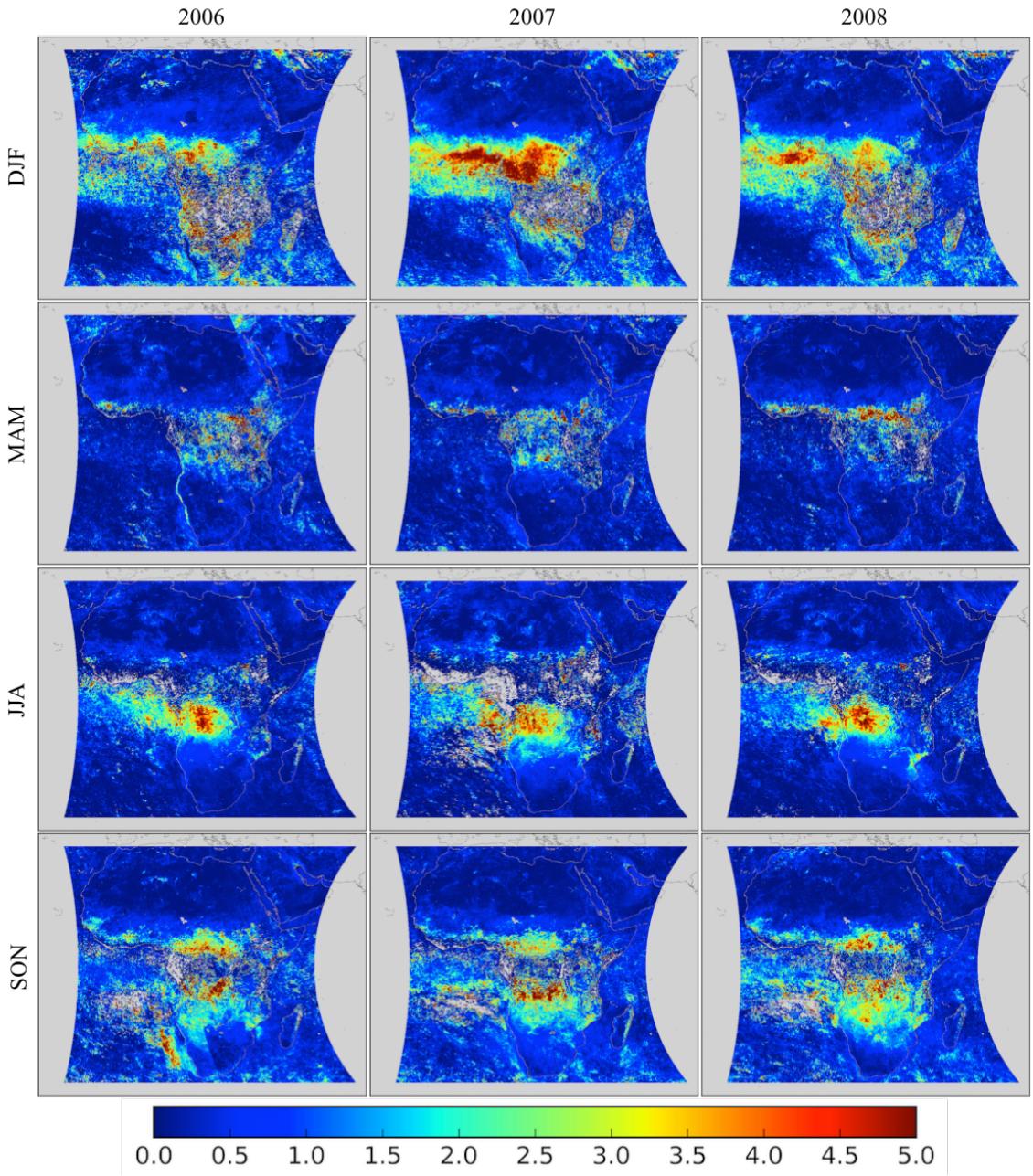

Figure 4.1: Seasonal variations of BC columnar volume concentration (mm^3/m^2) over Africa and Arabian Peninsula during the period 2006 – 2008 as retrieved by GRASP algorithm from POLDER/PARASOL satellite observations using the volume-weighted conversion model.

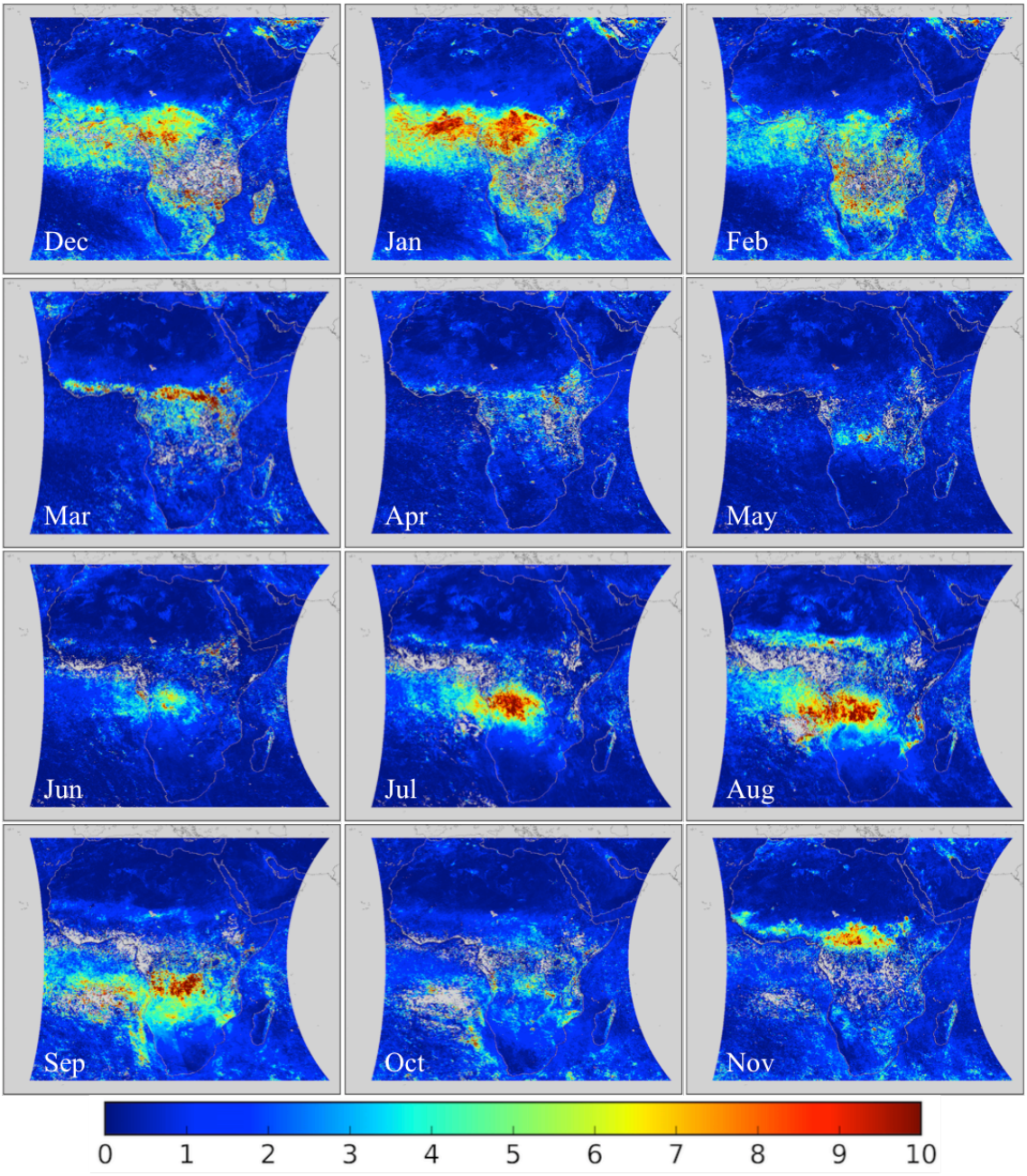

Figure 4.2: Monthly variations of BC columnar mass concentration (mg/m^2) over Africa and Arabian Peninsula averaged over the period 2006 – 2008 as retrieved by GRASP algorithm from POLDER/PARASOL satellite observations using the volume-weighted conversion model.

Table 4.1: Seasonal columnar volume concentration (mm^3/m^2) statistics for BC over Africa and Arabian Peninsula during the period 2006 – 2008 as retrieved by GRASP algorithm from POLDER/PARASOL satellite observations using the volume-weighted conversion model. The percentages (5%, 25%, 50%, 75% and 95%) of the values are determined by ordering the values of the variable from lowest to highest, which indicate in detail the distribution of the variable.

Year	Season	Average	Std	5%	25%	50%	75%	95%
2006	DJF	0.96	1.28	0.01	0.15	0.51	1.28	3.45
	MAM	0.51	0.89	0.01	0.08	0.25	0.58	1.81
	JJA	0.54	0.86	0.01	0.07	0.22	0.60	2.30
	SON	0.80	1.14	0.02	0.13	0.40	1.03	2.85
2007	DJF	1.08	1.41	0.03	0.18	0.54	1.42	4.02
	MAM	0.46	0.79	0.01	0.07	0.22	0.52	1.63
	JJA	0.67	1.12	0.01	0.07	0.25	0.76	2.83
	SON	0.79	1.07	0.03	0.15	0.42	1.01	2.75
2008	DJF	1.01	1.27	0.02	0.17	0.54	1.40	3.52
	MAM	0.41	0.83	0.01	0.05	0.16	0.43	1.55
	JJA	0.55	0.87	0.01	0.07	0.23	0.66	2.23
	SON	0.80	1.03	0.03	0.14	0.41	1.08	2.81

Table 4.2 Monthly columnar mass concentration (mg/m^2) statistics for BC over Africa and Arabian Peninsula averaged over the period 2006 – 2008 as retrieved by GRASP algorithm from POLDER/PARASOL satellite observations using the volume-weighted conversion model. The percentages (5%, 25%, 50%, 75% and 95%) of the values are determined by ordering the values of the variable from lowest to highest, which in detail indicate the distribution of the variable.

Month	Average	Std	5%	25%	50%	75%	95%
Dec	1.73	2.37	0.04	0.26	0.85	2.34	6.13
Jan	1.96	2.62	0.04	0.28	0.95	2.52	7.48
Feb	1.60	2.33	0.03	0.20	0.73	2.08	5.97
Mar	1.02	2.27	0.02	0.09	0.34	1.02	3.99
Apr	0.73	1.36	0.02	0.10	0.32	0.82	2.74
May	0.61	1.15	0.02	0.08	0.24	0.66	2.38
Jun	0.72	1.49	0.01	0.07	0.24	0.78	2.96
Jul	0.99	1.82	0.02	0.11	0.32	0.98	4.45
Aug	1.41	2.30	0.02	0.15	0.48	1.62	6.05
Sep	1.52	2.39	0.04	0.18	0.63	1.89	5.78
Oct	1.10	1.63	0.04	0.19	0.55	1.40	3.80
Nov	1.15	1.74	0.03	0.17	0.51	1.37	4.48

4.1.2 Brown carbon

Similarly to BC, the BrC also has an important seasonal and spatial variation over Africa and Arabian Peninsula. BrC concentration reaches the peaks during DJF and JJA, correspondingly associated with biomass burning in northern and southern Africa. Figures 4.3, 4.4 and Tables 4.3, 4.4 illustrate the temporal and spatial variations of BrC concentration. BrC concentration during MAM is less in quantity and area than in other three seasons, similarly to BC.

Indeed, the BrC concentration reaches the peaks during the same periods as BC because they are simultaneously generated from biomass burning combustion. However, a comparison between Figures 4.1, 4.2 and 4.3, 4.4, respectively, shows that the largest values of BC and BrC concentrations are distributed in different areas, especially during JJA and SON. BC is mainly enriched in the area near the biomass burning emissions, whereas BrC is generally concentrated over the ocean and near the west coast of Africa from Gabon south to northern Namibia during all seasons. Carbonaceous particles are transported by prevailing easterlies from the highland plateau over low-lying coastal plains and the Atlantic Ocean. There can be some rapid changes occurring in the relative concentrations of particle types with the aging of smoke. Previous studies (Haywood et al., 2003; Abel et al., 2003; Reid et al., 1998) have demonstrated that the fresh biomass burning aerosols have higher BC content than aged aerosol. During SAFARI-2000, for example, Abel et al. (2003) found that single scattering albedo has an increase from 0.84 to 0.90 between smoke close to the source and aged haze 5 h downwind from a large fire, which is attributed to changes in aerosol composition rather than size distribution.

The analysis of the BrC retrievals also point out on a limitation of the algorithm. It can be noted in Figures 4.3 and 4.4 (DJF and MAM) that some elevated BrC concentrations appear also over the Bodélé region, which is regarded as one of the strongest sources of dust in the world. In fact, the aerosol absorbing property attributed to BrC in this case should be associated with iron oxides in fine size fraction. Because BrC and iron oxide have the similar spectral absorption behavior (see Figure 2.6), it is difficult to distinguish BrC and iron oxide effectively only using the discrepancies of optical properties (absorbing and scattering) between them provided by satellite remote sensing. This is why, there is no iron oxide component assumed for the fine mode of the aerosol composition conversion model in the present algorithm. The hypothesis used is that the iron oxides are associated with mineral dust, which primary contribution is to the coarse mode size fraction. Nevertheless, a posteriorly analysis can be used for reattributing BrC to fine mode iron oxide in case of small Ångström Exponent that indicates pure dust events.

Note that the BrC columnar volume concentration (mm^3/m^2), which is directly retrieved by the algorithm, was converted to columnar mass concentration (mg/m^2) using the density value of 1.2 g/cm^3 (Turpin and Lim, 2001).

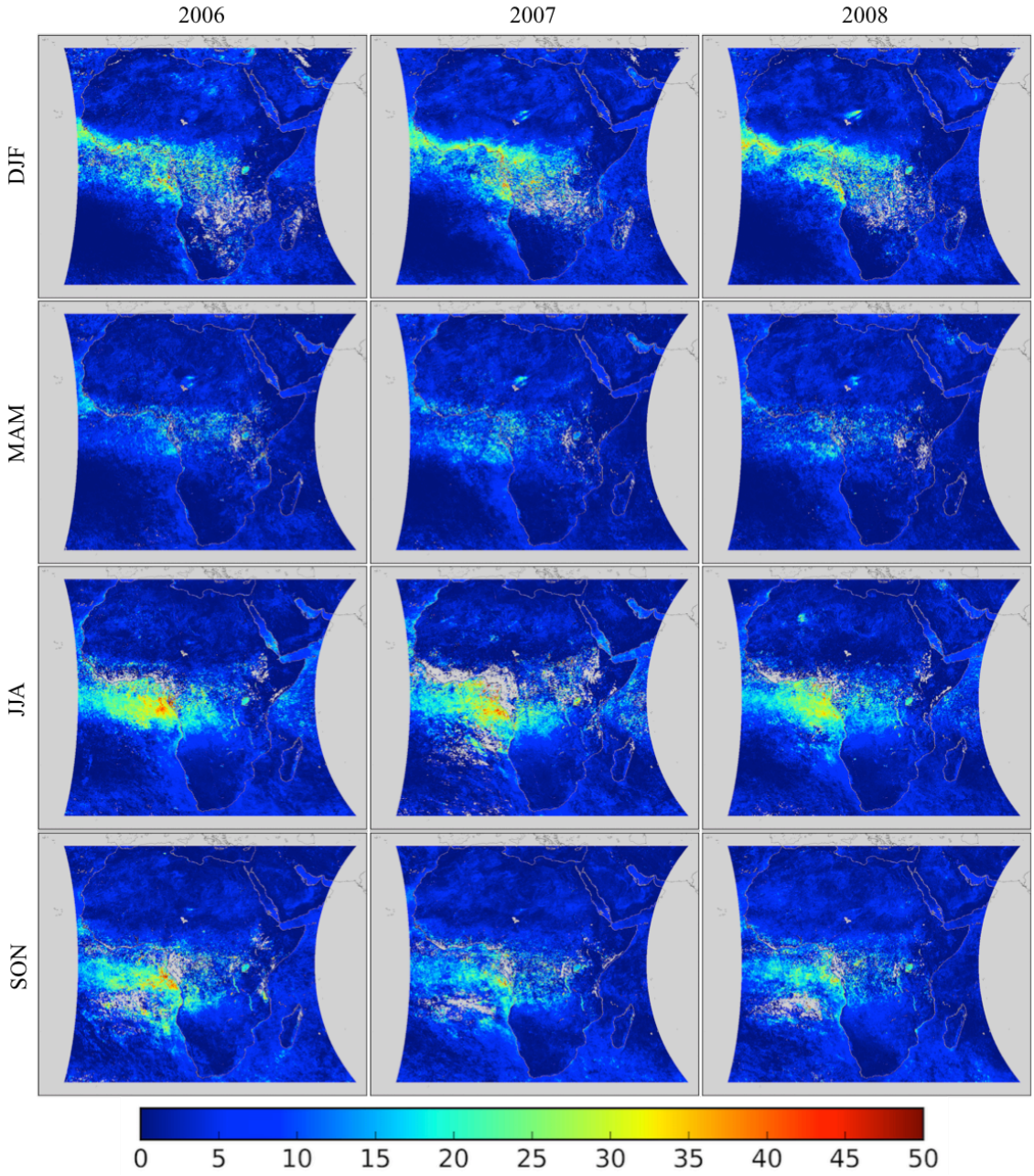

Figure 4.3: Seasonal variations of BrC columnar volume concentration (mm^3/m^2) over Africa and Arabian Peninsula during the period 2006 – 2008 as retrieved by GRASP algorithm from POLDER/PARASOL satellite observations using the volume-weighted conversion model.

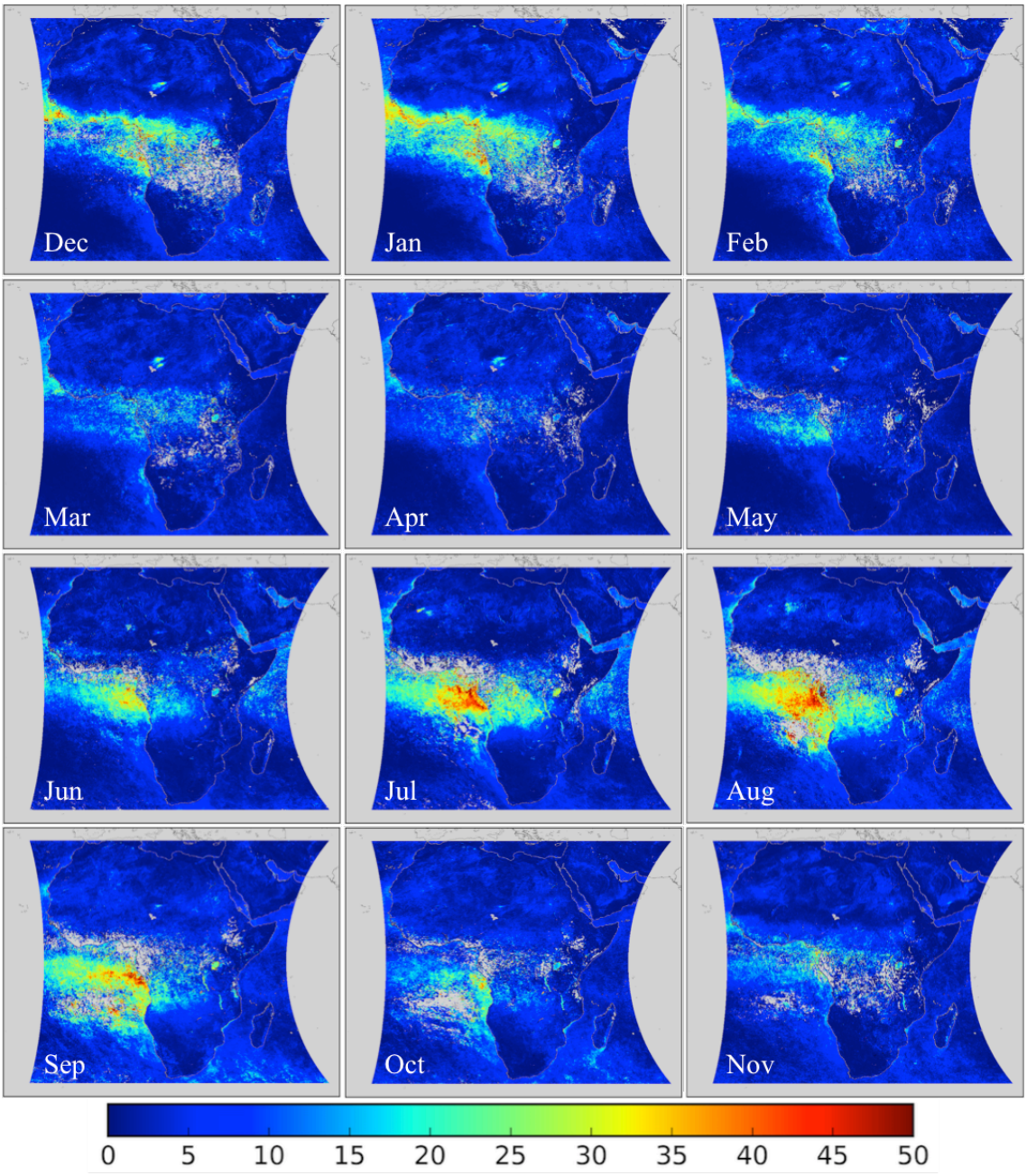

Figure 4.4: Monthly variations of BrC columnar mass concentration (mg/m^2) over Africa and Arabian Peninsula averaged over the period 2006 – 2008 as retrieved by GRASP algorithm from POLDER/PARASOL satellite observations using the volume-weighted conversion model.

Table 4.3: Seasonal columnar volume concentration (mm^3/m^2) statistics for BrC over Africa and Arabian Peninsula during the period 2006 – 2008 as retrieved by GRASP from POLDER/PARASOL satellite observations using the volume-weighted conversion model. The percentages (5%, 25%, 50%, 75% and 95%) of the values are determined by ordering the values of the variable from lowest to highest, which indicate in detail the distribution of the variable.

Year	Season	Average	Std	5%	25%	50%	75%	95%
2006	DJF	4.71	6.03	0.05	0.62	2.52	6.31	17.73
	MAM	2.98	4.04	0.08	0.51	1.61	3.84	10.75
	JJA	4.98	6.65	0.10	0.78	2.39	6.21	20.05
	SON	4.99	6.11	0.19	1.09	2.84	6.27	18.43
2007	DJF	5.08	6.26	0.11	0.96	2.91	6.49	18.90
	MAM	3.23	4.02	0.09	0.56	1.76	4.29	11.66
	JJA	5.08	7.12	0.06	0.65	2.24	6.29	20.52
	SON	4.42	5.06	0.24	1.06	2.63	5.82	15.08
2008	DJF	4.75	6.12	0.09	0.79	2.59	5.95	18.66
	MAM	2.95	3.64	0.08	0.55	1.74	3.96	10.08
	JJA	4.71	5.98	0.13	0.85	2.42	5.93	18.01
	SON	4.49	4.88	0.24	1.23	2.94	5.87	14.77

Table 4.4: Monthly columnar mass concentration (mg/m^2) statistics for BrC over Africa and Arabian Peninsula averaged over the period 2006 – 2008 as retrieved by GRASP algorithm from POLDER/PARASOL satellite observations using the volume-weighted conversion model. The percentages (5%, 25%, 50%, 75% and 95%) of the values are determined by ordering the values of the variable from lowest to highest, which indicate in detail the distribution of the variable.

Month	Average	Std	5%	25%	50%	75%	95%
Dec	5.00	6.96	0.10	0.75	2.51	6.27	19.39
Jan	6.08	8.29	0.09	0.82	2.95	7.56	24.80
Feb	5.56	6.98	0.08	0.82	3.12	7.57	19.88
Mar	4.00	5.81	0.08	0.54	1.89	5.14	15.11
Apr	3.39	4.51	0.09	0.55	1.75	4.45	12.28
May	3.19	4.63	0.07	0.44	1.45	3.98	12.36
Jun	4.56	7.01	0.07	0.54	1.82	5.55	18.84
Jul	5.72	8.50	0.10	0.67	2.15	6.83	24.59
Aug	6.70	9.24	0.13	0.89	3.04	8.33	27.55
Sep	6.44	8.19	0.25	1.27	3.44	8.07	24.44
Oct	4.61	5.36	0.22	1.12	2.80	6.05	15.28
Nov	3.93	4.95	0.14	0.75	2.16	5.26	13.55

4.1.3 Organic carbon/fine dust

Figures 4.5 and 4.7 show the temporal and spatial variations of OC or fine dust over Africa and Arabian Peninsula. As discussed in chapter 2, it is infeasible to separate OC and fine dust based only on the optical properties (absorption and scattering) provided by satellite observations. Therefore, OC and fine dust are shown and discussed together in Figures 4.5, 4.7 and Tables 4.5, 4.6. However, the Ångström Exponent is provided by the retrievals and can be helpful to separate between OC and fine dust cases, especially in pure dust regions (northern Africa and Arabian Peninsula with smaller Ångström Exponent) or pure biomass burning areas (mostly in southern Africa with larger Ångström Exponent), the maps of the derived Ångström Exponent are presented in Figures 4.6 and 4.8.

During DJF, the Harmattan winds occurring along the southern border of the Sahara induce sources on the border of the Sahel, particularly the Bodélé depression in Northern Chad. Aerosols are also transported very efficiently by winds towards the Atlantic Ocean and across the Sahel (Pye, 1987; Sokolik et al., 2001; Laurent et al., 2008). In Figures 4.5 and 4.7, the particles concentrated in northern Africa should be classified as fine dust, especially near the Bodélé depression, because Ångström Exponent in this region is very small (less than 0.5, see Figures 4.6 and 4.8). It illustrates that the fine dust is enriched over Bodélé depression during SON. In addition, many fires take place in south of approximately 13°N (Haywood et al., 2008) and the emissions of biomass burning around the gulf of Guinea are intense during DJF. As a result, mixing between dust and biomass burning aerosols may occur in such area during southward transport (Johnson et al., 2008a). Ångström Exponent (shown in Figures 4.6 and 4.8), retrieved over the ocean and near the west coast of Africa from Gabon south to northern Namibia, is ranging from 1.0 to 1.2 and indicating that the particles are rather a mixture of OC and fine dust. A number of field campaigns (the African Monsoon Multidimensional Analyses (AMMA, Formenti et al., 2008), the Dust Outflow Deposition to the Ocean (DODO, Formenti et al., 2008), the Saharan Mineral dUst ExperiMent (SAMUM, Ansmann et al., 2009), and the Dust And Biomass Experiment (DABEX, Johnson et al., 2008a, b)) show that atmospheric column may contain a multi layers structure of low level dust layer and elevated biomass burning layer during DJF. During MAM, the particles shown in Figures 4.5 and 4.7 consist predominately of fine dust. Indeed, the fires during this season have less intensity and cover a smaller area; the derived Ångström Exponent indicates stronger dust contribution.

During JJA, fine dust concentration is higher over northern Africa and Arabian Peninsula, where Ångström Exponent is usually smaller than 0.5. The Sistan region is considered as a major dust source in southwest Asia (Middleton, 1986a; Prospero et al., 2002; Léon and

Legrand, 2003; Ginoux et al., 2012; Goudie, 2013) because the strong persistent northwesterly to northeasterly winds known as the "wind of 120 days" (Middleton, 1986b; Hossenzadeh, 1997; Goudie and Middelton, 2006; Miri et al., 2007; Choobari et al., 2013) or locally known as Levar, can cause frequent dust and sand storms, especially during the period of June to August (Middleton, 1986b; Goudie and Middleton, 2000) and contribute to the deterioration of air quality (Rashki et al., 2013a). At the same time, over northern Africa, a progressive organization of convection from isolated cells to large-scale and quickly propagating systems attributed to the Intertropical Convergence Zone (ITCZ), are efficient in eroding bare soils to induce mineral dust (Marticorena et al., 2010; Touré et al., 2011).

On the contrary, over southern Africa, where Ångström Exponent is usually larger than 1.2, the particles are regarded as OC with high concentration. The main burning months are August, September and October (Cahoon et al., 1992; Andreae, 1993), which is in line with the derived highest OC concentrations over southern Africa in August, September and October (Figures 4.5 and 4.7). Note that the OC or fine dust columnar volume concentration (mm^3/m^2), which is directly retrieved by the algorithm, was converted to columnar mass concentration (mg/m^2) by their densities. When the retrieved Ångström Exponent is less than 1.0, it is assumed as pure dust using the density of 2.5 g/cm^3 (Formenti et al., 2014a, b). When the retrieved Ångström Exponent is larger than 1.2, it is assumed as pure OC using the density of 1.2 g/cm^3 (Turpin and Lim, 2001). When the retrieved Ångström Exponent is in the range of 1.0 – 1.2, it is assumed as a mixture of OC and dust using the density of 1.85 g/cm^3 (Turpin and Lim, 2001; Formenti et al., 2014a, b).

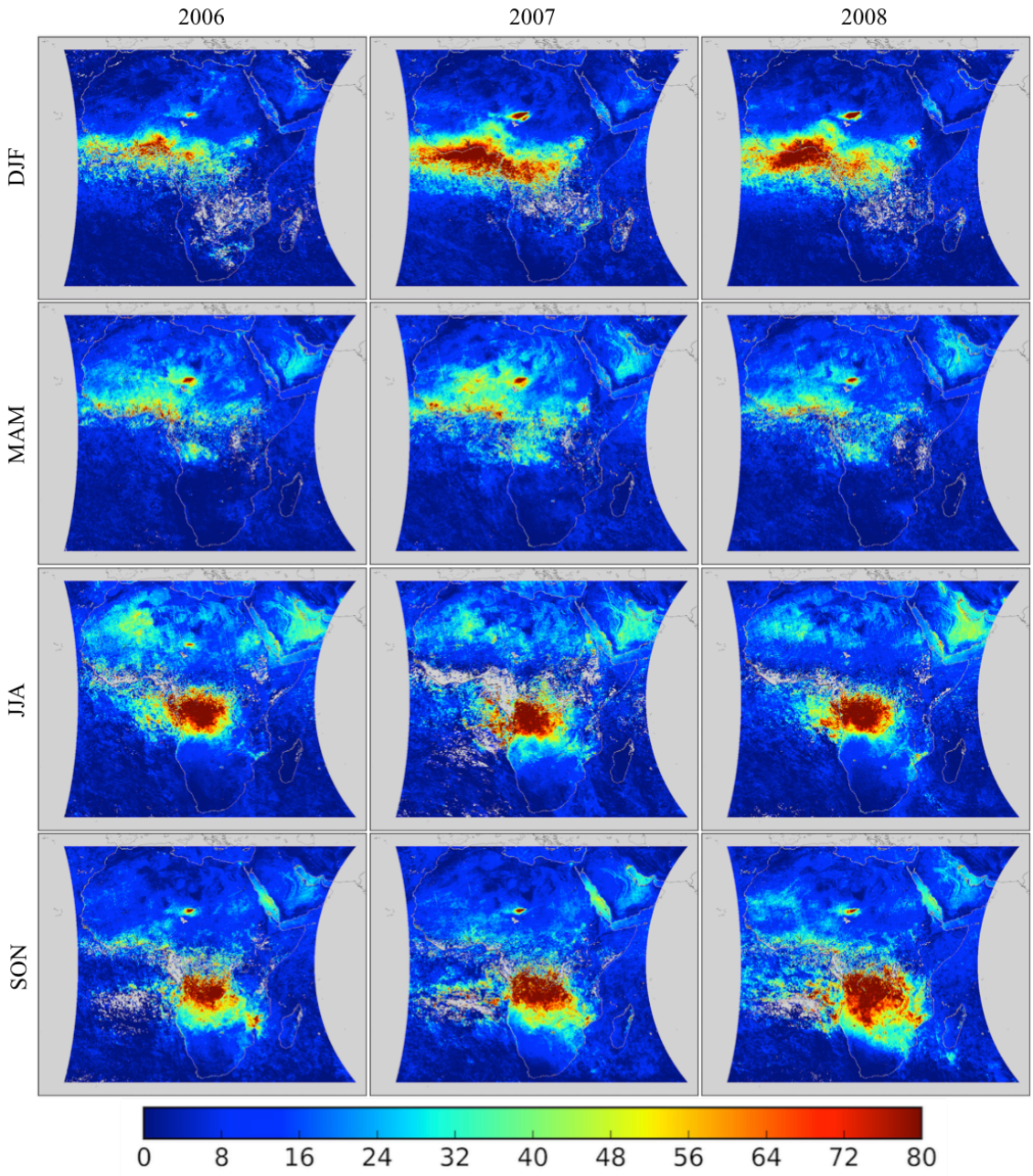

Figure 4.5: Seasonal variations of OC/fine dust columnar volume concentration (mm^3/m^2) over Africa and Arabian Peninsula during the period 2006 – 2008 as retrieved by GRASP algorithm from POLDER/PARASOL satellite observations using the volume-weighted conversion model.

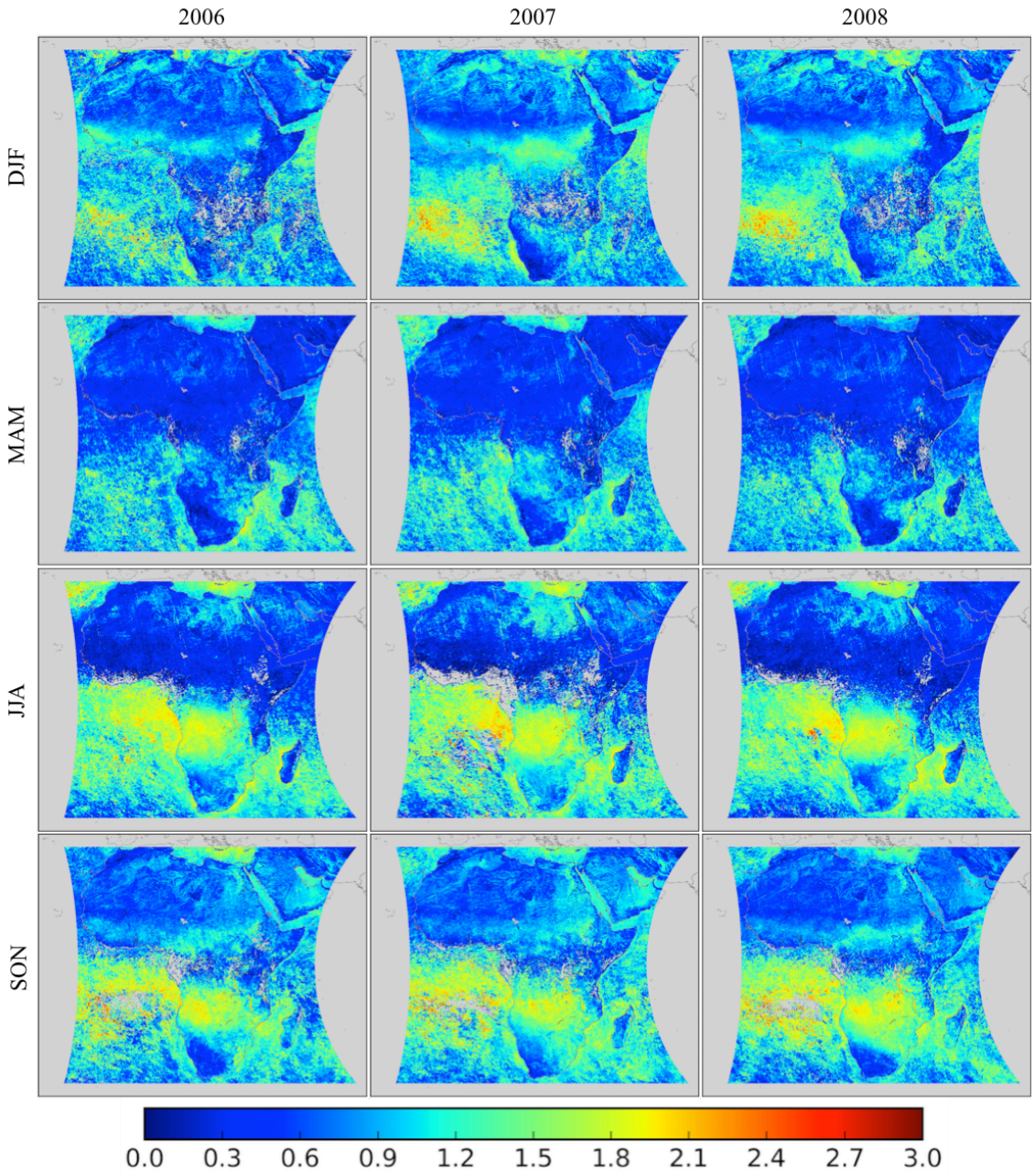

Figure 4.6: Seasonal variations of Ångström Exponent (0.670/0.865 μm) over Africa and Arabian Peninsula during the period 2006 – 2008 as retrieved by GRASP algorithm from POLDER/PARASOL satellite observations using the volume-weighted conversion model.

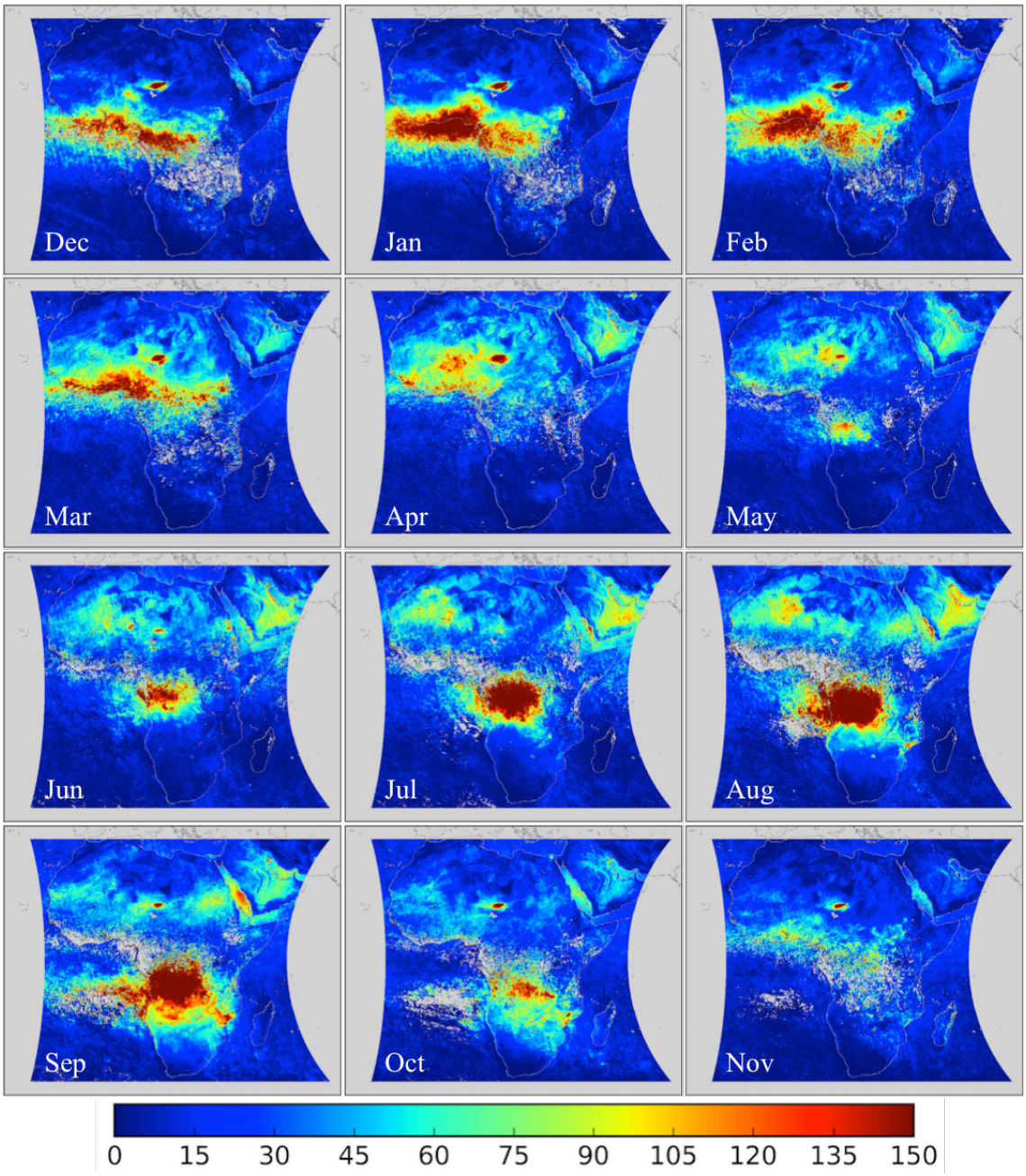

Figure 4.7: Monthly variations of OC/fine dust columnar mass concentration (mg/m^2) over Africa and Arabian Peninsula averaged over the period 2006 – 2008 as retrieved by GRASP algorithm from POLDER/PARASOL satellite observations using the volume-weighted conversion model.

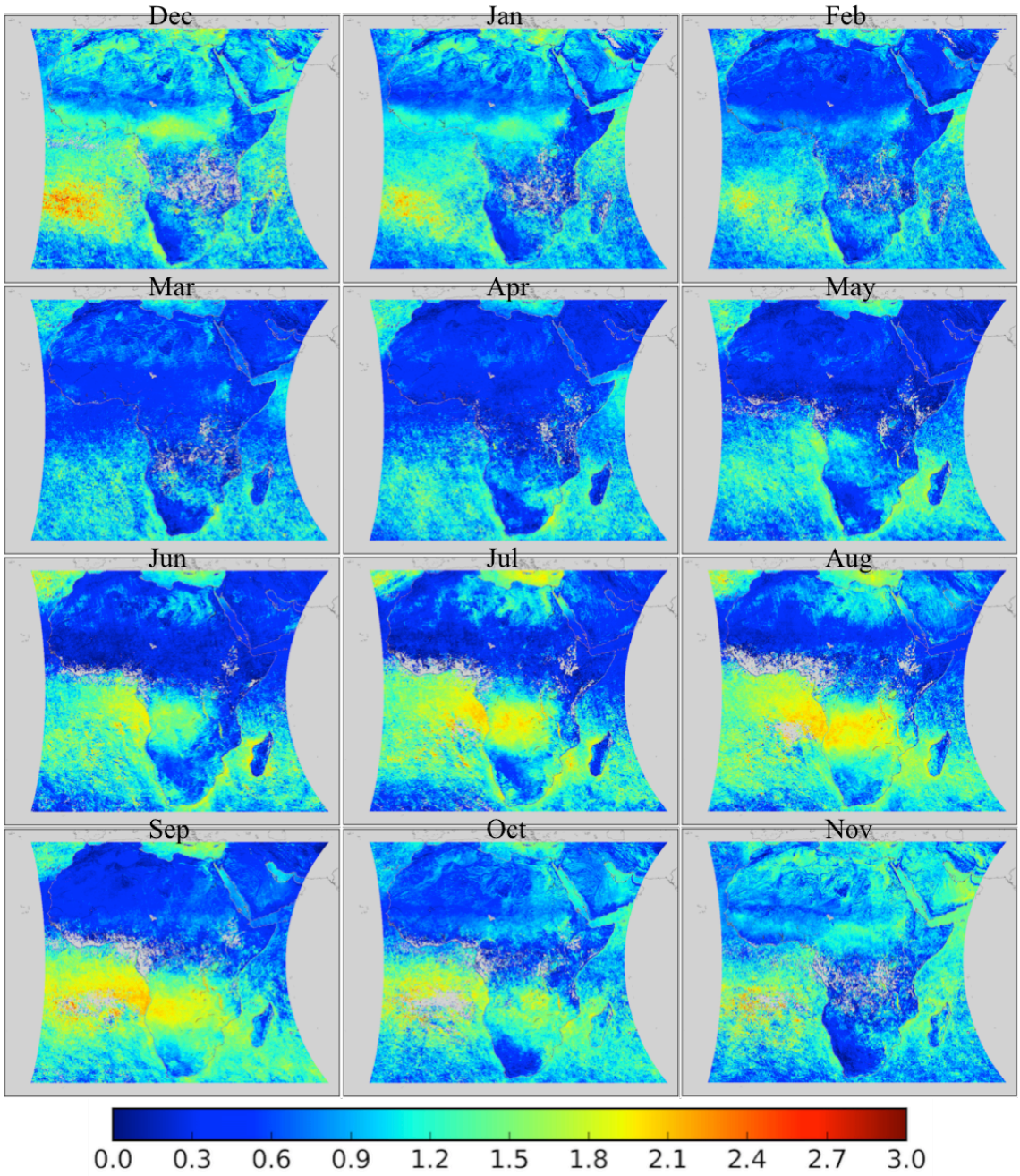

Figure 4.8: Monthly variations of Ångström Exponent (0.670/0.865 μm) over Africa and Arabian Peninsula averaged over the period 2006 – 2008 as retrieved by GRASP algorithm from POLDER/PARASOL satellite observations using the volume-weighted conversion model.

Table 4.5: Seasonal columnar volume concentration (mm^3/m^2) statistics for OC/fine dust over Africa and Arabian Peninsula during the period 2006 – 2008 as retrieved by GRASP algorithm from POLDER/PARASOL satellite observations using the volume-weighted conversion model. The percentages (5%, 25%, 50%, 75% and 95%) of the values are determined by ordering the values of the variable from lowest to highest, which indicate in detail the distribution of the variable.

Year	Season	Average	Std	5%	25%	50%	75%	95%
2006	DJF	9.15	14.41	0.09	0.81	4.00	11.49	36.88
	MAM	10.26	13.15	0.12	1.66	5.92	14.91	32.63
	JJA	15.07	18.49	0.28	2.86	10.12	20.70	45.46
	SON	12.28	16.66	0.19	2.59	7.61	14.76	43.39
2007	DJF	13.05	19.95	0.25	2.09	5.71	14.13	56.89
	MAM	12.31	13.81	0.29	2.72	7.71	17.82	38.12
	JJA	14.73	18.80	0.13	2.71	9.35	19.92	47.26
	SON	14.54	19.57	0.33	3.62	9.18	17.11	49.35
2008	DJF	12.02	19.17	0.14	1.27	4.85	12.93	52.56
	MAM	10.25	12.33	0.18	2.02	6.46	15.11	30.50
	JJA	14.26	18.03	0.32	3.03	9.42	18.42	44.86
	SON	16.75	20.86	0.22	4.05	10.53	20.38	60.64

Table 4.6: Monthly columnar mass concentration (mg/m^2) statistics for OC/fine dust over Africa and Arabian Peninsula averaged over the period 2006 – 2008 as retrieved by GRASP algorithm from POLDER/PARASOL satellite observations using the volume-weighted conversion model. The percentages (5%, 25%, 50%, 75% and 95%) of the values are determined by ordering the values of the variable from lowest to highest, which indicate in detail the distribution of the variable.

Month	Average	Std	5%	25%	50%	75%	95%
Dec	21.50	35.20	0.36	2.62	9.48	24.52	86.56
Jan	26.60	44.87	0.30	2.60	9.96	29.15	118.29
Feb	26.45	42.16	0.28	2.77	11.49	31.64	107.39
Mar	28.01	38.12	0.39	4.02	14.63	38.40	97.83
Apr	26.59	33.84	0.38	4.11	14.91	39.10	85.32
May	22.44	29.28	0.35	4.06	13.63	32.60	70.34
Jun	26.89	38.09	0.43	4.44	15.93	40.05	82.59
Jul	32.89	43.03	0.58	5.86	21.00	44.77	100.89
Aug	38.29	54.89	0.59	6.49	23.67	51.21	121.31
Sep	38.54	48.54	0.73	8.81	24.68	49.80	126.46
Oct	25.81	29.36	0.54	6.41	18.06	35.19	77.57
Nov	17.53	23.86	0.34	3.15	10.17	23.56	58.38

4.1.4 Coarse dust

Figure 4.9 and Table 4.7 show very important coarse dust concentration over Africa and Arabian Peninsula. The dust concentration also exhibits a pronounced seasonal cycle with the peaks, in both the intensity and the area covered, during MAM. Lower values are observed during JJA and DJF, and the lowest during SON. The average concentration of coarse dust during MAM is about twice as that during SON, as well as the peak of 192.84 mg/mm^2 in April and the lowest value of 87.82 mg/mm^2 in November (in Table 4.8), which is attributed to the analogous seasonal variations of the dust emissions in two regions: northern Africa and Arabian Peninsula. The detailed analysis of these two regions is discussed separately in the following.

In northern Africa, coarse dust concentration is high in all times of the year and varies depending on the winds annual cycle over the Sahara. The retrievals clearly show a "hot spot" of coarse dust concentration over Bodélé depression practically all year long (Figures 4.9 and 4.10). The Bodélé depression, located between the Tibesti Mountains and Lake Chad, is the most active dust source in the Sahara desert (Gasse, 2002; Prospero et al., 2002; Washington et al., 2003), caused by the coincidence of an extensive source of diatomite sediment and high velocity winds associated with the Bodélé Low Level Jet (Washington and Todd, 2005; Washington et al., 2006; Todd et al., 2006). High dust concentration over Bodélé depression is also observed in previous studies (e.g., Kalu, 1979; Herrmann et al., 1999; Brooks and Legrand, 2000; Koren and Kaufman, 2004; Washington and Todd, 2005; Washington et al., 2006) with the emission peaks during DJF and MAM.

During DJF, mineral dusts emitted from two persistent dust sources in southern Sahara – the Bodélé depression and the areas in between the east of Mauritania, the north of Mali and the south of Algeria (Prospero et al., 2002; Laurent et al., 2008; Washington et al., 2006; Shao et al., 2011) – are transported by the Harmattan winds southwestward over the Sahel toward the Gulf of Guinea into the Atlantic Ocean heading to the coast of South America (Kaufman et al., 2005b). Consequently, coarse dust concentration is higher over the Bodélé depression, the area near the west coast from Senegal south to Gabon on the equator, and over the Gulf of Guinea during DJF.

During MAM and JJA, the coarse dust concentration increases and covers larger regions in the northern Africa. Because the Intertropical Convergence Zone (ITCZ) displaces northward, it makes the surface monsoon flow intrude into the continent from the south-west towards the continental Sahel. Such change produces a progressive organization of convection from isolated cells to large-scale and quickly propagating systems, which usually do not precipitate

and are efficient in eroding bare soils to induce mineral dust (Marticorena et al., 2010; Touré et al., 2011). Thus, during JJA, the columnar dust content over western Africa results from the superimposition of local emission from the Sahel and remote transport of dust emitted in the Sahara (Tegen and Fung, 1994; Yoshioka et al., 2005; Marticorena et al., 2010). In addition, western Africa is prone to land-use change as the rapid demographic increase and desertification during drought periods (Dai, 2011), which may induce more dust sources (Carslaw et al., 2010). The emission of mineral dust by wind erosion over the semi-arid areas of the Sahel is possible to explain the seasonal maximum in the aerosol loading observed by satellites over western Africa (Tegen and Fung, 1994; Yoshioka et al., 2005; Forster et al., 2007). Dust concentration in September is substantially less and the minimum dust concentration is observed during SON in association with lower dust emission in northern Africa.

In addition, Figures 4.9 and 4.10 also illustrate that coarse dust concentration is particularly high over the Arabian Peninsula, central to southern Pakistan, as well as over the Oman and Arabian seas. Over this region, the maximum dust concentration is observed during JJA, followed by MAM, while dust concentration has substantially decreased during SON and DJF. Higher dust concentration during MAM and JJA is primarily caused by the strong northwesterly winds known as “shamal winds” and drier conditions. The JJA peak is caused by several major sources of dust that have maximum dust activity during JJA, including desert areas in Syria and Iraq where a strong northwesterly Shamal Wind is blowing (Choobari et al., 2014), and the third strongest source of dust, Arabian Peninsula, in the world (Goudie and Middleton, 2006). It is pointed that this area is also partly affected by dust originated from the Sahara (Goudie and Middleton, 2006) where a peak of dust activity during JJA has long been identified (e.g., Engelstaedter et al., 2006). Dust concentration during SON is substantially less, and the minimum dust concentration is observed during DJF in association with lower dust emission from both external and internal sources of dust.

It is noted that coarse dust concentration over Arabian Peninsula is lower during JJA in 2007 than that in 2006 and 2008 (see Figure 4.9). The lower dust activity during JJA in 2007 can be attributed to the water coverage in the Hamoun lakes and the growth vegetation in the basin (Rashki et al., 2013b; Sharifikia, 2013). The average value of coarse dust concentration during JJA in 2007 is 54.44 mm^3/mm^2, incomparison to 65.89 mm^3/mm^2 and 63.77 mm^3/mm^2, in 2006 and 2008, respectively (more details in Table 4.7). In addition, the retrieval also reveals that the spatial-averaged coarse dust concentration near the Arabian Sea during JJA in 2008 is much higher than that during JJA in 2006 and 2007, because of the enhanced dust activity and several dust storms originated from the Sistan region in June 2008. Figure 4.10

shows coarse dust concentration over Arabian Peninsula and Arabian Sea is much higher from April to July as the dust storms are more frequent during this period and decrease in frequency in August and September. Previous studies (Choobari et al., 2013; Rashki et al., 2013b) emphasized that the local and regional topography and meteorological dynamics, rather than synoptic and large-scale phenomena, controlled the dust activity over Sistan, which is a reason for the observed monthly variability. During the period of April to July, the areas of high concentration of coarse dust shift from Arabian Peninsula to Arabian Sea. In June and July, the dust air masses move southwards and reach the northern part of Arabian Sea. The results of the dust concentration retrievals appear to illustrate the dust-transport mechanisms and pathways that are under influence of synoptic and atmospheric dynamic processes (Washington and Todd, 2005; Todd et al., 2008; Kaskaoutis et al., 2012a, b).

Note that the dust columnar volume concentration (mm^3/m^2), which is directly retrieved by the algorithm, was converted to columnar mass concentration (mg/m^2) using the density value of 2.5 g/cm^3 (Formenti et al., 2014a, b).

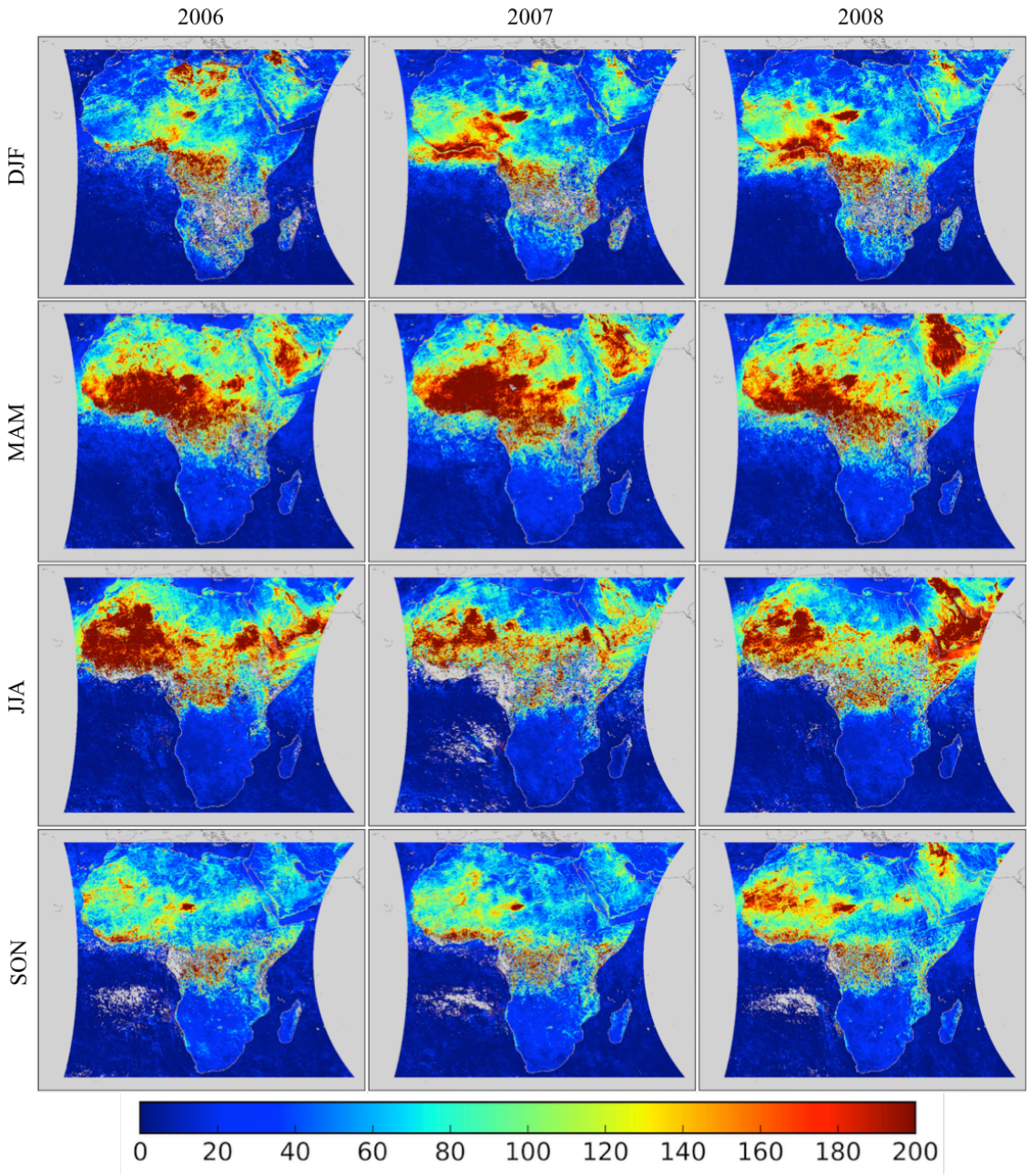

Figure 4.9: Seasonal variations of coarse dust columnar volume concentration (mm^3/m^2) over Africa and Arabian Peninsula during the period 2006 – 2008 as retrieved by GRASP algorithm from POLDER/PARASOL satellite observations using the volume-weighted conversion model.

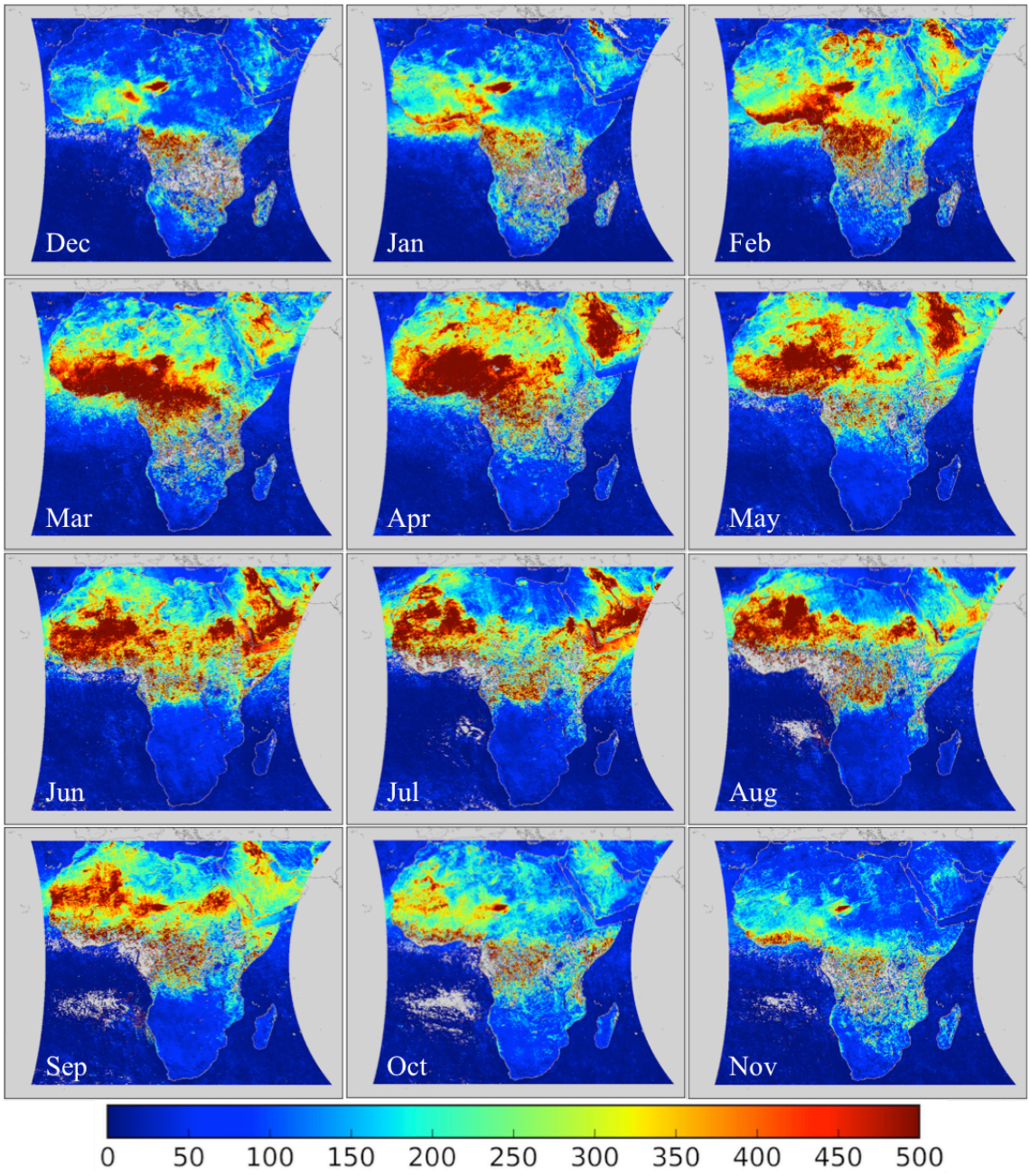

Figure 4.10: Monthly variations of coarse dust columnar mass concentration (mg/m^2) over Africa and Arabian Peninsula averaged over the period 2006 – 2008 as retrieved by GRASP algorithm from POLDER/PARASOL satellite observations using the volume-weighted conversion model.

Table 4.7: Seasonal columnar volume concentration (mm^3/m^2) statistics for coarse dust over Africa and Arabian Peninsula during the period 2006 – 2008 as retrieved by GRASP algorithm from POLDER/PARASOL satellite observations using the volume-weighted conversion model. The percentages (5%, 25%, 50%, 75% and 95%) of the values are determined by ordering the values of the variable from lowest to highest, which indicate in detail the distribution of the variable.

Year	Season	Average	Std	5%	25%	50%	75%	95%
2006	DJF	49.57	68.71	0.27	4.26	28.23	70.35	170.91
	MAM	68.88	84.15	1.26	6.92	35.01	104.68	230.47
	JJA	65.89	85.12	1.01	5.19	25.23	102.70	239.47
	SON	43.53	55.08	0.51	5.14	30.12	64.19	126.58
2007	DJF	50.76	65.59	0.63	6.11	31.62	72.59	165.39
	MAM	72.15	83.22	2.08	8.86	40.46	111.73	235.29
	JJA	54.44	75.16	0.52	5.05	21.84	81.68	193.20
	SON	42.74	54.78	0.62	5.16	27.24	62.78	127.72
2008	DJF	53.47	68.01	0.47	5.58	35.78	76.30	171.18
	MAM	70.95	80.20	1.99	8.73	42.53	109.94	222.94
	JJA	63.77	79.04	1.15	5.62	25.65	102.14	218.54
	SON	50.18	59.04	0.52	5.67	29.72	78.65	153.88

Table 4.8: Monthly columnar mass concentration (mg/m^2) statistics for coarse dust over Africa and Arabian Peninsula averaged over the period 2006 – 2008 as retrieved by GRASP algorithm from POLDER/PARASOL satellite observations using the volume-weighted conversion model. The percentages (5%, 25%, 50%, 75% and 95%) of the values are determined by ordering the values of the variable from lowest to highest, which indicate in detail the distribution of the variable.

Month	Average	Std	5%	25%	50%	75%	95%
Dec	92.93	156.21	0.67	9.67	50.32	117.72	312.54
Jan	114.72	174.68	0.73	10.61	60.85	149.04	415.17
Feb	157.88	210.42	0.67	11.59	91.48	232.16	523.45
Mar	176.84	230.22	2.14	16.46	96.12	250.53	617.26
Apr	192.84	249.69	2.52	16.65	95.58	290.00	659.79
May	167.27	213.24	2.80	17.49	76.26	260.29	555.13
Jun	171.44	234.10	1.77	13.69	71.61	256.97	610.52
Jul	154.74	221.40	1.62	12.49	56.46	222.73	579.64
Aug	140.05	212.87	1.18	10.34	48.99	192.01	541.11
Sep	149.06	200.64	0.93	11.77	71.65	226.73	493.77
Oct	119.45	162.53	1.28	13.63	72.78	167.85	381.14
Nov	87.82	134.36	0.95	11.42	49.05	117.74	286.26

4.1.5 Iron oxide

Iron content of airborne mineral dust has particular importance because the African dust is the major source of iron in the North Atlantic Ocean (Sarthou et al., 2003). The deposition of iron may induce an influence on the rate of nitrogen fixation by microorganisms, and then on the global carbon cycle (Mills et al., 2004; Moore et al., 2002). The atmospheric dust consists of different minerals, whose proportions depend on the soil mineralogy of the source region and surface wind speed, which can determine size resolved mineralogical composition of airborne dust (Marticorena and Bergametti, 1995; Caquineau et al., 1997; Alfaro et al., 1998; Moreno et al., 2006). The soil mineralogy is different between the Saharan and Sahelian source region (Pye, 1987; Claquin et al., 1999; Caquineau et al., 2002). The Saharan soil consists mainly of Calcisols or Arenosols, whereas the Sahel is dominated by weathered Plinthosols (e.g., iron oxides, kaolinite, quartz) (Pye, 1987; Claquin et al., 1999; Caquineau et al., 2002; Nickovic et al., 2012; Journet et al., 2014). Therefore, a distinction in the composition of dust transported in Sahara and Sahel can be expected. At the same time, when the Sahel region experiences the humid Monsoon flow from South-West, attributed to the northern displacement of ITCZ, the columnar dust over the Sahel is characterized by the superimposition of local emission and remote transport of dust emitted in the Sahara. The iron content of airborne dust, therefore, can have more complex spatial distribution than maps of soil mineralogy.

Figure 4.11 shows the retrieved iron oxide spatial distribution and seasonal variability. The concentration has a seasonal cycle that is similar to dust concentration. The iron oxide concentration over African continent reaches the peak during the MAM season, has lower values during JJA and DJF, and the lowest value during SON (Table 4.9). The average concentration of iron oxide in March (the peak of 2.69 mg/mm^2) is about twice as that in December (1.39 mg/mm^2), as shown in Table 4.10. The comparisons of Figures 4.9, 4.10 and Figures 4.11, 4.12 show that despite dust and iron concentrations reach peaks in the same season (MAM), the dust enrichment by iron is depending on the area. The retrieval reveals high iron concentration over Arabian Sea during JJA, which may be attributed to the dust originated from Saudi Arabia, known for presence of an important iron content (Krueger et al., 2004). The retrievals for MAM and JJA (Figures 4.11 and 4.12) also show high iron oxide concentration over western Africa, in particular around Niger and Mauritania, and near the west coast. This is in line with a study by Formenti et al. (2008) that demonstrates the higher iron oxide content in Sahelian dust originated locally from Niger and Mauritania in the Sahel belt, while the lower ones are in the Chad basin. Also, Lazaro et al., (2008) reported that the iron oxide content of dust transported to the Canary Islands, near the west coast, has the

tendency of higher values for source areas between 0°N – 20°N. It can also be noted that a "hot spot" of iron oxide concentration is observed over Tunisia in February 2006 (can be seen in Figures 4.11 and 4.12).

Note that the iron oxide columnar volume concentration (mm^3/m^2), which is directly retrieved by the algorithm, was converted to columnar mass concentration (mg/m^2) using the density value of 4.8 g/cm^3 (4.28 g/cm^3 for goethite and 5.25 g/cm^3 for hematite, Formenti et al., 2014a, b).

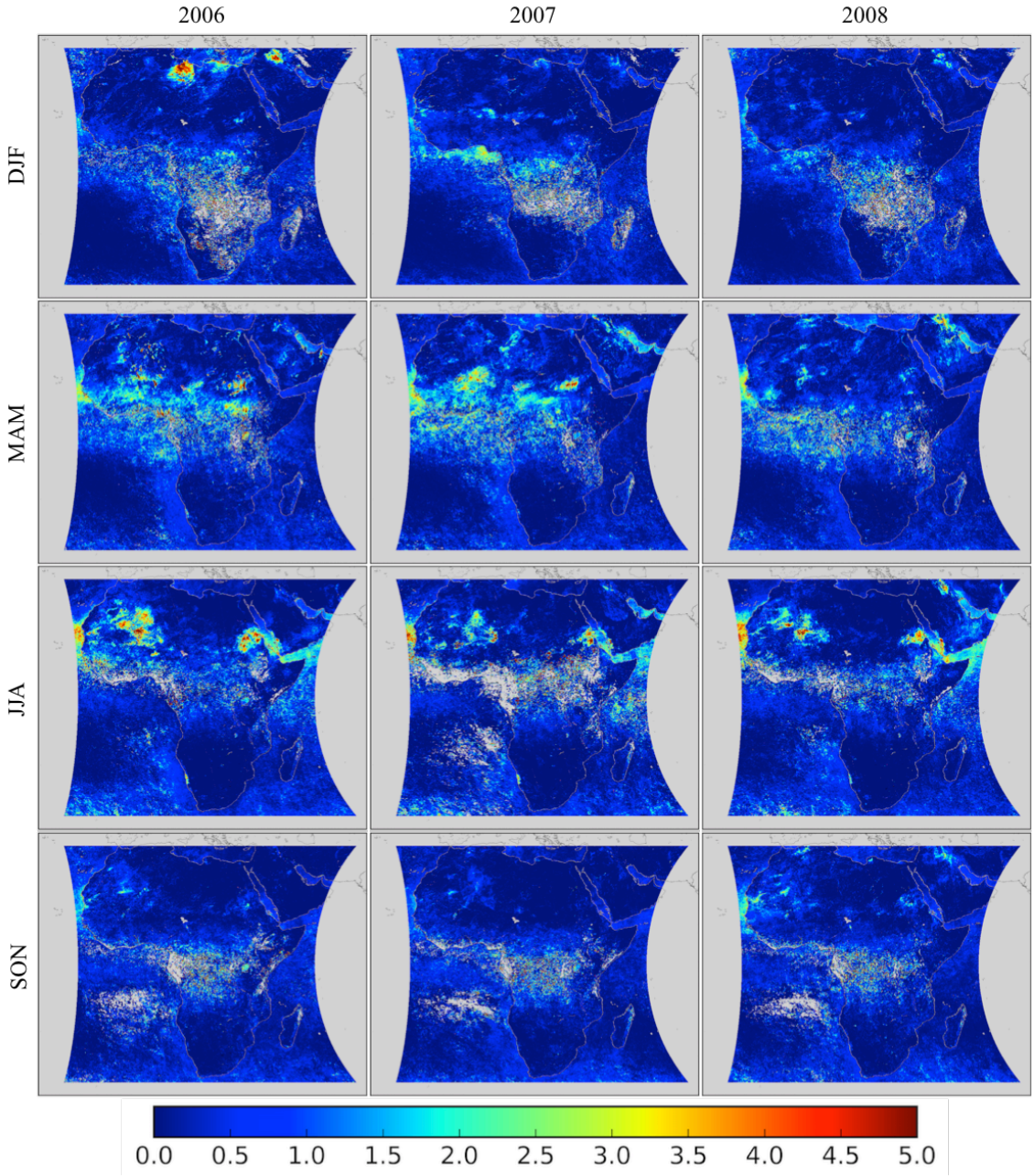

Figure 4.11: Seasonal variations of iron oxide columnar volume concentration (mm^3/m^2) over Africa and Arabian Peninsula during the period 2006 – 2008 as retrieved by GRASP algorithm from POLDER/PARASOL satellite observations using the volume-weighted conversion model.

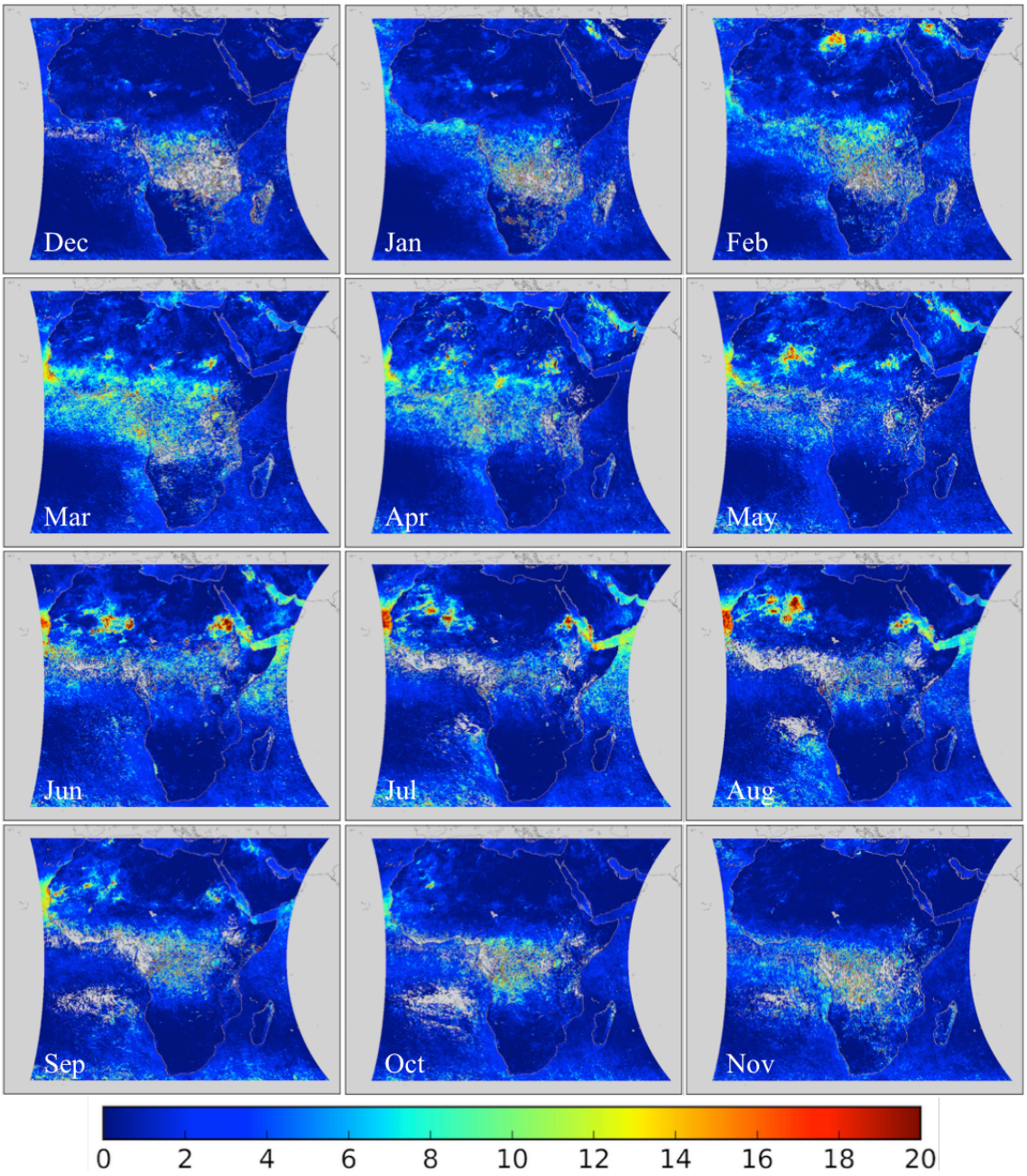

Figure 4.12: Monthly variations of iron oxide columnar mass concentration (mg/m^2) over Africa and Arabian Peninsula averaged over the period 2006 – 2008 as retrieved by GRASP algorithm from POLDER/PARASOL satellite observations using the volume-weighted conversion model.

Table 4.9: Seasonal columnar volume concentration (mm^3/m^2) statistics for iron oxide over Africa and Arabian Peninsula during the period 2006 – 2008 as retrieved by GRASP algorithm from POLDER/PARASOL satellite observations using the volume-weighted conversion model. The percentages (5%, 25%, 50%, 75% and 95%) of the values are determined by ordering the values of the variable from lowest to highest, which indicate in detail the distribution of the variable.

Year	Season	Average	Std	5%	25%	50%	75%	95%
2006	DJF	0.50	1.21	0.00	0.01	0.15	0.57	1.96
	MAM	0.55	0.90	0.00	0.05	0.27	0.73	1.95
	JJA	0.53	0.96	0.00	0.03	0.24	0.68	2.01
	SON	0.39	0.89	0.00	0.02	0.16	0.47	1.38
2007	DJF	0.42	1.03	0.00	0.02	0.15	0.49	1.60
	MAM	0.55	0.82	0.00	0.04	0.25	0.76	2.03
	JJA	0.54	1.23	0.00	0.02	0.16	0.61	2.15
	SON	0.36	0.95	0.00	0.01	0.12	0.42	1.26
2008	DJF	0.39	1.03	0.00	0.02	0.14	0.45	1.44
	MAM	0.48	0.78	0.00	0.04	0.23	0.64	1.74
	JJA	0.48	0.84	0.00	0.02	0.19	0.62	1.90
	SON	0.40	0.80	0.00	0.03	0.18	0.50	1.40

Table 4.10: Monthly columnar mass concentration (mg/m^2) statistics for iron oxide over Africa and Arabian Peninsula averaged over the period 2006 – 2008 as retrieved by GRASP algorithm from POLDER/PARASOL satellite observations using the volume-weighted conversion model. The percentages (5%, 25%, 50%, 75% and 95%) of the values are determined by ordering the values of the variable from lowest to highest, which indicate in detail the distribution of the variable.

Month	Average	Std	5%	25%	50%	75%	95%
Dec	1.39	4.87	0.01	0.04	0.28	1.32	5.54
Jan	1.76	4.70	0.01	0.05	0.39	1.83	7.34
Feb	2.30	5.12	0.01	0.07	0.64	2.69	9.29
Mar	2.69	4.73	0.01	0.14	0.90	3.41	10.98
Apr	2.54	4.60	0.01	0.14	0.90	3.20	10.12
May	2.26	3.92	0.01	0.13	0.85	2.84	9.06
Jun	2.60	5.39	0.01	0.09	0.78	3.07	10.77
Jul	2.20	4.48	0.01	0.07	0.56	2.49	9.85
Aug	2.17	4.76	0.01	0.06	0.52	2.42	9.51
Sep	2.01	4.53	0.01	0.07	0.52	2.34	8.31
Oct	1.68	3.77	0.01	0.07	0.51	1.88	6.86
Nov	1.61	4.16	0.01	0.04	0.36	1.66	6.85

4.1.6 Aerosol water content

The aerosol water content is retrieved for both fine and coarse size fractions. Figure 4.13 shows the variations of aerosol water content volume concentration in fine and coarse modes and total over Africa and Arabian Peninsula for years 2006 to 2008. It shows that the inter-annual variability of aerosol water content is quite stable. Figure 4.13 also shows that the coarse fraction water concentration is notably smaller over land than over ocean; the fine fraction, however, has nearly same variability over land and over ocean. Indeed, the "water" in the conversion model approximates composition of aerosol that includes inorganic species such as ammonium nitrate, ammonium sulfate and sea salts. Therefore, the high aerosol water content retrieved over ocean corresponds also to coarse marine sea salt aerosols. Over land, however, it can be rather attributed to anthropogenic aerosol containing ammonium nitrate or ammonium sulfate, which are typical for fine fraction. In addition, anthropogenic aerosols are expected to be more hygroscopic. The coarse mode aerosols over land are usually constituted of mineral dust, which is generally hydrophobic. Over ocean, however, the elevated coarse mode aerosol water content is logically corresponds to coarse particles of the sea salt aerosol. Figures 4.14 shows monthly variability of total aerosol water content mass concentration. Elevated aerosol water content is generally corresponding to warm months or to periods and regions affected by biomass burning aerosols.

It has to be mentioned here that some discontinuity between over land and over ocean retrievals can be observed around the Arabian Peninsula and Western Africa. This discontinuity can be suspected as an algorithmic artifact, however, worth noting that some mountains separate land and sea around the Arabian Peninsula, especially Red Sea, which can be a natural barrier between continental and marine aerosols. In addition, statistics of the pixels available for the retrievals form POLDER/PARASOL (see Figure 5.1) shows that the number of pixels over land is significantly higher than over ocean, which is rather due to cloud contamination. This discontinuity in the pixel statistics can also affect the mean values of the retrieved concentrations.

Note that the water columnar volume concentration (mm^3/m^2), which is directly retrieved by the algorithm, was converted to columnar mass concentration (mg/m^2) using the density value of 1.0 g/cm^3.

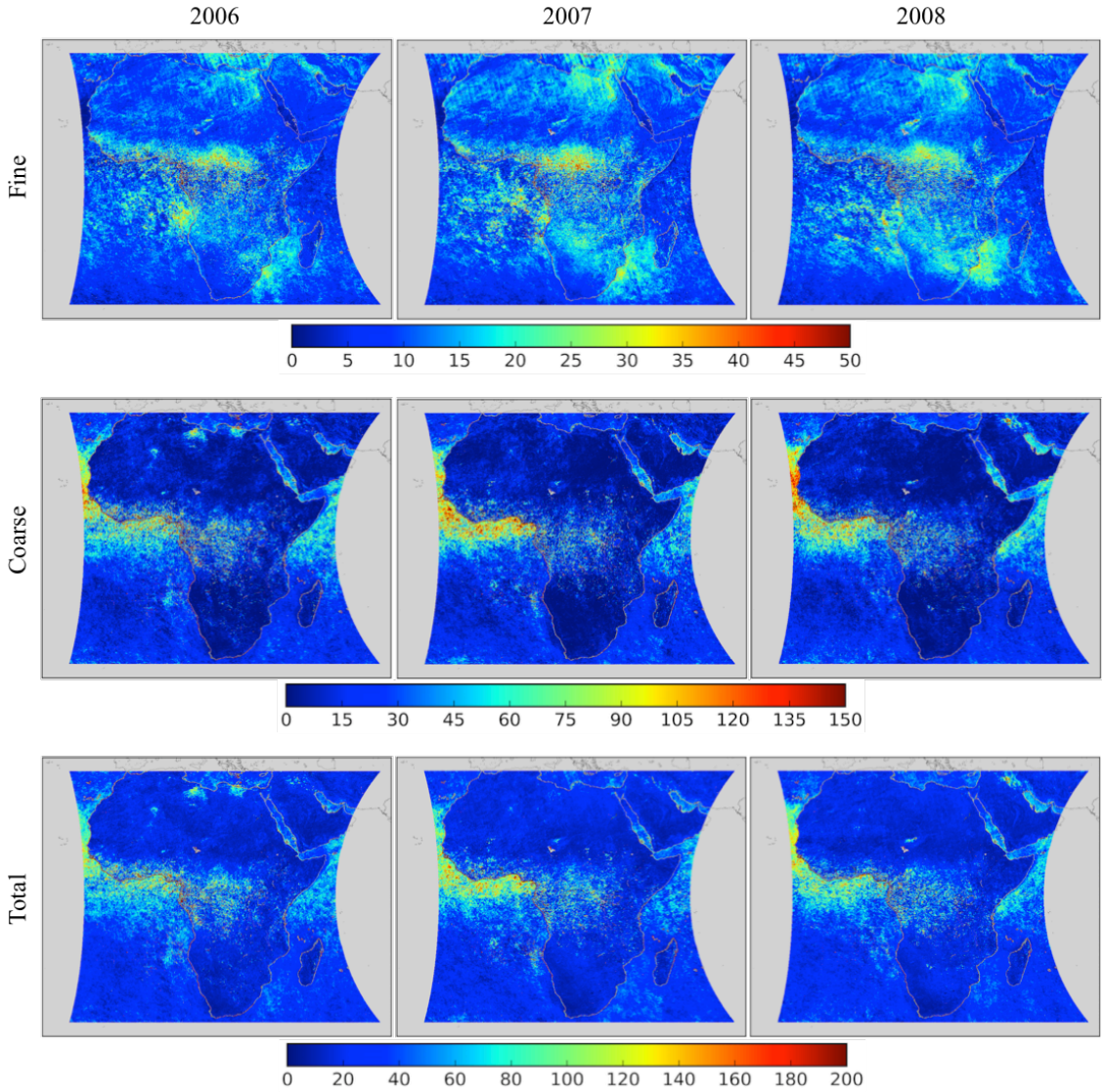

Figure 4.13: Interannual variations of water columnar volume concentration (mm^3/m^2) (fine mode, coarse mode and total) over Africa and Arabian Peninsula during the period 2006 – 2008 as retrieved by GRASP algorithm from POLDER/PARASOL satellite observations using the volume-weighted conversion model.

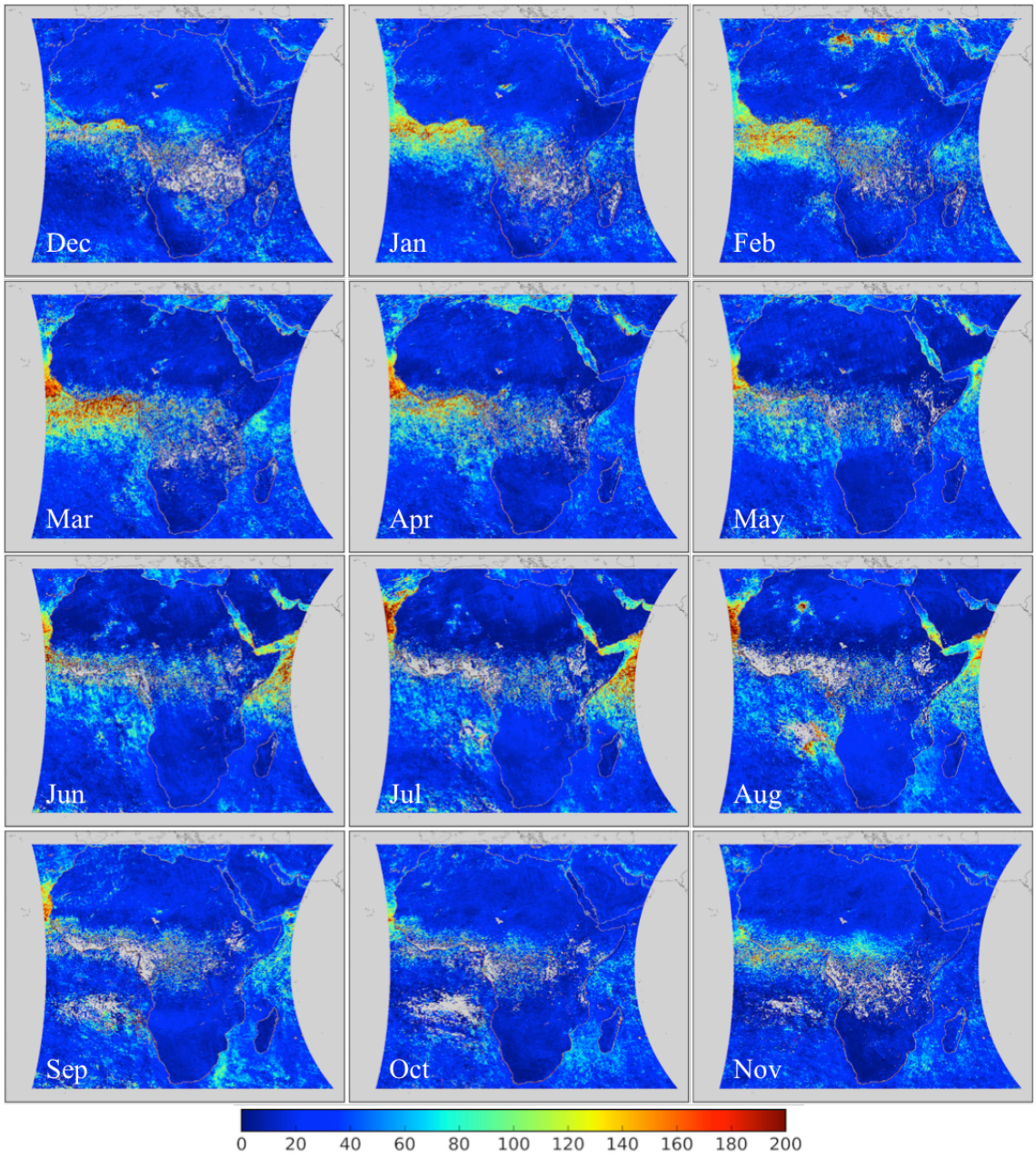

Figure 4.14: Monthly variations of total water columnar mass concentration (mg/m^2) over Africa and Arabian Peninsula averaged over the period 2006 – 2008 as retrieved by GRASP algorithm from POLDER/PARASOL satellite observations using the volume-weighted conversion model.

4.2 Maxwell-Garnett conversion model retrieval

The volume-weighted conversion model is a straightforward and transparent conversion approach that enabled studying the sensitivity limits of POLDER/PARASOL measurements to the aerosol composition. After finding an optimum configuration of aerosol species elements and their refractive indices, the algorithm was upgraded with the Maxwell-Garnett conversion model to obtain more species of aerosol composition. Aerosol composition retrievals with the Maxwell-Garnett conversion model utilizes the host determined by properties and proportions of ammonium nitrate and water, and relative humidity is also retrieved as part of this conversion model. The composition retrievals with Maxwell-Garnett conversion modes showed a good agreement with volume-weighted model for the temporal and spatial variations of all assumed aerosol compositions over Africa and Arabian Peninsula. For example, the retrieved black and brown carbon concentrations of volume-weighted and Maxwell-Garnett conversion model obtain high values over northern Africa during DJF and over southern Africa during JJA and SON. The retrieved dust and iron oxide concentrations of volume-weighted and Maxwell-Garnett conversion model are also similar, they reach peaks during MAM, lower values during JJA and DJF, and lowest during SON. In addition, both the volume-weighted and Maxwell-Garnett conversion models show a “hot spot” of coarse dust concentration over Bodélé depression throughout the year. However, some differences between the retrieved elements by the volume-weighted and the Maxwell-Garnett conversion model are also observed. For example, over the Bodélé region during MAM, artificially derived brown carbon concentrations in the case of Maxwell-Garnett conversion model is much less than that derived in the case of volume-weighted conversion model (Figures 4.3, 4.4 and 4.17, 4.18); the aerosol absorbing property in this case should be associated with iron oxides in fine size fraction. The iron oxide concentration retrieved by Maxwell-Garnett conversion model reaches the peak in April (Table 4.20). While the iron oxide concentration retrieved by the volume-weighted conversion model reaches the peak in March (Table 4.10). The details are discussed in the following.

4.2.1 Black carbon

Figures 4.15 and 4.16 show the retrieved temporal and spatial variations of black carbon columnar volume concentration over Africa and Arabian Peninsula. The Maxwell-Garnett model retrievals presents consistent with the volume weighted mixture model seasonal peaks of black carbon concentration during DJF and SON, as well as a lower magnitude and the area of coverage during MAM, reaching the smallest value in May (Tables 4.11 and 4.12). In addition, the Maxwell-Garnett model shows high black carbon concentration over northern

Africa during DJF and over southern Africa during JJA and SON, similar to the volume-weighted retrievals.

Comparisons of retrieved black carbon concentration between volume-weighted (Figures 4.1, 4.2; Tables 4.1, 4.2) and Maxwell-Garnett conversion models (Figures 4.15, 4.16; Tables 4.11, 4.12) show that the black carbon concentration retrieved by volume-weighted conversion model is slightly higher than that retrieved by Maxwell-Garnett conversion model, especially over southern Africa during DJF, where the available number of pixels of satellite observations is very small due to often clouds over this region. It is noted that the Maxwell-Garnett conversion model provides more spatially homogeneous retrievals than that obtained from the volume-weighted conversion model. It is because each of the assumed aerosol elements is independent for fine and coarse modes in the volume-weighted conversion model. While in the Maxwell-Garnett conversion model, the assumed ammonium nitrate and water in fine and coarse modes are connected by relative humidity.

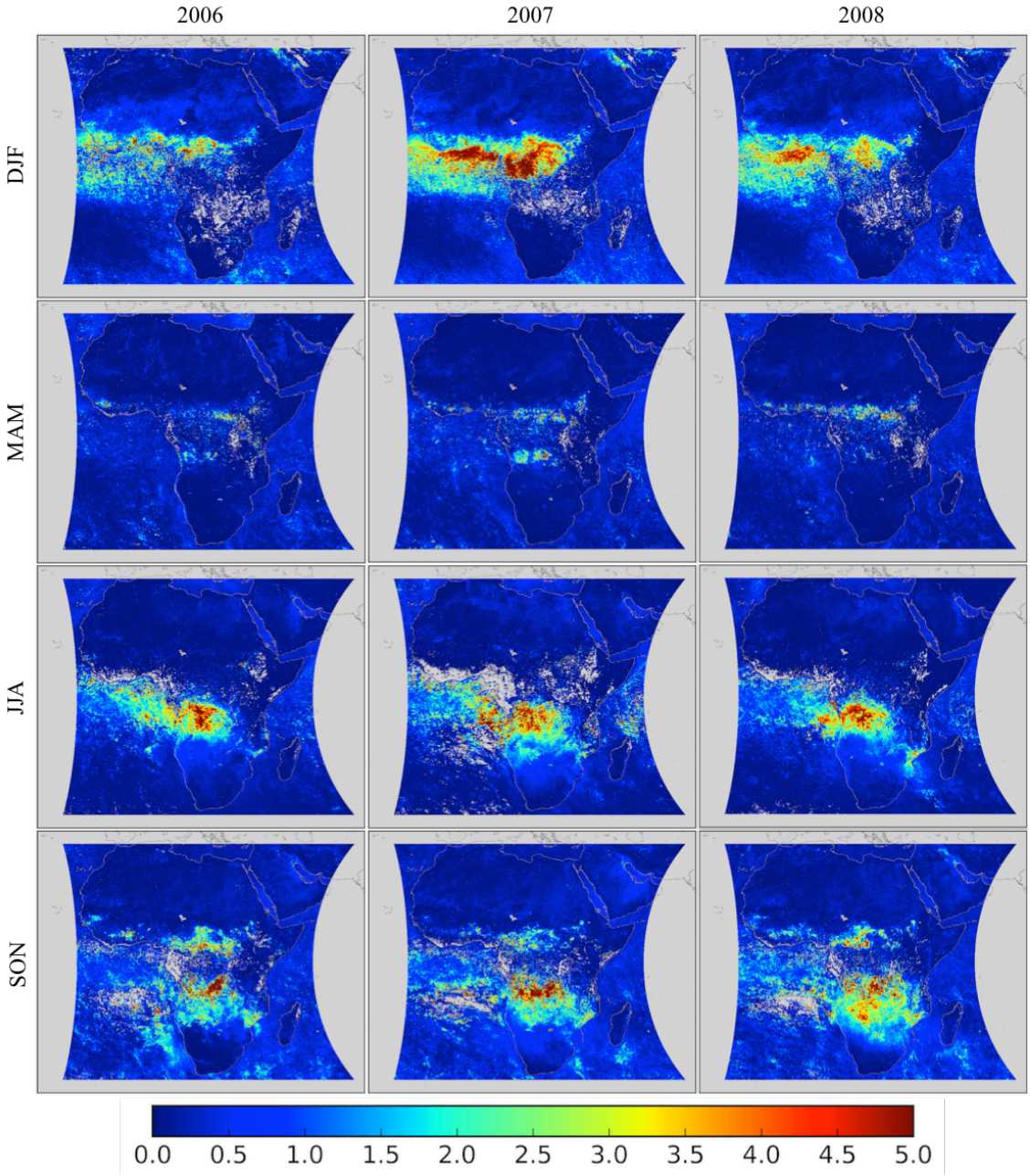

Figure 4.15: Seasonal variations of BC columnar volume concentration (mm^3/m^2) over Africa and Arabian Peninsula during the period 2006 – 2008 as retrieved by GRASP algorithm from POLDER/PARASOL satellite observations using the Maxwell-Garnett conversion model.

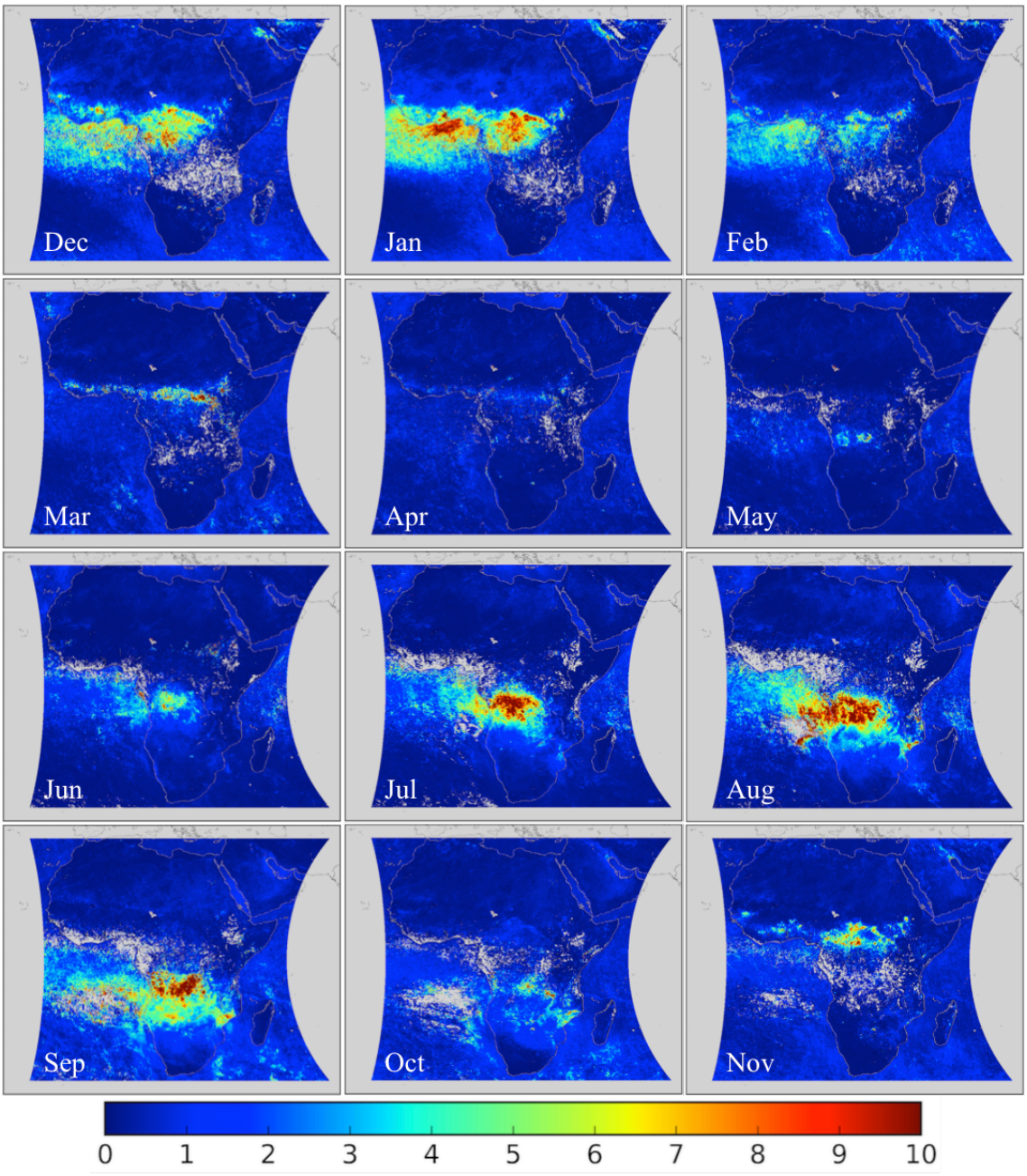

Figure 4.16: Monthly variations of BC columnar mass concentration (mg/m^2) over Africa and Arabian Peninsula averaged over the period 2006 – 2008 as retrieved by GRASP algorithm from POLDER/PARASOL satellite observations using the Maxwell-Garnett conversion model.

Table 4.11: Seasonal columnar volume concentration (mm^3/m^2) statistics for BC over Africa and Arabian Peninsula during the period 2006 – 2008 as retrieved by GRASP algorithm from POLDER/PARASOL satellite observations using the Maxwell-Garnett conversion model. The percentages (5%, 25%, 50%, 75% and 95%) of the values are determined by ordering the values of the variable from lowest to highest, which indicate the distribution of the variable.

Year	Season	Average	Std	5%	25%	50%	75%	95%
2006	DJF	0.53	0.73	0.01	0.09	0.26	0.67	1.98
	MAM	0.25	0.43	0.02	0.06	0.14	0.29	0.80
	JJA	0.44	0.78	0.02	0.07	0.16	0.39	2.06
	SON	0.57	0.87	0.03	0.12	0.27	0.66	2.07
2007	DJF	0.70	1.11	0.03	0.12	0.28	0.72	3.14
	MAM	0.26	0.44	0.02	0.06	0.14	0.30	0.86
	JJA	0.55	0.97	0.02	0.07	0.18	0.50	2.53
	SON	0.60	0.92	0.04	0.15	0.30	0.66	2.16
2008	DJF	0.58	0.83	0.02	0.11	0.27	0.67	2.42
	MAM	0.22	0.42	0.02	0.05	0.12	0.24	0.70
	JJA	0.44	0.75	0.02	0.07	0.17	0.43	1.91
	SON	0.64	0.90	0.04	0.14	0.29	0.76	2.48

Table 4.12: Monthly columnar mass concentration (mg/m^2) statistics for BC over Africa and Arabian Peninsula during the period 2006 – 2008 as retrieved by GRASP algorithm from POLDER/PARASOL satellite observations using the Maxwell-Garnett conversion model. The percentages (5%, 25%, 50%, 75% and 95%) of the values are determined by ordering the values of the variable from lowest to highest, which indicate the distribution of the variable.

Month	Average	Std	5%	25%	50%	75%	95%
Dec	1.09	1.69	0.05	0.19	0.46	1.20	4.59
Jan	1.28	2.10	0.04	0.17	0.49	1.34	5.71
Feb	0.90	1.36	0.03	0.14	0.39	1.08	3.52
Mar	0.54	1.29	0.02	0.08	0.23	0.54	1.90
Apr	0.38	0.64	0.02	0.09	0.20	0.44	1.23
May	0.34	0.64	0.02	0.07	0.17	0.38	1.14
Jun	0.53	1.08	0.02	0.08	0.20	0.50	2.22
Jul	0.83	1.70	0.03	0.11	0.26	0.69	3.84
Aug	1.16	2.18	0.03	0.14	0.38	1.01	5.37
Sep	1.29	2.18	0.05	0.21	0.51	1.39	5.22
Oct	0.77	1.12	0.05	0.19	0.41	0.91	2.72
Nov	0.68	1.08	0.04	0.17	0.36	0.76	2.27

4.2.2 Brown carbon

Figures 4.17 and 4.18 show the retrieved temporal and spatial variations of brown carbon columnar concentration over Africa and Arabian Peninsula by Maxwell-Garnett conversion model. The patterns are similar to the corresponding retrievals with volume-weighted conversion model. For example, brown carbon concentration reaches the peak during DJF. Brown carbon concentration during MAM is less in quantity and area than in other three seasons, particularly in May with the lowest value of 4.04 mg/m^2 (Table 4.13, 4.14). The Maxwell-Garnett retrievals also show the differences in spatial distributions of black carbon and brown carbon concentrations (see Figures 4.15, 4.16 and 4.17, 4.18).

Comparisons of retrieved brown carbon concentration between volume-weighted (Figures 4.3, 4.4; Tables 4.3, 4.4) and Maxwell-Garnett conversion models (Figures 4.17, 4.18; Tables 4.11, 4.12) show that the brown carbon concentration retrieved by volume-weighted model is a bit smaller than that retrieved by Maxwell-Garnett model. However, it is noted that, over the Bodélé region, brown carbon concentrations obtained from Maxwell-Garnett model is much less than that obtained from volume-weighted model, especially during MAM (Figures 4.3, 4.4 and 4.17, 4.18). The volume-weighted conversion model attributes the aerosol absorbing property associated with iron oxides in fine size fraction to brown carbon, while in case of the Maxwell-Garnett conversion model this artifact appears only during DJF, but not during MAM.

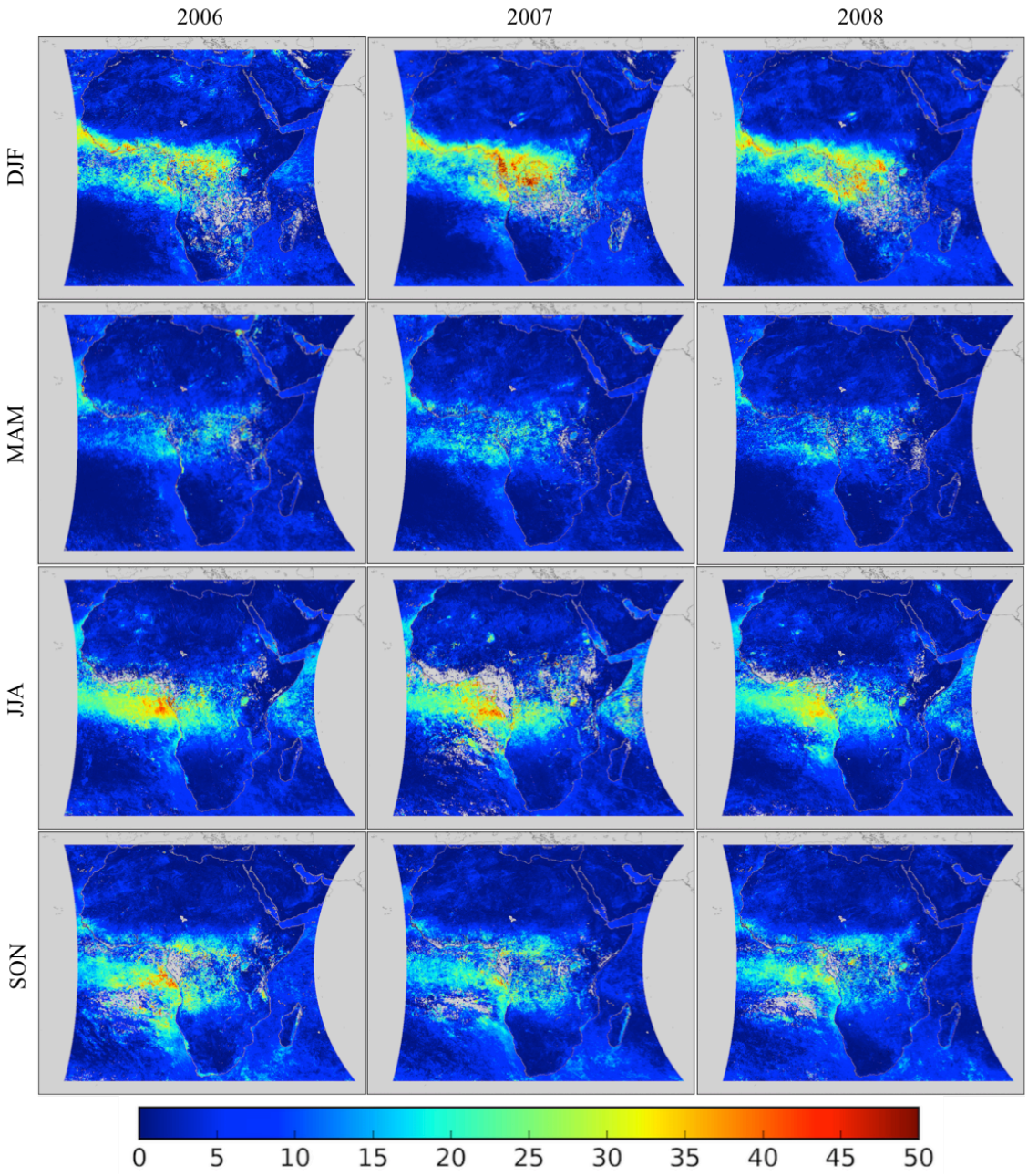

Figure 4.17: Seasonal variations of BrC columnar volume concentration (mm^3/m^2) over Africa and Arabian Peninsula during the period 2006 – 2008 as retrieved by GRASP algorithm from POLDER/PARASOL satellite observations using the Maxwell-Garnett conversion model.

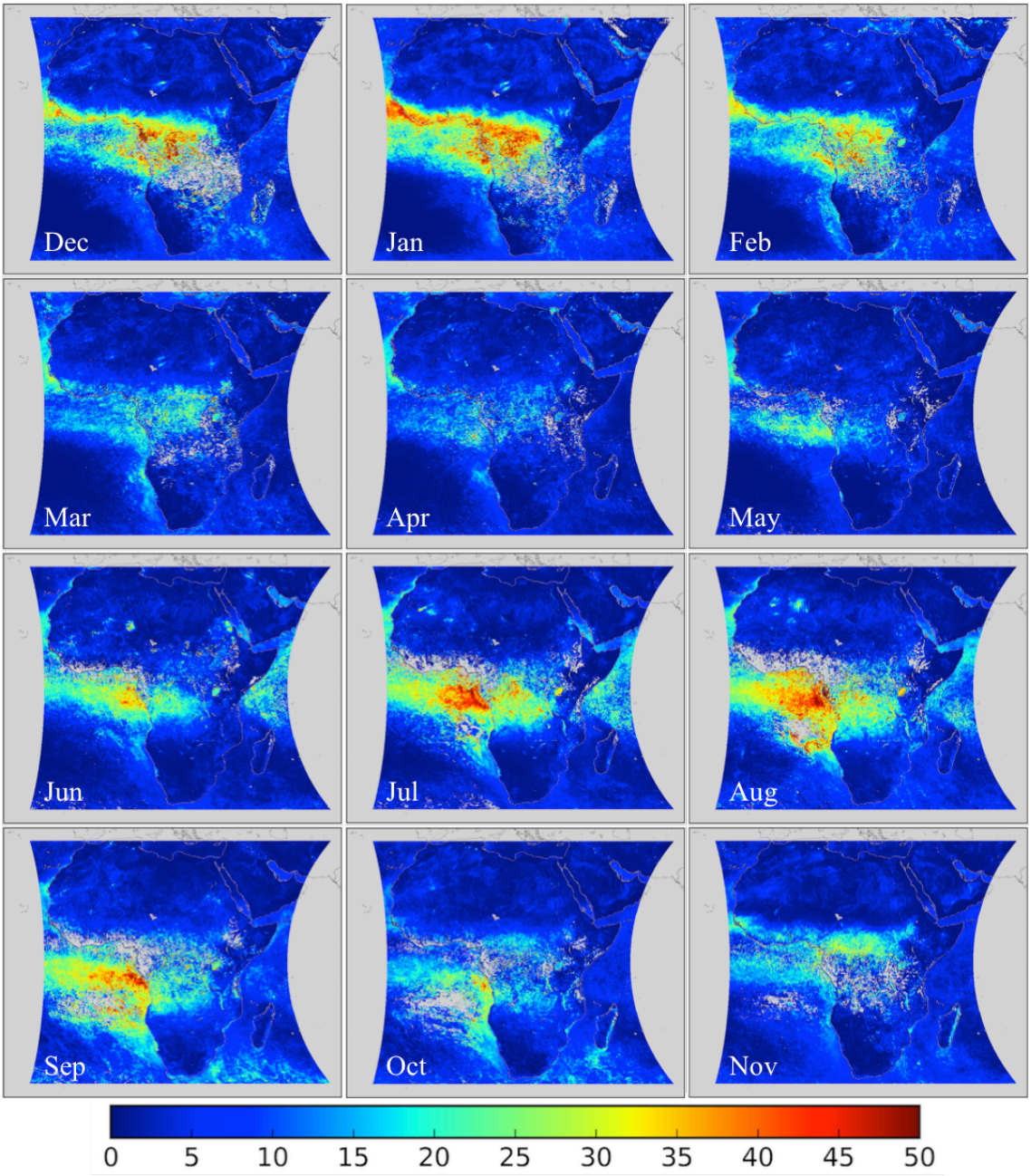

Figure 4.18: Monthly variations of BrC columnar mass concentration (mg/m^2) over Africa and Arabian Peninsula averaged over the period 2006 – 2008 as retrieved by GRASP algorithn from POLDER/PARASOL satellite observations using the Maxwell-Garnett conversion model.

Table 4.13: Seasonal columnar volume concentration (mm^3/m^2) statistics for BrC over Africa and Arabian Peninsula during the period 2006 – 2008 as retrieved by GRASP algorithm from POLDER/PARASOL satellite observations using the Maxwell-Garnett conversion model. The percentages (5%, 25%, 50%, 75% and 95%) of the values are determined by ordering the values of the variable from lowest to highest, which indicate the distribution of the variable.

Year	Season	Average	Std	5%	25%	50%	75%	95%
2006	DJF	6.36	7.47	0.18	1.02	3.71	8.65	22.97
	MAM	4.19	5.37	0.20	0.75	2.32	5.74	14.31
	JJA	6.22	7.57	0.25	1.11	3.13	8.26	23.42
	SON	6.62	7.23	0.34	1.42	4.02	9.22	21.94
2007	DJF	6.91	8.31	0.25	1.30	3.92	8.84	25.80
	MAM	4.12	4.89	0.22	0.78	2.15	5.71	14.64
	JJA	6.35	8.14	0.22	1.04	2.97	8.26	24.14
	SON	5.76	6.17	0.36	1.22	3.34	8.42	18.62
2008	DJF	6.38	7.69	0.24	1.20	3.63	8.08	24.28
	MAM	3.51	4.33	0.21	0.69	1.84	4.63	12.75
	JJA	5.79	7.02	0.28	1.05	2.87	7.63	21.67
	SON	5.74	5.93	0.39	1.43	3.61	8.01	18.51

Table 4.14: Monthly columnar mass concentration (mg/m^2) statistics for BrC over Africa and Arabian Peninsula during the period 2006 – 2008 as retrieved by GRASP algorithm from POLDER/PARASOL satellite observations using the Maxwell-Garnett conversion model. The percentages (5%, 25%, 50%, 75% and 95%) of the values are determined by ordering the values of the variable from lowest to highest, which indicate the distribution of the variable.

Month	Average	Std	5%	25%	50%	75%	95%
Dec	7.13	9.33	0.24	1.12	3.72	9.23	27.20
Jan	8.26	10.65	0.24	1.20	4.21	10.33	32.82
Feb	7.35	8.83	0.22	1.18	4.16	10.16	26.06
Mar	5.31	7.28	0.17	0.74	2.32	7.29	19.64
Apr	4.32	5.78	0.21	0.76	2.12	5.63	15.85
May	4.04	5.87	0.19	0.64	1.79	5.00	15.65
Jun	5.83	8.43	0.21	0.82	2.33	7.30	23.49
Jul	7.13	9.94	0.25	0.95	2.65	8.96	29.47
Aug	8.27	10.51	0.28	1.23	3.89	11.02	31.79
Sep	8.11	9.57	0.38	1.46	4.41	11.13	28.94
Oct	6.00	6.72	0.34	1.31	3.48	8.41	19.76
Nov	5.36	6.47	0.23	1.02	2.87	7.38	18.64

4.2.3 Organic carbon/fine dust

Temporal and spatial variations of organic carbon/fine dust over Africa and Arabian Peninsula are presented in Figures 4.19 and 4.21. The Ångström Exponent presented in Figures 4.20 and 4.22 helps to separate between organic carbon and fine dust cases, for instance, in pure dust regions (northern Africa and Arabian Peninsula with small Ångström Exponent) or pure biomass burning areas (mostly in southern Africa with higher Ångström Exponent). The same, as discussed in 4.1.3 for volume-weighted retrievals, classification of organic carbon and fine dust using Ångström Exponent can be used for retrievals with Maxwell-Garnett model. For example, the particles concentrated in northern Africa are classified as fine dust, especially near the Bodélé depression, because Ångström Exponent in this region is less than 1.0 (Figures 4.20 and 4.22). The particles are classified as a mixture of organic carbon and fine dust near the west coast of Africa from Gabon south to northern Namibia, where the Ångström Exponent changes between 1.0 and 1.2. At the same time, over southern Africa, where Ångström Exponent is usually larger than 1.2, the particles are regarded as organic carbon with high concentration.

Comparisons of retrieved organic carbon and fine dust between volume-weighted (Figures 4.5, 4.6; Tables 4.5, 4.6) and Maxwell-Garnett conversion models (Figures 4.19, 4.21; Tables 4.15, 4.16) show that the organic carbon and fine dust concentration retrieved by volume-weighted model is a bit higher than that retrieved by Maxwell-Garnett model. Specifically, the organic carbon and fine dust concentration retrieved by the Maxwell-Garnett conversion model reaches the peaks in August and September (30.8 mg/mm^2 and 30.4 mg/mm^2, respectively) and the lowest in November (13.8 mg/mm^2). While the organic carbon and fine dust concentration retrieved by the volume-weighted conversion model have the peaks of 38.3 mg/mm^2 and 38.5 mg/mm^2, in the same months, respectively, and the lowest also in November is 17.5 mg/mm^2.

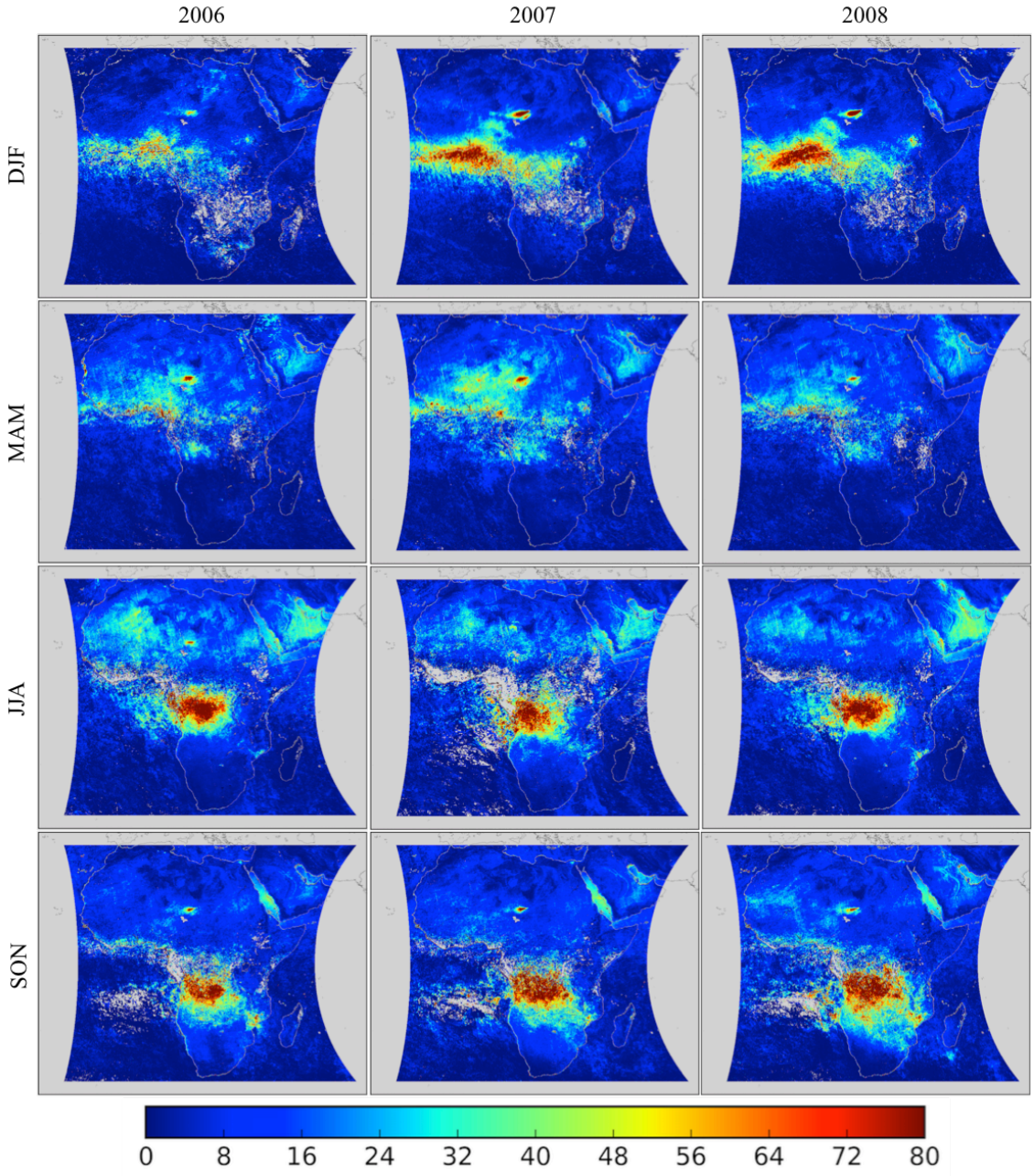

Figure 4.19: Seasonal variations of OC/fine dust columnar volume concentration (mm^3/m^2) over Africa and Arabian Peninsula during the period 2006 – 2008 as retrieved by GRASP algorithm from POLDER/PARASOL satellite observations using the Maxwell-Garnett conversion model.

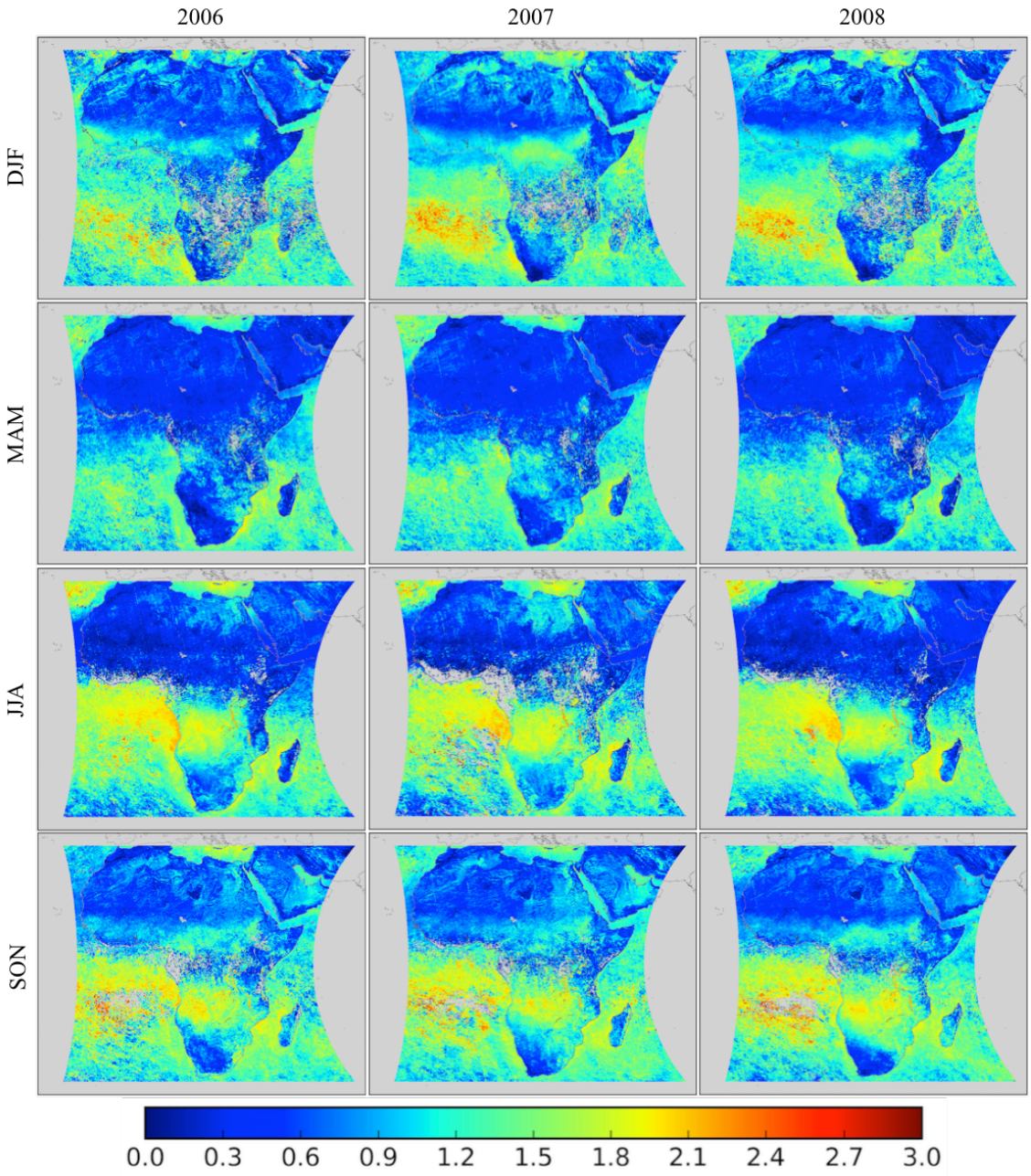

Figure 4.20: Seasonal variations of Ångström Exponent (0.670/0.865 μm) over Africa and Arabian Peninsula during the period 2006 – 2008 as retrieved by GRASP algorithm from POLDER/PARASOL satellite observations using the Maxwell-Garnett conversion model.

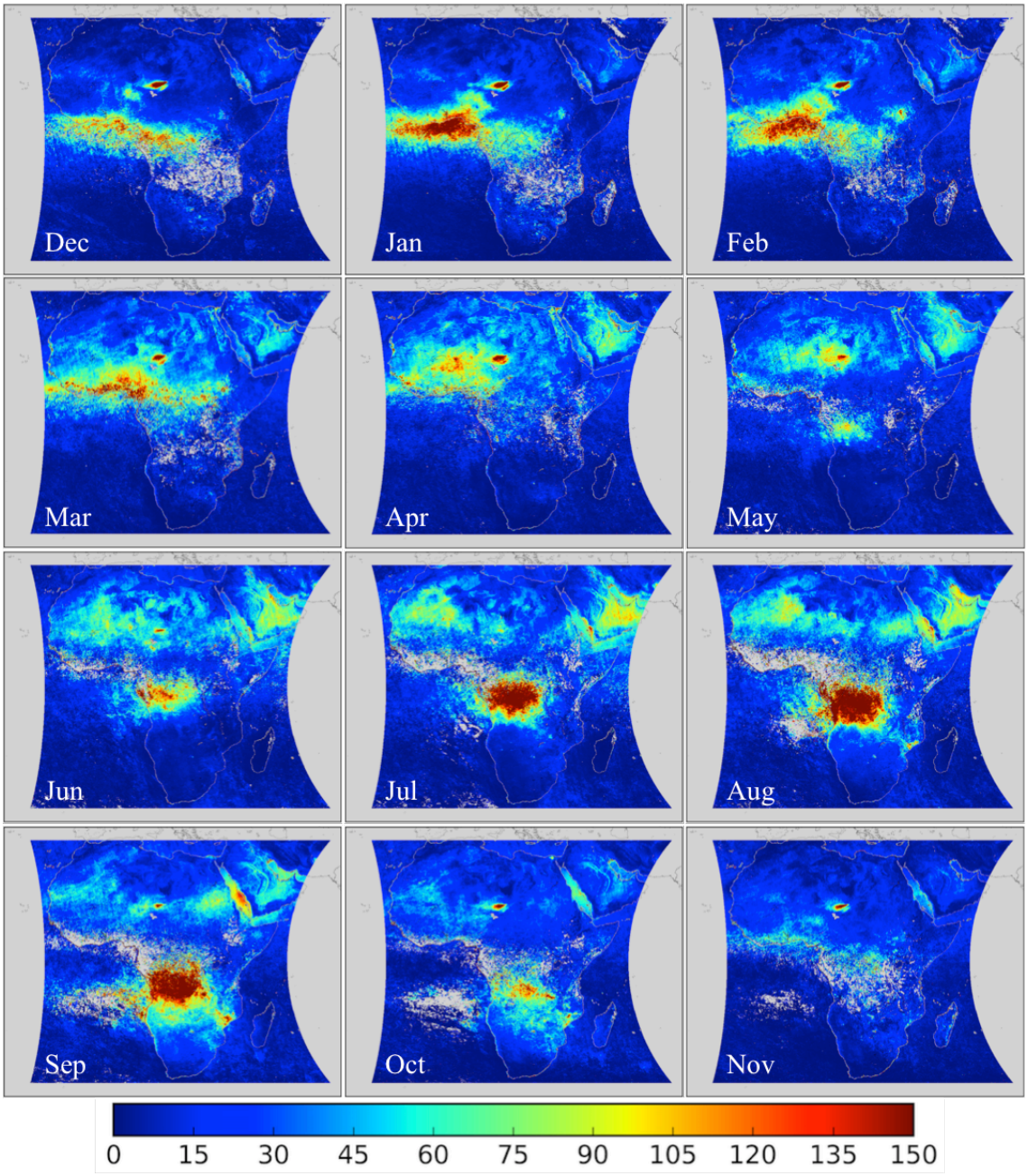

Figure 4.21: Monthly variations of OC/fine dust columnar mass concentration (mg/m^2) over Africa and West Africa averaged over the period 2006 – 2008 as retrieved by GRASP algorithm from POLDER/PARASOL satellite observations using the Maxwell-Garnett conversion model.

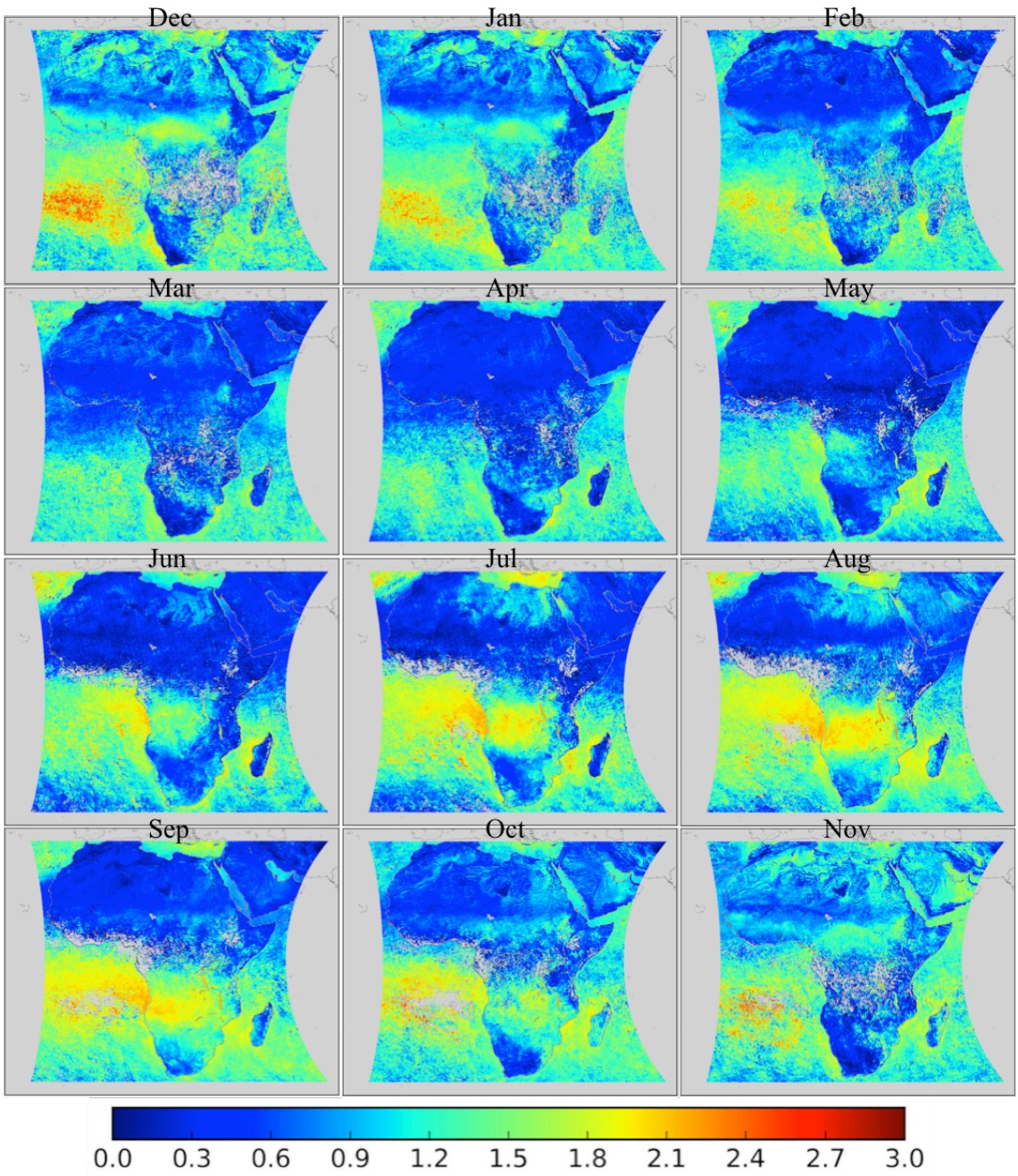

Figure 4.22: Monthly variations of Ångström Exponent (0.670/0.865 μm) over Africa and Arabian Peninsula averaged over the period 2006 – 2008 as retrieved by GRASP algorithm from POLDER/PARASOL satellite observations using the Maxwell-Garnett conversion model.

Table 4.15: Seasonal columnar volume concentration (mm^3/m^2) statistics for OC/fine dust over Africa and Arabian Peninsula during the period 2006 – 2008 as retrieved by GRASP algorithm from POLDER/PARASOL satellite observations using the Maxwell-Garnett conversion model. The percentages (5%, 25%, 50%, 75% and 95%) of the values are determined by ordering the values of the variable from lowest to highest, which indicate the distribution of the variable.

Year	Season	Average	Std	5%	25%	50%	75%	95%
2006	DJF	7.43	12.79	0.16	0.86	3.34	9.16	27.77
	MAM	9.52	13.26	0.31	1.52	5.28	13.63	29.76
	JJA	12.89	15.67	0.48	2.48	7.93	18.31	38.32
	SON	9.69	14.48	0.27	1.75	5.68	11.61	33.93
2007	DJF	10.13	16.28	0.30	1.78	4.72	10.80	41.93
	MAM	11.02	13.63	0.52	2.32	6.76	15.68	33.56
	JJA	12.01	15.67	0.31	2.21	7.06	16.15	38.87
	SON	11.23	16.68	0.39	2.37	6.64	13.07	39.01
2008	DJF	9.67	16.02	0.18	1.20	4.13	10.52	40.40
	MAM	9.40	12.30	0.41	1.84	5.86	13.62	27.27
	JJA	12.10	14.94	0.55	2.66	7.66	15.95	37.75
	SON	13.02	17.77	0.31	2.63	7.78	15.84	46.35

Table 4.16: Monthly columnar mass concentration (mg/m^2) statistics for OC/fine dust over Africa and Arabian Peninsula during the period 2006 – 2008 as retrieved by GRASP algorithm from POLDER/PARASOL satellite observations using the Maxwell-Garnett conversion model. The percentages (5%, 25%, 50%, 75% and 95%) of the values are determined by ordering the values of the variable from lowest to highest, which indicate the distribution of the variable.

Month	Average	Std	5%	25%	50%	75%	95%
Dec	16.88	29.77	0.39	2.51	7.77	18.59	66.57
Jan	20.06	35.98	0.36	2.33	8.08	21.53	84.20
Feb	21.52	36.49	0.36	2.41	9.16	25.70	83.60
Mar	24.48	35.54	0.60	3.28	12.31	33.75	83.83
Apr	24.38	34.15	0.68	3.49	12.92	35.10	78.96
May	20.88	28.86	0.74	3.67	12.00	29.65	66.27
Jun	24.35	32.56	0.75	3.89	13.08	36.45	77.64
Jul	28.22	37.60	0.90	5.02	16.05	39.26	89.92
Aug	30.82	44.31	0.90	5.29	17.07	40.86	99.63
Sep	30.41	40.55	0.91	5.67	18.09	39.85	100.01
Oct	20.60	28.40	0.50	3.99	13.02	27.68	64.47
Nov	13.78	23.93	0.31	2.24	7.43	17.48	45.88

Figure 4.23 shows the mass ratio of BC/(BrC+OC) only over land because low concentrations over ocean make the ratio uncertain. The ratio of BC/(BrC+OC) generated from biomass burning is different for the fires occurring in northern and southern Africa. The ratio is higher for the fires in northern Africa (up to 0.35 in December and January), while it is lower for the fires in southern Africa. Because organic particles dominate in the smoke from both flaming and smoldering fires, while BC particles are present with higher percentage from flaming fires than that from smoldering fires (Kaufman et al., 2002b; Pósfai et al., 2003). In addition, studies by Roessler et al. (1981) demonstrate that the degree of agglomeration and volatile contents of soot particles is determined by the fuel/air ratio. The particles produced at high fuel/air ratios are very agglomerated and contain primarily elemental carbon, whereas particles are less agglomerated and consist of considerable volatile organic material at low fuel/air ratios. Field campaign measurements in southern Africa also show that the average ratio of BC to OC for samples collected in the smoke plumes is lower than that of samples collected in the regional hazes (Kirchstetter et al., 2003), which indicates that the biomass burning in such areas produces less BC, but more OC.

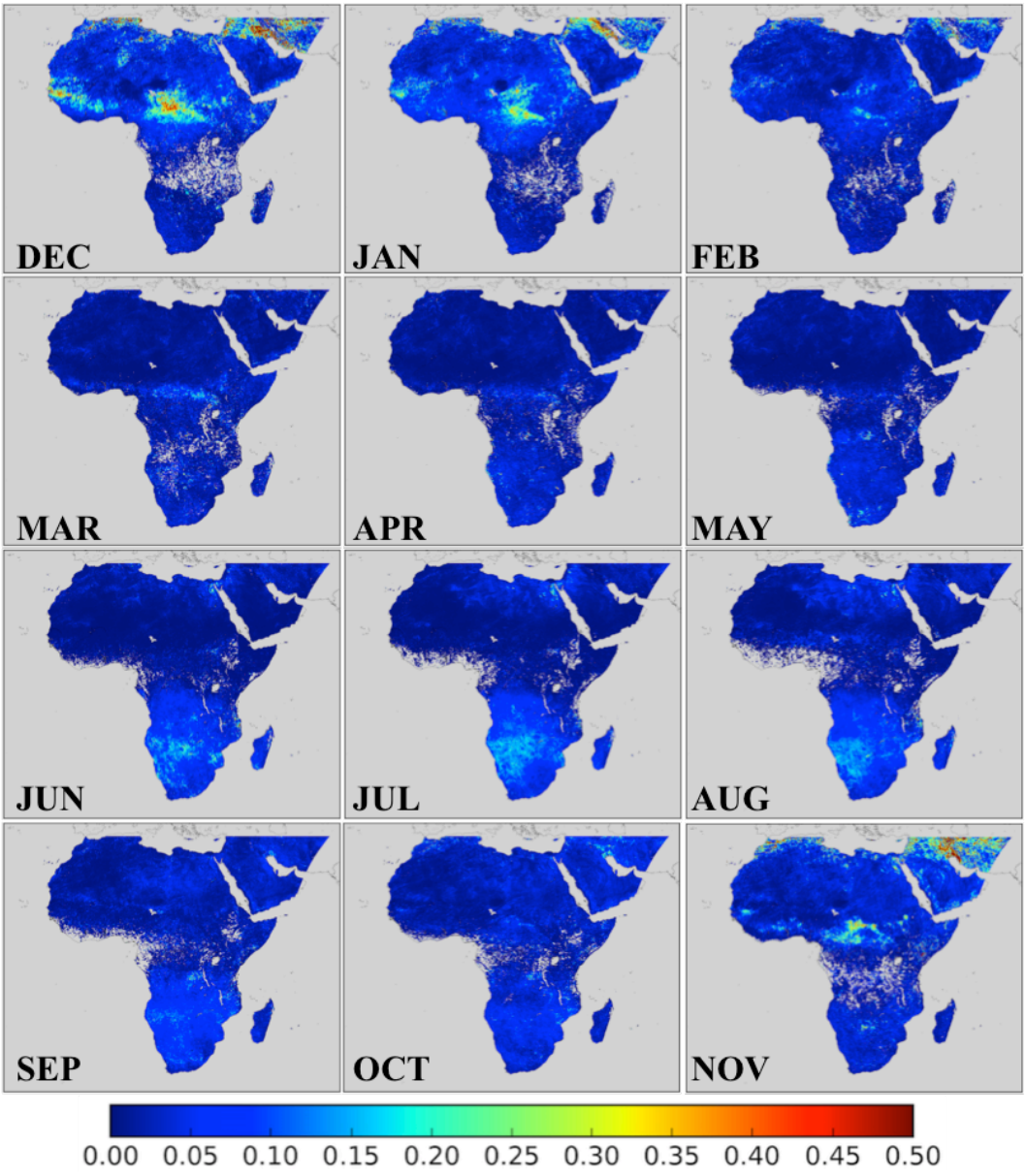

Figure 4.23: Monthly variations of the mass ratio of BC/(BrC+OC) over Africa and Arabian Peninsula retrieved by GRASP algorithm from POLDER/PARASOL satellite observations using the Maxwell-Garnett conversion model.

4.2.4 Coarse dust

The coarse dust retrievals using Maxwell-Garnett conversion model are also similar to the retrievals using volume-weighted conversion model. The coarse dust concentration over Africa and Arabian Peninsula have a pronounced seasonal cycle reaching the peak during MAM, lower values during JJA and DJF, and the lowest during SON (Figures 4.24, 4.25 and Tables 4.17, 4.18). The Maxwell-Garnett retrievals also show a “hot spot” of coarse dust concentration over Bodélé depression throughout the year, as well as high coarse dust concentration over the Arabian Peninsula from April to July.

Comparisons of retrieved coarse dust concentration between volume-weighted (Figures 4.9, 4.10; Tables 4.7, 4.8) and Maxwell-Garnett conversion models (Figures 4.24, 4.25; Tables 4.17, 4.18) show that the coarse dust concentration retrieved by volume-weighted model is practically identical with the retrieved by Maxwell-Garnett model. Namely, the coarse dust concentration retrieved with Maxwell-Garnett reaches a peak of 181 mg/mm^2 in April and a lowest value of 82 mg/mm^2 in November. While the coarse dust concentration retrieved by the volume-weighted conversion model reaches a peak of 193 mg/mm^2 in April and the lowest value of 88 mg/mm^2 in November.

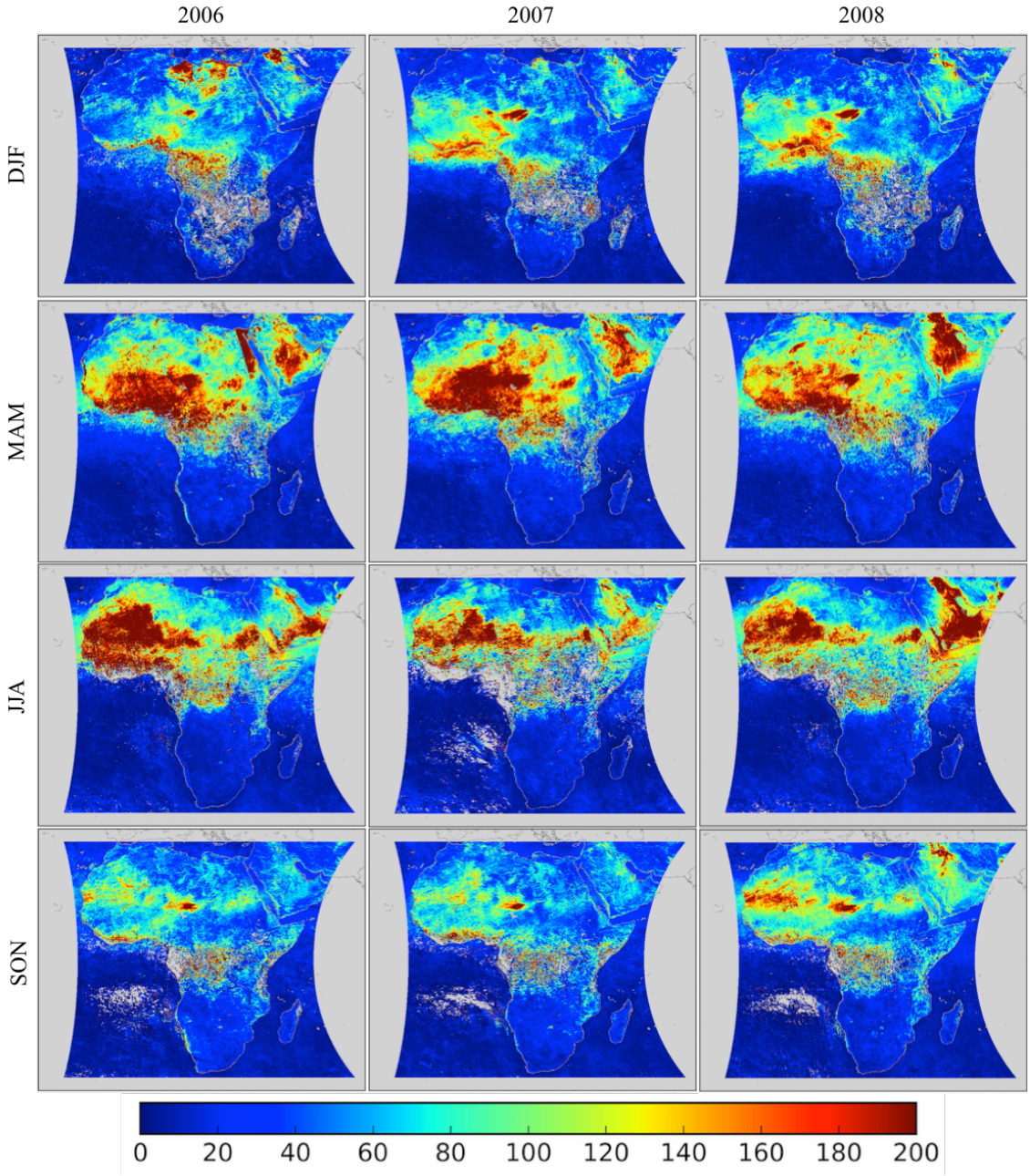

Figure 4.24: Seasonal variations of coarse dust columnar volume concentration (mm^3/m^2) over Africa and Arabian Peninsula during the period 2006 – 2008 as retrieved by GRASP algorithm from POLDER/PARASOL satellite observations using the Maxwell-Garnett conversion model.

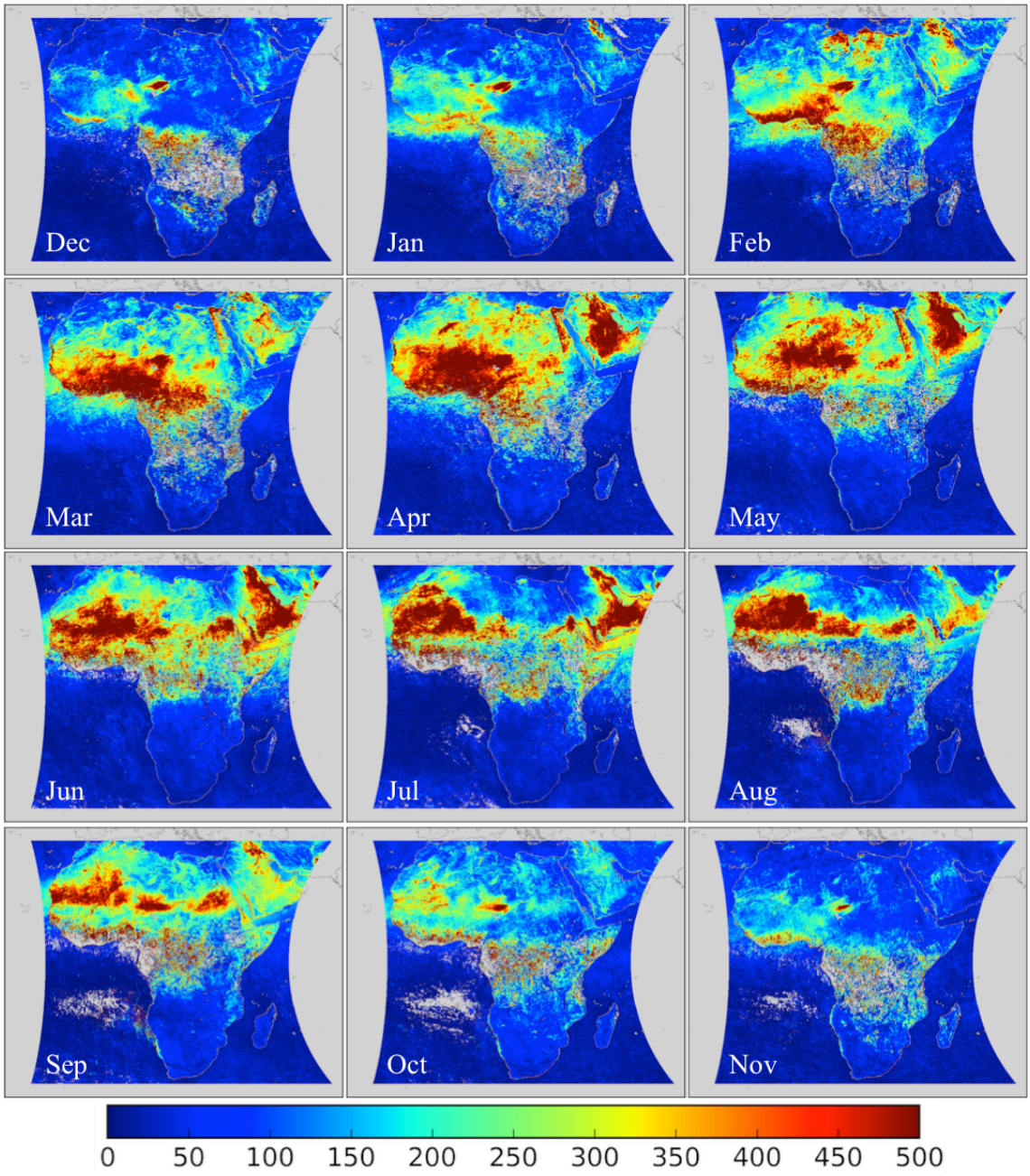

Figure 4.25: Monthly variations of coarse dust columnar mass concentration (mg/m^2) over Africa and Arabian Peninsula averaged over the period 2006 – 2008 as retrieved by GRASP algorithm from POLDER/PARASOL satellite observations using the Maxwell-Garnett conversion model.

Table 4.17: Seasonal columnar volume concentration (mm^3/m^2) statistics for coarse dust over Africa and Arabian Peninsula during the period 2006 – 2008 as retrieved by GRASP algorithm from POLDER/PARASOL satellite observations using the Maxwell-Garnett conversion model. The percentages (5%, 25%, 50%, 75% and 95%) of the values are determined by ordering the values of the variable from lowest to highest, which indicate the distribution of the variable.

Year	Season	Average	Std	5.0%	25%	50%	75%	95%
2006	DJF	45.03	65.61	1.75	7.59	26.11	59.44	148.34
	MAM	66.12	82.78	3.89	10.32	32.70	98.61	211.13
	JJA	62.95	81.66	3.12	8.83	24.66	93.08	226.22
	SON	40.77	52.25	2.34	9.25	28.35	56.42	112.58
2007	DJF	44.84	60.60	2.49	9.18	27.15	60.79	137.27
	MAM	66.32	74.51	5.04	12.09	36.70	101.43	209.62
	JJA	52.98	72.32	1.83	8.43	22.17	75.71	184.75
	SON	39.50	50.77	2.79	8.79	25.47	55.45	110.94
2008	DJF	46.96	62.03	2.44	8.20	30.84	64.41	143.88
	MAM	65.10	71.86	5.06	12.04	38.63	100.23	193.69
	JJA	61.02	76.13	3.65	9.41	25.75	91.50	209.11
	SON	46.35	55.05	2.55	9.07	28.10	69.26	136.14

Table 4.18: Monthly columnar mass concentration (mg/m^2) statistics for coarse dust over Africa and during the period 2006 – 2008 as retrieved by GRASP algorithm from POLDER/PARASOL satellite observations using the Maxwell-Garnett conversion model. The percentages (5%, 25%, 50%, 75% and 95%) of the values are determined by ordering the values of the variable from lowest to highest, which indicate the distribution of the variable.

Month	Average	Std	5%	25%	50%	75%	95%
Dec	85.27	145.78	2.34	17.07	48.79	103.15	265.23
Jan	102.70	161.75	2.93	18.25	56.87	127.11	347.44
Feb	141.66	191.28	2.63	18.99	81.88	200.33	460.74
Mar	158.53	201.32	4.89	24.23	86.88	221.86	531.96
Apr	181.39	229.25	6.57	24.47	87.50	271.38	604.46
May	164.29	209.68	8.03	26.62	75.88	246.34	538.65
Jun	167.32	223.45	5.92	23.32	71.33	245.33	580.98
Jul	150.87	213.43	4.02	19.93	58.22	208.90	567.50
Aug	133.29	201.48	2.51	17.72	49.57	173.29	518.06
Sep	139.34	182.23	2.68	20.25	69.92	206.62	453.87
Oct	109.90	150.29	4.23	22.52	67.87	147.01	334.41
Nov	82.08	128.00	3.63	20.06	48.46	103.59	244.66

4.2.5 Iron oxide

Figures 4.26 and 4.27 show spatial distribution and temporal variability of iron oxide retrieved by the Maxwell-Garnett conversion model. As for all other elements, for iron oxide there is also a close similarity in temporal and spatial patterns retrieved by Maxwell-Garnett and volume-weighted conversion model. Iron oxide concentration reaches a peak during MAM, lower values during JJA and DJF, and the lowest during SON (Figure 4.26 and Table 4.19). However, comparison of the concentrations values show (volume-weighted in Figures 4.11, 4.12, and Tables 4.9, 4.10 and Maxwell-Garnett in Figures 4.26, 4.27 and Tables 4.19, 4.20) that the maximal iron oxide concentration retrieved with volume-weighted model is less than that retrieved with Maxwell-Garnett. Specifically, the iron oxide concentration retrieved with Maxwell-Garnett conversion model reaches a peak in April with the value of 4.9 mg/mm^2 and the lowest in December with the value of 1.6 mg/mm^2 (Table 4.20). While the iron oxide concentration retrieved with volume-weighted conversion model reaches a peak in March with the value of 2.7 mg/mm^2 and the lowest in December with the value of 1.4 mg/mm^2 (Table 4.10).

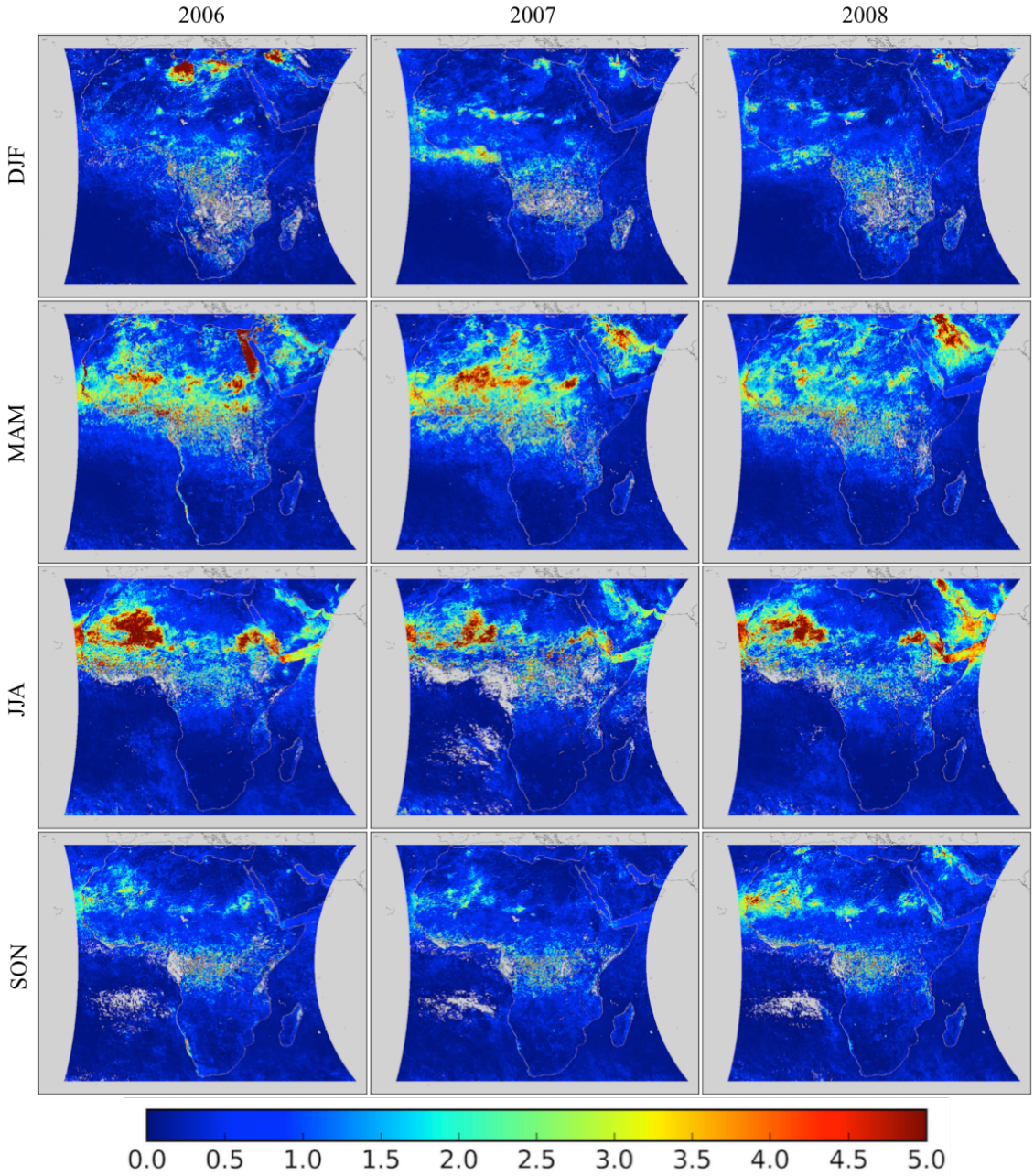

Figure 4.26: Seasonal variations of iron oxide columnar volume concentration (mm^3/m^2) over Africa and Arabian Peninsula during the period 2006 – 2008 as retrieved by GRASP algorithm from POLDER/PARASOL satellite observations using the Maxwell-Garnett conversion model.

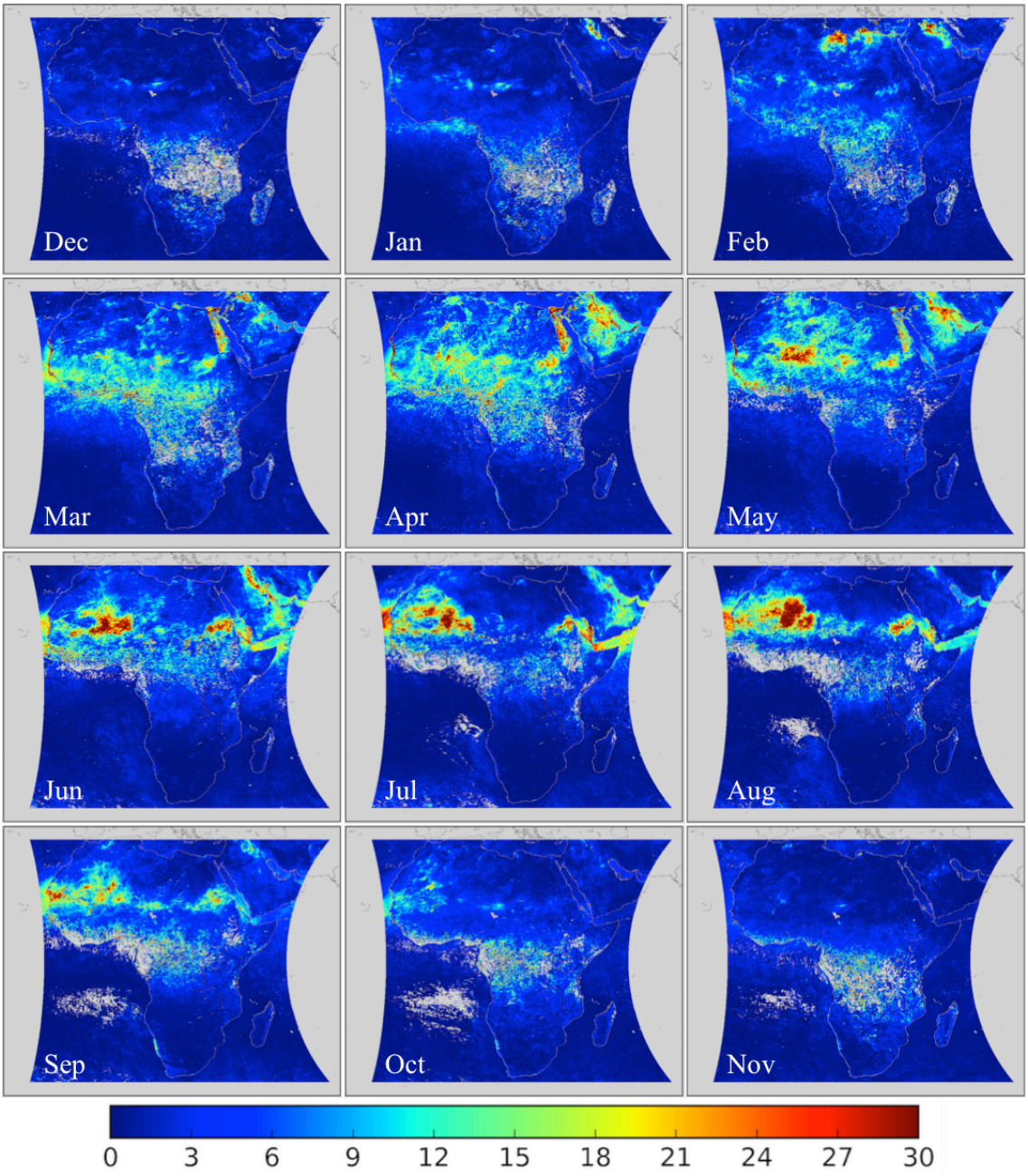

Figure 4.27: Monthly variations of iron oxide columnar mass concentration (mg/m^2) over Africa and Arabian Peninsula averaged over the period 2006 – 2008 as retrieved by GRASP algorithm from POLDER/PARASOL satellite observations using the Maxwell-Garnett conversion model.

Table 4.19: Seasonal columnar volume concentration (mm^3/m^2) statistics for iron oxide over Africa and Arabian Peninsula during the period 2006 – 2008 as retrieved by GRASP algorithm from POLDER/PARASOL satellite observations using the Maxwell-Garnett conversion model. The percentages (5%, 25%, 50%, 75% and 95%) of the values are determined by ordering the values of the variable from lowest to highest, which indicate the distribution of the variable.

Year	Season	Average	Std	5%	25%	50%	75%	95%
2006	DJF	0.57	0.99	0.02	0.08	0.23	0.65	2.11
	MAM	0.99	1.70	0.05	0.15	0.41	1.27	3.41
	JJA	0.84	1.29	0.03	0.11	0.32	0.97	3.56
	SON	0.47	0.63	0.03	0.11	0.24	0.59	1.62
2007	DJF	0.50	0.72	0.03	0.10	0.24	0.62	1.79
	MAM	0.95	1.18	0.05	0.15	0.43	1.35	3.40
	JJA	0.74	1.16	0.02	0.10	0.28	0.86	3.04
	SON	0.41	0.58	0.04	0.11	0.22	0.49	1.41
2008	DJF	0.48	0.68	0.03	0.09	0.25	0.60	1.64
	MAM	0.87	1.02	0.05	0.15	0.48	1.27	2.84
	JJA	0.81	1.19	0.03	0.12	0.31	0.95	3.41
	SON	0.55	0.72	0.03	0.12	0.28	0.69	1.93

Table 4.20: Monthly columnar mass concentration (mg/m^2) statistics for iron oxide over Africa and Arabian Peninsula during the period 2006 – 2008 as retrieved by GRASP algorithm from POLDER/PARASOL satellite observations using the Maxwell-Garnett conversion model. The percentages (5%, 25%, 50%, 75% and 95%) of the values are determined by ordering the values of the variable from lowest to highest, which indicate the distribution of the variable.

Month	Average	Std	5%	25%	50%	75%	95%
Dec	1.57	3.01	0.05	0.28	0.67	1.67	5.64
Jan	2.07	3.76	0.07	0.33	0.81	2.23	8.07
Feb	3.15	5.51	0.07	0.39	1.26	3.85	11.65
Mar	4.34	6.94	0.11	0.55	1.76	5.47	16.53
Apr	4.92	7.68	0.14	0.57	1.97	6.58	18.34
May	4.52	7.24	0.14	0.60	1.82	5.63	17.50
Jun	4.32	6.95	0.12	0.55	1.58	4.88	18.33
Jul	3.81	6.62	0.09	0.40	1.21	3.96	17.31
Aug	3.49	6.39	0.07	0.34	1.05	3.39	16.25
Sep	3.22	5.12	0.08	0.42	1.18	3.79	13.26
Oct	2.31	3.60	0.11	0.47	1.08	2.59	8.77
Nov	1.71	3.02	0.09	0.34	0.77	1.80	6.37

Figure 4.28 shows the ratio of iron oxides to coarse mode dust over Africa and Arabian Peninsula retrieved by GRASP using Maxwell-Garnett conversion model. The ratio of iron oxides to dust depends on the soil mineralogy of the source region. The mass ratio is up to about 5% over the dust region, which is consistent with literature. In addition, it has to be mentioned here that there are some limitations. The ratio of iron oxides to coarse mode dust is high over southern Africa. Because iron oxide is the only strongly absorbing component considered in the coarse mode of the used here composition conversion model. Therefore, any other large size strongly absorbing aerosol will be interpreted as iron oxide. This will be the case if, for example, black or BrC, will appear in the coarse mode. At the same time, some studies, e.g., Luo et al. (2008), consider that iron can exist in combustion aerosol (industry, biofuels and even biomass burning) and may even account for 50% of the global iron deposition budget. Guieu et al. (2005), for example, show based on experimental iron solubility measurement, that biomass burning may produce an important input of iron to the Mediterranean Sea and differ from the Saharan dust input. Thus, a certain amount of iron over the biomass burning regions can be real.

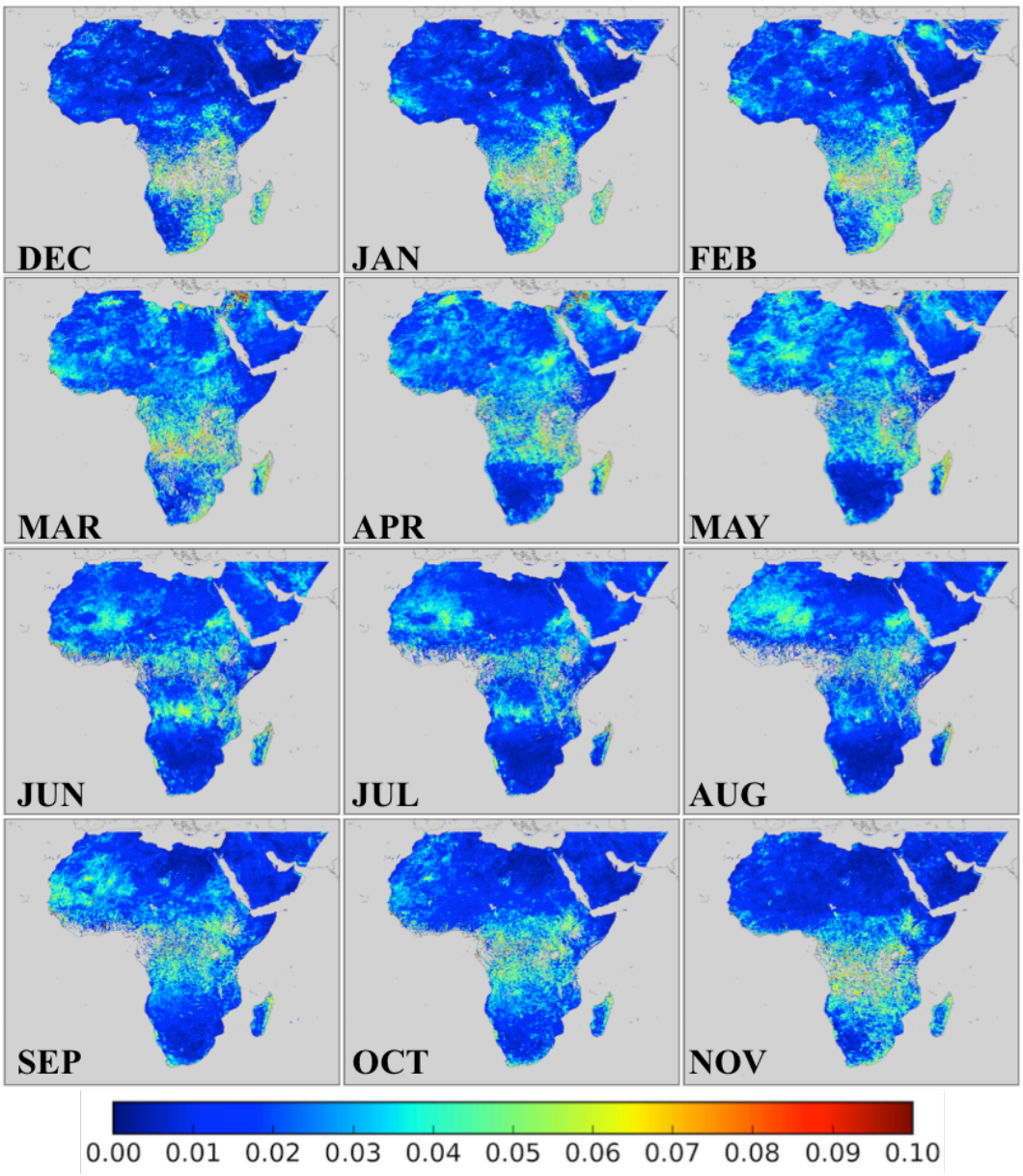

Figure 4.28: Monthly variations of the mass ratio of iron oxide/dust over Africa and Arabian Peninsula averaged as retrieved by GRASP algorithm from POLDER/PARASOL satellite observations using the Maxwell-Garnett conversion model.

4.2.6 Aerosol water content and ammonium nitrate

The volume concentrations of aerosol water content retrieved using the Maxwell-Garnett conversion model (Figures 4.29 and 4.30) generally present the same tendencies as the retrievals with the volume-weighted conversion model (discussed in 4.1.6). However, it can be noted that the aerosol water content concentrations retrieved by Maxwell-Garnett conversion model are somewhat smaller than that retrieved by the volume-weighted conversion model (Figures 4.13 and 4.14). This is due to presence of ammonium nitrate in

Maxwell-Garnett conversion model as an addition to water content element that represents the inorganic species including ammonium sulfate and sea salt.

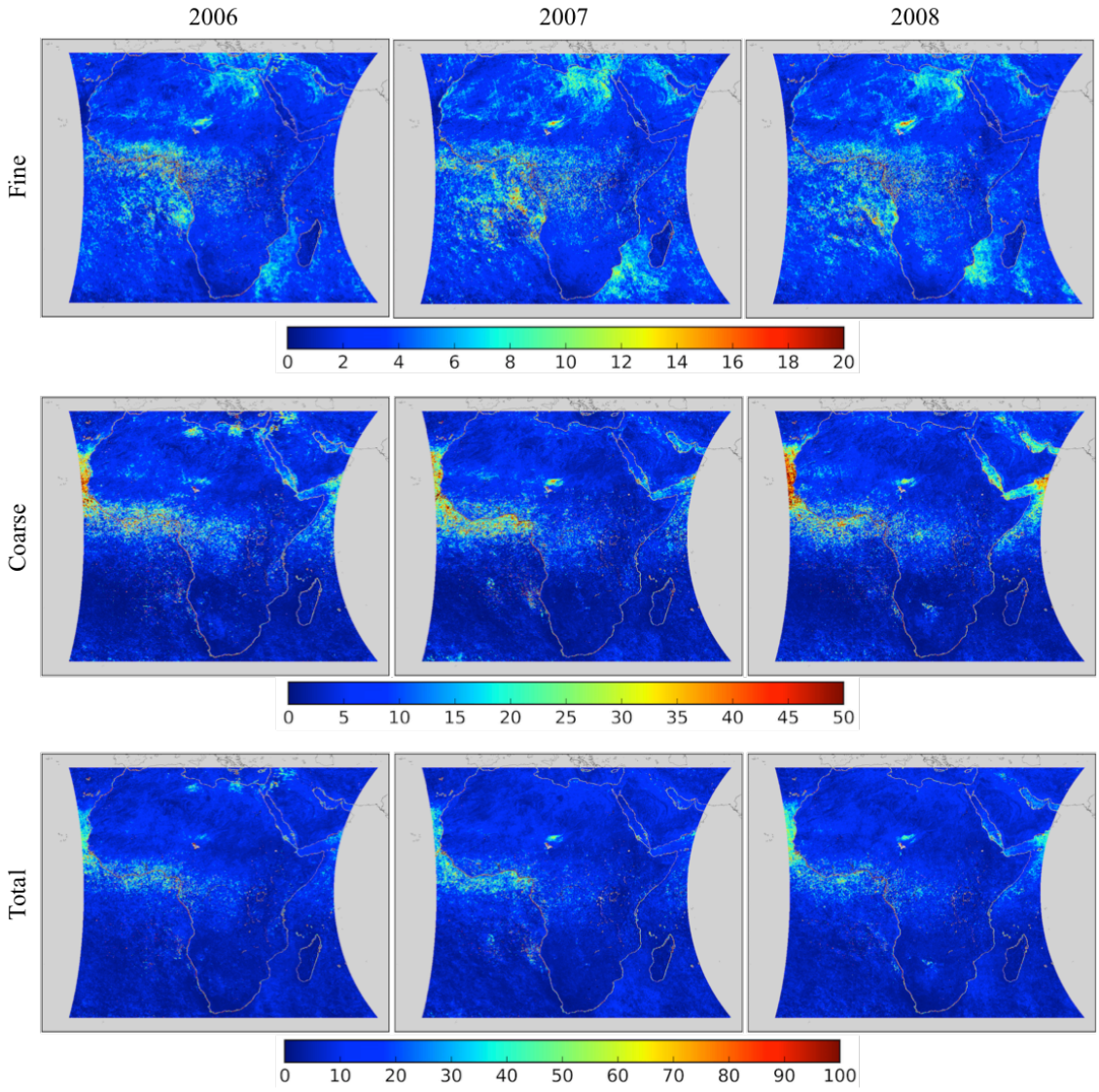

Figure 4.29: Interannual variations of water columnar volume concentration (mm^3/m^2) (fine mode, coarse mode and total) over Africa and Arabian Peninsula during the period 2006 – 2008 as retrieved by GRASP algorithm from POLDER/PARASOL satellite observations using the Maxwell-Garnett conversion model.

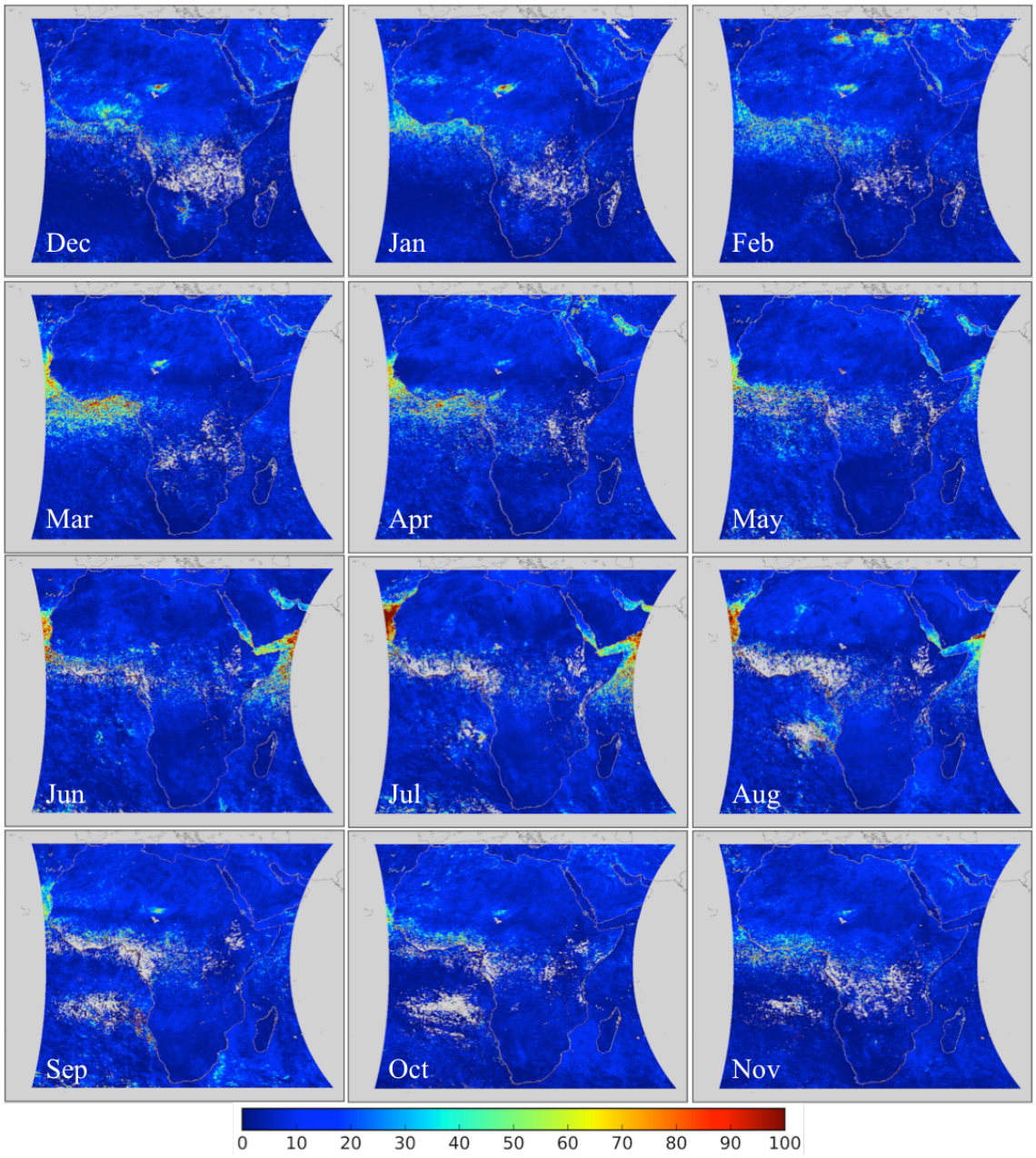

Figure 4.30: Monthly variations of total water columnar mass concentration (mg/m^2) over Africa and Arabian Peninsula averaged over the period 2006 – 2008 as retrieved by GRASP algorithm from POLDER/PARASOL satellite observations using the Maxwell-Garnett conversion model.

Figures 4.30 and 4.31 present the variations of ammonium nitrate volume concentration in fine and coarse modes, and total over Africa and Arabian Peninsula. It can be seen that the coarse mode ammonium nitrate volume concentration is rather larger over ocean than that over land, which can be predominately attributed to higher sea salt and relative humidity over ocean.

Comparisons of ammonium nitrate (Figure 4.31) with black carbon (Figure 4.16) and organic carbon (Figure 4.21) show that the distributions of these three compositions have similar spatial variations. The retrievals have good agreement with the study of Pósfai et al. (2003) that reports inorganic particles (e.g., ammonium sulfate) mixtures with organic and soot particles originated from biomass burning. The smoke particles seem to provide a favorable surface for the nucleation of sulfate, and coagulation can also bring soot and sulfate together. In addition, higher ammonium nitrate concentration is retrieved over southern Africa (Figure 4.32), especially in August and September. This is in line, for example, with (Piketh et al., 1999a) that reported a significant contribution of inorganic particles (such as, sulfur) derived from the burning of fossil fuels to the total aerosol loading over South Africa.

The nitrate formation on dust particles can result from the interaction with HNO_3 (Putaud et al., 2004; Koçak et al., 2007). An enrichment of sulfate and nitrate on dust particles can also occurs in marine environment and is associated with high humidity. The formation of thin water films on the surface or partial deliquescence (i.e., deliquescence of the soluble fraction contained in agglomerates) makes dust particles become wetted. More efficient transformation of sulfur dioxide to sulfate and nitrogen oxides to nitrate is attributed to the presence of liquid water. The nitrate formation on dust particles occurs even when the relative humidity is low (Putaud et al., 2004). Formation of sulfate and nitrate is also affected by the mineral composition. Previous studies (Ro et al., 2005; Sullivan et al., 2007; Matsuki et al., 2010; Fairlie et al., 2010) have indicated that nitrate formation is favoured on calcium carbonate particles compared to aluminium silicate, whereas the opposite behavior is observed for sulfate formation (Krueger et al., 2003; Laskin et al., 2005; Shi et al., 2008). In the present retrievals in Figures 4.31 and 4.32 it can be seen that some ammonium nitrate concentration appear in regions associated with dust. This indeed can be due to a lack of sensitivity and limitation of the algorithm. At the same time, as the above mentioned studies report, association of nitrate with dust is possible. A further validation and understanding of these retrievals thus will be needed.

Note that the ammonium nitrate columnar volume concentration (mm^3/m^2), which is directly retrieved by the algorithm, was converted to columnar mass concentration (mg/m^2) using the density value of 1.73 g/cm^3 (Tang, 1996)

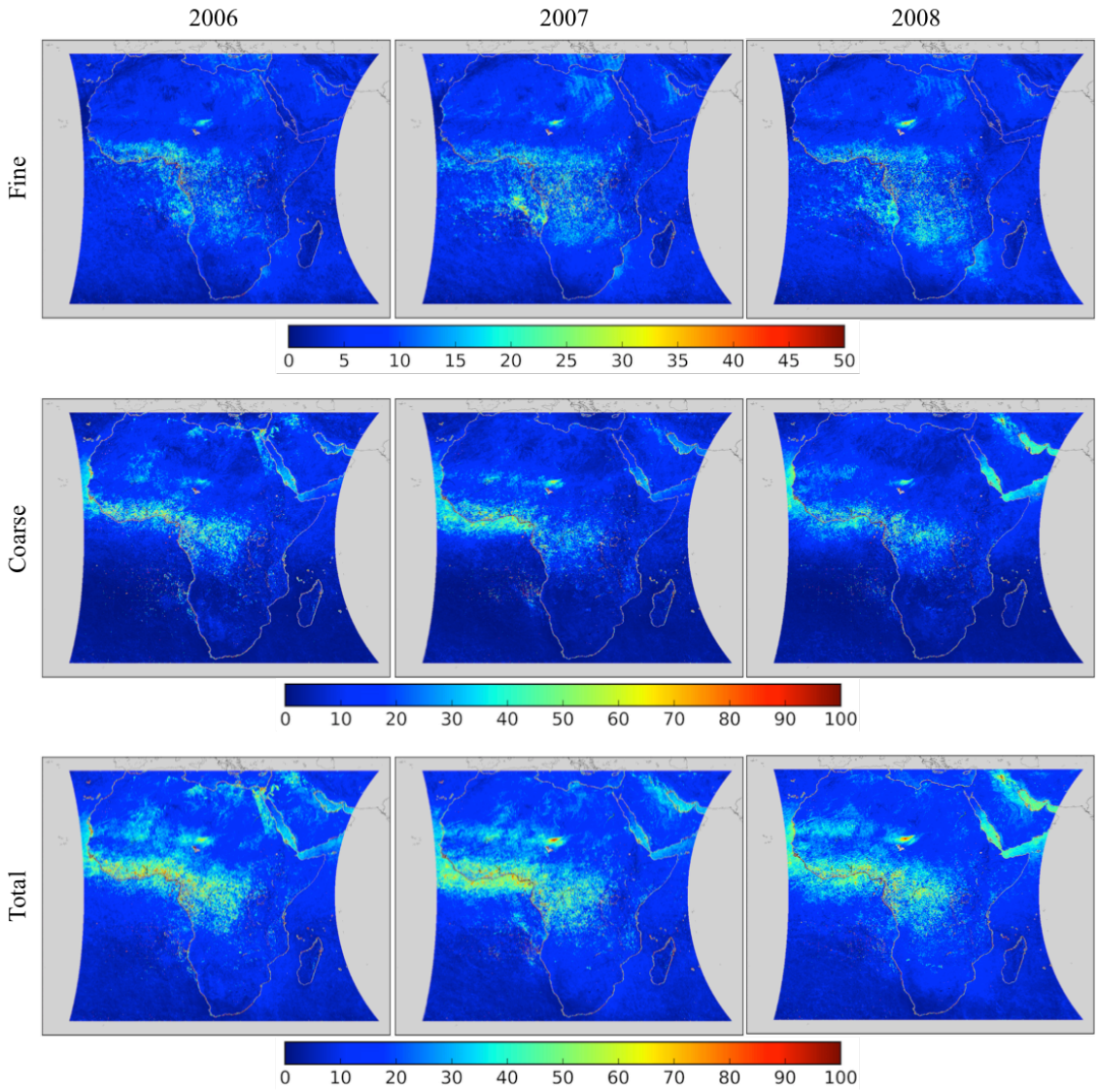

Figure 4.31: Interannual variations of ammonium nitrate columnar volume concentration (mm^3/m^2) (fine mode, coarse mode and total) over Africa and Arabian Peninsula during the period 2006 – 2008 as retrieved by GRASP algorithm from POLDER/PARASOL satellite observations using the Maxwell-Garnett conversion model.

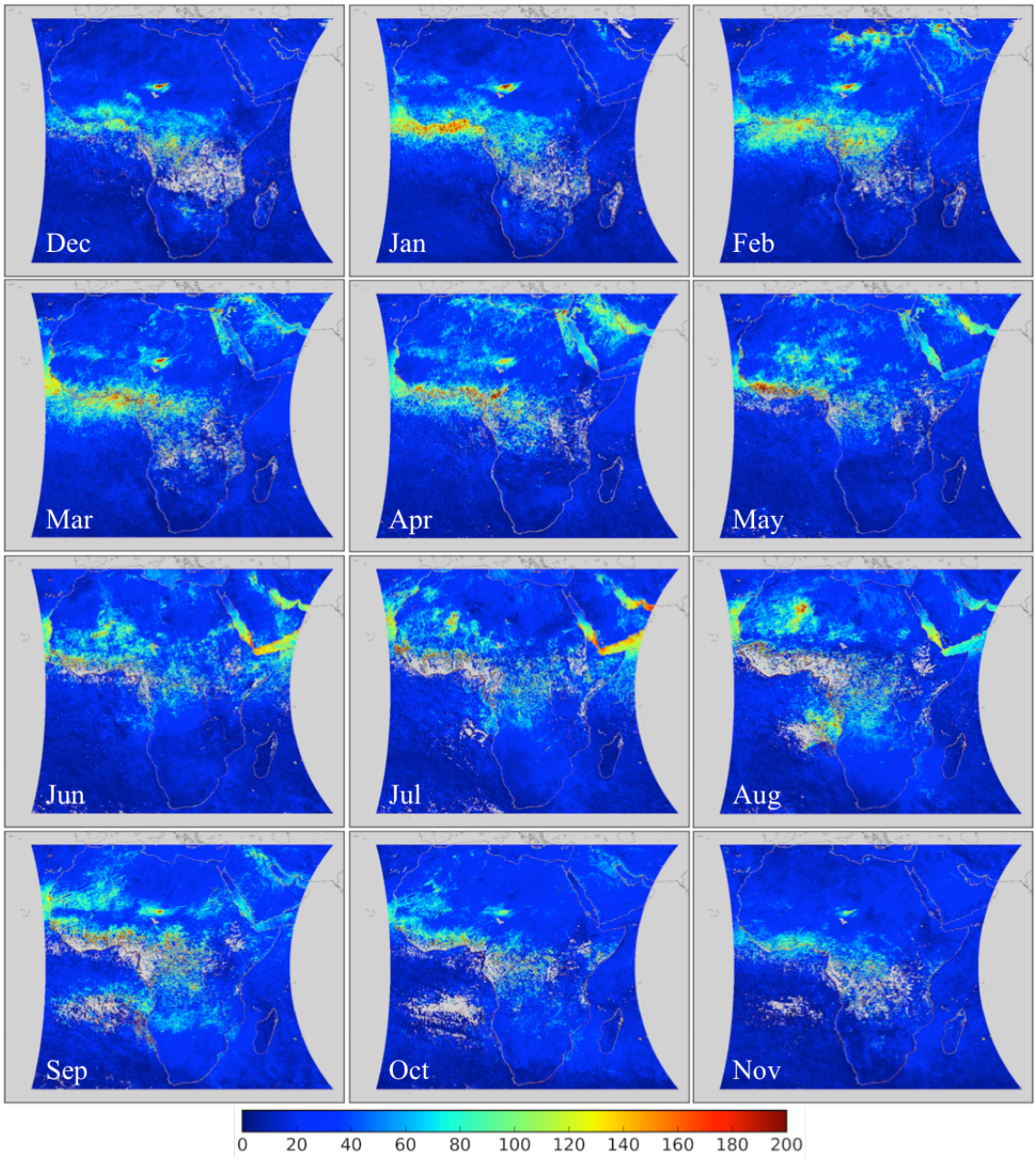

Figure 4.32: Monthly variations of total ammonium nitrate columnar mass concentration (mg/m^2) over Africa and Arabian Peninsula averaged over the period 2006 – 2008 as retrieved by GRASP algorithm from POLDER/PARASOL satellite observations using the Maxwell-Garnett conversion model.

4.3 Validation

4.3.1 Validation of aerosol optical property

The ground-based network of Sun/sky photometers – AERONET, which provides column-integrated aerosol optical properties at 8 wavelengths from 0.340 to 1.020 μm, plays a pivotal role for satellite validation. The AERONET data are especially useful as they provide comprehensive measurements of aerosol properties including AOT, Ångström Exponent and single-scattering albedo (Holben et al., 2001; Dubovik et al., 2002a). Data from AERONET measurements have been used for satellite and model validation (Kinne et al., 2001; Torres et al., 2002; Zhao et al., 2002). Figure 4.33 shows an inter-comparison of aerosol optical properties retrieved from POLDER/PARASOL observations using the composition conversion model with AERONET retrievals products at 6 sites in Africa during the period of 2006 to 2008. Because of a limited sensitivity to absorption when aerosol loading is low, single-scattering albedo is retrieved with sufficiently high accuracy only when the AOT at 0.440 μm is equal or higher than 0.4 and solar zenith angle is 50 degree or higher (Dubovik et al., 2000, 2002a). Therefore, the retrieved values of single-scattering albedo are much less available than the direct to Sun measurements and limited by the conditions of relatively high aerosol loading. Nevertheless, the comparisons shown in Figure 4.33 revealed the similarities and differences in three key parameters, such as AOT, Ångström Exponent and single-scattering albedo between AERONET and GRASP with composition module retrieval. Note that the data on Ångström Exponent and single-scattering albedo for all sites are presented in the same panels to increase the number of points and dynamic range. The results obtained from POLDER observations demonstrate good agreement with the AERONET data (e.g., R of ~ 0.95 for AOT and Ångström Exponent). Moreover, inversions of GRASP composition approaches (Maxwell-Garnett and volume-weighted) have even better agreement with AERONET data than the inversions with the classical approach, when complex refractive index is retrieved directly. This may be attributed to a better constraint of the retrievals by predefined spectral dependence of refractive index attributed to each of the aerosol composition. The composition approach also reduces the number of retrieved parameters, that is, instead of real and imaginary part of refractive index for each wavelength, fractions of elements are retrieved. For example, in the classical approach, there are 12 parameters for real and imaginary refractive index, while in the composition approach there are only 6 or 7 parameters for aerosol composition fraction in fine and coarse modes.

The inter-comparison, however, should be interpreted with caution because the AERONET data are from a point measurements and cannot always be representative of a satellite pixel

that is usually in a spatial scale of several kilometers resolution. Another and main limitation of this inter-comparison is that the retrieved aerosol composition is not validated directly, but only indirectly – by means of agreement between in the derived optical characteristics. Nonetheless, the comprehensive AERONET dataset provides a wide range of constraints to check the satellite inversion.

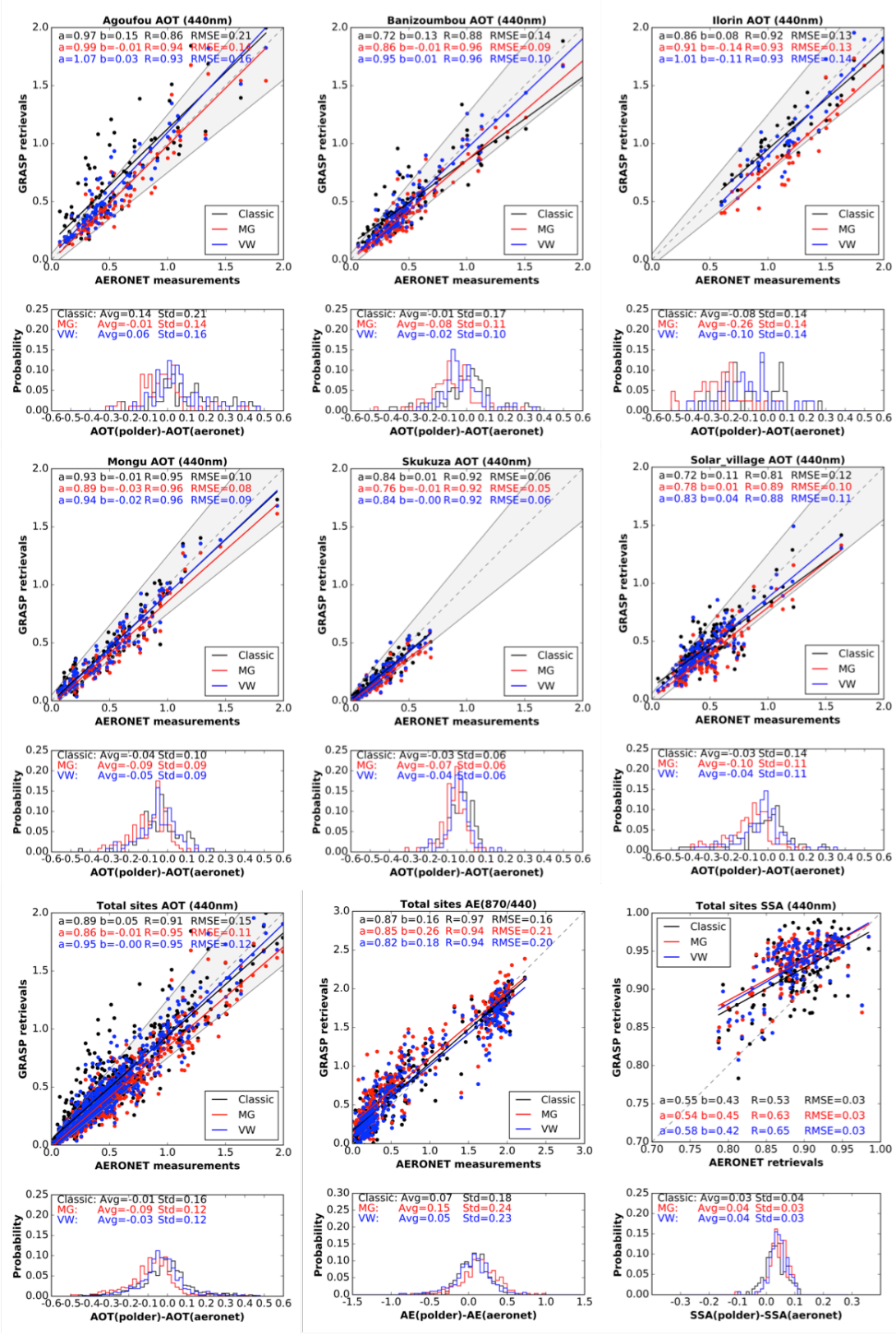

Figure 4.33: The inter-comparison of aerosol property parameters retrieved from POLDER/PARASOL during the period of 2006 to 2008 at 6 AERONET sites with the corresponding values provided by AERONET measurements. “Classic” denotes the previous approach of GRASP without aerosol composition retrieval, “MG” denotes the approach of Maxwell-Garnett conversion model, and “VW” denotes the approach of volume-weighted conversion model.

4.3.2 Comparison of composition retrieval with situ measurement

Validation of the inverted aerosol composition by in situ measurements should be most valid. However, this validation is not evident because in situ data are measured near the ground, while the retrievals obtained from satellite represent the total atmospheric column values. In addition, in situ data are for point measurements, thus may not always be representative of the satellite pixel that is usually in a large spatial scale and may not coincide temporally. Nevertheless, an effort was done on revision and extracting of appropriate field campaigns in situ data from literature. Figure 4.34 shows an inter-comparison of the retrieved BC concentration with measurements from field campaigns. DABEX is the Dust And Biomass EXperiment campaign dedicated to investigate the radiative effects and transport of dust and biomass aerosols emitted from the Sahara/Sahel regions of Africa (Hand et al., 2010). The BC was measured by a Single Wavelength Particle Soot Absorption Photometer assuming a mass absorption efficiency of 12 m^2/g on the day of 17, 19, 28 January and 7 February 2006. It coincides with the PARASOL measurements on the day of 19 and 28 January 2006. The BC mass concentration was measured by the AE30 Aethalometer with a Magee Scientific Model during AMMA (African Monsoon Multi-disciplinary Analysis) SOP-0 (the Special Observing Period conducted during January – February 2006) (Deboudt et al., 2010). In order to compare the retrieved values with the in situ measurements, an assumption of 3 km was done on the height of the aerosol layer (Labonne et al., 2007). The retrieved aerosol volume concentration was converted into surface mass concentration using this height of the aerosol layer and the BC density of 1.8 g/cm^3 (Park et al., 2004; Bond and Bergstrom, 2006). Note that the same aerosol layer height was systematically used for the inter-comparison purposes, thus an uncertainty in this assumption can affect the absolute values in the inter-comparison, but not the slope of the regression line. Because the in situ measurements are conducted during short periods and considering possible cloud coverage, the available data that can be matched with temporal and spatial scale are scarce. The limited available data shows, however, that the satellite retrieved and the in situ BC concentration values are in a reasonably good agreement.

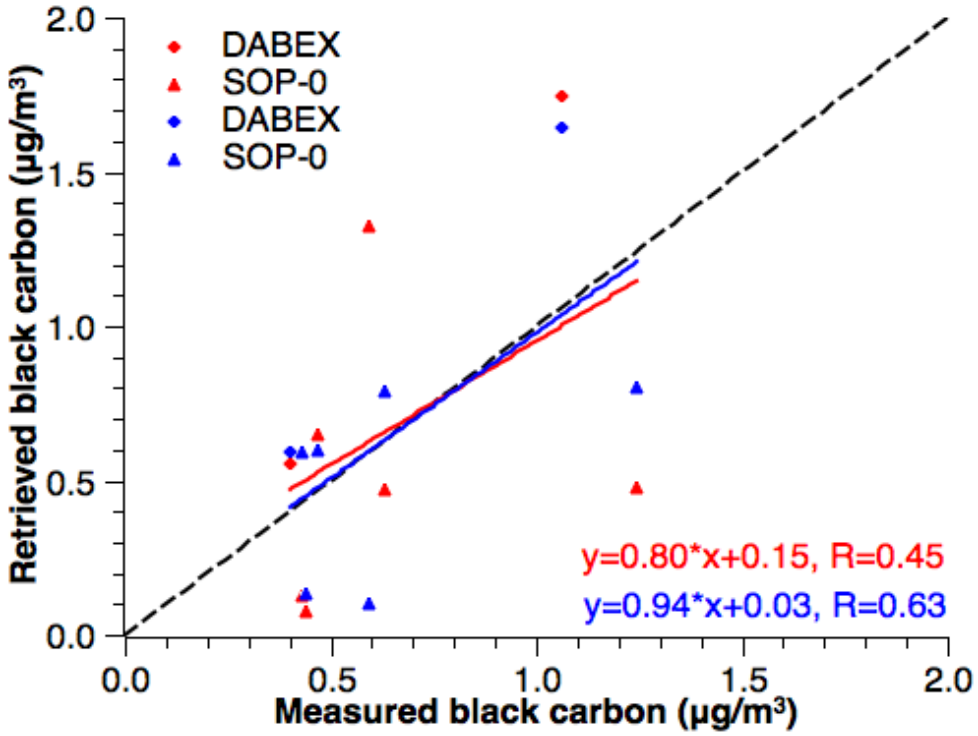

Figure 4.34: The comparison of BC mass concentration retrieved from POLDER/PARASOL with the corresponding values measured in two field campaigns: DABEX (Hand et al., 2010) and during AMMA SOP-0 (Deboudt et al., 2010). Red color denotes the mass concentration retrieved from the Maxwell-Garnett conversion model and blue color denotes the mass concentration retrieved from the volume-weighted conversion model.

Figure 4.35 shows an inter-comparison of retrieved BC concentration with one observed by aircraft from HIAPER (High-Performance Instrumented Airborne Platform for Environment Research) Pole-to-Pole Observations (HIPPO) deployments over the remote Pacific from 85°N to 67°S in 2009 – 2011. Five deployments were conducted over the 2009 – 2011 period and BC concentration was measured by a single-particle soot photometer (SP2) instrument (Schwarz, et al., 2010; Schwarz et al., 2013). The HIAPER HIPPO aircraft program (Wofsy et al., 2011) involved near continuous vertical profiling by the HIAPER aircraft from the surface to 8 km (with occasional forays to 14 km altitude) over the Pacific from 85°N to 67°S. In the Arctic, BC concentration tends to increase with altitude in spring and autumn, but peaks near the surface in winter when transport from midlatitudes takes place at low altitudes. Tropical concentrations are generally highest near the surface because of scavenging by deep convection. Because of obvious variations of BC concentration at different altitude levels, the average values of BC concentration are calculated by the aircraft measurements for three different altitude groups: H=500, 1000, and 5000 m.

The correlations shown in Figure 4.35 indicate that the retrieved BC concentration (Maxwell-Garnett and volume-weighted conversion model) has a reasonable agreement with

campaign measured BC concentration, which are the averaged values calculated from the available data under the height of 500 and 1000 m, respectively. However, there is no correlation for the case of H=5000 m; the retrieved values are much higher than the measured, which can be explained by very low values at high altitudes. No assumption on the aerosol layer height was done for conversion of the column satellite data in this case. Therefor, disagreement between the data sets, in case of 5000 m altitude, is rather effect of aerosol vertical distribution. In addition, the measurements of BC during the HIPPO campaign over ocean have very low values. Indeed, the AOT is low over the Pacific from 85°N to 67°S, which can also cause more uncertainty in the retrievals from POLDER/PARASOL satellite observations.

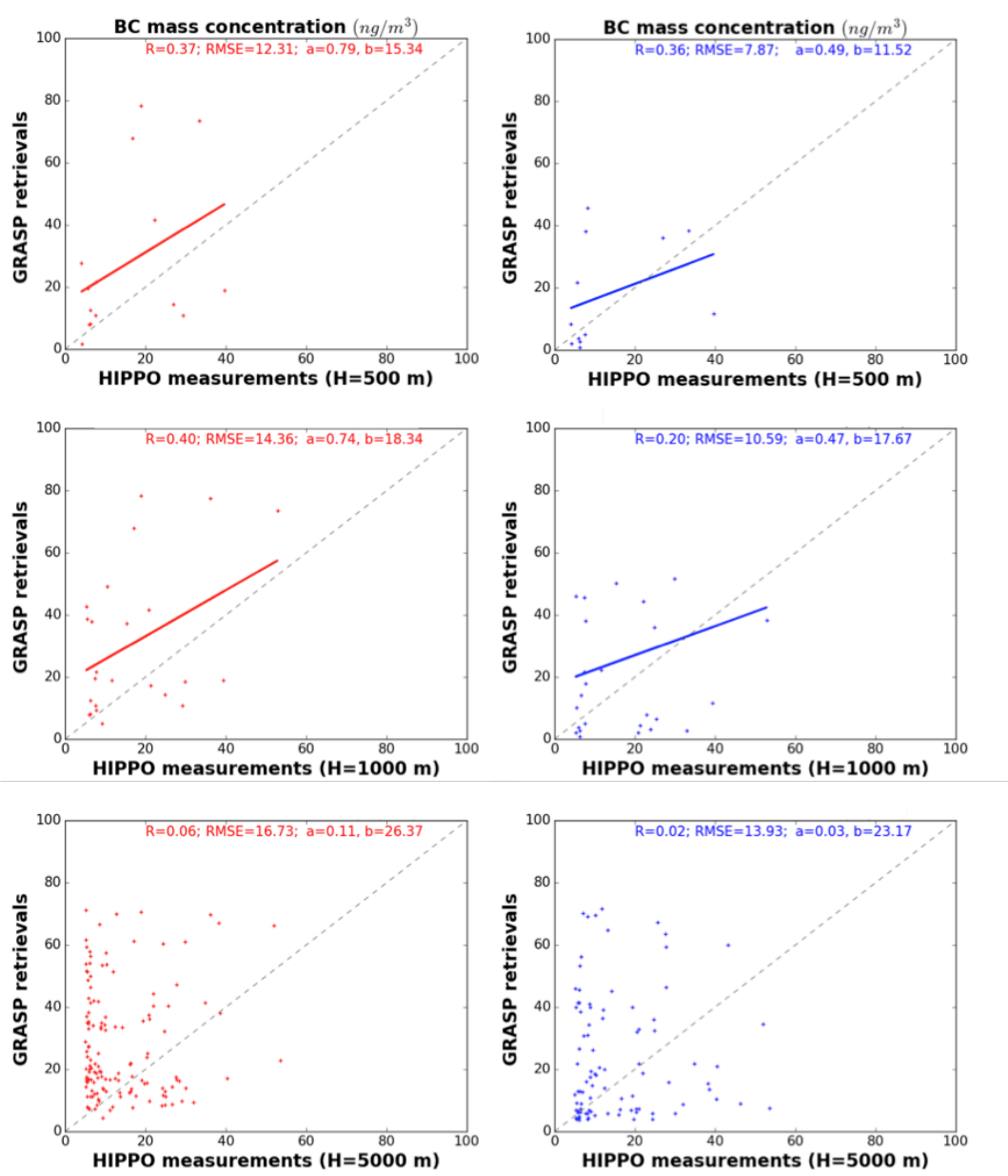

Figure 4.35: The comparison of BC mass concentration retrieved from POLDER/PARASOL with the corresponding values measured in HIPPO campaigns (Schwarz et al., 2011). Figures in the left column in red color denote the BC mass concentration retrieved using the Maxwell-Garnett conversion model

and figures in the right column in blue color denote the BC mass concentration retrieved using the volume-weighted conversion model. H=500, 1000 and 5000 m indicate that the averaged values of HIPPO BC mass concentration are calculated using the available measurements under different altitude levels.

4.4 Comparison of composition retrieval with GEOS-5/GOCART simulation

The Georgia Institute of Technology-Goddard Global Ozone Chemistry Aerosol Radiation and Transport (GOCART) model can simulate major tropospheric aerosol types, including sulfate, dust, OC, BC and sea salt aerosols. The model uses the assimilated meteorological fields generated from the Goddard Earth Observing System Data Assimilation System (GEOS DAS), which are model-assimilated global analyses constrained by meteorological observations. For aerosol simulation the GEOS-5/GOCART model consists of the modules such as emission, which includes sulfur, dust, BC, OC and sea salt emissions, and chemistry, which uses prescribed OH, H_2O_2 and NO_3 fields for gaseous sulfur oxidations. The GEOS-5/GOCART model reproduces the seasonal variations at most of the AERONET sites, especially the sites where biomass burning or dust aerosol dominate, even though the magnitudes do not always match the observations (Chin et al., 2002). The aerosol composition inversion product, presented in this thesis work, can be used to constrain the model simulations on large spatial scale.

Figure 4.36 shows the comparisons of BC and dust mass concentrations retrieved from POLDER satellite observation with those simulated by GEOS-5/GOCART model. The data used for the comparison covers African continent and Arabian Peninsula. Over these regions, the average BC mass concentration obtained from satellite composition inversion is of 0.80 mg/m^2 for the volume-weighted approach and 0.62 mg/m^2 for the Maxwell-Garnett approach. The averaged value simulated by GEOS-5/GOCART model, however, is only 0.46 mg/m^2. The model, therefore, tends to underestimate BC concentration by 25 – 40% over Africa and Arabian Peninsula, which is in line with a previously assessed underestimation of aerosol optical thickness of biomass burning aerosols by 30 – 40% for pollution and dust regions (Chin et al., 2009a). Chin et al. (2009a) considered usage of higher emission factors of carbonaceous aerosols than the commonly suggested values (e.g., Andreae and Merlet, 2001). Lower biomass burning aerosol optical thickness estimated by GEOS-5/GOCART model reveals the possibility that the dry mass burned estimates may be too low, as other studies have also suggested (e.g., Bian et al., 2007).

The average coarse dust mass concentration obtained from satellite composition inversion is of 208.91 mg/m^2 for volume-weighted approach and 189.70 mg/m^2 for Maxwell-Garnett approach. It is lower than that simulated by GEOS-5/GOCART model (322.73 mg/m^2). Thus, the model may tend to overestimate coarse dust concentration by 55 – 70% over Africa and Arabian Peninsula. The comparisons demonstrated that the values of modeled BC concentration are lower in pollution and biomass burning regions (southern Africa) but the values of modeled coarse dust concentration are higher in dust-dominated places (northern Africa and Arabian Peninsula) (e.g., Jones and Christoper, 2007; Ginoux et al., 2001).

It is worth noting that the obtained results are also in agreement with results obtained by another PhD study undertaken in LOA (Chen at al., in preparation), which estimated global emission sources of BC and dust based on inverse modeling procedure (Dubovik et al., 2008). The GEOS-Chem based inverse modeling algorithm is used in this study to retrieve desert dust, BC and OC aerosol emission sources simultaneously from GRASP aerosol product from POLDER/PARASOL. The retrieved emission sources indicated a reduction of ~30% for annual dust emission, while an increment of ~2 times for total BC and OC emissions in comparison to "prior model" emissions. Despite the GRASP aerosol product from POLDER/PARASOL is used in both cases, these two methods are completely independent, which solidify the derived tendencies on underestimation of BC and overestimation of dust emissions by global chemistry transport models.

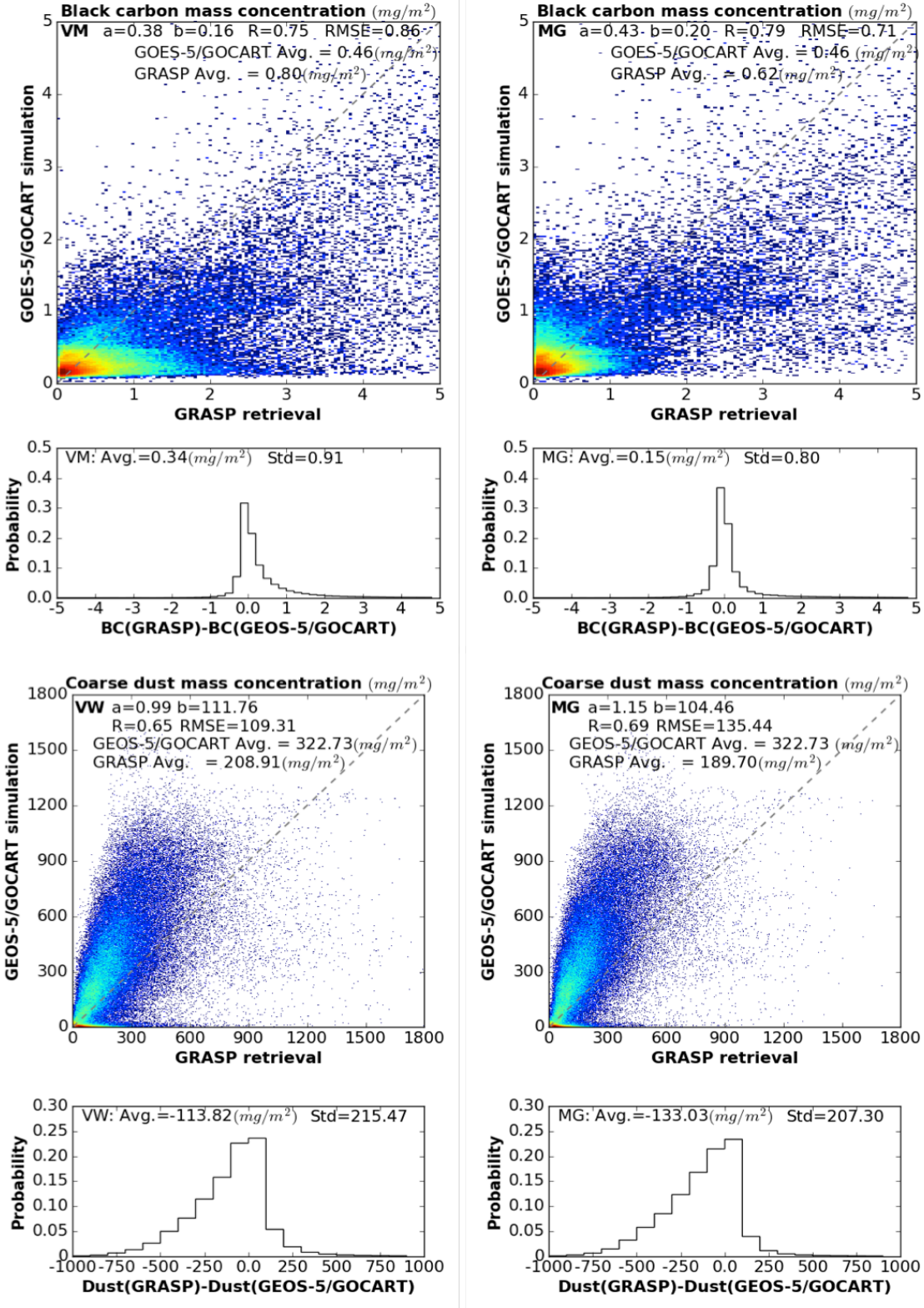

Figure 4.36: The comparison of BC and coarse dust mass concentration retrieved from POLDER/PARASOL with the corresponding values simulated by GEOS-5/GOCART model over Africa in 2008. “VW” denotes the approach of volume-weighted conversion model, and “MG” denotes the approach of Maxwell-Garnett conversion model.

Chapter 5

GRASP applications to POLDER observations over the globe

"When one must, one can."

------ Charlotte Whitton

The current chapter presents in detail seasonal variations of the retrieved aerosol composition over the globe. The retrievals employ POLDER/PARASOL observations in 2008 and conducted using the Maxwell-Garnett conversion model. One year of data was used because of time consumption of the calculations. Nevertheless, even one year of aerosol composition data for the entire globe can improve our understanding of the aerosol species variability and accuracy of modeling. While analyzing mean values from the satellite data on large spatial scale it can be important to know the frequency of the data occurrence. Figure 5.1 shows number of pixels, in 0.1° × 0.1° resolution, observed by POLDER/PARASOL in 2008. Over land observations present much larger number of pixels than over ocean, apparently due to clouds presence that is more abundant over oceans. Also over land, the different regions can have different pixel statistics. For example, the number of observations over northern Africa and West Asia is more than that over Asia, especially over China. Interpretation of the mean values can be significantly affected by these statistics, therefore, it is important to keep in mind the frequency of the observation occurrence for the following analysis.

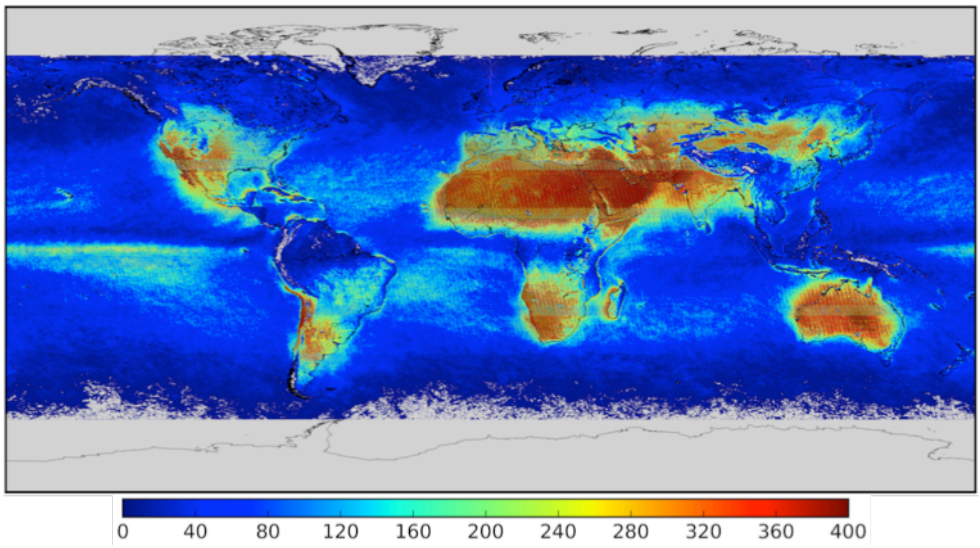

Figure 5.1: Number of pixels in 0.1 × 0.1 degree resolution observed by POLDER/PARASOL satellite over the globe in 2008.

5.1 Maxwell-Garnett conversion model

Figure 5.2 shows seasonal variations of aerosol optical thickness at 0.440 μm in 2008 derived from POLDER/PARASOL observations using the Maxwell-Garnett conversion model. Aerosol optical thickness exhibits a pronounced variability over the globe, reaching high values over Africa and Asia, especially during DJF and JJA. Elevated aerosol optical thickness over Africa are attributed to seasonal dust storms and biomass burning, while higher aerosol optical thickness over Asia, especially in the Asian megacities (e.g., Kanpur, India and Beijing, China), are attributed to industrial fossil fuel combustion due to economic activities and population density (e.g., Lawrence and Lelieveld, 2010). The aerosol composition over these high aerosol burden regions is expected to be quite different and dependent on seasons. Table 5.1 shows seasonal variability of the global mean concentrations of the retrieved aerosol compositions. A more detailed discussion of spatial patterns during every season and for each element is presented in following.

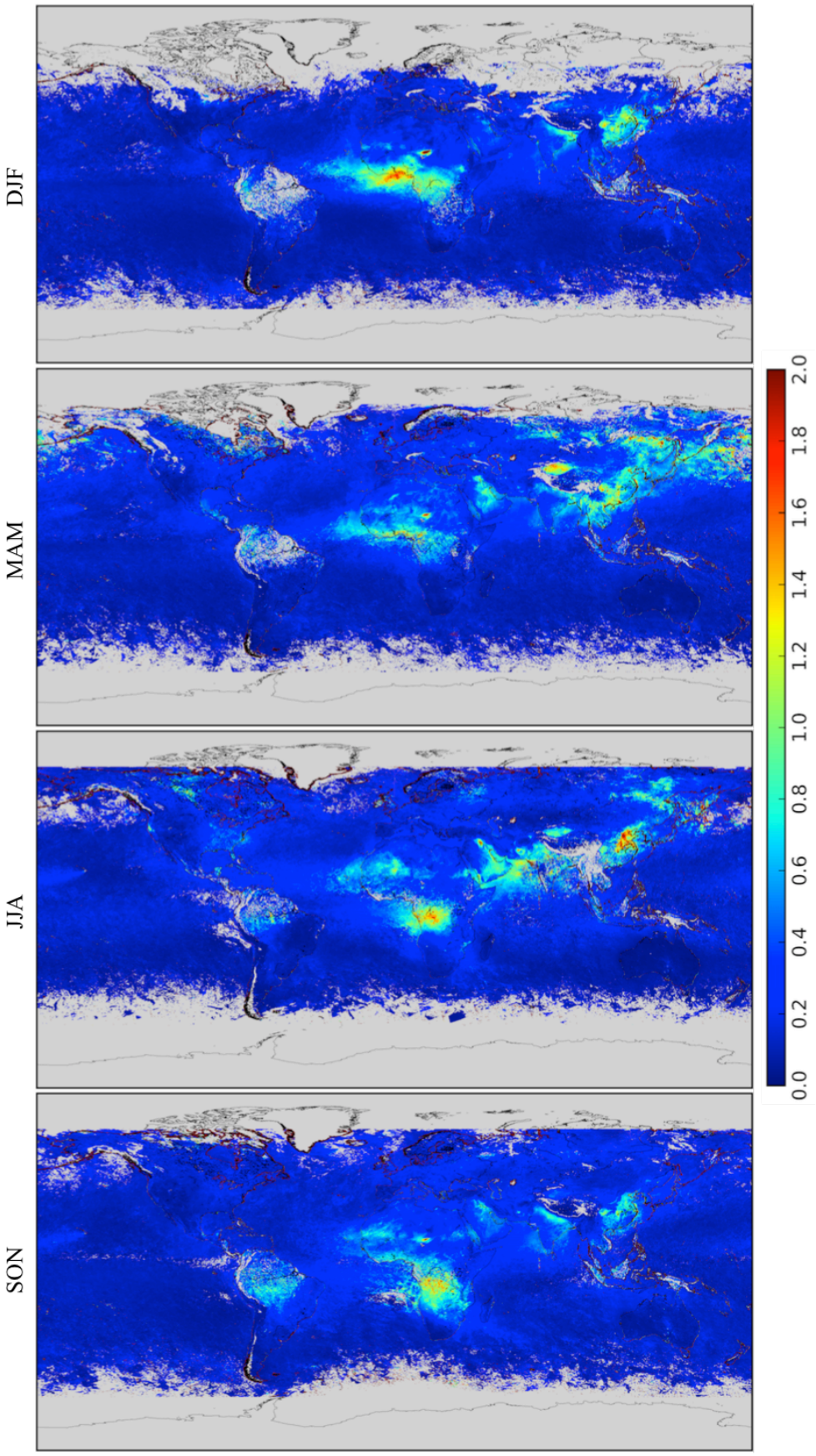

Figure 5.2: Seasonal variations of AOT at 0.440 μm in 2008 as retrieved by GRASP algorithm from POLODER/PARASOL satellite observations using the Maxwell-Garnett conversion model.

Table 5.1: Seasonal variations of aerosol composition for columnar volume concentration (mm^3/m^2) over the globe in 2008 as retrieved by GRASP algorithm from POLDER/PARASOL satellite observations using the Maxwell-Garnett conversion model. "AN" like denotes inorganic salts including ammonium nitrate, ammonium sulfate, and sea salts. "Water" denotes aerosol water content.

Season	BC	BrC	Fine dust OC	Coarse dust	Iron oxide	"AN" like	Water
DJF	0.47	5.71	5.29	28.37	0.36	11.92	8.50
MAM	0.34	6.13	7.80	35.20	0.50	13.49	10.03
JJA	0.35	6.28	6.89	33.71	0.48	14.27	11.84
SON	0.38	5.62	5.93	29.27	0.38	12.42	10.08

5.1.1 Black carbon

As can be seen in Figure 5.3, BC concentration exhibits a pronounced seasonal cycle with high variability over the globe; it reaches a global average peak of 0.47 mm^3/mm^2 during DJF, lower values during SON and JJA, and a minimum of 0.34 mm^3/mm^2 during MAM (see Table 5.1). The maximum BC concentration averaged over the globe during DJF is constituted from contributions by biomass burning in Sahel region, and by anthropogenic pollution in India and China. The fires occurring in the Sahel region generate higher percentage of BC than those in southern Africa during SON and JJA, as was discussed in Chapter 4. In addition, anthropogenic activity in India and China generates more BC during DJF, which is consistent with the previous studies. For example, Li et al. (2015) found that BC mass concentration averaged over the 12 years is higher (21.6 mg/ mm^2) during DJF than that during the other seasons. The study is based on retrieval of aerosol composition from AERONET measurements in Beijing and Kanpur sites during the period 2002 – 2013. It is noted that when the AOT is very low, such as over ocean, the accuracy of retrievals is expected to be low.

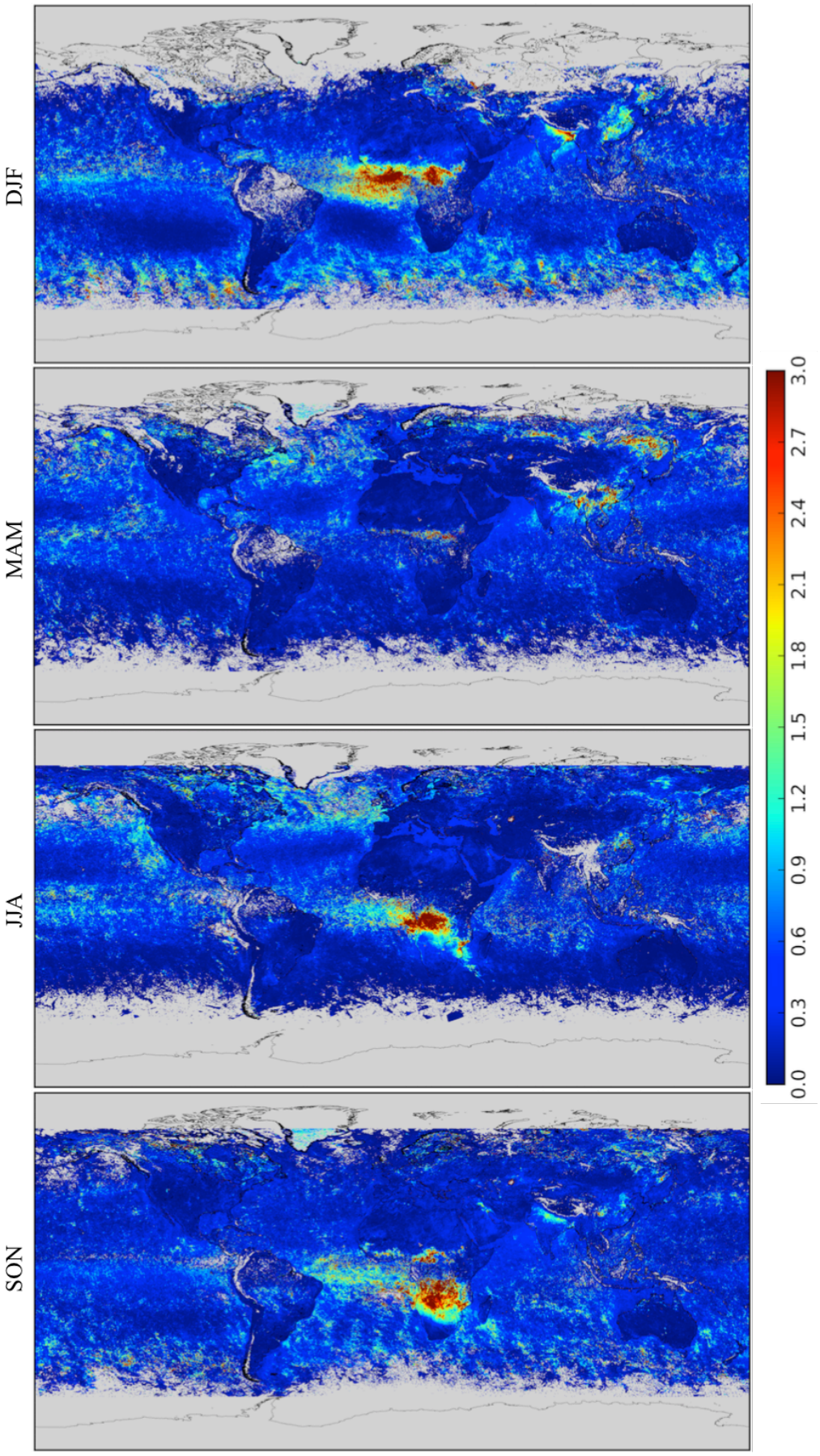

Figure 5.3: Seasonal variations of BC columnar volume concentration (mm^3/m^2) in 2008 as retrieved by GRASP algorithm from POLDER/PARASOL satellite observations using the Maxwell-Garnett conversion model.

5.1.2 Brown carbon

Figure 5.4 shows seasonal variations of BrC concentration over the globe in 2008. BrC concentration reaches a global average peak of 6.28 mm^3/mm^2 during JJA and the lowest value of 5.62 mm^3/mm^2 during SON (see Table 5.1), which is primary association with temporal variations of biomass burning over Africa and contribution of Asian anthropogenic activity. The comparison of BrC concentration (Figure 5.2) with BC concentration (Figure 5.3) reveals that despite both are emitted from biomass combustion, the high concentrations of brown and black carbon are not always collocated. Previous studies (Haywood et al., 2003; Abel et al., 2003; Reid et al., 1998) showed that the fresh biomass burning aerosols had higher BC content than aged aerosol. There are some rapid changes occurring in the relative concentration of particle types with the aging of smoke. For example, BC particles become gradually more aggregated with organic and sulfate particles during the aging of smoke (Pósfai et al., 2003). Therefore, BC in the area near the biomass burning emissions is retrieved with higher concentration, whereas BrC is generally enriched in downwind region of biomass burning, in particular near the coast where the relative humidity is high.

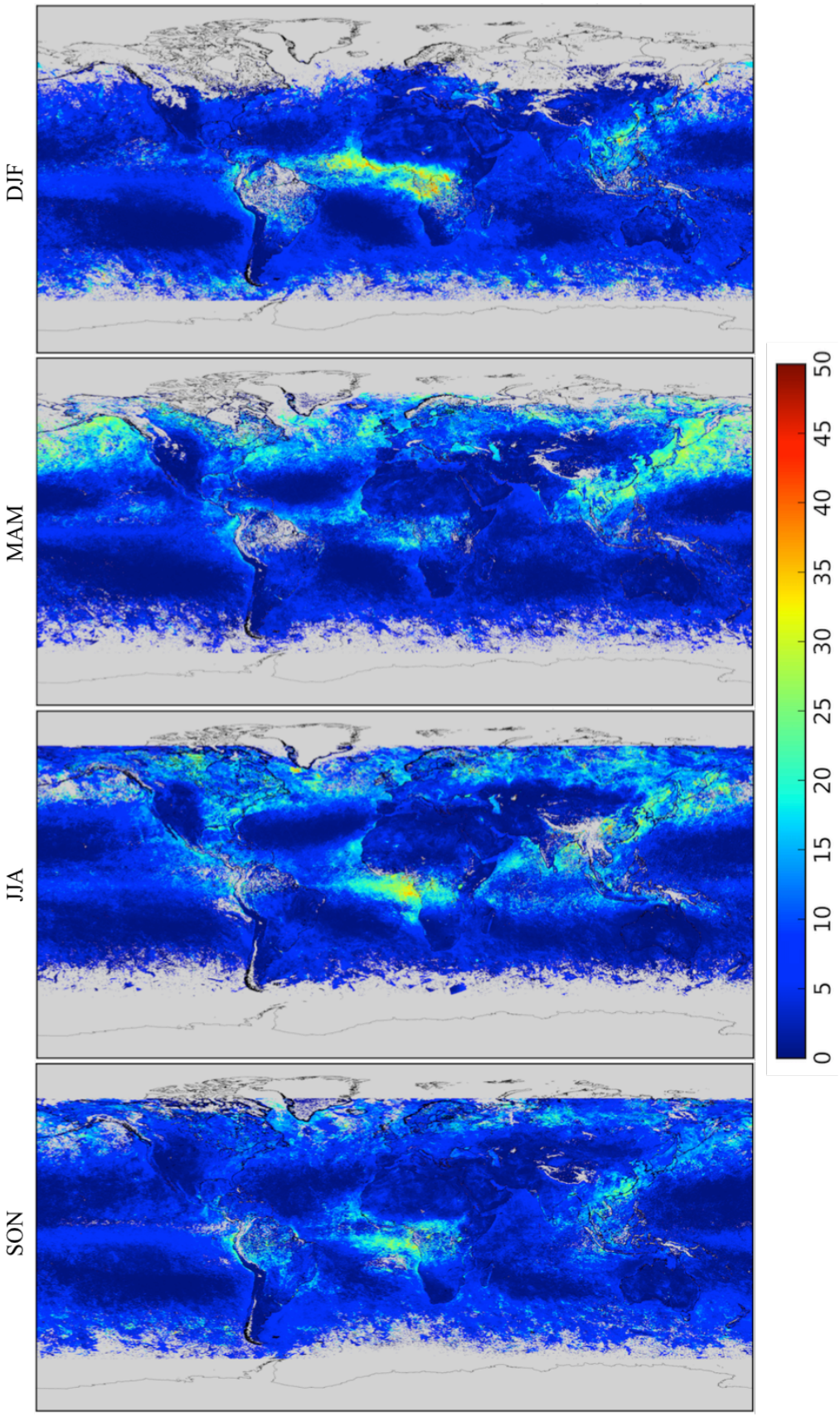

Figure 5.4: Seasonal variations of BrC columnar volume concentration (mm^3/m^2) in 2008 as retrieved by GRASP algorithm from POLDER/PARASOL satellite observations using the Maxwell-Garnett conversion model.

5.1.3 Organic carbon/fine dust

Figure 5.5 and Figure 5.6 shows seasonal variations of OC/fine dust concentration and Ångström Exponent over the globe in 2008, respectively. As discussed previously, due to similarity between refractive indexes of OC and non-absorbing dust (without iron oxide component), an additional information about aerosol size is needed for a proper interpretation of the retrieved component. Fine dust is predominately concentrated over northern Africa, Middle East, Central Asia and northwest China, where Ångström Exponent retrieved is very small. Especially, fine dust concentration is observed with the largest values over Bodélé depression during DJF, Taklimakan in China during MAM and Arabian Peninsula during JJA. OC is mainly enriched in the regions where the biomass burning takes place with high frequency, as well as larger Ångström Exponent retrieved, such as southern Africa, South America, India and China. High OC is also observed in China, especially in southern China (Sichuan Basin and the Pearl River Delta region), and urban South Asia (Zhang et al., 2008b; Decesari et al., 2010; Stone et al., 2010; Zhang et al., 2012). Secondary OC (SOC) also contributes to total concentrations of OC (Zhang et al., 2005; Miyazaki et al., 2006; Sullivan et al., 2006; Weber et al., 2007; Zhang et al., 2008b). The SOC can consist 55% of annually averaged total urban OC aerosols. The urban origin of OC in China is enhanced around May to June and October (Zhang et al., 2012), which may be an explanation of the retrieved high OC concentration during JJA in southern China (Figure 5.5). It is noted that OC concentrated in northern China during DJF is caused by the abundant combustion of fossil fuels in the heating period. Additionally, it can be noted that higher OC concentration is retrieved over South America during SON (Figure 5.5), which also corresponds to high Ångström Exponent (Figure 5.6). Indeed, this season is known as biomass burning that starts in July and peaks generally in August and September (e.g., Duncan et al., 2003).

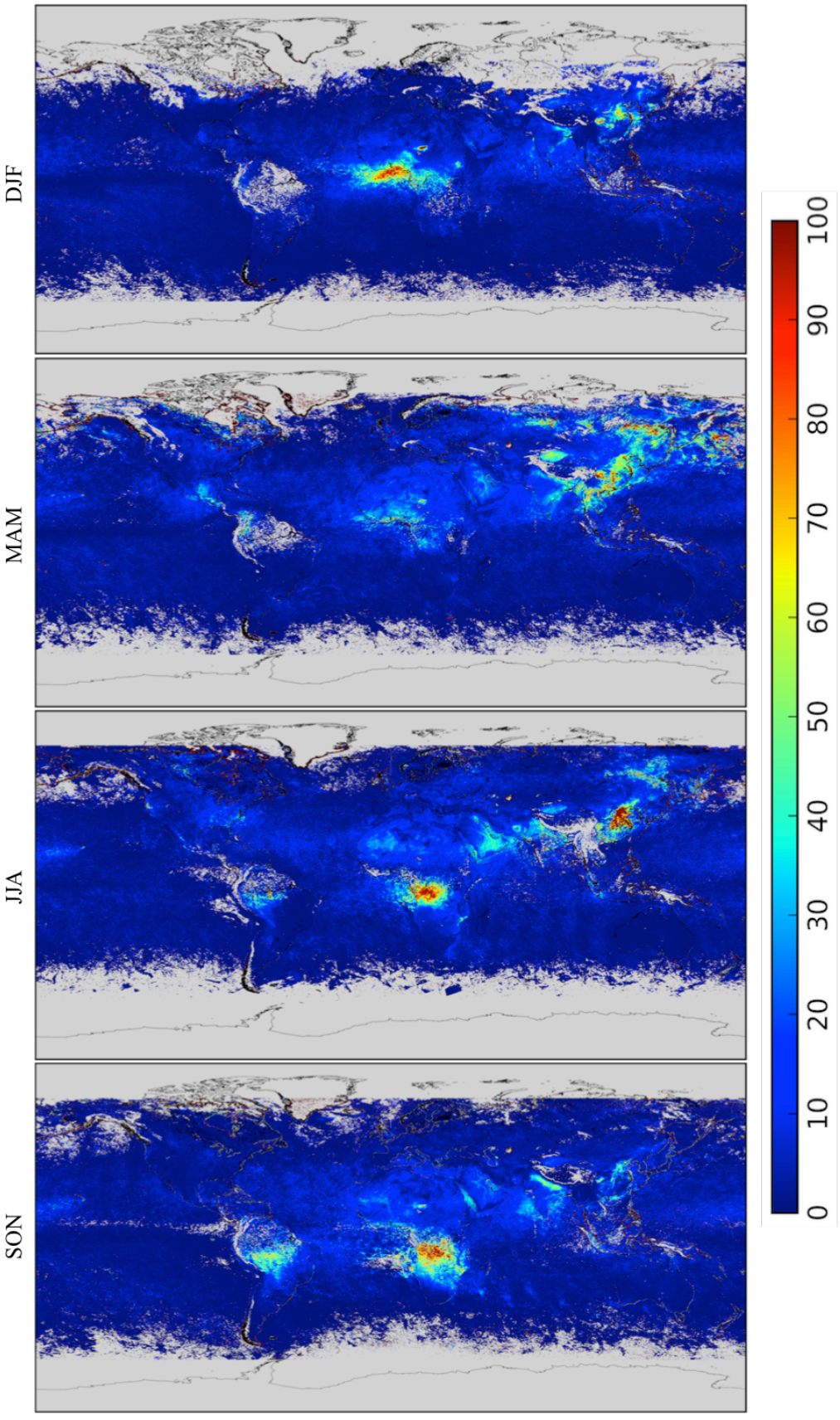

Figure 5.5: Seasonal variations of OC/fine dust columnar volume concentration (mm^3/m^2) in 2008 as retrieved by GRASP algorithm from POLDER/PARASOL satellite observations using the Maxwell-Garnett conversion model.

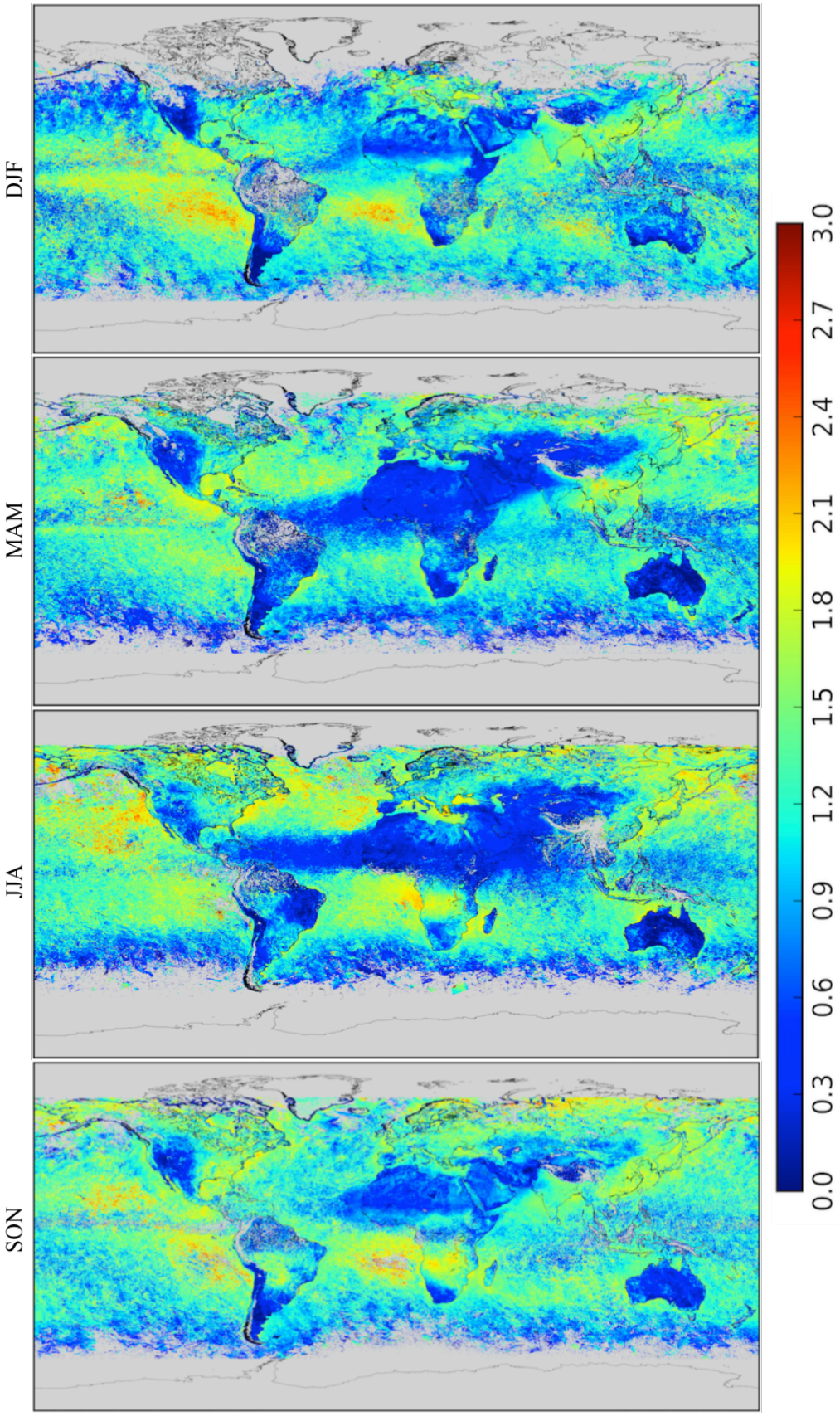

Figure 5.6: Seasonal variations of Ångström Exponent (0.670/0.865 μm) in 2008 as retrieved by GRASP algorithm from POLDER/PARASOL satellite observations using the Maxwell-Garnett conversion model.

5.1.4 Coarse dust

Seasonal variations of coarse dust concentration over the globe in 2008 are shown in Figure 5.7. Global coarse dust concentration during MAM and JJA (35.20 mm^3/mm^2 and 33.71 mm^3/mm^2, respectively) is much higher than that during DJF and SON (29.27 mm^3/mm^2 and 28.37 mm^3/mm^2, respectively). During MAM and JJA the global dust belt is extending from the west coast of North Africa, through the Middle East, into Central Asia, it covers Sahara, the Arabian Peninsula, Caspian Sea and Aral Sea regions in Central Asia, and Gobi and the Taklimakan in China (shown in Figure 5.7). All these desert areas show high dust activity during this period. In addition, elevated coarse dust concentration is also observed in Australia (area of Lake Eyre and The Great Artesian Basin) during DJF and SON. Coarse mode dust is also detected over Mexico during MAM and over arid regions in south of the USA during JJA. The coarse dust component also appears over the regions in Africa that are identified as biomass burning with high concentrations of BC and BrC in fine mode. Since dust is the only balk material assumed for the coarse mode aerosol, besides strongly absorbing iron oxide and non-absorbing water, the slightly absorbing coarse mode aerosols in these biomass burning regions are interpreted as dust. Therefore, the coarse dust component retrieved for biomass burning regions is response of the algorithm to presence of slightly absorbing coarse mode aerosol, which spectral absorption is different from iron oxide.

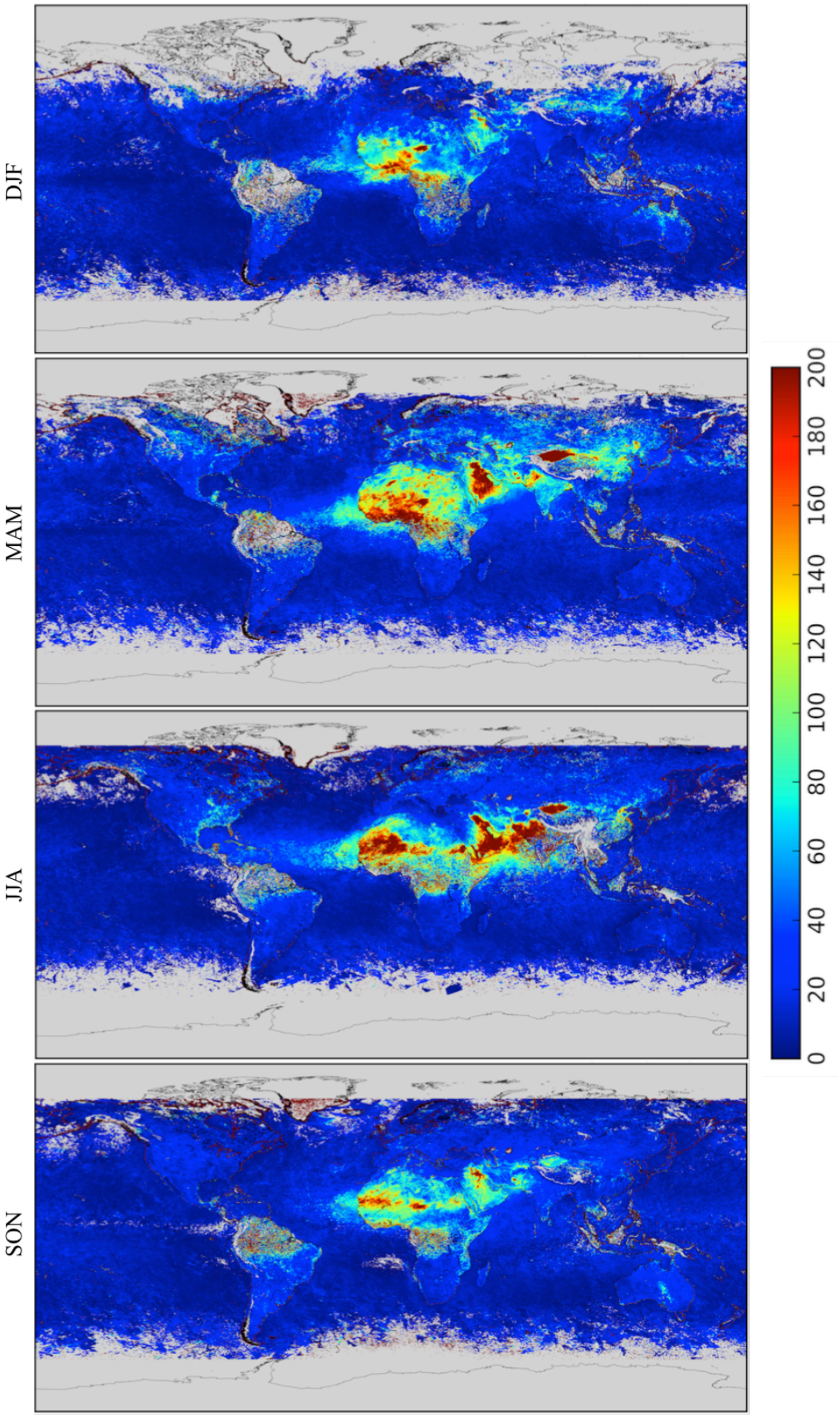

Figure 5.7: Seasonal variations of coarse dust columnar volume concentration (mm^3/m^2) in 2008 as retrieved by GRASP algorithm from POLDER/PARASOL satellite observations using the Maxwell-Garnett conversion model.

5.1.5 Iron oxide

Figure 5.8 shows seasonal variations of iron oxide concentration over the globe in 2008. As it was discussed for the African continent in Chapter 4, the iron oxide concentrations have similar patterns and seasonal variations as the coarse dust component. The high iron oxide concentrations are observed during MAM and JJA (global average values of 0.50 mm^3/mm^2 and 0.48 mm^3/mm^2, respectively), while lower concentration during DJF and SON (global average values of 0.36 mm^3/mm^2 and 0.38 mm^3/mm^2, respectively). As it was also discussed in Chapter 4, the maximums of iron oxide and coarse dust concentrations are not collocated because the elemental and mineralogical composition of mineral dust varies depending on the source region of emission. Retrievals on the global scale also present the regions of iron oxide transport over ocean. As can be expected, there are high iron oxide concentrations over east Atlantic that gradually decrease during the dust transport towards Americas. High iron oxide concentrations are also derived over the Arabian Peninsula and the Arabian Sea. It should be mentioned here that a discontinuity in the retrieved concentrations can be noted between over land and over water in the regions of the Red Sea and Arabian Sea. Given that such discontinuity does not appear in all coastal regions, the reason is most probably not in the algorithm failure. The reason for the discontinuity can be rather related to statistics of the number of pixels available from the observations, which vary significantly between over land and over ocean (see Figure 5.1). This statistics can affect the mean values calculations. In addition, attention should be drawn to the land topography in the considered regions, i.e. mountains that separate between land and sea. Finally, high iron oxide concentrations are also retrieved over Asia, especially during MAM, which is attributed to higher iron oxide content in the dust emitted from the Taklimakan desert located in northwest China.

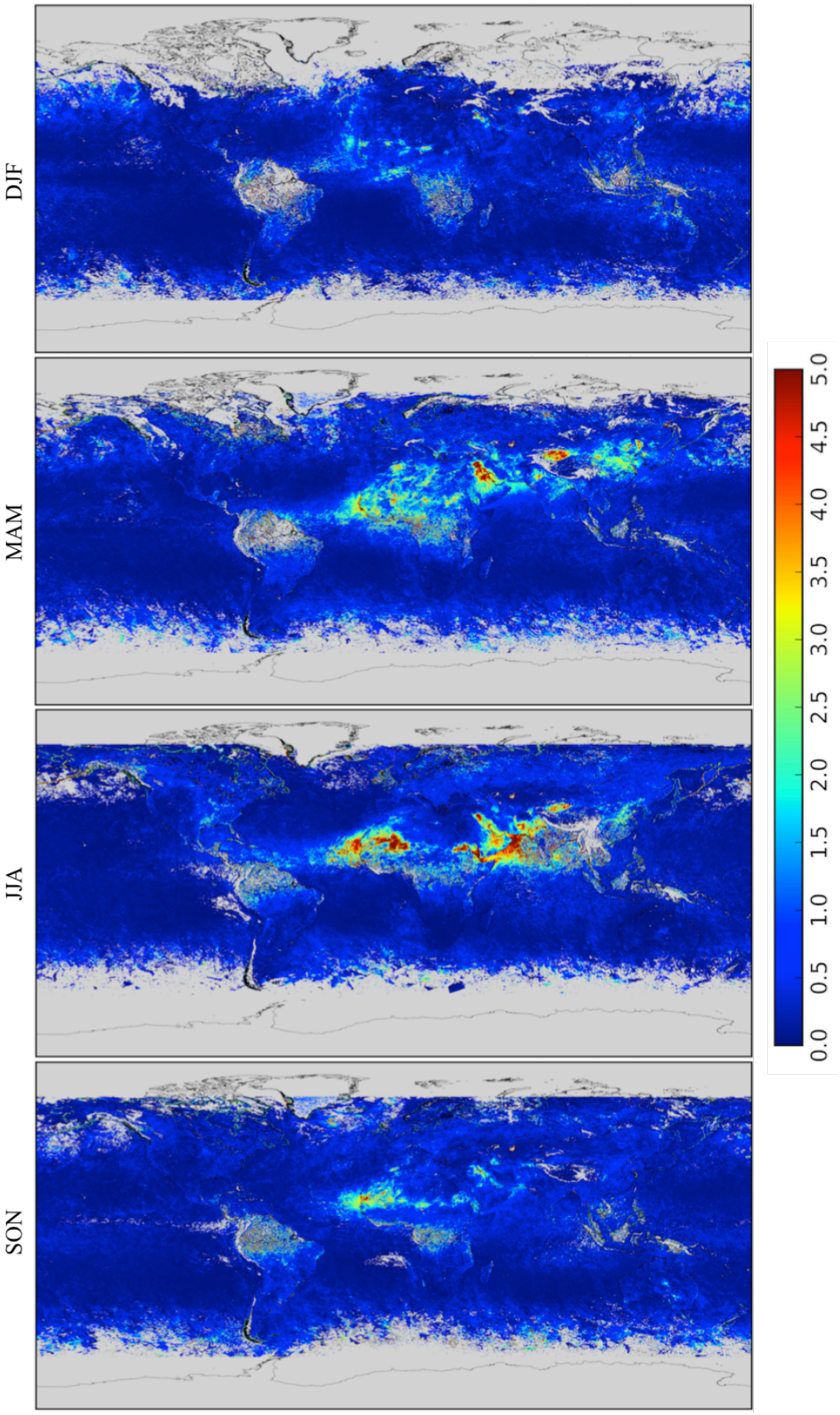

Figure 5.8: Seasonal variations of iron oxide columnar volume concentration (mm^3/m^2) in 2008 as retrieved by GRASP algorithm from POLDER/PARASOL satellite observations using the Maxwell-Garnett conversion model.

5.1.6 Aerosol water content and ammonium nitrate

Aerosol water content is strongly dependent upon aerosol composition and relative humidity, and it may constitute a significant fraction of the aerosol (Pilinis and Seinfeld, 1989). Aerosol water content should be well correlated with the concentration of hygroscopic composition (e.g., ammonium nitrate, ammonium sulfate and sea salt) and less correlated with hydrophobic composition at a given relative humidity. Figures 5.9 and 5.10 show the seasonal variations of aerosol water volume concentration in fine mode and total (fine and coarse) over the globe in 2008. More details of aerosol water content over Africa are discussed in Chapter 4. Figures 5.9 and 5.10 also show that water volume concentration for the aerosols over China and India are observed with high values, especially during DJF and SON, because more hygroscopic species (ammonium nitrate and ammonium sulfate) exist in the industrial aerosols (see Figures 5.11 and 5.12).

Figures 5.11 and 5.12 show the seasonal variations of ammonium nitrate volume concentration in fine mode and total over the globe in 2008. Ammonium nitrate volume concentration for the aerosols over China and India are observed with large values, especially in fine mode during DJF and SON (see Figure 5.11), which is attributed to the industrial aerosols of megacities with high population density and pollution level (e.g., ammonium nitrate and ammonium sulfate). The distributions of BC, OC and ammonium nitrate have similar spatial variations (Figures 5.3, 5.5, and 5.11), which is attributed to the mixing of inorganic particles (e.g., ammonium sulfate) with organic and soot particles originated from biomass burning. The carbonaceous particles may provide a favorable surface for the nucleation of sulfate, and coagulation can also bring soot and sulfate together.

It has to be mentioned here that some discontinuity between over land and over ocean retrievals can be observed around the Arabian Peninsula and Western Africa. Comparisons of Figures 5.9, 5.11 with Figures 5.10, 5.12 indicate that this discontinuity is in coarse mode retrievals. This discontinuity can be suspected as an algorithmic artifact, however, worth noting that some mountains separate land and sea around the Arabian Peninsula, especially Red Sea, which can be a natural barrier between continental and marine aerosols. In addition, statistics of the pixels available for the retrievals from POLDER/PARASOL (see Figure 5.1) shows that the number of pixels over land is significantly higher than over ocean, which is rather due to cloud contamination. This discontinuity in the pixel statistics can also affect the mean values of the retrieved concentrations.

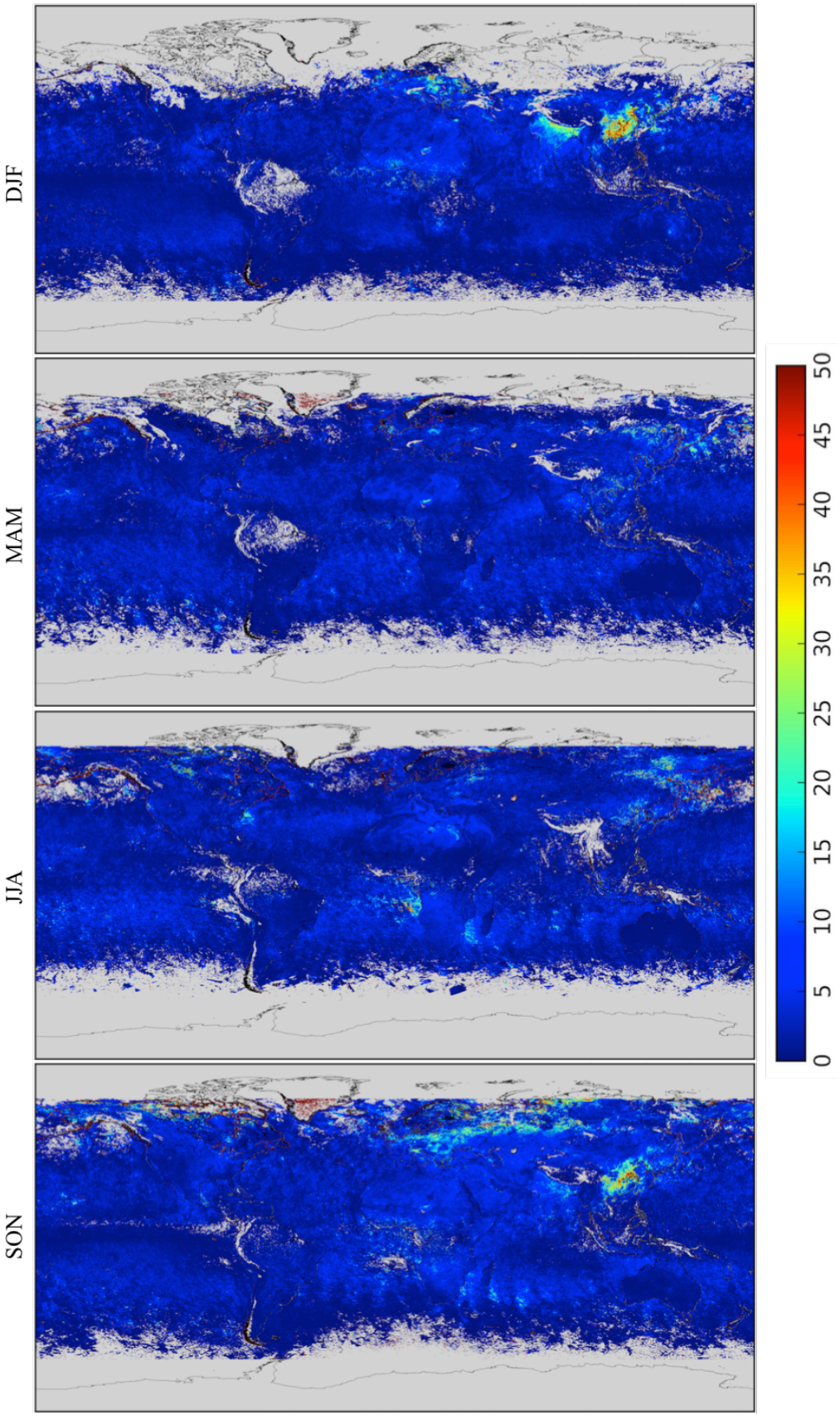

Figure 5.9: Seasonal variations of aerosol water columnar volume concentration (mm^3/m^2) in fine mode in 2008 as retrieved by GRASP algorithm from POLDER/PARASOL satellite observations using the Maxwell-Garnett conversion model.

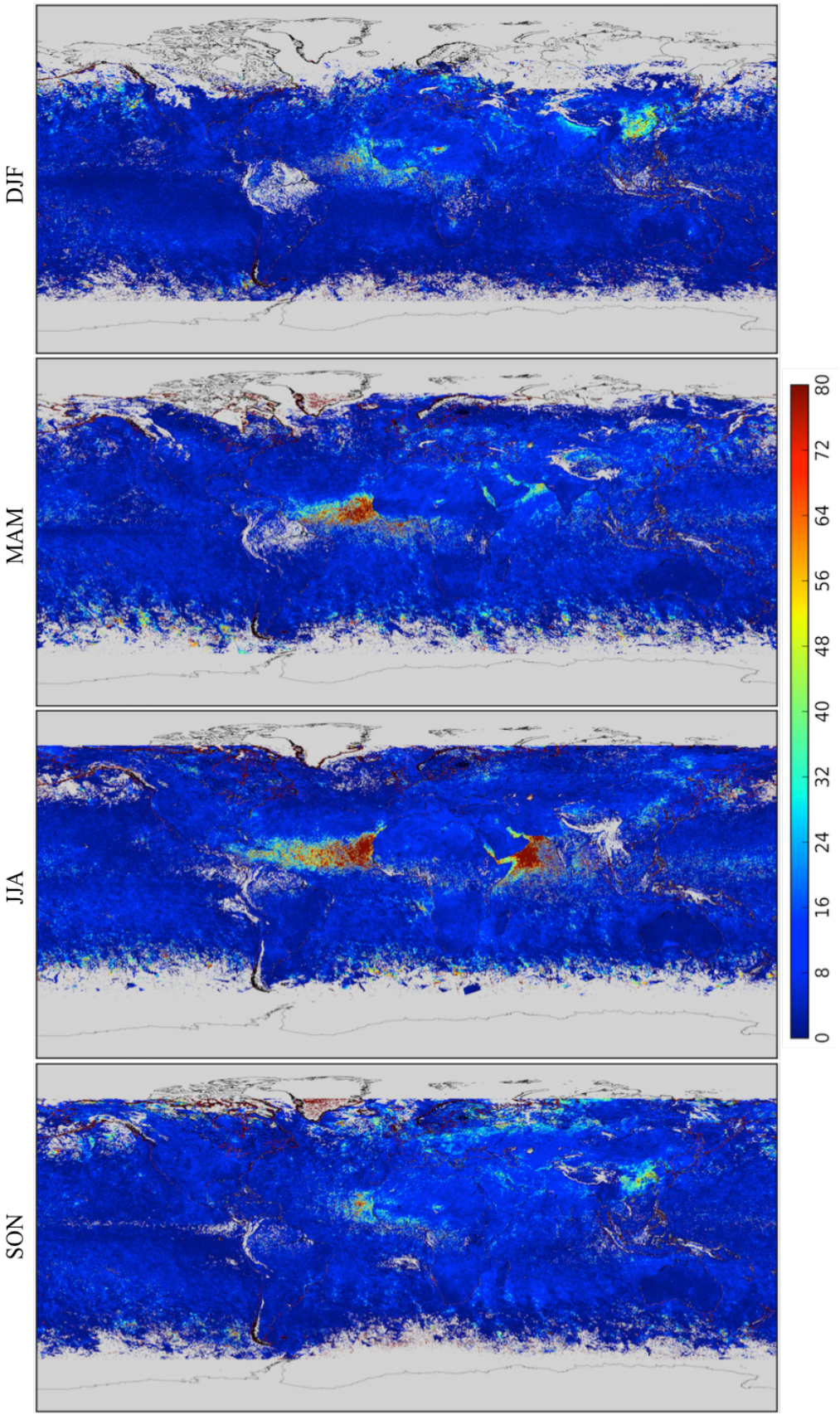

Figure 5.10: Seasonal variations of aerosol water columnar volume concentration (mm^3/m^2) in total (fine and coarse modes) in 2008 as retrieved by GRASP algorithm from POLDER/PARASOL satellite observations using the Maxwell-Garnett conversion model.

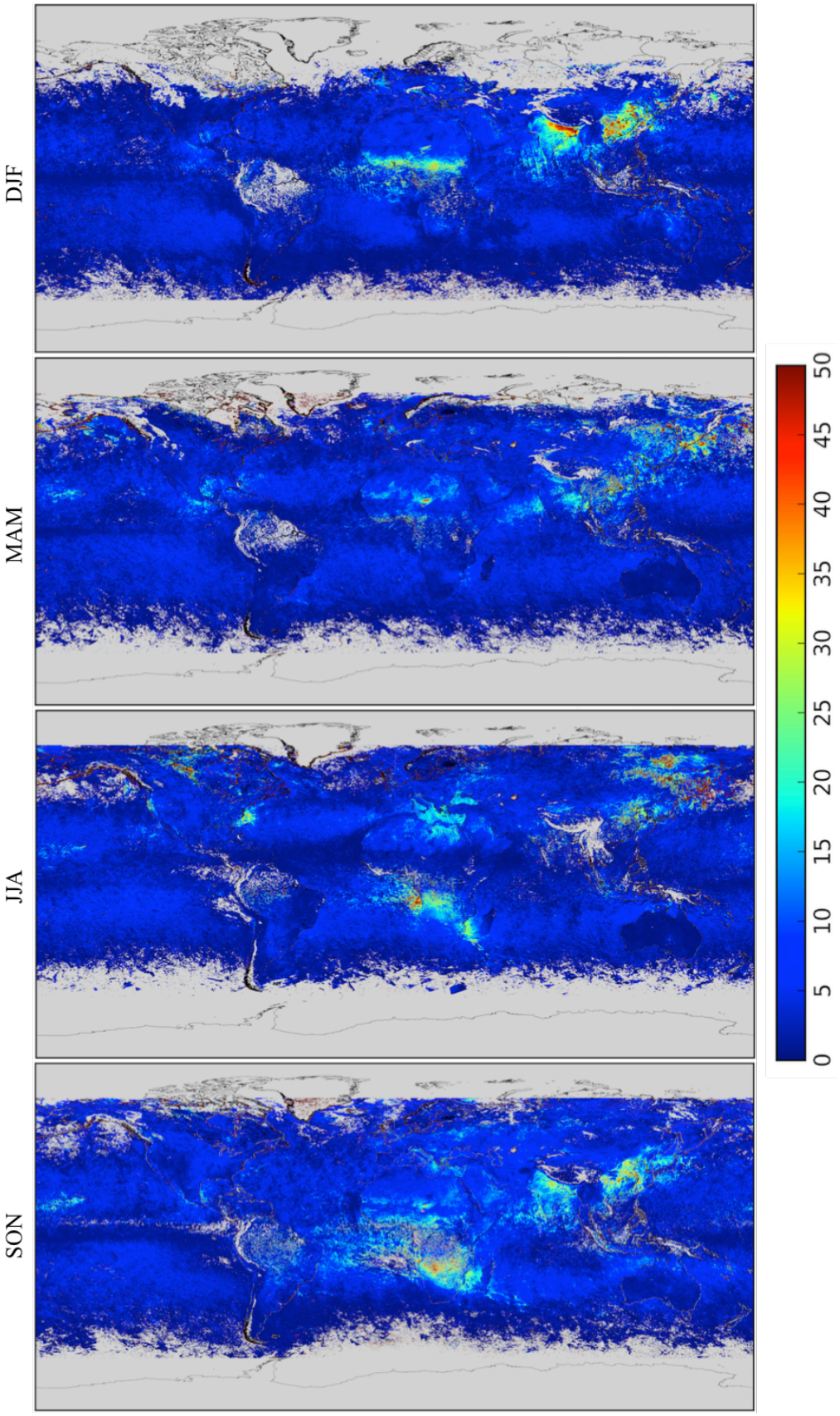

Figure 5.11: Seasonal variations of ammonium nitrate columnar volume concentration (mm^3/m^2) in fine mode in 2008 as retrieved by GRASP algorithm from POLDER/PARASOL satellite observations using the Maxwell-Garnett conversion model.

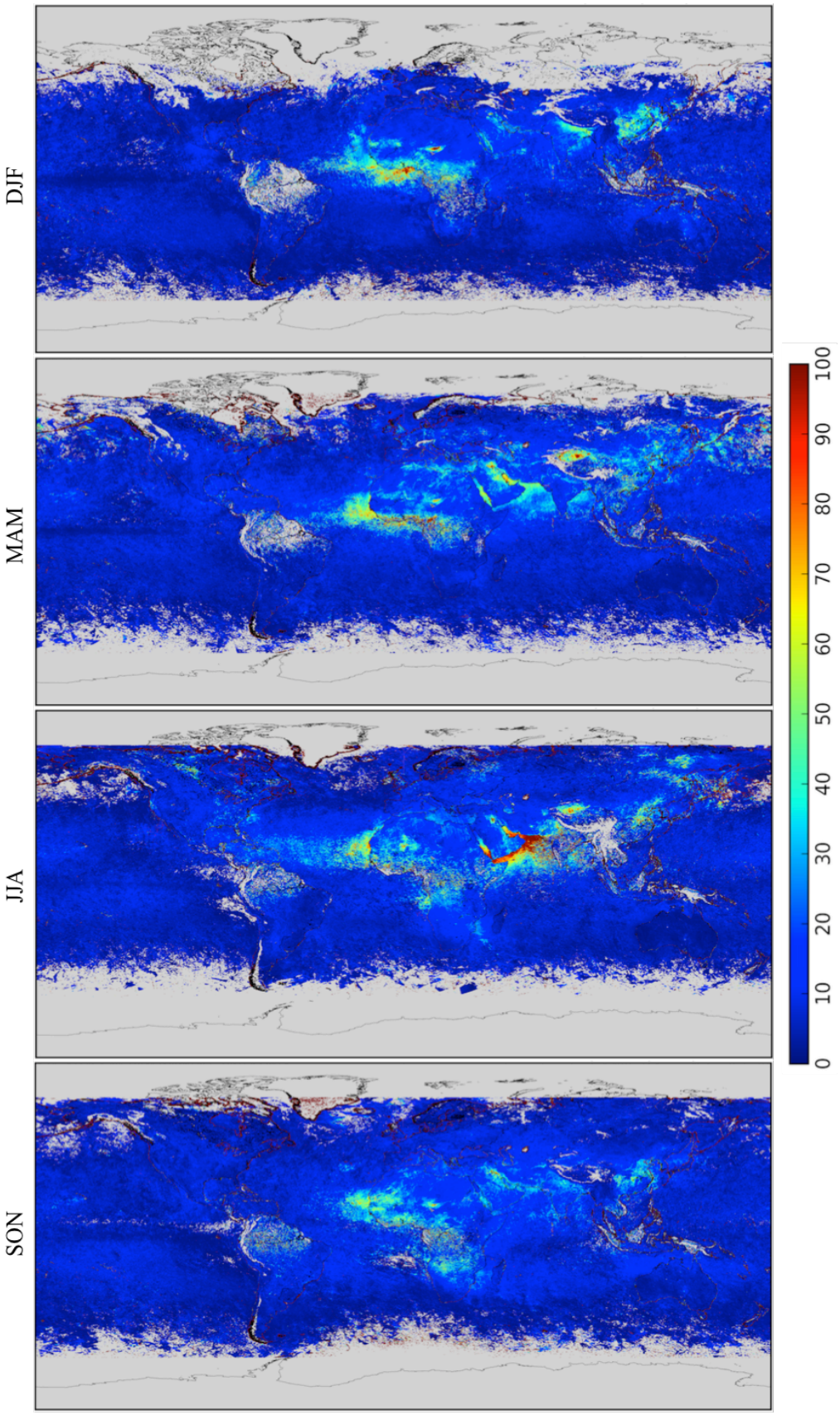

Figure 5.12: Seasonal variations of ammonium nitrate columnar volume concentration (mm^3/m^2) in total (fine and coarse modes) in 2008 as retrieved by GRASP algorithm from POLDER/PARASOL satellite observations using the Maxwell-Garnett conversion model.

5.2 Comparison of composition retrieval with GEOS-5/GOCART simulation

In addition to the comparison between results of GRASP retrievals and of GEOS-5/GOCART simulation over Africa and Arabian Peninsula presented in section 4.4, the data comparison on the global scale is presented in this section. Figure 5.13 shows correlations for BC and dust mass concentrations for all data over the globe in 2008. The global average BC mass concentration retrieved from satellite observation by the Maxwell-Garnett conversion model in GRASP (0.59 mg/m^2) is slightly less than the value simulated by GEOS-5/GOCART model (0.65 mg/m^2). However, in contrast to almost twice higher BC concentration retrieved by GRASP over Africa (discussed in Chapter 4), the retried BC concentrations over Asia are lower. Therefore, the GEOS-5/GOCART model performance has different tendencies in the BC concentration estimation for Africa and Asia. In respect to the global average coarse dust mass concentration, the retrieved by GRASP value (125.5 mg/m^2) is lower than that simulated by GEOS-5/GOCART (174.7 mg/m^2). The model therefore, tends to provide higher coarse dust concentration not only for the Africa region, but also for Asia (e.g., Taklimakan in China).

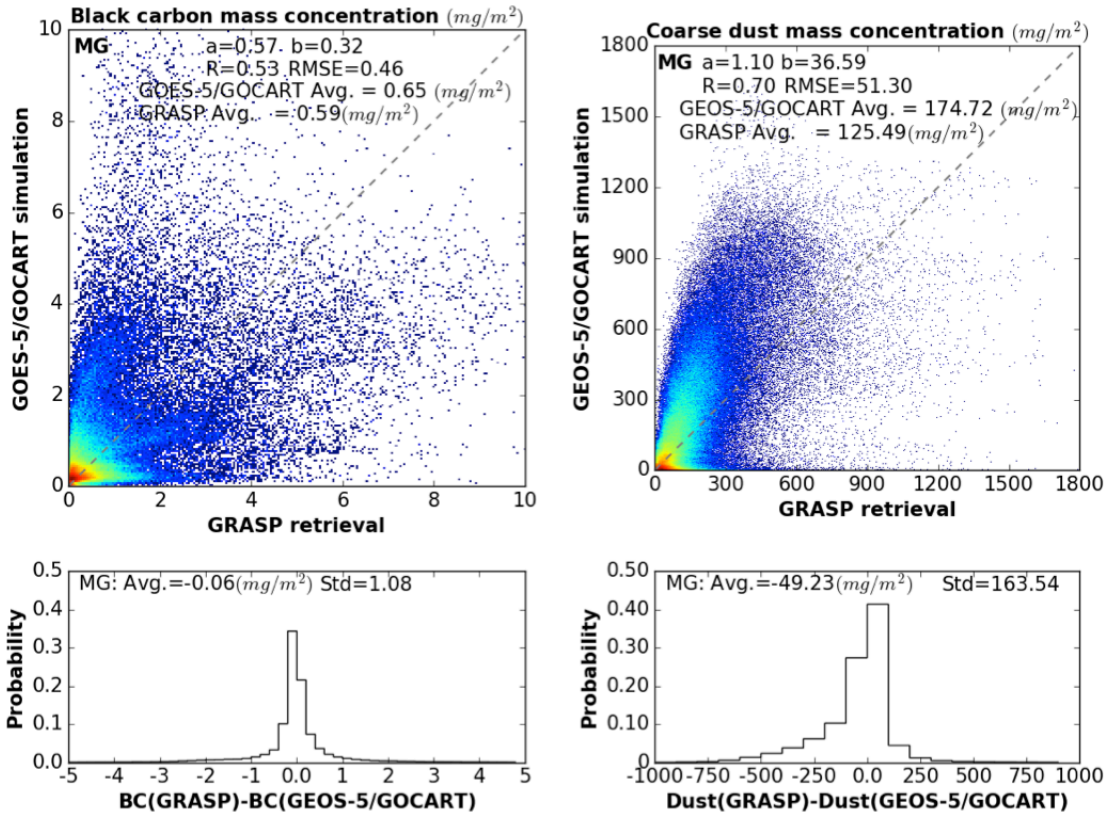

Figure 5.13: The comparisons of BC and coarse dust mass concentration retrieved from POLDER/PARASOL with the corresponding values simulated by GEOS-5/GOCART model over the globe in 2008. "MG" denotes the approach of Maxwell-Garnett conversion model in GRASP.

Chapter 6

GRASP applications to real Sun photometer measurements

"When you believe something can be done, really believe, your mind will find the ways to do it."

------ David J. Schwartz

In this chapter, the GRASP aerosol composition approach is applied to the retrievals of ground-based AERONET photometric observations. GRASP is a highly versatile algorithm, which is developed for characterizing atmospheric properties gathered from wide variety of remote sensing observations including satellite, ground-based and airborne measurements of atmospheric radiation and their combinations. The Sun/sky photometric measurements present sensitivity to aerosol complex refractive index and were already used for the aerosol composition retrievals (based on the post complex refractive index retrieval approach) (Schuster et al., 2005, 2009, 2016; Li et al., 2013, 2015; Wang et al., 2013), as was discussed in the introduction part. Therefore, application of GRASP with composition module approach to AERONET photometric measurements should not present a fundamental difficulty. In fact, modifications required in the code consisted only in deactivation of the surface properties retrievals.

6.1 Study area

Three AERONET sites in Africa that represent dust, biomass burning and mixed aerosol types were selected for a test study. It should be mentioned that application of GRASP to AERONET requires preparation of the input data files that are not automatized for the moment of this thesis work. Preparation of the input files is semi manual and thus is very time consuming, this is why only three sites and limited in time data series were selected for the

presented test study. Figure 6.1 shows location of the selected AERONET sites. First is the AERONET site of Banizoumbou (13.5° N, 2.7° E), which is a remote site located about 60 km east from the capital of Niamey, Niger. It is mainly affected by dust particles, in particular during MAM. The biomass burning season in West Africa occurs primarily from November through March. Therefore, aerosols are regarded as a dust case at Banizoumbou site in April. Second is the AERONET site of Skukuza (25.0° S, 31.6° E), which is a subtropical rural site located in the Kruger National Park in South Africa. Kumar et al. (2013) observed that the AOT at Skukuza site is mainly influenced by biomass burning with a minor contribution of sea salt, desert dust and urban-industrial aerosols. Therefore, aerosols are regarded as a biomass burning case at Skukuza site in September during the biomass burning season in the southern Africa. Third is the Ilorin site (8.3° N, 4.3° E), located in the sub-Sahel region of Nigeria in the northern Africa. This site is heavily influenced by both dust and biomass burning aerosols. A mixing of North African savanna biomass burning aerosols with desert dust from the Sahara and Sahel regions is expected to influence Ilorin, especially in January. The Ilorin site is therefore regarded as dust and biomass burning mixture case.

Figure 6.1: Map showing the three principal AERONET sites analyzed, Banizoumbou, Skukuza and Ilorin.

6.2 Maxwell-Garnett conversion model retrieval

The approach of Maxwell-Garnett conversion model is used for demonstrating application of GRASP/Composition to AERONET Sun/sky photometric measurements.

6.2.1 Dust case

The retrieved volume concentrations (Figure 6.2) of aerosol composition at Banizoumbou site in April 2007 demonstrate the algorithm performance in the case of desert dust. The retrieved volume concentration of coarse dust and iron oxide presents a mean value of 1535.7 mm^3/m^2 and 22.9 mm^3/m^2, respectively, which corresponds to about 1.5% of iron oxide in coarse mode dust. The retrieved OC/dust component of the fine mode is regarded as fine dust because the Ångström Exponent is small (0.18). The retrieved concentrations of BC and BrC are low, however, not negligible in some days. It can be due to appearance of some anthropogenic component, but also due to substitution of fine mode iron oxide by BC or BrC. It can happen due to absence of iron oxide in modeling of the fine mode aerosol composition. Therefore, if iron oxide presents in fine mode, it can be substituted by some concentrations of BC or BrC. Since fine mode of pure dust is expected to be small, significance of this artificial BC or BrC concentrations should not be very important. The water and ammonium nitrate mainly present in coarse mode, however, their concentrations are much lower than that of dust. The relative contributions of water and ammonium nitrate to the coarse mode aerosol constitute on average 33% and 16%, respectively, while it is 50% for dust (see Figure 6.3).

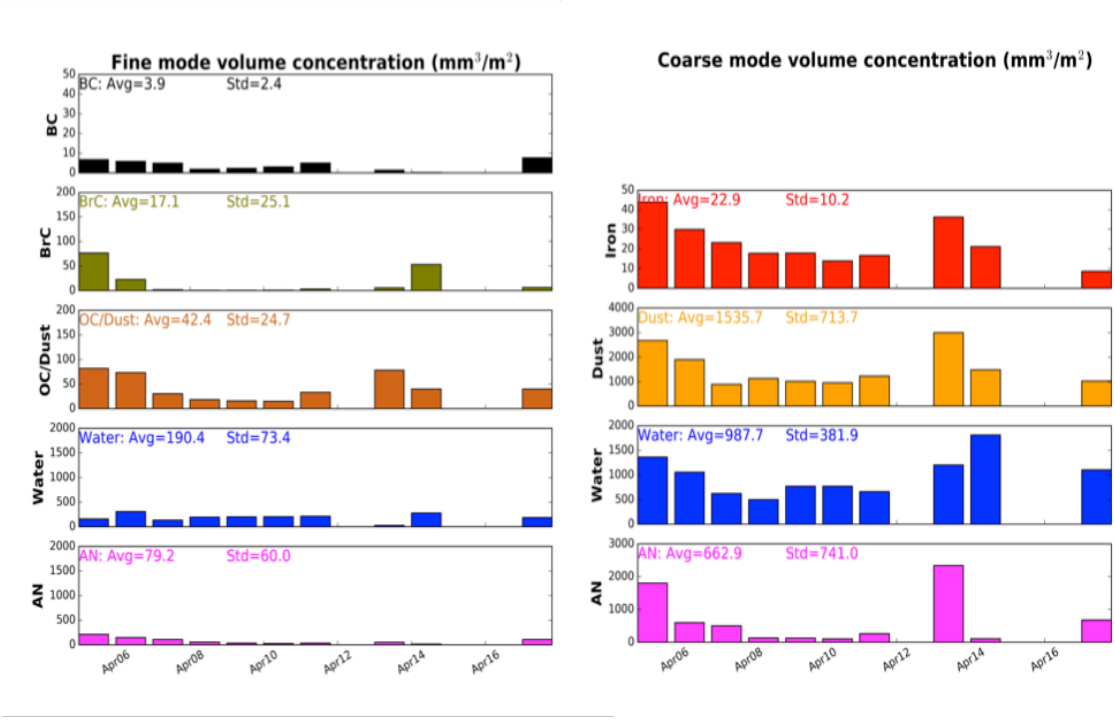

Figure 6.2: Volume concentration of aerosol composition at Banizoumbou AERONET site in April 2007 – represents a dust aerosol case. The retrievals are conducted using the Maxwell-Garnett conversion model.

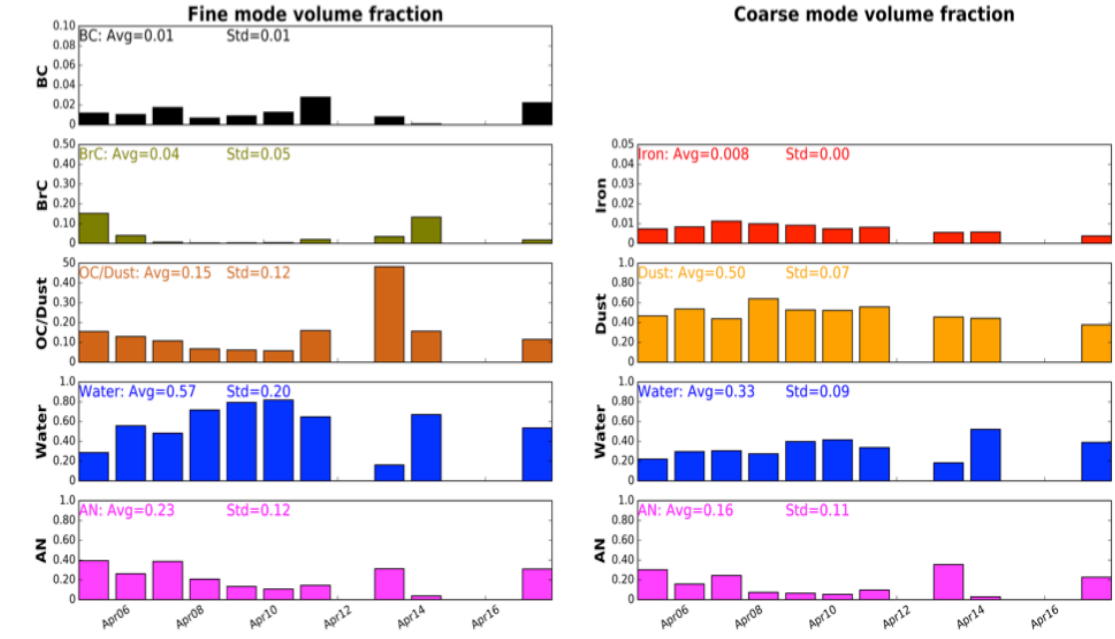

Figure 6.3: Volume fraction of aerosol composition at Banizoumbou AERONET site in April 2007 – represents a dust aerosol case. The retrievals are conducted using the Maxwell-Garnett conversion model.

6.2.2 Biomass burning case

Figure 6.4 and Figure 6.5 shows the volume concentration and fraction of aerosol composition at the Skukuza site in September 2007, which is regarded as biomass burning

aerosol case. It should be noted that the AOT in the case of Skukuza is considerably lower than in the case of Banizoumbou (see Figure 6.8). The volume concentrations, therefore, cannot be compared between two sites, but rather relative contributions of elements. The retrieved BC concentrations are relatively high and constitute on average 6% of fine mode aerosol concentration. The BrC concentrations, however, are low, and constitute only about 1%. It is noted that BC concentration is not very high with mean value of 8.4 mm^3/m^2 as the aerosol volume concentration is low (shown in Figure 6.8, AOT at 0.440 µm is around 0.5). The mean concentration of BrC is 0.8 mm^3/m^2. The composition of particles generated from different fires primarily depends on the nature of fuel (Turn et al., 1997). Biomass burning in the southern Africa generates more OC and less BrC, which is discussed in detail in Chapter 4. OC/dust retrieved in fine mode should be attributed to OC (Ångström Exponent of 1.5, is high in this case) and its mean fraction is 42%. Coarse dust and iron oxide concentrations are small with a mean value of 240.5 mm^3/m^2 and 0.4 mm^3/m^2, correspondingly, which is much less than that at Banizoumbou site (1535.7 mm^3/m^2 and 22.9 mm^3/m^2, correspondingly). In addition, water and ammonium nitrate are found nearly the same between the fine and coarse modes.

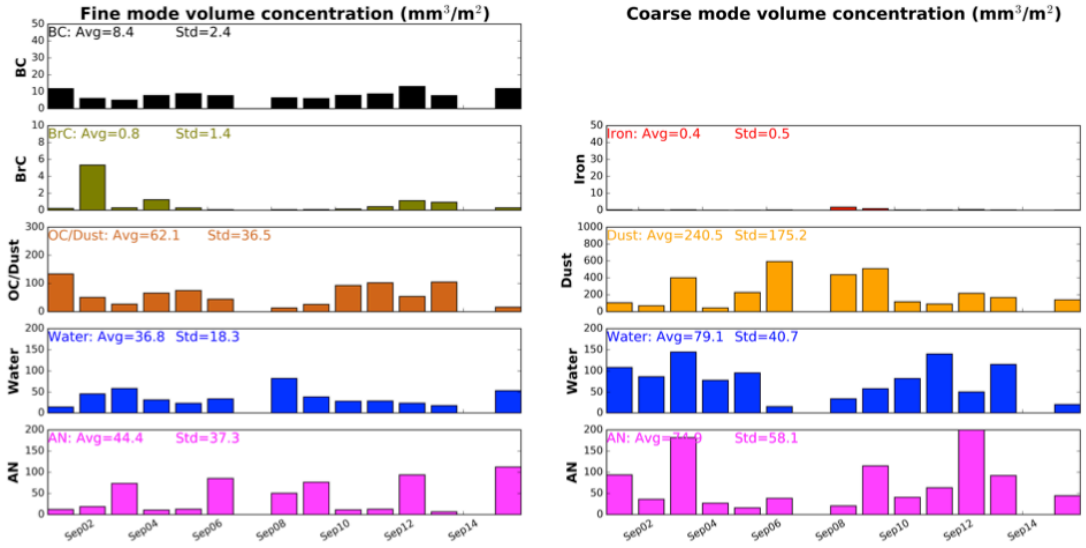

Figure 6.4: Volume concentration of aerosol composition at Skukuza AERONET site in September 2007 – represents a biomass burning aerosol case. The retrievals are conducted using the Maxwell-Garnett conversion model.

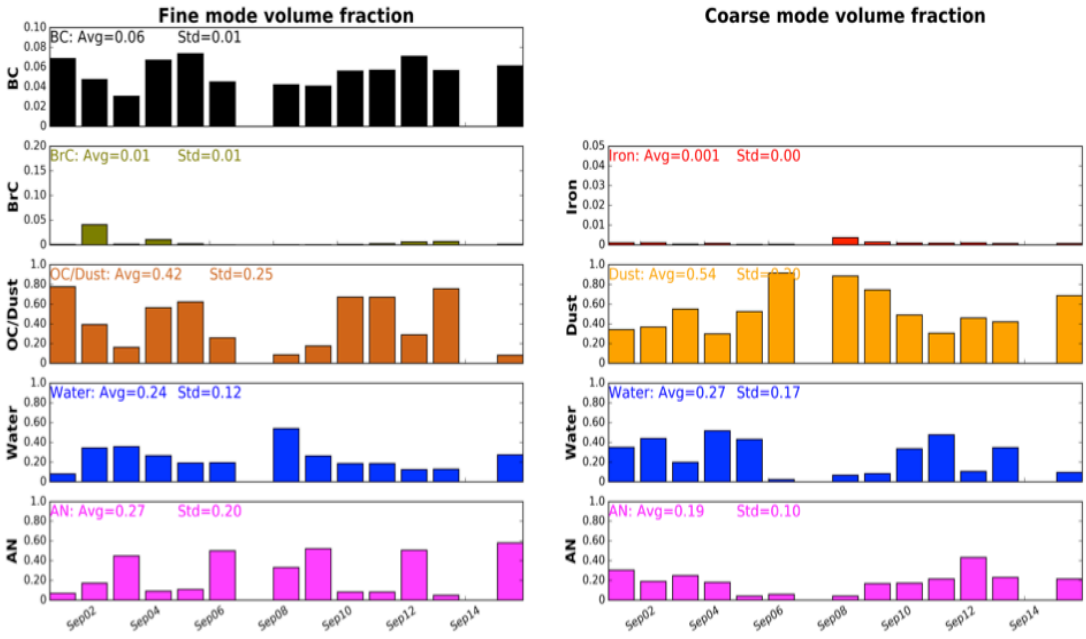

Figure 6.5: Volume fraction of aerosol composition at Skukuza AERONET site in September 2007 – represents a biomass burning aerosol case. The retrievals are conducted using the Maxwell-Garnett conversion model.

6.2.3 Mixing case

Figure 6.6 and 6.7 shows the volume concentration and fraction of aerosol composition at the Ilorin site in January 2007, which is regarded as a mixing of dust and biomass burning aerosol case. Since the Sahel biomass burning reaches its peak during DJF (Herman et al., 1997) associated with agricultural activities, dust transported from Sahara and emitted from the Bodélé depression may mix with the biomass burning particles. From inter-comparison between three presented sites it can be seen that the maximums of BrC volume concentration and fraction (the mean values of 127.9 mm^3/m^2 and 17%, respectively) are observed at the Ilorin site. As presented in chapter 4, higher BrC concentrations are also found over this area in the retrievals from POLDER/PARASOL observations. The mean value of BC concentration and fraction is 13.5 mm^3/m^2 and 2%, respectively. The OC/dust retrieved in fine mode should be attributed to a mixture of carbonaceous particles and dust particles (Ångström Exponent is about 0.5). Coarse dust and iron oxide concentration is retrieved with a mean value of 1412.4 mm^3/m^2 and 5.7 mm^3/m^2, respectively, which presents quite similar to Banizoumbou dust concentration, but significantly lower contribution of iron oxide. Water and ammonium nitrate fractions in fine mode (63% and 9%, respectively) are higher than that in coarse mode (42% and 5%, respectively), whereas the volume concentrations are higher in coarse mode because the volume concentrations of the entire coarse mode are more important.

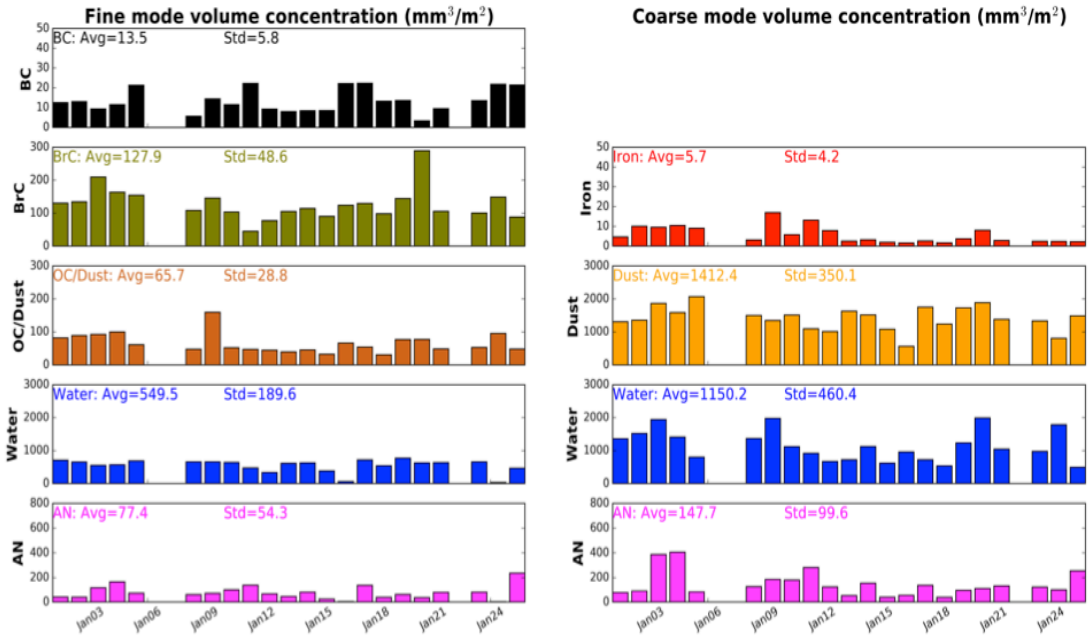

Figure 6.6: Volume concentration of aerosol composition at Ilorin AERONET site in January 2007 – represents a mixing of dust and biomass burning aerosol case. The retrievals are conducted using the Maxwell-Garnett conversion model.

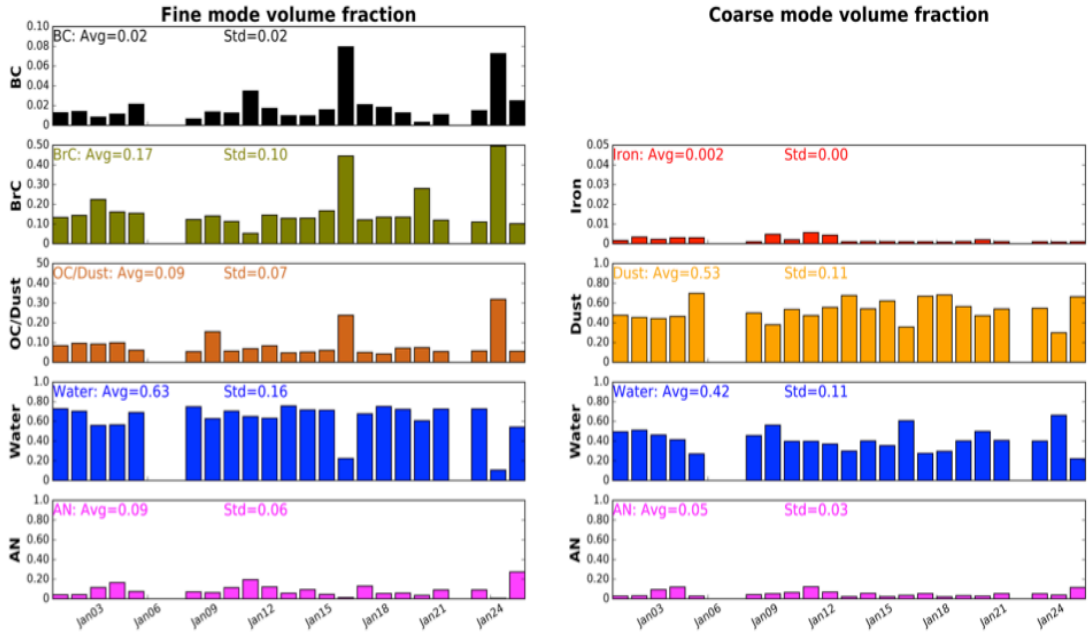

Figure 6.7: Volume fraction of aerosol composition at Ilorin AERONET site in January 2007 – represents a mixing of dust and biomass burning aerosol case. The retrievals are conducted using the Maxwell-Garnett conversion model.

6.3 Validation

6.3.1 Validation of aerosol optical property

Figure 6.8 presents the AOT and Ångström Exponent measured by AERONET versus those recalculated in GRASP retrieval procedure that implements aerosol composition model; the single-scattering albedo is that derived from conventional AERONET retrievals versus derived from GRASP/Composition retrievals. Figure6.8 shows that the aerosol properties are reproduced very well by GRASP/Composition approach not only for aerosol optical thickness and its spectral behavior, but also single-scattering albedo. The mean differences in AOT is about 0.01, which is on the level of AERONET calibration uncertainty, the difference in SSA is also well within the expected retrieval uncertainty of 0.03 (Dubovik at al., 2002). The correlation coefficient is nearly 1.0 for AOT and Ångström Exponent at Banizoumbou, Skukuza and Ilorin sites, respectively representing dust, biomass burning and mixing aerosol cases.

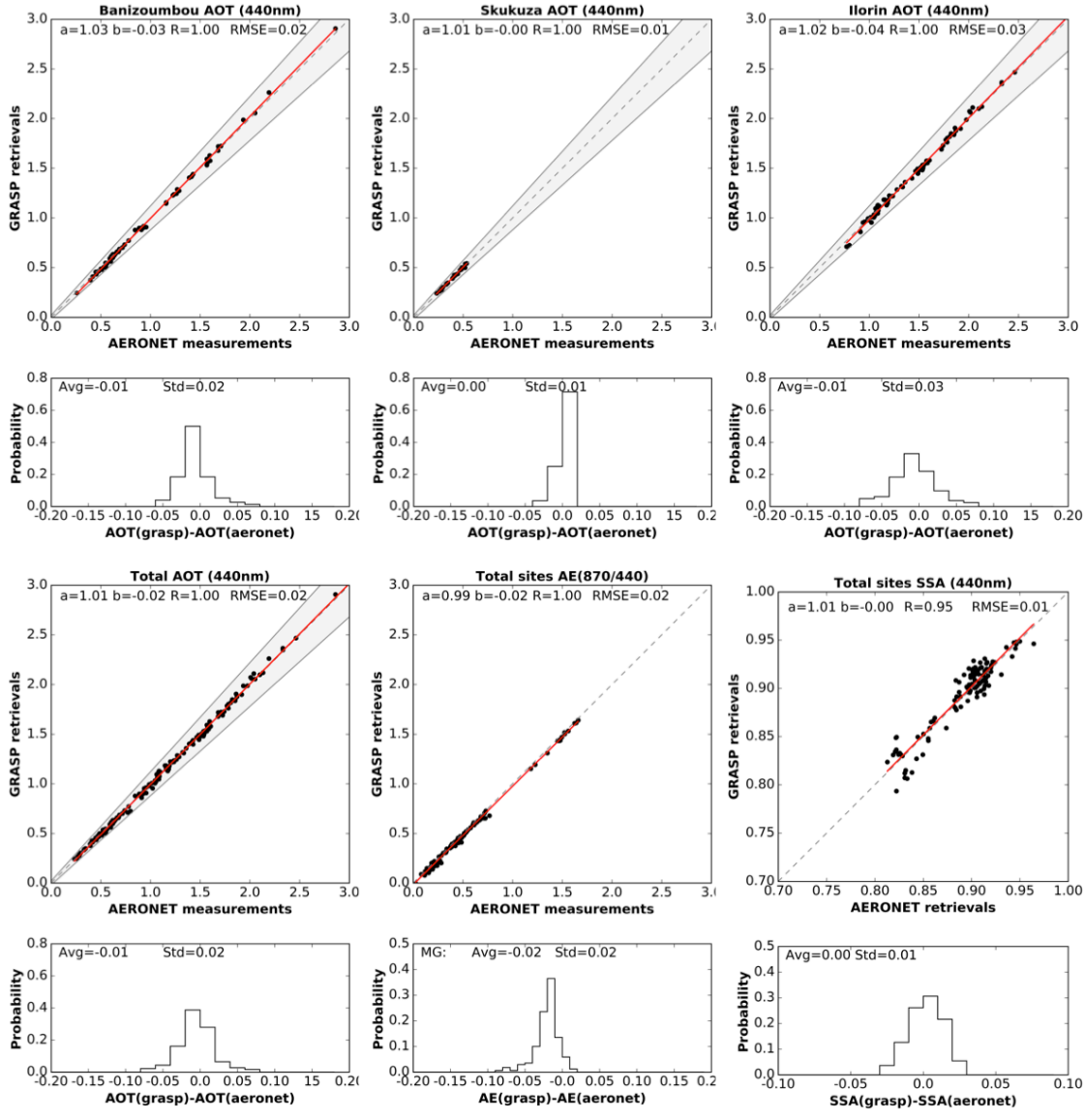

Figure 6.8: The comparison of aerosol optical properties derived from Sun/sky photometer measurements by GRASP using the Maxwell-Garnett conversion model with the corresponding values provided by AERONET conventional algorithm.

Chapter 7

Conclusion

"Life's like a movie, write your own ending."

------ Jim Henson

The information about composition of atmospheric aerosols has a great importance for various aspects of monitoring and understanding of climate and environment dynamics. Such information can be obtained using in situ sampling measurements or simulation by chemical transport models. However, in situ samplings have limited spatial and temporal coverage, while model estimations have large uncertainties. This thesis has discussed in detail a new approach of atmospheric aerosol composition retrieval from remote sensing observations. The methodology was developed and implemented in GRASP algorithm that is designed to invert the remote sensing observations from space-borne and ground-based instruments. The main goals were (ⅰ) to identify an adequate conversion model for linking refractive index to aerosol composition, which could cover entire range of aerosol complex refractive index and, simultaneously, should provide unique correspondence between each spectral realization of refractive index and aerosol composition; (ⅱ) to monitor and investigate the temporal and spatial variations of aerosol composition retrieved from remote sensing observations with wide spatial coverage and in different seasons; (ⅲ) to provide a useful data for the modelers constraining their model simulations globally or over regions where otherwise no data on aerosol composition is available, and to improve the accuracy and capability of aerosol model simulation.

In contrast to the majority of existing aerosol retrieval algorithms fitting the intermediate retrieval of the refractive index, the one developed in this work is fitting directly the remote sensing data (radiance and polarization) by a set of aerosol composition fraction for both fine and coarse aerosol modes, as well as by aerosol parameters such as sizes and shape; the spectral complex refractive index is then calculated from the retrieved aerosol composition

fractions. The approach is not only limited to the space-borne and ground-based instruments, but can be used for retrievals from all possible existing remote sensing instruments, both passive and active.

Chapter 3 shows the detailed descriptions of the full set of formulations necessary for realizing a aerosol composition approach developed for deriving detailed aerosol properties from remote sensing measurements, as well as a series of sensitivity tests conducted for the aerosol composition conversion model. The synthetic data were designed to mimic observations of real aerosol including composition information. Results of the tests showed that utilization of both the volume-weighted and Maxwell-Garnett conversion models allows the retrieval to distinguish amongst the assumed aerosol compositions with acceptable accuracy in all considered situations.

The performance of the developed algorithm has been demonstrated by application to POLDER/PARASOL observations in the chapter 4 and chapter 5. The obtained patterns of aerosol composition distribution agree with known physical expectations. BC, BrC and OC exhibit a pronounced seasonal cycle with high variability and their trends are similar to each other, which is mainly attributed to temporal variations of biomass burning in Africa and South America, but also to anthropogenic pollution in Asia (in particular India and China). BC and OC were found mainly be enriched in the areas near biomass burning emissions, whereas BrC is generally found concentrated in downwind regions of biomass burning. Indeed, generally organic particles are not aggregated in young smoke, but occur during aging that can form carbonaceous compound whose optical properties are similar to BrC. It is also noted that the fires occurring in northern Africa during DJF generate larger ratio of BC to OC than that in southern Africa during SON and JJA.

Dust and iron oxide concentration show a similar seasonal cycle with high variability, reaching a peak during MAM and a minimum during SON. Higher dust and iron oxide concentration are observed during MAM and JJA. The dust emissions during this period originate from the global dust belt extending from the west coast of North Africa, through the Middle East to Central Asia. It covers Sahara, Arabian Peninsula, Caspian Sea and Aral Sea regions in Central Asia, and Gobi and Taklimakan in China. Dust was also detected in the USA and Mexico during MAM and JJA. The maximums of iron oxide concentration are not co-located with those of dust; it is because the elemental and mineralogical composition of mineral dust can vary depending on the source region of emission.

The aerosol water content is retrieved for both fine and coarse size fractions in the volume-weighted conversion model and ammonium nitrate is also retrieved for both fine and coarse size fractions in the Maxwell-Garnett conversion model. Water content and ammonium nitrate

concentration for the aerosols over China and India are observed with large values, especially in fine mode during DJF and SON (see Figure 5.11), which is attributed to the industrial aerosols of megacities with high population density and pollution level (e.g., ammonium nitrate and ammonium sulfate). In addition, the coarse fraction water concentration is notably smaller over land than over ocean; the fine fraction, however, has nearly same variability over land and over ocean. The coarse mode aerosols over land are usually constituted of mineral dust, which is generally hydrophobic. Over ocean, however, the elevated coarse mode aerosol water content is logically corresponds to coarse particles of the sea salt aerosol.

An inter-comparison of aerosol optical properties derived from GRASP/Composition and from standard AERONET products demonstrated a very good agreement, whatever volume-weighted or Maxwell-Garnett conversion model was used. The comparison of BC retrieved by GRASP/Composition with corresponding values simulated by GEOS-5/GOCART chemical transport model has shown that the values of the modeled BC concentration are lower for biomass burning regions in Africa, but higher for anthropogenic pollution regions in Asia. However, the values of modeled by GEOS-5/GOCART coarse dust concentration are higher than the retrieved by GRASP/Composition in dust-dominated regions.

In the chapter 6, the Maxwell-Garnett conversion model in GRASP was applied to ground-based AERONET Sun/sky photometric measurements. Results demonstrate that the proposed approach can distinguish the aerosol compositions; the test ware conducted for sites dominated by dust, biomass burning, and mixture of dust and biomass burning aerosol. The GRASP/Composition retrievals of AOT, Ångström Exponent and single-scattering albedo presented a good agreement with the AERONET standard product.

As for limitations of the presented algorithm as applied to POLDER/PARASOL, a lack of sensitivity for distinguishing between iron oxide and absorbing carbonaceous species (BC and BrC) can be indicated. It is same for distinguishing between OC and dust. Thus, iron oxide is assumed to be in coarse mode, and BC and BrC in fine mode. The assumption can lead to some misinterpretation of presence of carbonaceous aerosol in pure dust regions, and vice versa, presence of iron oxide in pure biomass burning events. In addition, the discontinuity appearing only for coarse mode water content and ammonium nitrate between over land and over ocean retrievals observed around the Arabian Peninsula and Western Africa can be observed. Worth noting also that some mountains separate land and sea around the Arabian Peninsula, especially Red Sea, which can be a natural barrier between continental and marine aerosols. In addition, statistics of the pixels available for the retrievals from POLDER/PARASOL (see Figure 5.1) shows that the number of pixels over land is significantly higher than over ocean, which is rather due to cloud contamination. This

discontinuity in the pixel statistics can also affect the mean values of the retrieved concentrations.

The main perspective of this work is in constraining the chemical transport models, as discussed already. In addition, the product directly provides the aerosol classification and can be used for improvement of the particulate matter (PM) evaluation from remote sensing by means of better identification of the aerosol particles density for conversion of optical properties to mass concentration. Therefore, it is believed that the results of this work will significantly contribute to evaluation of aerosol climate forcings and environmental effects.

Bibliography:

Abdou, W., Diner, D., Martonchik, J., Bruegge, C., Kahn, R., Gaitley, B., and Crean, K.: Comparison of coincident MISR and MODIS aerosol optical depths over land and ocean scenes containing AERONET sites, J. Geophy. Res., 110, D10S07, doi:10.1029/2004JD004693, 2005.

Abel, S. J., Haywood, J. M., Highwood, E. J., Li, J., and Buseck, P. R.: Evolution of biomass burning aerosol properties from an agricultural fire in southern Africa, Geophys. Res. Lett., 30(15), 1783, doi:10.1029/2003GL017342, 2003.

Adams, P., Seinfeld, J., and Koch, D.: Global concentrations of tropospheric sulfate, nitrate, and ammonium aerosol simulated in a general circulation model, J. Geophys. Res., 104, 13791-13823, 1999.

Albrecht, B. A.: Aerosols, cloud microphysics, and fractional cloudiness, Science, 245, 1227, 1989.

Alfaro, S. C., Gaudichet, A., Gomes, L., and Maillé, M.: Mineral aerosol production by wind erosion: aerosol particle sizes and binding energies, Geophys. Res. Lett., 25, 991-994, 1998.

Alleaume, S., Hely, C., Le Roux, J., Koronitzi, S., Swap, R. J., Shugar, H. H., and Justice, C. O.: Using MODIS to evaluate heterogeneity of biomass burning in southern African savannas: A case study in Etosha, Int. J. Remote Sens., 26, 4219-4237, 2005.

Andreae, M. O., and Crutzen, P.: Atmospheric aerosols: Biogeochemical sources and role in atmospheric chemistry, Science, 276, 1052-1058, doi:10.1126/science.276.5315.1052, 1997.

Andreae, M. O., and Gelencsér, A.: Black carbon or brown carbon? The nature of light-absorbing carbonaceous aerosols, Atmos. Chem. Phys., 6(10), 3131-3148, 2006.

Andreae, M. O., Jones, C. D., and Cox, P. M.: Strong present-day aerosol cooling implies a hot future, Nature, 435(7046), 1187-1190, 2005.

Andreae, M. O.: Global distribution of fires seen from space, Eos Trans. AGU, 74, 129, 1993.

Andreae, M. O., and Merlet, P.: Emission of trace gases and aerosols from biomass burning, Global Biogeochem Cycles., 15(4), 955-966, 2001.

Ångström, A. K.: On the atmospheric transmission of Sun radiation and on dust in the air, Geogr. Ann., 11. 156-166, Doi: 10.2307/519399, 1929.

Ansmann, A., Baars, H., Tesche, M., Muller, D., Althausen, D., Engelmann, R., Pauliquevis, T., and Artaxo, P.: Dust and smoke transport from Africa to South America: Lidar profiling over Cape Verde and the Amazon rainforest, Geophys. Res. Lett., 36, L11802, 2009.

Antuña, J., Andrade, M., Landulfo, E., Clemesha, B., Quel, E., and Bastidas, A.: Building a Lidar network in Latin America: Progress and difficulties, in 23rd International Laser Radar Conference, Nara, Japan, July 24-28, 2006.

Arimoto, R., Balsam, W., Schloesslin, C.: Visible spectroscopy of aerosol particles collected on filters: iron-oxide minerals, Atmospheric Environment, 36(1), 89-96, 2002.

Arola, A., Schuster, G., Myhre, G., Kazadzis, S., Dey, S., and Tripathi, S. N.: Inferring absorbing organic carbon content from AERONET data, Atmos. Chem. Phys., 11(1), 215-225, 2011.

Ault, A. P., and Axson, J. L.: Atmospheric aerosol chemistry: spectroscopic and microscopic advances, Anal. Chem., 89(1), 430-452, 2017.

Barbosa, P. M., Grégoire, J. M., and Pereira, J. M. C.: An algorithm for extracting burned areas from time series of AVHRR GAC data applied at a continental scale, Remote Sens. Environ., 69, 253-263, 1999.

Bellouin, N., Jones, A., Haywood, J., and Christopher, S. A.: Updated estimate of aerosol direct radiative forcing from satellite observations and comparison against the Hadley Centre climate model, Journal of Geophysical Research, 113, D10205, doi:10.1029/2007JD009385, 2008.

Bernstein, J. A., Alexis, N., Barnes, C., Bernstein, I. L., Nel, A., Peden, D., Dian-Sanchez, D., Tarlo, S. M., and Williams, P. B.: Health effects of air pollution, J. Allergy Clin. Immunol., 114, 1116-1123, 2004.

Bevington, P. R.: Data reduction and error analysis for the physical sciences, McGraw-Hill, 1969.

Bian, H., Chin, M., Kawa, S. R., Duncan, B., Arellano, A., and Kasibhatla, P.: Sensitivity of global CO simulations to uncertainties in biomass burning sources, J. Geophys. Res., 112, D23308, doi:10.1029/2006JD008376, 2007.

Bohren, C., and Huffman, D.: Absorption and scattering of light by small particles, Wiley-VCH Verlag GmbH and Co. KGaA, 1983.

Bond, T. C., and Bergstrom, R. W.: Light absorption by carbonaceous particles: An investigative review, Aerosol science and technology, 40(1), 27-67, doi: 10.1080/02786820500421521, 2006.

Bond, T. C., Doherty, S. J., Fahey, D. W., Forster, P. M., Berntsen, T., DeAngelo, B. J., Flanner, M. G., Ghan, S., Kärcher, B., Koch, D., Kinne, S., Kondo, Y., Quinn, P. K., Sarofim, M. C., Schultz, M. G., Schulz, M., Venkataraman, C., Zhang, H., Zhang, S., Bellouin, N., Guttikunda, S. K., Hopke, P. K., Jacobson, M. Z., Kaiser, J. W., Klimont, Z., Lohmann, U., Schwarz, J. P., Shindell, D., Storelvmo, T., Warren, S. G., and Zender, C. S.: Bounding the role of black carbon in the climate system: A scientific assessment, J. Geophys. Res., 118(11), 5380-5552, 2013.

Bond, T. C., Charlson, R. J., and Heintzenberg, J.: Quantifying the emission of light-absorbing particles: Measurements tailored to climate studies, Geophys. Res. Lett., 25(3), 337-340, 1998.

Bösenberg, J., and Hoff, R.: Plan for the implementation of the GAW Aerosol Lidar Observation Network GALION, WMO/TD-No. 1443 178, GAW, 2007.

Bösenberg, J.: EARLINET-A European Aerosol Research Lidar Network, advances in laser remote sensing, in: Selected papers 20th Int. Laser Radar Conference (ILRC), Vichi, France, 10-14 July 2000, pp. 155-158, 2000.

Boucher, O.: Air traffic may increase cirrus cloudiness, Nature, 397, 30-31, 1999.

Brook, R. D., Rajagopalan, S., Pope, C. A., Brook, J. R., Bhatnagar, A., Diez-Roux, A. V., Holguin, F., Hong, Y., Luepker, R. V., Mittleman, M. A., Peters, A., Siscovick, D., Smith, S. C., Whitsel, L., and Kaufman J. D.: Particulate matter air pollution and cardiovascular disease, Circulation, 121(21), 2331-2378, 2010.

Brooks, N., and Legrand, M.: Dust variability over northern Africa and rainfall in the Sahel, in Linking Climate Change to Land Surface Change, edited by S. McLaren and D. Kniveton, pp. 1 - 25, Springer, New York, 2000.

Buajarern, J., Mitchem, L., Reid, J. P.: Characterizing multiphase organic/inorganic/aqueous aerosol droplets, J. Phys. Chem. A, 111(50), 13038-13045, 2007.

Cahoon, D. R. Jr., Stocks, B. J., Levine, J. S., Cofer III, W. R., and O'Neill, K. P.: Seasonal distribution of African savanna fires, Nature, 359, 812-815, 1992.

Caquineau, S., Gaudichet, A., Gomes, L., and Legrand, M.: Mineralogy of Saharan dust transported over northwestern tropical Atlantic Ocean in relation to source regions, J. Geophys. Res., 107, 4251, doi:10.1029/2000jd000247, 2002.

Caquineau, S., Magonthier, M.-C., Gaudichet, A., and Gomes, L.: An improved procedure for the X-ray diffraction analysis of low-mass atmospheric dust samples, Eur. J. Mineral., 9, 157-166, 1997.

Carslaw, K. S., Boucher, O., Spracklen, D. V., Mann, G. W., Rae, J. G. L., Woodward, S., and Kulmala, M.: A review of natural aerosol interactions and feedbacks within the Earth system, Atmos. Chem. Phys., 10, 1701-1737, doi:10.5194/acp-10-1701-2010, 2010.

Chaikovsky, A., Bril, A., Denisov, S., and Balashevich, N.: Algorithms and software for lidar data processing in GIS-LiNet, in: Reviewed and Revised Papers Presented at the 23rd International Laser radar Conference, 24-28 July 2006, Nara, Japan, edited by Chikao Nagasave, N. S., pp. 667-670, 2006.

Chami, M., Santer, R., and Dilligeard, E.: Radiative transfer model for the computation of radiance and polarization in an atmosphere-ocean system: polarization properties of suspended matter for remote sensing, Appl. Optics, 40, 2398-2416, 2001.

Charlock, T. P., and Sellers, W. D.: Aerosol effects on climate: Calculations with time-dependent and steady-state radiative-convective models, J. Atmos. Sci., 37, 1327-1341, 1980.

Chen, C. and Cahan, B.: Visible and ultraviolet optical properties of single-crystal and polycrystalline hematite measured by spectroscopic ellipsometry, J. Opt. Soc. Am., 71, 932-934, 1981.

Chen, W., Kahn, R., Nelson, D., Yau, K., and Seinfeld, J.: Sensitivity of multi-angle imaging to optical and microphysical properties of biomass burning aerosols, Journal of Geophysical Research, 113, D10203, doi:10.1029/2007JD009414, 2008.

Chen, Y., and Bond, T. C.: Light absorption by organic carbon from wood combustion, Atmospheric Chemistry and Physics, 10(4), 1773-1787, 2010.

Chin, M., Diehl, T., Dubovik, O., Eck, T. F., Holben, B. N., Sinyuk, A., and Streets, D. G.: Light absorption by pollution, dust, and biomass burning aerosols: a global model study and evaluation with AERONET measurements, Ann. Geophys., 27, 3439-3464, 2009a.

Chin, M., Kahn, R. A., Remer, L. A., Yu, H., Rind, D, Feingold, G., Quinn, P. K., Schwartz, S. E., Streets, D. G., DeCola, P., and Halthore, R: Atmospheric aerosol properties and climate impacts, Tech. rep., U.S., 2009b.

Chin, M., Ginoux, P., Kinne, S., Torres, O., Holben, B. N., Duncan, B. N., Martin, R. V., Logan, J. A., Higurashi, A., and Nakajima, T.: Tropospheric aerosol optical thickness from the GOCART model and comparisons with satellite and Sun photometer measurements, 59(3), 461-483, 2002.

Choobari, O. A., Zawar-Reza, P., and Sturman, A.: Low level jet intensification by mineral dust aerosols. Ann. Geophys., 31, 625-632, doi: 10.5194/angeo-31-625-2013, 2013.

Choobari, O. A., Zawar-Reza, P., and Sturman, A.: The global distribution of mineral dust and its impacts on the climate system: a review. Atmos. Res., 138, 152-165, 2014.

Chowdhary, J., Cairns, B., and Travis, L. D.: Case studies of aerosol retrievals over the ocean from multiangle, multispectral photopolarimetric remote sensing data, J. Atmos. Sci., 59, 383-397, 2002.

Chowdhary , J., Cairns, B., Mishchenko, M. I., Hobbs, P. V., Cota, G. F., Redemann, J., Rutledge, K., Holben, B. N., and Russell, E.: Retrieval of aerosol scattering and absorption properties from photopolarimetric observations over the ocean during the CLAMS experiment, J. Atmos. Sci., 62, 1093-1117, 2005.

Chowdhary, J., Cairns, B., and Travis, L. D.: Contribution of water-leaving radiance to multiangle, multispectral polarization observations over the open ocean: bio-optical model results for case 1 water, Appl. Optics, 45, 5543-5567, 2006.

Chylek, P., and Coakley, J. A.: Aerosols and climate, Science, 183, 75-77, 1974.

Claquin, T., Schulz, M., and Balkanski, Y. J.: Modeling the mineralogy of atmospheric dust sources, J. Geophys. Res., 104, 22243-22256, 1999.

Collins, W., Rasch, P., Eaton, B., Khattatov, B., Lamarque, J., and Zender, C.: Simulating aerosols using a chemical transport model with assimilation of satellite aerosol retrievals: Methodology for INDOEX, Journal of Geophysical Research, 106, 7313-7336, 2001.

Cooke, W. F., Liousse, C., Cachier, H., and Feichter, J.: Construction of a 1° × 1° fossil fuel emission data set for carbonaceous aerosol and implementation and radiative impact in the ECHAM4 model, J. Geophys. Res., 104(D18), 22137–22162, doi:10.1029/1999JD900187, 1999.

Costa, M., Levizzani, V., and Silva, A. M.: Part Ⅱ: Aerosol characterization and direct radiative forcing assessment over the ocean: Application to test cases and validation, Journal of Applied Meteorology, 43, 1818-1833, 2004.

Cox, C., and Munk, W.: Measurements of the roughness of the sea surface from photographs of the Sun's glitter, J. Opt. Soc. Am., 44, 838-850, 1954.

Crutzen, P. J., and Andreae, M. O.: Biomass burning in the tropics: Impacts on atmospheric chemistry and biogeochemical cycles, Science., 250, 1669-1678, 1990.

Crutzen, P. J., Heidt, L. E., Krasnec, J. P., Pollock, W. H., and Seiler, W.: Biomass burning as a source of atmospheric gases CO, H_2, N_2O, NO, CH_3Cl and COS, Nature., 282, 253-256, 1979.

Dai, A.: Drought under global warming: a review, Wiley Interdisciplinary Reviews: Climate Change, 2, 45-65, doi:10.1002/wcc.81, 2011.

Deboudt, K., Flament, P., Choël, M., Gloter, A., Sobanska, S., and Colliex C.: Mixing state of aerosols and direct observation of carbonaceous and marine coatings on African dust by individual particle analysis, J. Geophys. Res., 115, D24207, doi:10.1029/2010JD013921, 2010.

Decesari, S., Facchini, M. C., Carbone, C., Giulianelli, L., Rinaldi, M., Finessi, E., Fuzzi, S., Marinoni, A., Cristofanelli, P., Duchi, R., Bonasoni, P., Vuillermoz, E., Cozic, J., Jaffrezo, J., L., and Laj, P.: Chemical composition of PM10 and PM1 at the high-altitude Himalayan station Nepal Climate Observatory-Pyramid (NCO-P) (5079 m a.s.l.), Atmos. Chem. Phys., 10, 4583-4596, 2010.

Delmas, R. A., Loudjani, P., Podaire, A., and Menaut, J.-C.: Biomass burning in Africa: An assessment of annually burned biomass, in Global Biomass Burning, Atmospheric, Climatic, and Biospheric Implications, edited by J. S. Levine, pp. 126-132, MIT Press, Cambridge, Mass, 1991.

Derimian, Y., Karnieli, A., Kaufman, Y. J., Andreae, M. O., Andreae, T. W., Dubovik, O., Maenhaut, W., and Koren, I.: The role of iron and black carbon in aerosol light absorption, Atmos. Chem. Phys., 8, 3623-3637, 2008.

Deschamps, P. Y., Bréon, F. M., Leroy, M., Podaire, A., Bricaud, A., Buriez, J. C. and Seze, G.: The POLDER mission: Instrument characteristics and scientific objectives, IEEE Transactions on geoscience and remote sensing, 32(3), 598-615, 1994.

Deuzé, J., Bréon, F., Devaux, C., Goloub, P., Herman, M., Lafrance, B., Maignan, F., Marchand, A., Nadal, F., Perry, G., and Tanré, D.: Remote sensing of aerosols over land surfaces from POLDER-ADEO-1 polarized measurements, Journal of Geophysical Research, 106, 4913-4926, 2001.

Diner, D., Beckert, J., Bothwell, G., and Rodriguez, J.: Performance of the MISR instrument during its first 20 months in Earth orbit, IEEE Transactions on Geoscience and Remote Sensing, 40, 1449-1466, 2002.

Dinar, E., Riziq, A. A., Spindler, C., Erlick, C., Kiss, G., and Rudich, Y.: The complex refractive index of atmospheric and model humic-like substances (HULIS) retrieved by a cavity ring down aerosol spectrometer (CRD-AS), Faraday discussions, 137, 279-295, 2008.

Dockery, D. W., Pope, C. A., Xu, X. P., Spengler, J. D., Ware, J. H., Fay, M. E., Ferris, B. G., and Speizer, F. E.: An association between air-pollution and mortality in 6 United States Cities, New England Journal of Medicine, 329, 1753-1759, 1993.

Dockery, D. W., Speizer, F. E., Stram, D. O., Ware, J. H., Spengler, J. D., and Ferris, B. G.: Effects of inhalable particles on respiratory health of children, American Review of Respiratory Disease, 139, 587-294, 1989.

Doicu, A.: Numerical regularization for atmospheric inverse problem, Springer, Berlin, 2010.

Downing, H. G., and Williams, D.: Optical constants of water in the infrared, J. Geophys. Res., 80, 1656-1661, 1975.

Dubovik, O., and King, M.: A flexible inversion algorithm for retrieval of aerosol optical properties from Sun and sty radiance measurements, J. Geophys. Res., 105, 20673-20696, 2000.

Dubovik, O., Holben, B. N., Eck, T. F., Smirnov, A., Kaufman, Y. J., King, M. D., Tanré, D., and Slutsker, I.: Variability of absorption and optical properties of key aerosol types observed in worldwide locations, J. Atmos. Sci., 59(3), 590-608, 2002a.

Dubovik, O., Holben, B. N., Lapyonok, T., Sinyuk, A., Mishchenko, M. I., Yang, P., and Slutsker, I.: Non-spherical aerosol retrieval method employing light scattering by spheroids, Geophys. Res. Lett., 29, 1415, doi:10.1029/2001GL014506, 2002b.

Dubovik, O., Herman, M., Holdak, A., Lapyonok, T., Tanré, D., Deuzé, J. L., Ducos, F., Sinyuk, A., and Lopatin, A.: Statistically optimized inversion algorithm for enhanced retrieval of aerosol properties from spectral multi-angle polarimetric satellite observations, Atmos. Meas. Tech., 4, 975-1018, 2011.

Dubovik, O., Lapyonok, T., Litvinov, P., Herman, M., Fuertes, D., Ducos, F., Lopatin, A., Chaikovsky, A., Torres, B., Derimian, Y., Huang, X., Aspetsberger, M., and Federspiel, C.: GRASP: a versatile algorithm for characterizing the atmosphere, SPIE Newsroom, 25, 2014.

Dubovik, O.: Optimization of numerical inversion in photopolarimetric remote sensing, in photopolarimetry in remote sensing (pp. 65-106), Springer Dordrent, 2004.

Dubovik, O., Lapyonok, T., Kaufman, Y., Chin, M., Ginoux, P., Kahn, R. A., and Sinyuk, A.: Retrieving global aerosol sources from satellites using inverse modeling, Atmos. Chem. Phys., 8, 209-250, doi:10.5194/acp-8-209-2008, 2008.

Dubovik, O., Lapyonok, T., Kaufman, Y., Chin, M., Ginoux, P., and Sinyuk, A.: Retriving global sources of aerosols from MODIS observations by inverting GOCART model, Atmospheric Chemistry and Physics Discussions, 7, 3629-3718, 2007.

Dubovik, O., Smirnov, A., Holben, B. N., King, M. D., Kaufman, Y. J., Eck, T. F., and Slutsker, I.: Accuracy assessments of aerosol optical properties retrieved from Aerosol Robotic Network (AERONET) Sun and sky radiance measurements, J. Geophys. Res., 105(D8), 9791-9806, doi:10.1029/2000JD900040, 2000.

Dubovik, O., Smirnov, A., Lapyonok, T., Sinyuk, A., Mishchenko, M. I., Yang, P., Eck, T. F., Volten, H., Munoz, O., Veihelmann, B., van der Zander, W. J., Sorokin, M., and Slutsker, I.: Application of light scattering by spheroids for accounting for particle non-sphericity in remote sensing of desert dust, J. Geophys. Res., 111, D11208, doi:10.1029/2005JD006619, 2006.

Duncan, B. N., Martin, R. V., Staudt, A. C., Yevich, R., and Logan, J. A.: Interannual and seasonal variability of biomass burning emissions constrained by satellite observations, J. Geophys. Res., 108(D2), 4100, doi:10.1029/2002JD002378, 2003.

Eck, T. F., Holben, B. N., Reid, J. S., Dubovik, O., Smirnov, A., O'Neill, N. T., Slutsker, I., and Kinne, S.: Wavelength dependence of the optical depth of biomass burning, urban, and desert dust aerosols, J. Geophys. Res., 104(D24), 31333-31349, 1999.

Eck, T. F., Holben, B. N., Ward, D. E., Mukelabai, M. M., Dubovik, O., Smirnov, A., Schafer, J. S., Hsu, N. C., Piketh, S. J., Queface, A., Le Roux, J., Swap, R. J., and Slutsker, I.: Variability of biomass burning aerosol optical characteristics in southern Africa during the SAFARI 2000 dry season campaign and a comparison of single scattering albedo estimates from radiometric measurements, J. Geophys. Res., 108(D13), 8477, doi:10.1029/2002JD002321, 2003.

Engelstaedter, S., Tegen, I., and Washington, R.: North African dust emissions and transport. Earth-Sci. Rev., 79 (1-2), 73-100, 2006.

Fairlie, T. D., Jacob, D. J., Dibb, J. E., Alexander, B., Avery, M. A., van Donkelaar, A., and Zhang, L.: Impact of mineral dust on nitrate, sulfate, and ozone in transpacific Asian pollution plumes, Atmos. Chem. Phys., 10, 3999-4012, doi:10.5194/acp-10-3999-2010, 2010.

Feingold, G., Eberhard, W., Veron, D., and Previdi, M.: First measurements of the Twomey indirect effect using ground-based remote sensors, Geophysical Research Letters, 30, 1287, 2003.

Finlayson-Pitts, B. J., Pitts, J. N.: Tropospheric air pollution: ozone, airborne toxics, polycyclic aromatic hydrocarbons, and particles, Science, 276, 1045-1051, 1997.

Formenti, P., Caquineau, S., Chevaillier, S., Klaver, A., Desboeufs, K., Rajot, J. L., Belin, S., and Briois, V.: Dominance of goethite over hematite in iron oxides of mineral dust from Western Africa: Quantitative partitioning by X-ray absorption spectroscopy, Journal of Geophysical Research: Atmospheres, 119(22), doi:10.1002/2014JD021668, 2014a.

Formenti, P., Caquineau, S., Desboeufs, K., Klaver, A., Chevaillier, S., Journet, E., and Rajot, J. L.: Mapping the physico-chemical properties of mineral dust in western Africa: mineralogical composition, 14, 10663-10686, doi:10.5194/acp-14-10663-2014, 2014b.

Formenti, P., Rajot, J. L., Desboeufs, K., Caquineau, S., Chevaillier, S., Nava, S., Gaudichet, A., Journet, E., Triquet, S., Alfaro, S., Chiari, M., Haywood, J. M., Coe, H., and Highwood, E. J.: Regional variability of the composition of mineral dust from Western Africa: results from the AMMA SOP0/DABEX and DODO, J. Geophys. Res., 113, D00C13, 2008.

Forster, P., et al.: Changes in atmospheric constituents and in radiative forcing, in Climate Change 2007: The Physical Science Basis. Contribution of Working Group I to the Fourth Assessment Report of the Intergovernmental Panel on Climate Change, Cambridge Univ. Press, Cambridge, U.K. and New York, NY, USA, 2007.

Garstang, M., Ellery, W. N., Scholes, T. S., Scholes, M. C., Swap, R. J., and Tyson, P. D.: The contribution of aerosol- and water- borne nutrients to the functioning of the Okavango Delta, Botswana, S. Afr. J. Sci., 94, 215-222, 1998.

Gasse, F.: Diatom inferred salinity and carbonate oxygen isotopes in Holocene waterbodies of the western Sahara and Sahel (Africa), Quat. Sci. Rev., 21, 737-767, 2002.

Gauderman, W. J., Avol, E., Gilliland, F., Vora, H., Thomas, D., Berhane, K., McConnell, R., Kuenzli, N., Lurmann, F., Rappaport, E., Margolis, H., Bates, D., and Peters, J.: The effect of air pollution on lung development from 10 to 18 years of age, New England Journal of Medicine, 351, 1057-1067, 2004.

Ghosh G.: Dispersion-equation coefficients for the refractive index and birefringence of calcite and quartz crystals, Optics communications, 163(1), 95-1-2, 1999.

Ginoux, P. Chin, M., Tegen, I., Prospero, J. M., Holben, B., Dubovik, O., and Lin, S.-J.: Sources and distributions of dust aerosols simulated with the GOCART model, 106(D17), 20255-20273, 2001.

Ginoux, P. A., Prospero, J. M., Gill, T. E., Hsu, C., and Zhao, M.: Global-scale attribution of anthropogenic and natural dust sources and their emission rates based on MODIS Deep Blue aerosol products, Rev. Geophys, 50, RG3005, http://dx.doi.org/10.1029/2012RG000388, 2012.

Gleason, J. F., Hsu, N. C., and Torres, O.: Biomass burning smoke measured using backscattered ultraviolet radiation: SCAR-B and Brazilian smoke interannual variability, J. Geophys. Res., 103, 31969-31978, 1998.

Gosse, S. F., Wang, M., Labrie, D., and Chylek, P.: Imaginary part of the refractive index of sulfates and nitrates in the 0.7-2.6 μm spectral region, Appl. Opt., 36, 3622-3634, 1997.

Goudie, A. S.: Desert dust and human health disorders. Environ, Int., 63, 101-113, 2013.

Goudie, A. S., and Middleton, N.J.: Desert dust in the global system, Springer, 2006.

Goudie, A. S., and Middleton, N. J.: Dust storms in south west Asia, Acta Universitatis Carolinae., Supplement 73-83, 2000.

Goudie, A. S., and Middleton, N. J.: Saharan dust storms: nature and consequences, Earth Sci. Rev., 56, 179-204, 2001.

Govaerts, Y. M., Wagner, S., Lattanzio, A., and Watts, P.: Joint retrieval of surface reflectance and aerosol optical depth from MSG/SEVIRI observations with an optimal estimation approach: 1. Therory, J. Geophys. Res., 111, D02203, doi:10.1029/2009JD011779, 2010.

Guieu, C., Bonnet, S., Wagener, T., and Loye-Pilot, M. D.: Biomass burning as a source of dissolved iron to the open ocean?, Geophys. Res. Lett., 32, L19608, doi:10.1029/2005GL022962, 2005.

Hale, G. M., and Querry, M. R.: Optical constants of water in the 200 nm to 200 μm wavelength region, Appl. Opt., 12, 555-563, 1973.

Hand, V. L., Capes, G., Vaughan, D. J., Formenti, P., Haywood, J. M., and Coe, H.: Evidence of internal mixing of African dust and biomass burning particles by individual particle analysis using electron beam techniques, J. Geophys. Res., 115, D13301, doi:10.1029/2009JD012938, 2010.

Hansen, J. E.: Multiple scattering of polarized light in planetary atmospheres, part 2: Sunlight reflected by terrestrial water clouds, J. Atmos. Sci., 28(8), 1400-1426, 1971.

Hasekamp, O. P., and Landgraf, J.: Retrieval of aerosol properties over the ocean from multispectral single-viewing-angle measurements of intensity and polarization: Retrieval approach, information content, and sensitivity study, J. Geophys. Res., 110, D20207, doi:10.1029/2005JD006212, 2005.

Hasekamp, O. P., and Landgraf, J.: Retrieval of aerosol properties over land surfaces: capabilities of multiple-viewing-angle intensity and polarization measurements, Appl. Optics, 46, 3332-3344, 2007.

Haywood, J. M., and Boucher, O.: Estimates of the direct and indirect radiative forcing due to tropospheric aerosols: A review, Reviews of Geophysics, 38, doi: 10.1029/1999RG000078, 2000.

Haywood, J. M., and Shine, K. P.: The effect of anthropogenic sulfate and soot on the clear sky planetary radiation budget, Geophys. Res. Lett., 22(5), 603-606, 1995.

Haywood, J. M., Osborne, S. R., Francis, P., Keil, A., Formenti, P., Andrea, M., and Kaye, P.: The mean physical and optical properties of regional haze dominated by biomass burning aerosol measured from the C-130 aircraft during SAFARI-2000, J. Geophys. Res., 108(D13), 8473, doi:10.1029/2002JD002226, 2003.

Haywood, J. M., Pelon, J., Formenti, P., Bharmal, N., Brooks, M., Capes, G., Chazette, P., Chou, C., Christopher, S., Coe, H., Cuesta, J., Derimian, Y., Desboeufs, K., Greed, G., Harrison, M., Heese, B., Highwood, E. J., Johnson, B., Mallet, M., Marticorena, B., Marsham, J., Milton, S., Myhre, G., Osborne, S. R., Parker, D. J., Rajot, J. L., Schulz, M., Slingo, A., Tanré, D., and Tulet, P.:

Overview of the dust and biomass-burning experiment and African monsoon multidisciplinary analysis special observing period-0, J. Geophys. Res., 113, D00C17, 2008.

Helas, G., Andreae, M. O., and Meinrat, O.: SA'ARI 94: A preliminary view of results, J. Afr. J. Sci., 91, 360-362, 1995.

Herman, J., Bhartia, P., Torres, O., Hsu, C., Seftor, C., and Celarier, E.: Global distribution of UV-absorbing aerosols from Nimbus-7/TOMS data, J. Geophys. Res., 102, 16911-16922, 1997.

Herman, M., Deuzé, J. L., Marchant, A., Roger, B., and Lallart, P.: Aerosol remote sensing from POLDER/ADEOS over the ocean: Improved retrieval using a nonspherical particle model, J. Geophys, Res., 110, D10S02, doi:10.1029/2004JD004798, 2005.

Herrmann, J. R., Stahr, K., and Jahn, R.: The importance of source region identification and their properties for soil-derived dust: the case of Harmattan dust sources for eastern West Africa, Contribut. Atmos. Phys., 72, 141-150, 1999.

Hess, M., Koepke, P., and Schult, I.: Optical properties of aerosols and clouds: The software package OPAC, Bulletin of the American Meteorological Society, 79, 831-844, 1998.

Hinds, W.C.: Aerosol Technology: Properties, Wiley, New York, 1999.

Hoffer, A., Gelencsér, A., Guyon, P., Kiss, G., Schmid, O., Frank, G. P., Artaxo, P., and Andreae, M. O.: Optical properties of humic-like substances (HULIS) in biomass-burning aerosols, Atmos. Chem. Phys., 6(11), 3563-3570, 2006.

Holben, B. N., Eck, T. F., Slutsker, I., Tanré, D., Buis, J. P., Setzer, A., Vermote, E., Reagan, J. A., Kaufman, Y. J., Nakajima, T., Lavenu, F., Jankowiak, I., and Smirnov, A.: AERONET-A federated instrument network and data archive for aerosol characterization, Remote sensing of environment, 66(1), 1-16.

Holben, B. N., Tanré, D., Smirnov, A., Eck, T. F., Slutsker, I., Abuhassan, N., Newcomb, W. W., Schafer, J. S., Chatenet, B., Lavenu, F., Kaufman, Y. J., Vande Castle, J., Setzer, A., Markham, B., Clark, D., Frouin, R., Halthore, R., Karneli, A., O'Neill, N. T., Pietras, C., Pinker, R. T., Voss, K., and Zibordi, G.: An emerging ground-based aerosol climatology: aerosol optical depth from AERONET, J. Geophys. Res., 106, 12067-12098, 2001.

Hossenzadeh, S. R.: One hundred and twenty days winds of Sistan. Iran. J. Res. Geogr., 46, 103-127, 1997.

Houghton, J. T., Ding, Y., Griggs, D. J., Noguer, M., van der Linden, P. J., Dai, X., Maskell, K., and Johnson, C.A.: Climate Change 2001: The Scientific Basis (Contribution of Working Group I to the Third Assessment Report of the Intergovernmental Panel on Climate Change), Cambridge University Press, Cambridge, 2001.

Hsu, N., Herman, J., Bhartia, P., Seftor, C., Torres, O., Thompson, A., Gleason, J., Eck, T., and Holben, B.: Detection of biomass burning smoke from TOMS measurements, Geophys. Res. Lett., 23(7), 745-748, 1996.

Hsu, N., Tsay, S., King, M., and Herman, J.: Aerosol properties over bright-reflecting source regions, IEEE Transactions on Geoscience and Remote Sensing, 42, 557-569, 2004.

Husar, R., Prospero, J., and Stowe, L.: Characterization of tropospheric aerosols over the oceans with the NOAA advanced very high resolution radiometer optical thickness operational product, Journal of Geophysical Research, 102, 16889-16909, 1997.

Jacobson, M. Z.: Isolating nitrated and aromatic aerosols and nitrated aromatic gases as sources of ultraviolet light absorption. J. Geophys. Res., 104(D3), 3527-3542, 1999.

Jickells, T. D., An, Z. S., Andersen, K. K., Baker, A. R., Bergametti, G., Brooks, N., Cao, J. J., Boyd, P. W., Duce, R. A., Hunter, K. A., Kawahata, H., Kubilay, N., laRoche, J., Liss, P. S., Mahowald, N., Prospero, J., Ridgwell, A. J., Tegen, I., and Torres, R.: Global iron connections between desert dust, ocean biogeochemistry, and climate, science, 308(5718), 67-71, 2005.

Johnson, B. T., Osborne, S. R., Haywood, J. M., and Harrison, M. A. J.: Aircraft measurements of biomass burning aerosol over West Africa during DABEX, J. Geophys. Res., 113, 762-770, doi:10.1029/2008JD009848, 2008a.

Johnson, B. T., Heese, B., McFarlane, S. A., Chazette, P., Jones, A., and Bellouin, N.: Vertical distribution and radiative effects of mineral dust and biomass burning aerosol over west Africa during DABEX, J. Geophys. Res., 113, D00C12, doi: 10.1029/2008JD009848, 2008b.

Jones, T. A. and Christopher, S. A: MODIS derived fine mode fraction characteristics of marine, dust, and anthropogenic aerosols over the ocean, constrained by GOCART, MOPITT, and TOMS, J. Geophys. Res., 112(D22), 2007.

Journet, E., Balkanski, Y., and Harrison, S. P.: A new data set of soil mineralogy for dust-cycle modeling, Atmos. Chem. Phys., 14, 3801-3816, doi: 10.5194/acp-14-3801-2014, 2014.

Jung, C. R., Lin, Y. T., and Hwang, B. F.: Ozone, particulate matter, and newly diagnosed Alzheimer's disease: a population-based cohort study in Taiwan, J. Alzheimer's Dis. 44(2), 573-584, 2015.

Justice, C.O., Vermote, E., Townshend, J. R., Defries, R., Roy, D. P., Hall, D. K., Salomonson, V. V., Privette, J. L., Riggs, G., Strahler, A., Lucht, W., Myneni, R. B., Knyazikhin, Y., Running, S. W., Nemani, R. R., Wan, Z. M., Huete, A. R., van Leeuwen, W., Wolfe, R. E., Giglio, L., Muller, J. P., and Barnsley, M. J.: The Moderate Resolution Imaging Spectroradiometer (MODIS): Land remote sensing for global change research, IEEE T. Geosci. Remote, 36, 1228-1249, 1998.

Kacenelenbogen, M.: Application de la télédétection spatiale á la surveillance de la pollution en aérosols, Ph.D. thesis, Université de Lille 1, Villeneuve d'Ascq, France, 2008.

Kahn, R., Banerjee, P., McDonald, D., and Diner, D.: Sensitivity of multiangle imaging to aerosol optical depth, and to pure-particle size distribution and composition over ocean, Journal of Geophysical Research, 103, 32195-32213, 1998.

Kahn, R., Gaitley, R., Martonchik, J., Diner, D., Crean, K., and Holben, B.: MISR global aerosol optical depth validation based on two years of coincident AERONET observations, Journal of Geophysical Research, 110, D10S04, doi:10.1029/2004JD004706, 2005.

Kalashnikova, O., and Kahn, R.: Ability of multiangle remote sensing observations to identify and distinguish mineral dust types: Part 2. Sensitivity over dark water, Journal of Geophysical Research, 111, D11207, doi:10.1029/2005JD006756, 2006.

Kalman, R. E.: A new approach to linear filtering and prediction problems, J. Basic. Eng., 82, 35-40, 1960.

Kalu, A. E.: The African dust plume: its characteristics and propagation across West Africa in winter, in Saharan dust: Mobilisation, transport and deposition, edited by C. Morales, pp. 95- 118, John Wiley, Hoboken, N. J, 1979.

Kanakidou, M., Seinfeld, J. H., Pandis, S. N., Barnes, I., Dentener, F. J., Facchini, M. C., Van Dingenen, R., Ervens, B., Nenes, A., Nielsen, C. J., Swietlicki, E., Putaud, J. P., Balkanski, Y., Fuzzi, S., Horth, J., Moortgat, G. K., Winterhalter, R., Myhre, C. E. L., Tsigaridis, K., Vignati, E., Stephanou, E. G., and Wilson, J.: Organic aerosol and global climate modelling: a review, Atmospheric Chemistry and Physics, 5, 1053-1123, 2005.

Kapustin, V. N., Clarke, A. D., Shinozuka, Y., Howell, S., Brekhovskikh, V., Nakajima, T., and Higurashi, A.: On the determination of a cloud condensation nuclei from satellite: Challenges and possibilities, Journal of Geophysical Research, 111, D04202, doi:10.1029/2004JD005527, 2006.

Kaskaoutis, D. G., Kosmopoulos, P. G., Nastos, P. T., Kambezidis, H. D., Sharma, M., and Mehdi, W.: Transport pathways of Sahara dust over Athens, Greece as detected by MODIS and TOMS. Geom. Nat. Haz. Risk., 3, 35-54, 2012a.

Kaskaoutis, D. G., Nastos, P. T., Kosmopoulos, P. G., and Kambezidis, H. D.: Characterizing the long-range transport mechanisms of different aerosol types over Athens, Greece during 2000-2005, Int. J. Climatol., 32, 1249-1270, 2012b.

Katsouyanni, K., Touloumi, G., Samoli, E., Gryparis, A., Le Tertre, A., Monopolis, Y., Rossi, G., Zmirou, D., Ballester, F., Boumghar, A., Anderson, H. R., Wojtyniak, B., Paldy, A., Braunstein, R., Pekkanen, J., Schindler, C., and Schwartz, J.: Confounding and effect modification in the short-term effects of ambient particles on total mortality: results from 29 European cities within the APHEA2 project, Epidemiology, 12, 521-531, 2001.

Kaufman, Y. J., Boucher, O., Tanré, D., Chin, M., Remer, L. A., and Takemura, T.: Aerosol anthropogenic component estimated from satellite data, Geophysical Research Letters, 32, L17804, doi:10.1029/2005GL023125, 2005a.

Kaufman, Y. J., Koren, I., Remer, L. A., Tanré, D., Ginoux, P., and Fan, S.: Dust transport and deposition observed from the Terra-Moderate Resolution Imaging Spectroradiometer (MODIS) spacecraft over the Atlantic Ocean, J. Geophys. Res., 110, D10S12, 2005b.

Kaufman, Y. J., Martins, J., Remer, L. A., Schoeberl, M., and Yamasoe, M.: Satellite retrieval of aerosol absorption over the oceans using sunglint, Geophysical Research Letters, 29, 1928, doi:10.1029/2002GL015403, 2002a.

Kaufman, Y. J.: Solution of the equation of radiative transfer for remote sensing over nonuniform surface reflectivity, J. Geophys. Res., 87, 4137-4147, 1982.

Kaufman, Y. J., Tanré, D., and Boucher, O.: A satellite view of aerosols in the climate system, Nature., 419, 215-223, doi:10.1038/nature01091, 2002b.

Kaufman, Y. J., Tanré, D., Remer, L. A., Vermote, E., Chu, A., and Holben, B.: Operational remote sensing of tropospheric aerosol over land from EOS moderate resolution imaging spectroradiometer, Journal of Geophysical Research, 102, 17051-17067, 1997.

Keil, A., and Haywood, J. M.: Solar radiative forcing by biomass burning aerosol particles during SAFARI 2000: A case study based on measured aerosol and cloud properties, J. Geophys. Res., 108(D13), 145-160, doi:10.1029/2002JD002315, 2003.

Kerker, M., Scheiner, P., Cooker, D., and Kratohvil, J. : Absorption index and color of colloidal hematite, J. Colloid Interf. Sci., 71, 176-187, 1979.

King, M. D., Kaufman, Y., Tanré, D., and Nakajima, T.: Remote sensing of tropospheric aerosols: past, present, and future, Bulletin of the American Meteorological Society, 80, 2229-2259, 1999.

Kinne, S., Holben, B., Eck, T., Smirnov, A., Dubovik, O., Slutsker, I., Tanré, D., Zibozdi, G., Lohmann, U., Ghan, S., Easter, R., Chin, M., Ginoux, P., Takemura, T., Tegen, I., Koch, D., Kahn, R., Vermote, E., Stowe, L., Torres, O., Mishchenko, M., Geogdzhayev, I., and Hiragushi, A.: How well do aerosol retrievals from satellites and representation in global circulation models match ground-based AEROENT aerosol statistics?, Remote Sensing and Climate Modeling: Synergies and Limitations, M. Beniston and M. M. Verstratete, Eds., Kluwer Academic, 103-158, 2001.

Kinne, S., Lohmann, U., Feichter, J., Schulz, M., Timmreck, C., Ghan, S., Easter, R., Chin, M., Ginoux, P., Takemura, T., Tegen, I., Koch, D., Herzog, M., Penner, J., Pitari, G., Holben, B., Eck, T., Smirnov, A., Dubovik, O., Slutsker, I., Tanré, D., Torres, O., Mishchenko, M., Geogdzhayev, I., Chu, D. A., and Kaufman, Y. J.: Monthly averages of aerosol properties: A global comparison among models, satellite data and AERONET ground data, Journal of Geophysical Research, 108, doi:10.1029/2001JD001253,2003.

Kinne, S., Schulz, M., Textor, C., Guibert, S., Balkanski, Y., Bauer, S. E., Berntsen, T., Berglen, T. F., Boucher, O., Chin, M., Collins, W., Dentener, F., Diehl, T., Easter, R., Feichter, J., Fillmore, D. Ghan, S., Ginoux, P., Gong, S., Grini, A., Hendricks, J., Herzog, M., Horowitz, L., Isaksen, I., Iversen, T., Kirkavag, A., Kloster, S., Koch, D., Kristjansson, J. E., Krol, M., Lauer, A., Lamarque, J. F., Lesins, G., Liu, X., Lohmann, U., Montanaro, V., Myhre, G., Penner, J. E., Pitari, G., Reddy, S., Seland, O., Stier, P., Takemura, T., and Tie, X.: An AeroCom initial assessment – optical properties in aerosol component modules of global models, Atmos. Chem. Phys., 6, 1815-1834, 2006.

Kirchstetter, T. W., Novakov, T., and Hobbs, P. V.: Evidence that the spectral dependence of light absorption by aerosols is affected by organic carbon, Journal of Geophysical Research: Atmospheres, 109(D21), 2004.

Kirchstetter, T. W., Novakov, T., Hobbs, P. V., and Magi, B.: Airborne measurements of carbonaceous aerosol in southern Africa during the dry biomass burning season, J. Geophys. Res., 108(D13), 8476, doi:10.1029/2002JD002171, 2003.

Koçak, M., Mihalopoulos, N., and Kubilay, N.: Chemical composition of the fine and coarse fraction of aerosols in the northeastern Mediterranean, Atmos. Environ., 41, 7351-7368, 2007.

Koch, D., and Del Genio, A.: Black carbon absorption effects on cloud cover, review and synthesis, Atmospheric Chemistry and Physics, pp. 7685-7696, 2010.

Koch, D., Schulz, M., Kinne, S., McNaughton, C., Spackman, J. R., Balkanski, Y., Bauer, S., Berntsen, T., Bond, T. C., Boucher, O., Chin, M., Clarke, A., De Luca, N., Dentener, F., Diehl, T., Dubovik, O., Easter, R., Fahey, D. W., Feichter, J., Fillmore, D., Freitag, S., Ghan, S., Ginoux, P., Gong, S., Horowitz, L., Iversen, T., Kirkevåg, A., Klimont, Z., Kondo, Y., Krol, M., Liu, X., Miller, R., Montanaro, V., Moteki, N., Myhre, G., Penner, J. E., Perlwitz, J., Pitari, G., Reddy, S., Sahu, L., Sakamoto, H., Schuster, G., Schwarz, J. P., Seland, Ø., Stier, P., Takegawa, N., Takemura, T., Textor, C., van Aardenne, J. A., and Zhao, Y.: Evaluation of black carbon estimations in global aerosol models, Atmos. Chem. Phys., 9, 9001-9026, 2009.

Koepke, P.: Effective reflectance of oceanic white caps, Appl.Optics, 23, 1816-1824, 1984.

Koepke, P., Hess, M., Schult, I., and Shettle, E. P.: Global aerosol data set. MPI Meteorologie Hanburg Rep, 243(44), 7017-7039.

Kokhanovsky, A. A., Bréon, F.-M., Cacciari, A., Carboni, E., Diner, D., Di Nicolantonio, W., Grainger, R. G., Grey, W. M. F., Höller, R., Lee, K.-H., Li, Z., North, P. R. J., Sayer, A. M., Thomas, G. E., and von Hoyningen-Huene, W. .: Aerosol remote sensing over land: A comparison of satellite retrievals using different algorithms and instruments, Atmos. Res., 85, 372-394, 2007.

Koren, I., and Kaufman, Y. J.: Direct wind measurements of Saharan dust events from Terra and Aqua satellites, Geophys. Res. Lett., 31 (6), 337-357, 2004

Kou, L., Labrie, D., and Chylek, P.: Refractive indices of water and ice in the 0.65-2.5 μm spectral range, Appl. Opt., 32, 3531-3540, 1993.

Koven, C. D., and Fung, I.: Inferring dust composition from wavelength-dependent absorption in Aerosol Robotic Network (AERONET) data, J. Geophys. Res., 111(D14), 2006.

Krueger, B. J., Grassian, V. H., Cowin, J. P., and Laskin, A.: Heterogeneous chemistry of individual mineral dust particles from different dust source regions: the importance of particle mineralogy, Atmospheric Environment, 38, 6253-6261, 2004.

Krueger, B. J., Grassian, V. H., Laskin, A., and Cowin, J. P.: The transformation of solid atmospheric particles into liquid droplets through heterogeneous chemistry: Laboratory insights into the processing of calcium containing mineral dust aerosol in the troposphere, Geophys. Res. Lett., 30, 1148, doi:10.1029/2002gl016563, 2003.

Kulmala, M., Vehkamäki, H., Petäjä, T., Dal Maso, M., Lauri, A., Kerminen, V. M., Birmili, W., and McMurry, P. H.: Formation and growth rates of ultrafine atmospheric particles: A review of observations, Journal of Aerosol Science, 35, 143-176, 2004.

Kumar, K. R., Sivakumar, V., Reddy, R. R., Gopal, K. R., and Adesina, A. J.: Inferring wavelength dependence of AOD and Angstrom exponent over a sub-tropical station in South Africa using AERONET data: Influence of meteorogy, long-rang transport and curvature effect, Science of the Total Environment, 461, 397-408, 2013.

Labonne, M., Bréon, F. M., and Chevallier, F.: Injection height of biomass burning aerosols as seen from a spaceborne lidar, Geophys. Res. Let., 34, L11806, doi:10.1029/2007GL029311, 2007.

Lafon, S., Sokolik, I. N., Rajot, J. L., Caquineau, S., and Gaudichet, A.: Characterization of iron oxides in mineral dust aerosols: Implications for light absorption, J. Geophys. Res., 111, D21, doi:10.1029/2005jd007016, 2006.

Laskin, A., Iedema, M. J., Ichkovich, A., Graber, E. R., Taraniukb, I., and Yinon, R.: Direct observation of completely processed calcium carbonate dust particles, Faraday Discuss., 130, 453-468, 2005.

Laurent, B., Marticorena, B., Bergametti, G., Léon, J. F., and Mahowald, N. M.: Modeling mineral dust emissions from the Sahara desert using new surface properties and soil database, J. Geophys. Res., 113, D14218, doi:10.1029/2007jd009484, 2008.

Lawrence, M. G., and Lelieveld, J.: Atmospheric pollutant outflow from southern Asia: A review, Atmos. Chem. Phys., 10, 11017-11096, 2010.

Lazaro, F. J., Gutierrez, L., Barrón, V., and Gelado, M. D.: The speciation of iron in desert dust collected in Gran Canaria (Canary Islands): Combined chemical, magnetic and optical analysis, Atmos. Environ., 42, 8987-8996, 2008.

Leaitch, W. R., Strapp, J. W., Wiebe, H. A., and Isaac, G. A.: Measurements of scavenging and transformation of aerosol inside cumulus, Precipitation Scavenging, Dry Deposition and Resuspension, 53-66, 1982.

Lenoble, J., Herman, M., Deuzé, J. L., Lafrance, B., Santer, R., and Tanré, D.: A successive order of scattering code for solving the vector equation of transfer in the earth's atmosphere with aerosols, J. Quant. Spectrosc. Radiat. Trans., 107(3), 479-507, 2007.

Léon, J. F., and Legrand, M.: Mineral dust sources in the surroundings of the north Indian Ocean. Geophys. Res. Lett., 30 (6), 1309, http://dx.doi.org/10.1029/2002GL016690, 2003.

Lesins, G., Chylek, P., and Lohmann U.: A study of internal and external mixing scenarios and its effect on aerosol optical properties and direct radiative forcing, Journal of Geophysical Research, 107(D10), doi:10.1029/2001JD000973, 2002.

Levi, Y. and Rosenfeld, D.: Ice nuclei, rainwater chemical composition, and static cloud seeding effects in Israel, J. Appl. Meteorol., 35, 1494-1501, 1996.

Levin, Z., Ganor, E., and Gladstein, V.: The effects of desert particles coated with sulfate on rain formation in the eastern Mediterranean, J. Appl. Meteorol., 35, 1511-1523, 1996.

Levy, R., Remer, L., Mattoo, S., Vermote, E., and Kaufman, Y.: Second-generation algorithm for retrieving aerosol properties over land from MODIS spectral reflectance, Journal of Geophysical Research, 112, D13211, doi:10.1029/2006JD007811, 2007.

Li, R., Kaufman, Y., Hao, W., Salmon, I., and Gao, B.: A technique for detecting burn scars suing MODIS data, IEEE Transactions on Geoscience and Remote Sensing, 42, 1300-1308, 2004.

Li, X., and Strahler, A. H.: Geometrical-optical bidirectional reflectance modeling of the discrete crown vegetation canopy: effect of crown shape and mutual shadowing, IEEE T. Geosci. Remote, 30, 276-292, 1992.

Li, Z., Gu, X., Wang, L., Li, D., Xie, Y., Li, K., Dubovik, O., Schuster, G., Goloub, P., Zhang, Y., Li, L., Ma, Y., and Xu, H.: Aerosol physical and chemical properties retrieved from ground-based

remote sensing measurements during heavy haze days in Beijing winter, Atmospheric Chemistry and Physics, 13(20), 10171-10183, 2013.

Li, Z., Li, L., Zhang, F., Li, D., Xie, Y., and Xu, H.: Comparison of aerosol properties over Beijing and Kanpur: Optical, physical properties and aerosol component composition retrieved from 12 years ground-based Sun-sky radiometer remote sensing data, J. Geophys. Res., 120(4), 1520-1535, 2015.

Lindesay, J. A., Andreae, M. O., Goldammer, J. G., Harris, G., Annegarn, H. J., Garsta, M., Scholes, R. J., and van Wilgen, B. W.: International geosphere-biosphere programme/international global atmospheric chemistry SAFARI-92 field experiment: Background and overview, J. Geophys. Res., 101(D19), 23521-23530, doi: 10.1029/96JD01512, 1996.

Liousse, C., Penner, J. E., Chuang, C., Walton, J. J., Eddleman, H., and Cachier, H.: A global three-dimensional model study of carbonaceous aerosols, J. Geophys. Res., 101, 19411-19432, 1996.

Litvinov, P., Hasekamp, O., Cairns, B., and Mishchenko, M.: Reflection models for soil and vegetation surfaces from multiple-viewing angle photopolarimetric measurements, J. Quant. Spectrosc. Radiat. Trans., 111, 529-539, 2010.

Litvinov, P., Hasekamp, O., and Cairns, B.: Models for surface reflection of radiance and polarized radiance: Comparison with airborne multi-angle photopolarimetric measurements and implications for modeling top-of-atmosphere measurements, Remote Sens. Environ., 115, 781-792, 2011.

Liu, H., Pinker, R., and Holben, B.: A global view of aerosols from merged transport models, satellite, and ground observations, Journal of Geophysical Research, 110, D10S15, doi:10.1029/2004JD4695, 2005.

Lohmann, U., and Feichter, J.: Global indirect aerosol effects: a review, Atmos. Chem. Phys., 5, 715-737, 2005.

Lohmann, U., and Hoose, C.: Sensitivity studies of different aerosol indirect effects in mixed- phase clouds, Atmospheric Chemistry and Physics, 9(22), 8917-8934, 2009.

Lohmann, U., Karcher, B., and Timmreck, C.: Impact of the Mount Pinatubo eruption on cirrus clouds formed by homogeneous freezing in the ECHAM4 GCM, J. Geophys. Res., 108, 4568, 2003.

Longtin, D. R., Shettle, E. P., Hummel, J. R., and Pryce, J. D.: A wind dependent desert aerosol model: radiative properties, OPTIMETRICS INC BURLINGTON MA, 1988.

Luo, C., Mahowald, N., Bond, T., Chuang, P. Y., Artaxo, P., Siefert, R., Chen, Y., and Schauer, J.: Combustion iron distribution and deposition, Global Biogeochem. Cycles, 22, GB1012, doi:10.1029/2007GB002964, 2008.

Lyapustin, A. I., and Kaufman, Y. J.: Role of adjacency effect in the remote sensing of aerosol, J. Geophys. Res, 106, 909-916, 2001.

Maenhaut, W., Salma, I., Cafmeyer, J., Annegarn, H. J., and Andreae, M. O.: Regional atmospheric aerosol composition and sources in the eastern Transvaal, South Africa, and impact on biomass burning, J. Geophys. Res., 101, 23631-23650, 1996.

Mahowald, N. M., Baker, A. R., Bergametti, G., Brooks, N, Duce, R. A., Jickells, T. D., Kubilay, N., Prospero, J. M., and Tegen, I.: Atmospheric global dust cycle and iron inputs to the ocean, Global biogeochemical cycles, 19(4), 2005.

Maignan, F., Bréon, F. M., and Lacaze, R.: Bidirectional reflectance of Earth targets: Evaluation of analytical models using a large set of spaceborne measurements with emphasis on the Hot Spot, Remote Sens. Environ., 90, 210-220, 2004.

Maignan, F., Bréon, F. M., Fédéle, E., and Bouvier, M.: Polarized reflectances of natural surfaces: Spaceborne measurements and analytical modeling, Remote Sens. Environ., 113, 2642-2650, 2009.

Marticorena, B., and Bergametti, G.: Modeling the atmospheric dust cycle: 1. Design of a soil-derived dust emission scheme, J. Geophys. Res., 100, 16415-16430, doi:10.1029/95jd00690, 1995.

Marticorena, B., Chatenet, B., Rajot, J. L., Traoré, S., Coulibaly, M., Diallo, A., Koné, I., Maman, A., NDiaye, T., and Zakou, A.: Temporal variability of mineral dust concentrations over west Africa: analyses of a pluriannual monitoring from the AMMA Sahelian dust transect, Atmos. Chem. Phys., 10, 8899-8915, doi:10.5194/acp-10-8899-2010, 2010.

Martins, J., Tanré, D., Remer, L., Kaufman, Y., Mattoo, S., and Levy, R.: MODIS cloud screening for remote sensing of aerosol over oceans using spatial variability, Geophys. Res. Lett., 29, 2002.

Martonchik, J., Diner, D., Kahn, R., and Gaitley, B.: Comparison of MISR and AERONET aerosol optical depths over desert sites, Geophys. Res. Lett., 31, L16102, 2004.

Martonchik, J., Diner, D., Kahn, R., Verstraete, M., Pinty, B., Gordon, H., and Ackerman, T.: Techniques for the retrieval of aerosol properties over land and ocean using multiangle data, IEEE Transactions on Geoscience and Remote Sensing, 36, 1212-1227, 1998.

Massie, S., Torres, O., and Smith, S.: Total Ozone Mapping Spectrometer (TOMS) observations of increases in Asian aerosol in winter from 1979 to 2000, Journal of Geophysical Research, 109, D18211, doi:10.1029/2004JD004620, 2004.

Matsuki, A., Quennehen, B., Schwarzenboeck, A., Crumeyrolle, S., Venzac, H., Laj, P., and Gomes, L.: Temporal and vertical variations of aerosol physical and chemical properties over West Africa: AMMA aircraft campaign in summer 2006, Atmos. Chem. Phys., 10, 8437-8451, doi:10.5194/acp-10-8437-2010, 2010.

Menaut, J.-C., Abbadie, L., Lavenu, F., Loudjani, P., and Podaire, A.: Biomass burning in West African savannas, in Global Biomass Burning, Atmospheric, Climatic, and Biospheric Implications, edited by J. S. Levine, pp. 133-142, MIT Press, Cambridge, Mass., 1991.

Middleton, N. J.: A geography of dust storms over southwest Asia, J. Climatol., 6, 183-196, 1986a.

Middleton, N. J.: Dust storms in the Middle East, J. Arid Environ., 10, 83-96, 1986b.

Mills, M. M., Ridame, C., Davey, M., La Roche, J., and Geider, R. J.: Iron and phosphorus co limit nitrogen fixation in the eastern tropical North Atlantic, Nature, 429(6989), 292-294, 2004.

Miri, A., Ahmadi, A., Ghanbar, A., and Moghaddamnia, A.: Dust storms impacts on air pollution and public health under hot and dry climate. Int. J. Energy Environ., 2, 101-105, 2007.

Mishchenko, M. I., Geogdzhayev, I. V., Rossow, W. B., Cairns, B., Carlson, B. E., Lacis, A. A., Liu, L., and Travis, L. D.: Long-term satellite record reveals likely recent aerosol trend, Science, 315, 1543, 2007a.

Mishchenko, M. I., Carirns, B., Hansen, J. E., Travis, L. D., Kopp, G., Schueler, G., Fafaul, B. A., Hooker, R. J., Maring, H. B., and Itchkawich, T.: Accurate monitoring of terrestrial aerosols and total solar irradiance: introducing the Glory Mission, Bulletin of the American Meteorological Society, 88(5), 677-691, 2007b.

Mishchenko, M. I., Geogdzhayev, I. V., Cairns, B., Rossow, W., and Lacis, A.: Aerosol retrievals over the ocean by use of channels 1 and 2 AVHRR data: Sensitivity analysis and preliminary results, Applied Optics, 38, 7325-7341, 1999.

Mishchenko, M. I., and Travis, L. D.: Satellite retrieval of aerosol properties over the ocean using polarization as well as intensity of reflected sunlight, J. Geophys. Res., 102(D14), 16989-17013, 1997.

Miyazaki, Y., Kondo, Y., Takegawa, N., Komazaki, Y., Kawamura, K., Mochida, M., Okuzawa, K., and Weber, R., J.: Time-resolved measurements of water-soluble organic carbon in Tokyo, J. Geophys. Res., 111, D23206, 2006.

Moore, J. K., Doney, S. C., Glover, D. M., and Fung, I. Y.: Iron cycling and nutrient limitation patterns in surface waters of the World Ocean, Deep Sea Res., Part Ⅱ, 49, 463-507, 2002.

Moreno, T., Querol, X., Castillo, S., Alastuey, A., Cuevas, E., Herrmann, L., Mounkaila, M., Elvira, J., and Gibbons, W.: Geochemical variations in aeolian mineral particles from the Sahara-Sahel Dust Corridor, Chemosphere, 65, 261-270, 2006.

Mounkaila, M., Herrmann, L., Gaiser, T., and Maurer, T.: Spectral and mineralogical properties of potential dust sources on a transect from Sahara to Sahel in Chad, paper presented at 2nd Workshop on Mineral Dust, Paris, Lab. Interuniv. des Syst. Atmos., Paris, 10-12, September, 2003.

Myhre, G., Shindell, D., Bréon, F. M., Collins, W., Fuglestvedt, J., Huang, J., Koch, D., Lamarque, J. F., Lee, D., Mendoza, B., Nakajima, T., Robock, A., Stephens, G., Takemura, T., and Zhang, H.: Anthropogenic and natural radiative forcing, in: Climate Change 2013: the physical science basis. Contribution of working group I to the fifth assessment report of the intergovernmental panel on climate change. Cambridge University Press, Cambridge, United Kingdom and New York, NY, USA.

Nadal, F., and Bréon, F. M.: Parameterization of surface polarized reflectance derived from POLDER spaceborne measurements, IEEE T. Geosci. Remote, 37, 1709-1718, 1999.

Nakajima, T., Tanaka, M., and Yamauchi, T.: Retrieval of the optical properties of aerosols from aureole and extinction data, Appl. Optics, 22, 2951-2959, 1983.

Nakajima, T., Tonna, G., Rao, R., Kaufman, Y. J., and Holben, B. N.: Use of sky brightness measurements from ground for remote sensing of particulate polydispersions, Applied Optics, 35, 2672-2686, 1996.

Nakajima, T., Yoon, S. C., Ramanathan, V., Shi, G.-Y., Takemura, T., Higurashi, A., Takamura, T., Aoki, K., Sohn, B.-J., Kim, S.-W., Tsuruta, H., Sugimoto, N., Shimizu, A., Tanimoto, H., Sawa, Y.,

Lin, N.-H., Lee, C.-T., Goto, D., and Schutgens, N.: Overview of the atmospheric brown cloud east Asian regional experiment 2005 and a study of the aerosol direct radiative forcing in east Asia, Journal of Geophysical Research, 112, doi:10.1029/2007JD009009, 2007.

Nickovic, S., Vukovic, A., Vujadinovic, M., Djurdjevic, V., and Pejanovic, G.: Technical Note: High-resolution mineralogical database of dust-productive soils for atmospheric dust modeling, Atmos. Chem. Phys., 12, 845–855, doi:10.5194/acp-12-845-2012, 2012.

O'Dowd, C. D., Jimenez, J. L., Bahreini, R., Flagan, R. C., Seinfeld, J. H., Hameri, K., Pirjola, L., Kulmala, M., Jennings, S. G., and Hoffmann, T.: Marine aerosol formation from biogenic iodine emission, Nature, 417, 632-636, 2002.

Orlovsky, N., Orlovsky, L., and Durdyev, A.: Dust storms in Turkmenistan, J. Arid Environ., 60(1), 83-97, 2005.

Orr, C., Hurd, F. K., and Corbett, W. J.: Aerosol size and relative humidity, J. Colloid Sci., 13, 4720482, 1958.

Ota, Y., Higurashi, A., Nakajima, T., and Yokota, T.: Matrix formulations of radiative transfer including the polarization effect in a coupled atmosphere-ocean system, J. Quant. Spectrosc. Radiat. Trans., 111, 878-894, 2010.

Palmer, K. P., and Williams, D.: Optical properties of water in the near infrared, J. Opt. Soc. Am., 64, 1107-1110, 1974.

Park, K., Kittelson, D. B., Zachariah, M. R., and McMurry, P. H.: Measurement of inherent material density of nanoparticles agglomerates, Journal of Nanoparticle Research, 6, 267-272, 2004.

Penner, J. E., Hegg, D., and Leaitch, R.: Unravelling the role of aerosols in climate change, Environ. Sci. Technol., 35, 332A-340A, doi: 10.1021/es0124414, 2001.

Phillips, D. L.: A technique for numerical solution of certain integral equation of first kind, J. Assoc. Comp. Mach., 9, 84-97, 1962.

Piketh, S. J., Annegarn, H. J.:, and Tyson, P. D.: Lower tropospheric aerosol loadings over South Africa: The relative contribution of aeolian dust, industrial emissions and biomass burning, J. Geophys. Res., 104(D1), 1597-1607, doi:10.1029/1998JD100014, 1999a.

Piketh, S. J., Swap, R. J., Anderson, C. A., Freiman, M. T., Zunckel, M., and Held, G.: The Ben MacDhui high altitude trace gas and aerosol transport experiment, S. Afr. J. Sci., 95, 35-43, 1999b.

Pilinis, C., Pandis, S. N., and Seinfeld, J. H.: Sensiticity of direct climate forcing by atmospheric aerosols to aerosol and composition, Journal of Geophysical Research, 100, 18739-18754, 1995.

Pincus, R., and Baker, M.: Effect precipitation on the albedo susceptibility of clouds in the marine boundary layer, Nature, 372(6503), 250-252, 1994.

Pope, C. A., Burnett, R. T., Thun, M. J., Calle, E. E., Krewski, D., Ito, K., and Thurston, G. D.: Lung cancer, cardiopulmonary mortality, and long-term exposure to fine particulate air pollution, Journal of the American Medical Association, 287, 1132-1141, 2002.

Pope, C. A., Burnett, R. T., Thurston, G. D., Thun, M. J., Calle, E. E., Krewski, D., Godleski, J. J.: Cardiovascular mortality and long-term exposure to particulate air pollution, Circulation, 109, 71-77, 2004.

Pope, C. A., and Dockery, D. W.: Acute Health-effects of PM10 pollution on symptomatic and asymptomatic children, American Review of Respiratory Disease, 145, 1123-1128, 1992.

Pope, C. A., Dockery, D. W., Spengler, J. D., and Raizenne, M. E.: Respiratory health and PM10 pollution – a daily time-series analysis, American Review of Respiratory Disease, 144, 668-674, 1991.

Pope, C. A., Ezzati, M., and Dockery, D. W.: Fine particulate air pollution and life expectancy in the United State, New England Journal of Medicine, 360(4), 376-386, 2009.

Pöschl, U.: Formation and decomposition of hazardous chemical components contained in atmospheric aerosol particles, J. Aerosol Med., 15, 203-212, 2002.

Pósfai, M., Simonics, R., Li, J., Hobbs, P. V., and Buseck, P. R.: Individual aerosol particles from biomass burning in southern Africa: Compositions and size distributions of carbonaceous particles, J. Geophys. Res., 108(D13), 8483, doi:10.1029/2002JD002291, 2003.

Press, W. H., Teukolsky, S. A., Vetterling, W. T., and Flannery, B. P.: Numerical recipes in Fortran: the art of scientific computing, Cambridge University Press, 1993.

Prospero, J. M., Ginoux, P., Torres, O., Nicholson, S. E., and Gill, T. E.: Environmental characterization of global sources of atmospheric soil dust identified with the Nimbus 7 Total Ozone Mapping Spectrometer (TOMS) absorbing aerosol product, Rev. Geophys., 40, 2011-2024, 2002.

Putaud, J. P., Van Dingenen, R., Dell'Acqua, A., Raes, F., Matta, E., Decesari, S., Facchini, M. C., and Fuzzi, S.: Size-segregated aerosol mass closure and chemical composition in Monte Cimone (I) during MINATROC, Atmos. Chem. Phys., 4, 889-902, doi:10.5194/acp-4-889-2004, 2004.

Pye, K.: Aeolian Dust and Dust Deposits., Academic Press, London, UK, 334 pp., 1987.

Quaife, T., and Lewis, P.: Temporal constraints on Linear BRDF model parameters, IEEE T. Geosci. Remote, 48, 2445-2450, 2010.

Radke, L. F.: Preliminary measurements of the size distribution of cloud interstitial aerosols, Precipitation Scavenging, Dry Deposition and Resuspension, 71-78, 1983.

Raes, F., Van Dingenen, R., Vignati, E., Wilson, J., Putaud, J. P., Seinfeld, J. H., Adams, P.: Formation and cycling of aerosols in the global troposphere, Atmos. Environ., 34, 4215-4240, 2000.

Rahman, H., Pinty, B., and Verstrate, M. M.: Coupled surface atmosphere reflectance (CSAR) model 2. Semiempirical surface model usable with NOAA/AVHRAA data, J. Geophys. Res, 98, 20791-20801, 1993.

Ramanathan, V., Crutzen, P., Kiehl, J., and Rosenfeld, D.: Aerosols, climate, and the hydrological cycle, Science, 294, 2119-2124, doi:10.1126/science.1064034, 2001.

Ramanathan, V., and Carmichael, G.: Global and regional climate changes due to black carbon, Nature geoscience, 1(4), 221-227, 2008.

Rashki, A., deW Rautenbach, C. J., Eriksson, P. G., Kaskaoutis, D. G., and Gupta, P.: Temporal changes of particulate concentration in the ambient air over the city of Zahedan, Iran. Air Qual. Atmos. Health., 6(1), 123-135, 2013a.

Rashki, A., Eriksson, P. G., Rautenbach, C. J. deW., Kaskaoutis, D. G., Grote, W., Dykstra, J.: Assessment of chemical and mineralogical characteristics of airborne dust in the Sistan region, Iran. Chemosphere., 90, 227-236, 2013b.

Reid, J. S., and Hobbs, P. V.: Physical and optical properties of smoke from individual biomass fires in Brazil, J. Geophys. Res., 103, 32013-32030, 1998.

Reid, J. S., Hobbs, P. V., Ferek, R. J., Blake, D. R., Martins, J. V., Dunlap, M. R., and Liousse, C.: Physical chemical and optical properties of regional hazes dominated by smoke in Brazil, J. Geophys. Res., 103(D24), 32041-32050, 1998.

Remer, L., Kaufman, Y., Tanré, D., Mattoo, S., Chu, D., Martins, J., Li, R., Ichoku, C., Levy, R., Kleidman, R., Eck, T., Vermote, E., and Holben, B.: The MODIS aerosol algorithm, products and validation, Journal of the Atmospheric Sciences, 62, 947-973, 2005.

Remer, L., Tanré, D., Kaufman, Y., Ichoku, C., Mattoo, S., Levy, R., Chu, D., Holben, B., Dubovik, O., Smirnov, A., Martins, J., Li, R., and Ahman, Z.: Validation of MODIS aerosol retrieval over ocean, Geophysical Research Letters, 29, 8008, doi:10.1029/2001/GL013204, 2002.

Remer, L. A., Kleidman, R. G., Levy, R. C., Kaufman, Y. J., Tanré, D., Mattoo, S., Martins, J. V., Ichoku, C., Koren, I., Yu, H., and Holben, B. N.: Global aerosol climatology from the MODIS satellite sensors, J. Geophys. Res., 113, D14S01, doi:10.1029/2007JD009661, 2008.

Ritz, B., Lee, P. C., Hansen, J., Lassen, C. F., Ketzel, M., Sorensen, M., and Raaschou-Nielsen, O.: Traffic-related air pollution and Parkinson's disease in Denmark: a case control study, Environ. Health Perspect., 124(3), 351-356, 2016.

Ro, C., Huwang, H., Kim, H., Chun, Y., and Grieken, R. V.: Singleparticle characterization of four "Asian dust" samples collected in Korea, using low-Z particle electron probe X-ray microanalysis, Environ. Sci. Technol., 39, 1409-1419, 2005.

Rodgers, C. D.: Inverse methods for atmospheric sounding: theory and practice, World Scientific, Singapore, 2000.

Roessler, D. M., Faxvog, F. R., Stevenson, R., and Smith, G. W.: Optical properties and morphology of particulate carbon: Variation with air/fuel ratio, in Particulate Carbon: Formation During Combustion, edited by D. C. Siegla and G. W. Smith, pp. 57- 84, Plenum, New York, 1981.

Rosenfeld, D.: Aerosols, clouds, and climate, Science, 312, 10.1126/science.1128972, 2006.

Ross, J. K.: The radiation regime and architecture of plant stands, Dr. W. Junk Publishers, The Hague, doi: 10.1007/978-94-009-8647-3, 1981.

Rozanov, V. V., and Lyapustin, A. I.: Similarity of radiative transfer equation: Error analysis of phase function truncation techniques, J. Quant. Spectrosc. Radiat. Trans., 111, 1964-1979, 2010.

Samet, J., Wassel, R., Holmes, K. J., Abt, E., and Bakshi, K.: Research priorities for airborne particulate matter in the United States, Environ. Sci. Technol., 39, 209A-304A, 2005.

Sarthou, G., Baker, A. R., Blain, S., Achterberg, E. P., Boye, M., Bowie, A. R., Croot, P., Laan, P., de Baar, H. J. W., Jickells, T. D., and Worsfold, P. J.: Atmospheric iron deposition and sea-surface dissolved iron concentrations in the eastern Atlantic Ocean, Deep Sea Research Part I: Oceanographic Research Papers, 50, 1339-1352, 2003.

Schkolnik, G., Chand, D., Hoffer, A., Andreae, M. O., Erlick, C., Swietlicki, E., and Rudich, Y.: Constraining the density and complex refractive index of elemental and organic carbon in biomass burning aerosol using optical and chemical measurements, Atmospheric Environment, 41(5), 1107-1118, 2007.

Schnaiter, M., Gimmler, M., Llamas, I., Linke, C., Jäger, C., and Mutschke, H.: Strong spectral dependence of light absorption by organic carbon particles formed by propane combustion, Atmospheric Chemistry and Physics, 6(10), 2981-2990, 2006.

Schnaiter, M., Schmid, O., Petzold, A., Fritzsche, L., Klein, K. F., Andreae, M. O., Helas, G., Thielmann, A., Gimmler, M., Möhler, O., Linke, C., and Schurath, U.: Measurement of wavelength-resolved light absorption by aerosols utilizing a UV-VIS extinction cell, Aerosol Science and Technology, 39(3), 249-260, 2005.

Scholes, M., and Andreae, M. O.: Biogenic and pyrogenic emissions from Africa and their impact on the global atmosphere, Ambio., 29, 23-29, 2000.

Schuster, G. L., Lin, B., and Dubovik, O.: Remote sensing of aerosol water uptake, Geophysical Research Letters, 36, L03814, doi:10.1029/2008GL036576, 2009.

Schuster, G. L., Dubovik, O., and Arola, A.: Remote sensing of soot carbon-Part 1: distinguishing different absorbing aerosol species, Atmos. Chem. Phys., 16, 1565-1585, doi:10.5194/acp-16-1565-2016, 2016.

Schuster, G. L., Dubovik, O., Holben, B. N., Clothiaux, E. E.: Inferring black carbon content and specific absorption from Aerosol Robotic Network (AERONET) aerosol retrievals, Journal of Geophysical Research: Atmospheres, 110(D10), 2005.

Schuster, G. L., Dubovik, O., and Holben, B. N.: Angstrom exponent and bimodal aerosol size distributions, J. Geophys. Res., 111, D07207, doi:10.1029/2005JD006328, 2006.

Schwartz, J., Dockery, D. W., and Neas, L M.: Is daily mortality associated specifically with fine particles?, Journal of Air and Waste Management Association, 46, 927-939, 1996.

Schwarz, J. P., Samset, B. H., Perring, A. E., Spackman, J. R., Gao, R. S., Stier, P., Schulz, M., Moore, F. L., Ray, E. A., and Fahey, D. W.: Global-scale seasonally resolved black carbon vertical profiles over the Pacific, Geophys. Res. Lett., 40, 5542-5547, 2013.

Schwarz, J. P., Spackman, J. R., Gao, R. S., Watts, L. A., Stier, P., Schulz, M., Davis, S. M., Wofsy, S. C., and Fahey, D. W.: Global-scale black carbon profiles observed in the remote atmosphere and compared to models, Geophys. Res. Lett., 37, L18812, 2010.

Seiler, W., and Crutzen, P. J.: Estimates of gross and net fluxes of carbon between the biosphere and the atmosphere from biomass burning, Clim. Change., 2, 207-247, 1980.

Seinfeld, J. H., Pandis, S. N.: Atmospheric Chemistry and Physics: From Air Pollution to Climate Change, Wiley, New York, 1998.

Shao, Y., Wyrwoll, K.-H., Chappell, A., Huang, J., Lin, Z., McTainsh, G. H., Mikami, M., Tanaka, T. Y., Wang, X., and Yoon, S.: Dust cycle: An emerging core theme in Earth system science, Aeolian Research, 2, 181-204, doi:10.1016/j.aeolia.2011.02.001, 2011.

Sharifikia, M.: Environmental challenges and drought hazard assessment of Hamoun Desert Lake in Sistan region, Iran, based on the time series of satellite imagery. Nat. Hazard., 65, 201-217, 2013.

Shi, Z., Krom, M. D., Jickells, T. D., Bonneville, S., Carslaw, K. S., Mihalopoulos, N., Baker, A. R., and Benning, L. G.: Impacts on iron solubility in the mineral dust by processes in the source region and the atmosphere: A review, Aeolian Research, 5, 21-42, 2012.

Shi, Z., Zhang, D., Hayashi, M., Ogata, H., Ji, H., and Fujiie, W.: Influences of sulfate and nitrate on the hygroscopic behaviour of coarse dust particles, Atmos. Environ., 42, 822-827, 2008.

Smirnov, A., Holben, B., Eck, T., Dubovik, O., and Slutsker, I.: Cloud-screening and quality control algorithms for the AERONET database, Remote Sensing of Environment, 73, 337-349, 2000.

Sokolik, I. N., Winker, D. M., Bergametti, G., Gillette, D. A., Carmichael, G., Kaufman, Y. J., Gomes, L., Schuetz, L., and Penner, J. E.: Introduction to special section: Outstanding problems in quantifying the radiative impacts of mineral dust, J. Geophys. Res., 106, 18015-18027, doi:10.1029/2000jd900498, 2001.

Sokolik, I. N., and Toon O. B.: Incorporation of mineralogical composition into models of the radiative properties of mineral aerosol from UV to IR wavelengths, Journal of Geophysical Research, 104(D8), 9423-9444, 1999.

Streets, D. G., Gupta, G., Waldhoff, S. T., Wang, M. Q., Bond, T. C., and Yiyun, B.: Black carbon emissions in China, Atmospheric environment, 35(25), 4281-4296, 2001.

Stone, E., Schauer, J., Quraishi, T. A., and Mahnood, A.: Chemical characterization and source apportionment of fine and coarse particulate matter in Lahore, Pakistan, Atmos. Environ, 44, 1062-1070, 2010.

Sullivan, A., Peltier, R. E., Brock, C. A., Gouw, J. A. d., Holloway, J. S., Warneke, C., Wollny, A. G., and Weber, R. J.: Airborne measurements of carbonaceous aerosol soluble in water over northeastern united states: Method development and an investigation into water-soluble organic carbon sources, J. Geophys. Res., 111, D23S46, doi:10.1029/2006JD007072, 2006.

Sullivan, R. C., Guazzotti, S. A., Sodeman, D. A., and Prather, K. A.: Direct observations of the atmospheric processing of Asian mineral dust, Atmos. Chem. Phys., 7, 1213-1236, doi:10.5194/acp-7-1213-2007, 2007.

Sun, H., Biedermann, L., and Bond, T. C.: Color of brown carbon: A model for ultraviolet and visible light absorption by organic carbon aerosol, Geophysical Research Letters, 34(17), 2007.

Swap, R. J., Annegarn, H. J., Suttles, J. T., King, M. D., Platnick, S., Privette, J. L., and Scholes, R. J.: Africa burning: A thematic analysis of the Southern African Regional Science Initiative (SAFARI 2000), J. Geophys. Res., 108(D13), 8465, doi:10.1029/2003JD003747, 2003.

Swap, R. J., Annegarn, H. J., Suttles, J. T., Haywood, J., Helmlinger, M. C., Hely, C., Hobbs, P. V., Holben, B. N., Ji, J., King, M. D., Landmann, T., Maenhaut, W., Otter, L., Pak, B., Piketh, S. J., Platnick, S., Privette, J., Roy, D., Thompson, A. M., Ward, D. and Yokelson, R.: The Southern African Regional Science Initiative (SAFARI 2000): Overview of the dry season field campaign, S. Afr. J. Sci., 98, 125-130, 2002.

Swap, R. J., Garstang, M., Macko, S. A., Tyson, P. D., Maenhaut, W., Artaxo, P., Kallberg, P., and Talbot, R.: The long-range transport of southern African aerosol to the tropical South Atlantic, J. Geophys. Res., 101(D19), 23777-23791, doi:10.1029/95JD01049, 1996.

Takemura, T., Nakajima, T., Dubovik, O., Holben, B. N., and Kinne, S.: Single-scattering albedo and radiative forcing of various aerosols species with a global three-dimensional model, J. Clim., 15, 333-352, 2002.

Tang, I. N.: Chemical and size effects of hygroscopic aerosols on light scattering coefficients, J. Geophys. Res., 101, 19245-19250, 1996.

Tang, I. N.: Deliquescence properties and particle size change of hygroscopic aerosols, Brookhaven National Lab., Upton, NY (USA), 1979.

Tang, I. N.: Phase transformation and growth of aerosol particles composed of mixed salts, J. Aerosol Sci., 7, 361-371, 1976.

Tang, I. N., and Munkelwitz, H. R.: Composition and temperature dependence of the deliquescence properties of hygroscopic aerosols, Atmos. Environ., 27A, 467-473, 1993.

Tang, I. N., and Munkelwitz, H. R.: Simultaneous determination of refractive index and density of an evaporating aqueous solution droplet, Aeros. Sci. & Tech., 15, 201-207, 1991.

Tang, I. N., and Munkelwitz, H. R.: Water activities, densities, and refractive indices of aqueous sulfates and sodium nitrate droplets of atmospheric importance, J. Geophys. Res., 99, 18801-18808, 1994.

Tang, I. N., Wong, W. T., and Munkelwitz, H. R.: The relative importance of atmospheric sulfates and nitrates in visibility reduction, Atmos. Environ., 15, 2463-2471, 1981.

Tanré, D., Bréon, F. M., Deuzé, J. L., Dubovik, O., Ducos, F., Francois, P., Goloub, P., Herman, M., Lifermann, A., and Waquet, F.: Remote sensing of aerosols by using polarized, directional and spectral measurements within the A-Train: the PARASOL mission, Atmospheric Measurement Techniques, 4(7), 1383-1395, 2011.

Tanré, D., Herman, M., and Deschamps, P. Y.: Influence of the background contribution upon space measurements of ground reflectance, Appl. Optics, 20(20), 3676-3684, 1981.

Tanré, D., Kaufman, Y. J., Herman, M., and Mattoo, S.: Remote sensing of aerosol properties over oceans using the MODIS/EOS spectral radiances, J. Geophys. Res., 102, 16971-16988, 1997.

Tanré, D., Kaufman, Y. J., Holben, B. N., Chatenet, B., Karnieli, A., Lavenu, F. Blarel, L., Dubovik, O. Remer, L. A., and Smirnov, A.: Climatology of dust aerosol size distribution and optical properties derived from remotely sensed data in the solar spectrum, J. Geophy. Res., 106(D16), 18205-18217, 2001.

Tarantola, A.: Inverse problem theory: methods for data fitting and model parameter estimation, Elsevier, Amsterdam, 1987.

Tegen, I., and Fung, I.: Modeling of mineral dust in the atmosphere: Sources, transport, and optical thickness, J. Geophys. Res., 99, 22897-22914, 1994.

Terblanche, D. E., Mittermaier, M. P., Piketh, S. J., Bruintjies, R. T., and Burger, R. P.: The Aerosol Recirculation and Rainfall Experiment (ARREX): An initial study on aerosol-cloud interactions over South Africa, S. Afr. J. Sci., 96, 15-21, 2000.

Textor, C., Schulz, M., Guibert, S., Kinne, S., Balkanski, Y., Bauer, S., Berntsen, T., Berglen, T., Boucher, O., Chin, M., Dentener, F., Diehl, T., Easter, R., Feichter, H., Fillmore, D., Ghan, S., Ginoux, P., Gong, S., Grini, A., Hendricks, J., Horowitz, L., Huang, P., Isaksen, I., Iversen, T., Kloster, S., Koch, D., Kirkevag, A., Kristjansson, J. E., Krol1, M., Lauer, A., Lamarque, J. F., Liu, X., Montanaro, V., Myhre, G., Penner, J., Pitari, G., Reddy, S., Seland, Ø., Stier, P., Takemura, T., and Tie, X.: Analysis and quantification of the diversities of aerosol life cycles within AeroCom, Atmospheric Chemistry and Physics, 6, 1777-1813, 2006.

Tikhonov, A. N.: On the solution of incorrectly stated problems and a method of regularization, Dokl. Akad. Nauk SSSR, 151, 501-504, 1963.

Tikhonov, A. N., and Arsenin, V. Y.: Solution of ill-posed problems, Washington, DC: Winston, 1977.

Todd, M. C., Bou Karam, D., Cavazos, C., Bouet, C., Heinold, B., Baldasano, J. M., Cautenet, G., Koren, I., Perez, C., Solmon, F., Tegen, I., Tulet, P., Washington, R., and Zakey, A.: Quantifying uncertainty in estimates of mineral dust flux: An intercomparison of model performance over the Bodélé Depression, northern Chad, J. Geophys. Res., 113, D24107, 2008.

Todd, M. C., Washington, R., Martins, V., Lizcano, G., Dubovik, O., M'Bainayel, S., and Engelstaedter, S.: Properties of mineral dust from the Bodélé depression, Northern Chad during BodEx 2005, J. Geophys. Res., 112(D6), 541-553, 2006.

Torres, B.: Study on the influence of different error sources on sky radiance measurements and inversion-derived aerosol products in the frame of AERONET, Ph.D. thesis, University of Valladolid, 2012.

Torres, O., Bharia, P., Herman, J., Ahmad, Z., and Gleason, J.: Derivation of aerosol properties from satellite measurements of backscattered ultraviolet radiation: Theoretical bases, Journal of Geophysical Research, 103, 17009-17110, 1998.

Torres, O., Bharia, P., Herman, J., Sinyuk, A., Ginoux, P., and Holben, B.: A long-term record of aerosol optical depth from TOMS observations and comparison to AERONET measurements, Journal of the Atmospheric Sciences, 59, 398-413, 2002.

Torres, O., Bharia, P., Sinyuk, A., Welton, E., and Holben, B.: Total ozone mapping spectrometer measurements of aerosol absorption from space: Comparison to SAFARI 2000 ground-based observations, Journal of Geophysical Research, 110, D10S18, doi:10.1029/2004JD004611, 2005.

Touré, A. A., Rajot, J. L., Garba, Z., Marticorena, B., Petit, C., and Sebag, D.: Impact of very low crop residues cover on wind erosion in the Sahel, Catena., 85, 205-214, 2011.

Turn, S. Q., Jenkins, B. M., Chow, J. C., Pritchett, L. C., Campbell, D., Cahill, T., and Whalen, S. A.: Elemental characterization of particulate matter emitted from biomass burning: Wind tunnel derived source profiles for herbaceous and wood fuels, J. Geophys. Res., 102, 3683-3699, 1997.

Turpin, B. and Lim, H. J.: Species contributions to PM2.5 mass concentrations: revisiting common assumptions for estimating organic mass, Aerosol Sci. Tech., 35, 602-610, 2001.

Twomey, S.: On the numerical solution of Fredholm integral equations of the first kind by the inversion of the linear system produced by quadrature, J. Assoc. Comp. Mach., 10, 97-101, 1963.

Twomey, S.: Pollution and the planetary albedo, Atmospheric Environment, 8, 1251-1256, 1974.

Twomey, S.: The influence of pollution on the shortwave albedo of clouds, Journal of the Atmospheric Science, 34, 1149-1152, 1977.

Tyson, P. D., and Gatebe, C. K.: The atmosphere, aerosols, trace gases and biogeochemical change in southern Africa: A regional integration, S. Afr. J. Sci., 97, 106-118, 2001.

Usher, C. R., Michel, A. E., and Grassian, V. H.: Reactions on mineral dust, Chem. Rev., 103(12), 4883-4940, 2003.

Veihelmann, B., Levelt, P. F., Stammes, P., and Veefkind, J. P.: Simulation study of the aerosol information content in OMI spectral reflectance measurements, Atmos. Chem. Phys., 7, 3115-3127, 2007.

Virtanen, A., Joutsensaari, J., Koop, T., Kannosto, J., Yli-Pirilä, P., Leskinen, J., Mäkelä, J. M., Holopainen, J. K., Pöschl, U., Kulmala, M., Worsnop, D. R., and Laaksonen, A.: An amorphous solid state of biogenic secondary organic aerosol particles, Nature, 467(7317), 824-827, 2010.

Voss, K. J., Morel, A., and Antoine, D.: Detailed validation of the bidirectional effect in various case 1 waters for application to ocean color imagery, Biogeosciences, 4, 781-789, 2007.

Wagner, S. C., Govaerts, Y. M., and Lattanzio, A.: Joint retrieval of surface reflectance and aerosol optical depth from MSG/SEVIRI observations with an optimal estimation approach: 2. Implementation and evaluation, J. Geophys. Res., 115, D02204, doi:10.1029/JD011780, 2010.

Wandinger, U., Mattis, I., Tesche, M., Ansmann, A., Bösenberg, J., Chaikovski, A., Freudenthaler, V., Komguem, L., Linné, H., Matthias, V., Pelon, J., Sauvage, L., Sobolewski, P., Vaughan, G., and Wiegner, M.: Air mass modification over Europe: EARLINET aerosol observations from Wales to Belarus, Journal of Geophysical Research, 109, 2004.

Wang, L., Li, Z., Tian, Q., Ma, Y., Zhang, F., Zhang, Y., Li, D., Li, K., and Li, L.: Estimate of aerosol absorbing components of black carbon, brown carbon, and dust from ground-based remote sensing data of sun-sky radiometers, J. Geophys. Res., 118(12), 6534-6543, 2013.

Wanner, W., Li, X., and Strahler, A. H.: On the derivation of kernels for kernel-driven models of bidirectional reflectance, J. Geophys. Res., 100(D10), 21077-21089, 1995.

Waquet, F., Cairns, B., Knobelspiesse, K., Chowdhary, J., Travis, L. D., Schmid, B., and Mishchenko, M. I.: Polarimetric remote sensing of aerosols over land, J. Geophys. Res., 114, D01206, doi:10.1029/2008JD010619, 2009.

Waquet, F., Cornet, C., Deuzé, J. L., Dubovik, O., Ducos, F., Goloub, P., Herman, M., Lapyonok, T., Labonnote, L. C., Riedi, J., Tanré, D., Thieuleux, F., and Vanbauce, C.: Retrieval of aerosol microphysical and optical properties above liquid clouds from POLDER/PARASOL polarization measurements, Atmos. Meas. Tech., 6, 991-1016, 2013.

Waquet, F., Goloub, P., Deuzé, J. L., Leon, J. F., Auriol, F., Verwaerde, C., Balois, J. Y., and Francois, P.: Aerosol retrieval over land using a multiband polarimeter and comparison with path radiance method, J. Geophys. Res., 112, D11214, doi:10.1029/2006JD008029, 2007.

Washington, R., and Todd, M.C.: Atmospheric controls on mineral dust emission from the Bodélé Depression, Chad: The role of the low level jet. Geophys. Res. Lett, 32, L17701, http://dx.doi.org/10.1029/2005GL023597, 2005.

Washington, R., Todd, M. C., Engelstaedter, S., M'bainayel, S., and Mitchell, F.: Dust and the Low Level Circulation over the Bodélé Depression, Chad: Observations from BoDEx 2005, J. Geophys. Res., 111, D03201, doi:10.1029/2005JD006502, 2006.

Washington, R. W., Todd, M. C., Middleton, N., and Goudie, A. S.: Dust-storm source areas determined by the total ozone monitoring spectrometer and surface observations, Ann. Assoc. Am. Geogr., 93, 297-313, 2003

Weber, R. J., McMurry, P. H., Mauldin III, R. L., Tanner, D. J., and Eisele F. L.: New particle formation in the remote troposphere: A comparison of observations at various sites, Geophys. Res. Lett., 26, 307-310, doi: 10.1029/1998GL900308, 1999.

Weber, R. J., Sullivan, A. P., Peltier, R. E., Russell, A., Yan, B., Zheng, M., Gouw, J. A. d., Warneke, C., Brock, C., Holloway, J. S., Atlas, E. L., and Edgerton, E.: A study of secondary organic aerosol formation in the anthropogenicinfluenced southeastern united states, J. Geophys. Res., 112, D13302, doi:10.1029/12007JD008408, 2007.

Wellenius, G. A., Burger, M. R., Coull, B. A., Schwartz, J., Suh, H. H., Koutrakis, P., Schlaug, G., Gold, D. R., and Mittleman, M. A.: Ambient air pollution and the risk of acute ischemic stroke, Arch. Intern, Med., 172(3), 229-234, 2012

Williams, J., de Reus, M., Krejci, R., Fischer, H., Ström, J.: Application of the variability-size relationship to atmospheric aerosol studies: estimating aerosol lifetimes and ages, Atmos. Chem. Phys., 2, 133-145, 2002.

Winker, D., Hunt, W. H., and McGill, M. J.: Initial performance assessment of CALIOP, Geophysical Research Letters, L19803, doi: 10.1029/2007GL030135, 2007.

Winker, D., Pelon, J., Coakley, J. J. A., Ackerman, S., Charlson, R., Colarco, P., Flamant, P., Fu, Q., Hoff, R., Kittaka, C., Kubar, T. L., Treut, H. L., McCormick, M. P., Mégie, G., Poole, L., Powell, K., Trepte, C., Vaughan, M. A., and Wielicki, B.A.: The CALIPSO mission: A global 3D view of aerosol and clouds, Bulletin of the American Meteorological Society, 91, 1211-1229, 2010.

Wofsy, S. C., Team, H. S., Cooperating Modellers, T., and Satellite, T.: HIAPER Pole-to-Pole Observations (HIPPO): Fine-grained, global-scale measurements of climatically important atmospheric gases and aerosols, Phil. Trans. Math. Phys. Eng. Sci., 369(1943), 2073-2086, 2011.

Yoshioka, M., Mahowald, N., Dufresne, J.-L., and Luo, C.: Simulation of absorbing aerosol indices for African dust, J. Geophys. Res., 110, D18S17, doi:10.1029/2004jd005276, 2005.

You, Y., Renbaum-Wolff, L., Carreras-Sospedra, M., Hanna, S. J., Hiranuma, N., Kamal, S., Smith, M. L., Zhang, X., Wever, R. J., Shilling, J. E., Dabdub, D., Martin, S. T., and Bertram A. K.: Images reveal that atmospheric particles can undergo liquid-liquid phase separations, Proceeding of the National Academy of Sciences, 109(33), 13188-13193, 2012.

Yu, H., Dickinson, R., Chin, M., Kaufman, Y., Holben, B., Geogdzhayev, I., and Mishchenko, M.: Annual cycle of global distributions of aerosol optical depth from integration of MODIS retrievals

and GOCART model simulations, Journal of Geophysical Research, 108, 4128, doi:10.1029/2002JD002717, 2003.

Yu, H., Dickinson, R., Chin, M., Kaufman, Y., Zhou, M., Zhou, L., Tian, Y., Dubovik, O., and Holben, B.: The direct radiative effect of aerosols as determined from a combination of MODIS retrievals and GOCART simulations, Journal of Geophysical Research, 109, D0326, doi:10.1029/2003JD003914, 2004.

Yu, H., Kaufman, Y., Chin, M., Feingold, G., Remer, L., Anderson, T., Balkanski, Y., Bellouin, N., Boucher, O., Christopher, S., DeCola, P., Kahn, R., Koch, D., Loeb, N., Reddy, M. S., Schulz, M., Takemura, T., and Zhou, M.: A review of measurement-based assessments of aerosol direct radiative effect and forcing, Atmospheric Chemistry and Physics, 6, 613-666, 2006.

Yu, H., Remer, L. A., Chin, M., Bian, H., Kleidman, R., and Diehl, T.: A satellite-based assessment of trans-Pacific transport of pollution aerosol, Journal of Geophysical Research, 113, D14S12, doi:10.1029/2007JD009349, 2008.

Zhang, J., and Christopher, S. A.: Longwave radiative forcing of Saharan dust aerosols estimated from MODIS, MISR, and CERES observations on Terra, Geophys. Res. Lett., 30(23), 2188, doi:10.1029/2003GL018479, 2003.

Zhang, J., Reid, J. S., Westphal, D. L., Baker, N. L., and Hyer, E. J.: A system for operational aerosol optical depth data assimilation over global oceans, Journal of Geophysical Research, 113, doi:10.1029/2007JD009065, 2008a.

Zhang, X. Y., Wang, Y. Q., Niu, T., Zhang, X. C., Gong, S. L., Zhang, Y. M., and Sun, J. Y.: Atmospheric aerosol compositions in China: spatial/temporal variability, chemical signature, regional haze distribution and comparisons with global aersols, Atmos. Chem. Phys., 12, 779-799, 2012.

Zhang, X. Y., Wang, Y. Q., Wang, D., and Gong, S. L.: Characterization and sources of regional-scale transported carbonaceous and dust aerosols from different pathways in costal and sandy land areas of China, J. Geophys. Res., 110, D15301, doi:15310.11029/12004JD005457, 2005.

Zhang, X. Y., Wang, Y. Q., Zhang, X. C., Guo, W., and Gong, S. L.: Carbonaceous aerosol composition over various regions of China during 2006, J. Geophys. Res., 113, D14111, doi:10.1029/2007JD009525, 2008b.

Zhao, T. X.-P., Laszlo, I., Guo, W., Heidinger, A., Cao, C., Jelenak, A., Tarpley, D., and Sullivan, J.: Study of long-term trend in aerosol optical thickness observed from operational AVHRR satellite instrument, Journal of Geophysical Research, 113, D07201, doi:10.1029/2007JD009061, 2008

Zhao, T. X.-P., Stowe, L. L., Smirnov, A., Crosby, D, Sapper, J., and McClain, R.: Development of a global validation package for satellite oceanic aerosol optical thickness retrieval based on AERONET observations and its application to NOAA/NESDIS operational aerosol retrievals, J. Atmos. Sci., 59, 294-312, 2002.

Zhu, X., Prospero, J. M., Savoie, D. L., Millero, F. J., Zika, R. G., and Saltzman, E. S.: Photoreduction of iron (III) in marine mineral aerosol solutions, J. Geophys. Res., 98, 9039-9046, 1993.